

AD-A232 468

36
1

A SEARCH FOR STRANGE ATTRACTORS
IN THE SATURATION OF MIDDLE ATMOSPHERE GRAVITY WAVES

DTIC
ELECTE
MAR 08 1991
S D D

A THESIS
Presented to
The Academic Faculty

by

Jason Pierce Tuell

In Partial Fulfillment
of the Requirements for the Degree
Doctor of Philosophy
from
The School of Earth and Atmospheric Science

Georgia Institute of Technology
September 1990

91 3 05 099

REPORT DOCUMENTATION PAGE

Form Approved
OMB No. 0704-0188

Public reporting burden for this collection of information is estimated to average 1 hour per response, including the time for reviewing instructions, searching existing data sources, gathering and maintaining the data needed, and completing and reviewing the collection of information. Send comments regarding this burden estimate or any other aspect of this collection of information, including suggestions for reducing this burden, to Washington Headquarters Services, Directorate for Information Operations and Reports, 1215 Jefferson Davis Highway, Suite 1204 Arlington, VA 22202-4302 and to the Office of Management and Budget, Paperwork Reduction Project (0704-0188), Washington, DC 20503

1. AGENCY USE ONLY (Leave blank)		2. REPORT DATE September 1990	3. REPORT TYPE AND DATES COVERED THESIS/DISSERTATION	
4. TITLE AND SUBTITLE A Search for Strange Attractors in the Saturation of Middle Atmosphere Gravity Waves			5. FUNDING NUMBERS	
6. AUTHOR(S) Jason Pierce Tuell				
7. PERFORMING ORGANIZATION NAME(S) AND ADDRESS(ES) AFIT Student Attending: Georgiz Institute of Technology			8. PERFORMING ORGANIZATION REPORT NUMBER AFIT/CI/CIA-90-036D	
9. SPONSORING/MONITORING AGENCY NAME(S) AND ADDRESS(ES) AFIT/CI Wright-Patterson AFB OH 45433-6583			10. SPONSORING/MONITORING AGENCY REPORT NUMBER	
11. SUPPLEMENTARY NOTES				
12a. DISTRIBUTION/AVAILABILITY STATEMENT Approved for Public Release IAW 190-1 Distributed Unlimited ERNEST A. HAYGOOD, 1st Lt, USAF Executive Officer			12b. DISTRIBUTION CODE	
13. ABSTRACT (Maximum 200 words)				
14. SUBJECT TERMS			15. NUMBER OF PAGES 249	
			16. PRICE CODE	
17. SECURITY CLASSIFICATION OF REPORT	18. SECURITY CLASSIFICATION OF THIS PAGE	19. SECURITY CLASSIFICATION OF ABSTRACT	20. LIMITATION OF ABSTRACT	

NSN 7540-01-280-5500

Standard Form 298 (Rev. 2-89)
Prescribed by ANSI Std. Z39-18
298-102

GENERAL INSTRUCTIONS FOR COMPLETING SF 298

The Report Documentation Page (RDP) is used in announcing and cataloging reports. It is important that this information be consistent with the rest of the report, particularly the cover and title page. Instructions for filling in each block of the form follow. It is important to *stay within the lines* to meet optical scanning requirements.

Block 1. Agency Use Only (Leave blank).

Block 2. Report Date. Full publication date including day, month, and year, if available (e.g. 1 Jan 88). Must cite at least the year.

Block 3. Type of Report and Dates Covered. State whether report is interim, final, etc. If applicable, enter inclusive report dates (e.g. 10 Jun 87 - 30 Jun 88).

Block 4. Title and Subtitle. A title is taken from the part of the report that provides the most meaningful and complete information. When a report is prepared in more than one volume, repeat the primary title, add volume number, and include subtitle for the specific volume. On classified documents enter the title classification in parentheses.

Block 5. Funding Numbers. To include contract and grant numbers; may include program element number(s), project number(s), task number(s), and work unit number(s). Use the following labels:

C - Contract	PR - Project
G - Grant	TA - Task
PE - Program Element	WU - Work Unit Accession No.

Block 6. Author(s). Name(s) of person(s) responsible for writing the report, performing the research, or credited with the content of the report. If editor or compiler, this should follow the name(s).

Block 7. Performing Organization Name(s) and Address(es). Self-explanatory.

Block 8. Performing Organization Report Number. Enter the unique alphanumeric report number(s) assigned by the organization performing the report.

Block 9. Sponsoring/Monitoring Agency Name(s) and Address(es). Self-explanatory.

Block 10. Sponsoring/Monitoring Agency Report Number. (If known)

Block 11. Supplementary Notes. Enter information not included elsewhere such as: Prepared in cooperation with..., Trans. of..., To be published in.... When a report is revised, include a statement whether the new report supersedes or supplements the older report.

Block 12a. Distribution/Availability Statement. Denotes public availability or limitations. Cite any availability to the public. Enter additional limitations or special markings in all capitals (e.g. NOFORN, REL, ITAR).

DOD - See DoDD 5230.24, "Distribution Statements on Technical Documents."
DOE - See authorities.
NASA - See Handbook NHB 2200.2.
NTIS - Leave blank.

Block 12b. Distribution Code.

DOD - Leave blank.
DOE - Enter DOE distribution categories from the Standard Distribution for Unclassified Scientific and Technical Reports.
NASA - Leave blank.
NTIS - Leave blank.

Block 13. Abstract. Include a brief (Maximum 200 words) factual summary of the most significant information contained in the report.

Block 14. Subject Terms. Keywords or phrases identifying major subjects in the report.

Block 15. Number of Pages. Enter the total number of pages.

Block 16. Price Code. Enter appropriate price code (NTIS only).

Blocks 17. - 19. Security Classifications. Self-explanatory. Enter U.S. Security Classification in accordance with U.S. Security Regulations (i.e., UNCLASSIFIED). If form contains classified information, stamp classification on the top and bottom of the page.

Block 20. Limitation of Abstract. This block must be completed to assign a limitation to the abstract. Enter either UL (unlimited) or SAR (same as report). An entry in this block is necessary if the abstract is to be limited. If blank, the abstract is assumed to be unlimited.

A SEARCH FOR STRANGE ATTRACTORS
IN THE SATURATION OF MIDDLE ATMOSPHERE GRAVITY WAVES

A THESIS
Presented to
The Academic Faculty

by
Jason Pierce Tuell



Accession For	
NTIS CRAD1	<input checked="" type="checkbox"/>
DIC 712	<input type="checkbox"/>
Unpublished	<input type="checkbox"/>
Journal	<input type="checkbox"/>
By	
Date 8/1	
Institution / Office	
DI 1	Available for Special
A-1	

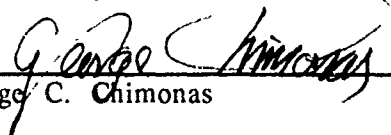
In Partial Fulfillment
of the Requirements for the Degree
Doctor of Philosophy
from
The School of Earth and Atmospheric Science

Georgia Institute of Technology
September 1990


A SEARCH FOR STRANGE ATTRACTORS
IN THE SATURATION OF MIDDLE ATMOSPHERE GRAVITY WAVES

APPROVED


Robert G. Roper, Chairman


George C. Chimonas


Derek Cunlold


Anca Deliu


Carl G. Justus

Date Approved by Chairman

9/25/90

**This thesis is dedicated to my wife, Isabel B. Whiston,
whose patience made it possible.**

TABLE OF CONTENTS

	Page
ACKNOWLEDGEMENT	vii
LIST OF TABLES	viii
LIST OF ILLUSTRATIONS	ix
SUMMARY	xiii
 Chapter	
I. INTRODUCTION	1
1.1 Motivation.	3
1.2 Organization.....	6
 II. GRAVITY WAVES AND CHAOS IN FLUIDS.....	 9
2.1 Chaos in Laboratory Experiments.....	9
2.1.1 Closed Systems.....	9
2.1.1.1 Rayleigh-Bénard Convection	10
2.1.1.2 Couette-Taylor Flow	11
2.1.2 Open Systems.....	12
2.1.3 Routes to Chaos.....	14
2.1.3.1 Intermittency.....	15
2.1.3.2 Frequency Locking.....	15
2.1.3.3 Period Doubling	15
2.1.3.4 Periodic-Quais-Periodic-Chaotic Sequence.....	16
2.2 Chaos in the Atmosphere.....	16
2.2.1 Short Time Scales.....	16
2.2.2 Long Time Scales.....	17

2.3 Gravity Waves and Gravity Wave Breaking.....	20
2.3.1 Conventional Saturation Theory.....	23
2.3.2 Slantwise Static Instability Theory.....	28
2.3.3 Nonlinear Mechanisms.....	32
III. THE METHODS OF ANALYSIS.....	35
3.1 The Grassberger-Procaccia Correlation Integral Algorithm.....	35
3.1.1 Concepts of Dimension.....	37
3.1.2 Building Phase Space Vectors.....	39
3.1.3 Trajectories in Phase Space.....	40
3.1.4 Derivation of the Grassberger-Procaccia Algorithm.....	40
3.1.5 Generalized Correlation Integral.....	45
3.2 Limitations of the Grassberger-Procaccia Algorithm.....	48
3.2.1 Noise.....	48
3.2.2 Filtering and Digitizing Errors.....	49
3.2.3 Number of Points.....	50
3.2.4 Time Delay.....	51
3.2.5 The Norm.....	53
3.2.6 Non-Stationary Data Sets.....	54
3.3 Extension of the Grassberger-Correlation Integral.....	55
3.3.1 The Normalization Factor.....	58
3.4 Autocorrelation Analysis.....	58
3.5 Power Spectrum Analysis.....	60
IV. OVERVIEW OF THE DATA.....	65
4.1 Theory Of Partial Reflection Radars.....	65
4.2 Saskatoon Partial Reflection Radar.....	67
4.3 Overview of the Data.....	67

V. ANALYSIS AND INTERPRETATION.....	108
5.1 Analysis.....	108
5.1.1 Calculating the Best Choice for Time Delay.....	108
5.1.2 Autocorrelation.....	109
5.1.3 Calculating W.....	110
5.1.4 Implementing the Grassberger-Procaccia Algorithm.....	111
5.2 Power Spectrum Analysis.....	112
5.3 Interpretation.....	116
5.3.1 Interpreting the Slope as a Function of ϵ	116
5.3.2 Calculating the Slope.....	118
5.3.3 Why Noise?.....	118
5.3.3.1 Difficulties with the Algorithm.....	119
5.3.3.2 Difficulties with the Data.....	120
5.3.3.3 Invalid Hypothesis.....	123
VI. CONCLUSION AND RECOMMENDATIONS FOR FUTURE WORK.....	200
6.1 Conclusions.....	200
6.2 Recommendations for Future Work.....	201
APPENDICES	
APPENDIX A.....	205
APPENDIX B.....	223
BIBLIOGRAPHY.....	241

ACKNOWLEDGEMENTS

I wish to thank the members of my reading committee whose comments and suggestions made this a much better work. Their efforts were appreciated; I hope it shows in the final product.

I wish to acknowledge the help of Scott Ward who assisted with the figures in the Appendices.

The inspiration for this thesis came in the form of a book given to me by mother-in-law, Isabelle Whiston. Little did she know that she would provide me with much more than a weekend's diversion.

My office mate and friend, Eric Schmidt, deserves special credit. He sacrificed his own time carefully proofreading the many drafts of this thesis. Many of the small details are correct because he found the mistakes.

Special thanks are due my advisor, Dr. Bob Roper. He invested many hours listening to me grope my way to an understanding of the problem. Any flaws in this work are entirely my own. He served a role more important than advisor during this process; he became a good friend.

A meow of thanks to Osbert, who clung to life until the very end. Research is easier with a cat asleep on your desk. Dead cats, on the other hand, further science not a whit.

This could not have been completed without the support, patience and grace of my wife, Isabel. She was a silent and uncomplaining witness to the labors that brought this forth.

LIST OF TABLES

Table 3.1	Dimension definitions.....	37
Table 4.1	Summary of mean and variance changes in the data.....	69
Table 5.1	Lag for the first local minimum in the mutual information.....	109
Table 5.2	Lag (λ) for the first zero in the autocorrelation.....	110
Table 5.3	The value of W for each antenna and level (N=1500, m=13).....	111
Table 5.4	Slope for power law curve fits between 1-2 and 6-10 s.....	114

LIST OF ILLUSTRATIONS

Figure 2.1	Nonvertical orientation for the potential temperature gradient. Interchanges of air parcels along axes within the shaded regions such as the s axis are unstable (adapted from Hines, 1988).....	34
Figure 3.1	Correlation integral of the sine function with period equal to thirty with 10% external noise. The total number of points is 2000.....	62
Figure 3.2	Kolmogorov entropy (K_2) for the correlation integral of the sine function shown in Figure 3.1 plotted as a function of increasing embedding dimension. The curve asymptotically approaches the value of 0, indicating periodic behavior.....	63
Figure 3.3	Phase space portrait of a sine function with period of 300 for a time delay of $t=1$ and a time delay equal to the first zero in the autocorrelation, i.e. $t=75$	64
Figure 4.1	Depiction of a diffraction pattern on the ground moving past the antenna array. The antennas are shown by the squares and the direction of motion of the pattern is indicated by the arrow.....	72
Figure 4.2	Receiving array of Saskatoon radar in the Y configuration, (adapted from Meek and Manson, 1987).....	73
Figure 4.3	Autocorrelation for antenna #1 at 94 km for points 14000 through 16000 (i.e., data from the contaminated third file).....	74
Figure 4.4	Power spectrum for antenna #1 at 94 km. This includes the data from the contaminated second and third files.....	75

Figure 4.5	Data from antenna #1 for (a) 76 km; (b) 79 km; (c) 82 km; (d) 85 km; (e) 88 km; (f) 91 km; and (g) 94 km. The data starts at 18:31:00 GMT. The figure is on the following pages.....	76-83
Figure 4.6	Data from antenna #2 for (a) 76 km; (b) 79 km; (c) 82 km; (d) 85 km; (e) 88 km; (f) 91 km; and (g) 94 km. The data starts at 18:31:00 GMT. The figure is on the following pages.....	84-91
Figure 4.7	Data from antenna #3 for (a) 76 km; (b) 79 km; (c) 82 km; (d) 85 km; (e) 88 km; (f) 91 km; and (g) 94 km. The data starts at 18:31:00 GMT. The figure is on the following pages.....	92-99
Figure 4.8	Data from antenna #4 for (a) 76 km; (b) 79 km; (c) 82 km; (d) 85 km; (e) 88 km; (f) 91 km; and (g) 94 km. The data starts at 18:31:00 GMT. The figure is on the following pages.....	100-107
Figure 5.1	Mutual information for antenna #1 calculated from the first 6000 points for levels 76 through 94 km.....	126
Figure 5.2	Mutual information for antenna #2 calculated from the first 6000 points for levels 76 through 94 km.....	127
Figure 5.3	Mutual information for antenna #3 calculated from the first 6000 points for levels 76 through 94 km.....	128
Figure 5.4	Mutual information for antenna #4 calculated from the first 6000 points for levels 76 through 94 km.....	129
Figure 5.5	Autocorrelation (2000 point groups) for antenna #1 for (a) 76 km, (b) 79 km, (c) 82 km, (d) 85 km, (e) 88 km, (f) 91 km and (g) 94 km.....	130-133
Figure 5.6	Autocorrelation (2000 point groups) for antenna #2 for (a) 76 km, (b) 79 km, (c) 82 km, (d) 85 km, (e) 88 km, (f) 91 km and (g) 94 km.....	134-137

Figure 5.7	Autocorrelation (2000 point groups) for antenna #3 for (a) 76 km, (b) 79 km, (c) 82 km, (d) 85 km, (e) 88 km, (f) 91 km and (g) 94 km.....	138-141
Figure 5.8	Autocorrelation (2000 point groups) for antenna #4 for (a) 76 km, (b) 79 km, (c) 82 km, (d) 85 km, (e) 88 km, (f) 91 km and (g) 94 km.....	142-145
Figure 5.9	Correlation integral plotted as a function of embedding dimension m for points 1 through 1500 from antenna 1 for (a) 76 km; (b) 79 km; (c) 82 km; (d) 85 km (e) 88 km; (f) 91 km and (g) 94 km.....	146-152
Figure 5.10	Power spectral density for antenna #1 for (a) 76 km, (b) 79 km, (c) 82 km, (d) 85 km, (e) 88 km, (f) 91 km and (g) 94 km.....	153-156
Figure 5.11	Power spectral density for antenna #2 for (a) 76 km, (b) 79 km, (c) 82 km, (d) 85 km, (e) 88 km, (f) 91 km and (g) 94 km.....	157-160
Figure 5.12	Power spectral density for antenna #3 for (a) 76 km, (b) 79 km, (c) 82 km, (d) 85 km, (e) 88 km, (f) 91 km and (g) 94 km.....	161-164
Figure 5.13	Power spectral density for antenna #4 for (a) 76 km, (b) 79 km, (c) 82 km, (d) 85 km, (e) 88 km, (f) 91 km and (g) 94 km.....	165-168
Figure 5.14	Power law fits for the power spectra from antenna #1 for (a) 76 km, (b) 76 km, (c) 79 km, (d) 79 km, (e) 82 km, (f) 82 km, (g) 85 km, (h) 85 km, (i) 88 km, (j) 88 km, (k) 91 km and (l) 94 km.....	169-174
Figure 5.15	Power law fits for the power spectra from antenna #2 for (a) 76 km, (b) 76 km, (c) 79 km, (d) 79 km, (e) 82 km, (f) 82 km, (g) 85 km, (h) 85 km, (i) 88 km, (j) 91 km and (k) 94 km.....	175-180

- Figure 5.16 Power law fits for the power spectra from antenna #3 for
 (a) 76 km, (b) 79 km, (c) 79 km, (d) 82 km, (e) 82 km, (f)
 85 km, (g) 88 km, (h) 91 km, (i) 91 km and (j) 94 km..... 181-185
- Figure 5.17 Power law fits for the power spectra from antenna #4 for
 (a) 76 km, (b) 79 km, (c) 82 km, (d) 82 km, (e) 85 km, (f)
 85 km, (g) 88 km, (h) 88 km, (i) 91 km and (j) 94 km..... 186-190
- Figure 5.18 Idealized depiction of the slope of the natural logarithm
 of the correlation integral as a function of ϵ . The figure
 is divided into four distinct regions as indicated by the
 dashed lines.....191
- Figure 5.19 Slope of the correlation integral plotted as a function of
 embedding dimension for points 1 through 1500 from
 antenna 1 for (a) 76 km; (b) 79 km; (c) 82 km; (d) 85 km
 (e) 88 km; (f) 91 km and (g) 94 km..... 192-198
- Figure 5.20 Correlation integral (a) and corresponding slope (b) for
 82 km for antenna #1 (N=5000 points).....199

SUMMARY

In this study, we searched for evidence of a strange attractor associated with the saturation of middle atmosphere gravity waves in the echo data from a partial reflection radar located in Saskatoon, Canada. Theiler's extension of the Grassberger-Procaccia correlation integral algorithm was used to estimate the fractal dimension of the attractor.

Chaotic regimes have been observed in experimental fluid studies of the transition from ordered to turbulent behavior. Breaking gravity waves are thought to decay to turbulence, transporting momentum from the lower to upper atmosphere. ^{By} Extending ~~the results from~~ ^{study results} laboratory studies to middle atmosphere gravity waves, it seems reasonable to expect to find a strange attractor in gravity wave saturation.

Echo data was analyzed because it offered a high sampling rate. The Grassberger-Procaccia algorithm places stringent requirements upon the amount of data necessary to obtain an accurate estimate of the system dimension; a large number of points is required.

We did not detect a strange attractor with dimension < 3 in the data from the Saskatoon partial reflection radar for the time scales (6 min 39 s) which were studied. Because of the small number of points which were examined, we can not assert that there was only noise in the data. However, the supporting evidence from the power spectra suggest that we mainly investigated time scales in the viscous and inertial regions.

This study can not assert that a strange attractors is absent in gravity wave absorption. The data requirements to implement the Grassberger-Procaccia algorithm make it unlikely that such an attractor, if it exists, will be detected. Calculations of the amount of data necessary to estimate the dimension indicate that over 6 hours of data would be required to detect a strange attractor in gravity wave absorption.

CHAPTER I

INTRODUCTION

In the last 10 years, MLT (mesosphere, lower thermosphere) radars have been increasingly important in the observation of the middle atmosphere¹. During this same period, gravity waves and gravity wave saturation have been recognized as playing a vital role in the maintenance and modification of the mesospheric circulation and temperature distribution (Fritts, 1984). In addition, this same period also saw great advances in the area popularly referred to as "chaos theory".

Chaotic behavior (or the presence of strange attractors²) has been observed in experimental studies of the transition from laminar to turbulent fluid flow (see Swinney (1983) for a review of early experimental results for different systems). Gravity waves undergoing saturation³ break down; the end product is turbulence. Techniques have been developed to determine the presence and dimension of a strange attractor in a set of data (Grassberger and Procaccia, 1983, 1984). It does not seem unreasonable to expect to find a strange attractor associated with the saturation of middle atmosphere gravity waves.

Saturation of middle atmosphere gravity waves has been inferred from theory and direct observations. Gravity wave saturation currently provides the only known mechanism for the observed structure of the mesospheric

¹ In this thesis, the commonly accepted definition of the middle atmosphere, i.e., that region of the atmosphere which encompasses the stratosphere and mesosphere, will be used. This definition roughly includes the region of the atmosphere from 10 to 100 km.

² An attractor is defined as "strange" if its phase space trajectories diverge exponentially on the average.

³ The term "gravity wave saturation" refers to any process that acts to limit or maintain constant wave amplitudes with height.

circulation (most importantly, the closing of the mesospheric jets) and the observed temperature structure. Examples of the indirect evidence of gravity wave saturation include observations of regions of enhanced turbulent diffusion, measurements of super-adiabatic lapse rates in the mesosphere and lower thermosphere and measurements of momentum drag in the mesosphere (see Fritts (1984) for a detailed description and list of references for these different observations). The most direct evidence comes from the observations of Kelvin-Helmholtz billows near the summer mesopause, as revealed in the perturbation of noctilucent clouds.

Chaos theory has provided some insights into the transition of fluid flows from orderly to turbulent regimes. Traditional analysis of meteorological data has centered on the search for wavelike or periodic behavior. Tools such as Fourier analysis yield no meaningful results when applied to aperiodic signals. Irregular or aperiodic signals usually are filtered out or deemed noise. This noise may hide the presence of a strange attractor within the data. As Froehling et al. (1981) point out, "power spectral analysis, for example, characterizes aperiodic behavior by the presence of broadband noise in the power spectrum, but broadband noise can be produced by systems requiring either a small or large number of phase space dimensions."⁴

The technique of Grassberger and Procaccia (1983, 1984) has been used to examine various experimental data sets. Atmanspacher et al. (1988) employed the correlation integral technique of Grassberger and Procaccia to examine the chaotic attractor associated with X-ray counts from the neutron star Her X-1. Tsonis and Elsner (1988) employed this same technique on daytime vertical wind velocities in the boundary layer. Brandstätter and Swinney (1987) applied the Grassberger-Procaccia algorithm to experimental data obtained from the observation of Couette-Taylor flow. Elgar and Mayer-Kress (1989) applied the correlation integral technique to ocean wave data and found

⁴ Froehling et al. (1981), p605.

a system with a correlation dimension⁵ greater than 9. Osborne et al. (1986) used the Grassberger-Procaccia algorithm to find a correlation dimension of 1.4 in the motions of buoys in the Pacific ocean. There are many additional studies in which this technique was used; some are described in later chapters.

1.1 Motivation

This study proposes to search for a strange attractor associated with the saturation of middle atmosphere gravity waves in the echo data obtained from a partial reflection radar located in Saskatoon, Canada. This study rests on the hypothesis that there is a strange attractor associated with the saturation of middle atmosphere gravity waves and that it can be detected in middle atmosphere data.

We chose to use the raw echo data from the partial reflection radar because it had a high sampling rate; the normal post-processing which retrieves horizontal winds yields only one data point for approximately two minutes of echo data and introduces a degree of smoothing to the signal. The relationship between the echoes and the dynamics and physics of the middle atmosphere is not completely understood; this drawback will hinder the interpretation of the physical meaning of any attractor that might be found. The data set studied here was chosen because of the possibility that it contained gravity waves and it was given to us (free!).

The laboratory studies described in Chapter 2 suggest that there is a transitional regime in many fluids between laminar and random behavior. This transitional regime occurs when some critical stability parameter is exceeded. Once this critical threshold is passed, the flow is considered chaotic and is characterized by a low dimension, non-integer attractor. The dimension of these systems is integer for stability parameter values which are below the critical level but becomes non-integer once this critical threshold is passed

⁵ See Chapter III for a discussion of the different definitions of dimension.

and increases as the stability of the system decreases. However, these systems take many different routes from ordered (i.e., periodic) to chaotic behavior; there does not appear to be a universal route to chaotic behavior. This will be discussed in detail in Chapter III.

Upward propagating gravity waves are thought to grow until they become unstable and decay to turbulence, transporting momentum from the lower atmosphere to the upper atmosphere. Their stability changes continuously as the gravity waves propagate upward and is a function of the wave, the atmosphere through which it propagates and the interaction between the wave (or waves, as is the more likely scenario) and the atmosphere. If the results from laboratory studies can be extended to gravity waves in the atmosphere, the saturation of middle atmosphere gravity waves may also be characterized by a transitional regime and hence a strange attractor. The dimension of this attractor should be a function of altitude, since the stability of the gravity wave is a function of atmospheric variables which vary with height. The dimension of the gravity wave should become non-integer once it becomes saturated and should increase as the wave propagates upward past the saturation level.

This study does not depend on the exact mechanism of gravity wave saturation; there are many different conceptual models of gravity wave breaking. It assumes only that gravity waves do become saturated in the middle atmosphere. There are some mechanisms which limit gravity wave growth (e.g., nonlinear wave-wave interaction) but do not result in wave breaking. In addition, other types of fluid instabilities occur in the middle atmosphere besides those associated with gravity waves, e.g., Kelvin-Helmholtz instability. The Kelvin-Helmholtz instability is supported by observations of billow clouds near the summer mesopause (Fritts, 1984).

We focus on gravity waves because the vertical profiles generated by the radar can be used to monitor the changes in the system dimension as the wave propagates upward and the stability changes. This does not rule out

detecting strange attractors in the data which are the result of some other type of wave and instability. If chaotic behavior in the transition from laminar to turbulent flow is universal then we should find evidence of strange attractors for fluid instabilities other than gravity waves. Two different models of gravity wave instability are reviewed in the hope that finding a strange attractor may offer insight into which model better describes gravity wave saturation.

The hypothesis that there is a strange attractor associated with the saturation of middle atmosphere gravity waves which we will be able to detect rests on many assumptions. The biggest assumption is that the transition to chaotic behavior observed in experimental studies is applicable to the types of fluid instabilities that occur in the atmosphere. The second assumption is that we will be able to detect the presence of a strange attractor in atmospheric data.

None of the fluid studies that have shown the transition from order to chaos in the laboratory are a particularly apt analogy for atmospheric gravity waves. Closed systems (e.g., Rayleigh-Bénard convection, Couette-Taylor flow) are very dissimilar to gravity waves. The experimental system closest to gravity waves in which the transition to chaotic behavior is observed is the excited jet (Bonetti and Boon, 1989). Chaotic behavior may be specific to these systems and not indicative of a more universal behavior.

We might not be able to detect a strange attractor in gravity wave saturation even if it exists. Experimental studies offer the opportunity to make a long series of observations of a fluid under precisely controlled conditions. Such controlled conditions do not exist in the atmosphere; the atmosphere changes continuously. The search for strange attractors in atmospheric data has been largely unsuccessful despite studies which claim to find them (see Chapter II for a summary of these studies and our critique). Measurements of the atmosphere are rarely stationary (in the statistical sense) and never contain as much data as one would like. These two problems create an almost

insurmountable obstacle to detecting strange attractors in atmospheric data as will be discussed in later chapters.

The data set may not contain any evidence of gravity wave saturation. In laboratory studies, measurements can be made at several locations in the fluid (especially for closed systems) and over a long period of time under precisely controlled conditions. In the case of the excited jet, measurements were made at one location as the flow streamed by. We can not measure gravity waves in a similar manner. Under ideal conditions, gravity waves will propagate through the volume of the atmosphere that is probed by the radar and thereby be detected. It may be unlikely that gravity waves will undergo saturation in the volume of the atmosphere that is directly being measured. However, the turbulence left behind by gravity wave saturation may be detected as it is advected over the radar site by the mean wind.

1.2 Organization

This work is divided into six chapters. The first chapter, "Introduction", is almost complete by this point. The second chapter is titled "Gravity Waves and Chaos in Fluids" followed by chapter III, "The Methods of Analysis". The data and its source are reviewed in Chapter IV, "Overview of the Data". The fifth chapter, "Analysis and Interpretation", contains the analysis of the data and describes its meaning. The final chapter, "Conclusion and Recommendations for Future Work", provides a summary of the conclusions and suggestions for further work

Chapter II gives a brief review of some of experimental work done on different types of fluid flows in which chaotic behavior was observed. It describes some of the most common routes to chaotic behavior observed in fluid experiments and how they are interpreted. Chapter II also contains a brief account of attempts at detecting strange attractors in atmospheric data and the different flaws in many of these studies. The chapter concludes with a

very brief review of gravity wave theory; it focuses on two of the many possible mechanisms behind gravity wave saturation in the upper atmosphere.

Chapter III describes the methods used to analyze the data. Because analyzing meteorological data for chaotic behavior is relatively new, most of the chapter is devoted to a detailed overview of the Grassberger-Procaccia correlation integral algorithm. The strengths, weaknesses and limitations of this algorithm are thoroughly reviewed. The chapter concludes with a brief overview of the more conventional autocorrelation and power spectrum analysis that will be used to supplement the analysis of system dimension.

The data used in this analysis is described in Chapter IV. The theory behind partial reflection radar measurement techniques is briefly reviewed because it adds some insight into how to interpret the data. The data set contained a number of deficiencies which limited the scope of the analysis; these are also described in Chapter IV.

Chapter V covers the implementation of the analysis, the results and their interpretation. The first section describes the implementation of the Grassberger-Procaccia algorithm along with the necessary supporting analysis. A sample of the results of this analysis is given in the following section. The chapter concludes with the interpretation and discussion of the results of the analysis of the system dimension.

The conclusions and recommendations for future work are given in Chapter VI. This thesis leaves many unanswered questions which provide ample room for further research. While no evidence of chaotic behavior was found in this data set, there still remains more work to be done on both refining the analysis technique as applied to atmospheric data and searching for chaotic behavior in the generation of atmospheric turbulence.

Appendix A contains the complete set of graphs depicting the results of the correlation integral algorithm analysis. These are included in their entirety to fully document the negative results of this study. The

corresponding slopes of the figures shown in Appendix A are included in Appendix B. The slope of the correlation integral should be equal to the fractal dimension of the attractor if there are sufficient points to fully saturate the attractor in phase space.

CHAPTER II

GRAVITY WAVES AND CHAOS IN FLUIDS

This chapter reviews some of the work on chaotic behavior in different types of fluid regimes observed in laboratory experiments. It also provides a brief description of attempts to find evidence of a fractal dimension (and thus a strange attractor) in atmospheric data. It concludes with a general description of internal gravity waves in the atmosphere and a discussion of two possible mechanisms of gravity wave breaking.

2.1 Chaos in Laboratory Experiments

Laboratory experiments which examine chaotic behavior in fluids can be divided into two categories: those in open systems and those in closed systems. In closed systems, the fluid is confined between rigid boundaries. In open systems, the fluid is either not bound by rigid boundaries or the boundaries are far enough away as to not influence the flow. Couette-Taylor flow and Rayleigh-Bénard convection are examples of closed systems. The excited jet is an open system whose description will follow that of the closed systems.

2.1.1 Closed Systems

Two of the most frequently examined closed systems are Rayleigh-Bénard convection and Couette-Taylor flow. Both systems provide well defined examples of the transition to chaotic behavior as exemplified by weakly developed turbulence.

In the Rayleigh-Bénard system, the fluid is confined between two parallel plates which are held at different temperatures, usually by heating the lower plate. The fluid develops convective cells whose behavior is a function of the dimensionless Rayleigh number, $R_d = (g\alpha d^3/\kappa\nu)\Delta T$, where g is the acceleration due to gravity, α the thermal expansion coefficient, d the distance between the two plates, κ the thermal diffusivity, ν the kinematic viscosity and ΔT the temperature boundary conditions on the side walls (Swinney, 1983).

In the Couette-Taylor system, the fluid is confined between two concentric cylinders which rotate independently at angular velocity Ω_i and Ω_o . Most studies have focused on the case where the rotation rate of the inner cylinder is zero. The behavior of Couette-Taylor flow is governed by the dimensionless Reynold's number, $R = ((b - a)b\Omega_o/\nu)$, where a and b are the radii of the inner and outer cylinders respectively, Ω_o is the angular velocity of the outer cylinder, and ν is the kinematic viscosity (Swinney, 1983).

2.1.1.1 Rayleigh-Bénard Convection

Bonetti and Boon (1989) note that the low dimension chaotic attractor in Rayleigh-Bénard convection is "a consequence of the high confinement imposed by the boundaries on the internal flow which results in strong coupling between modes"¹. The end result is spatially coherent "frozen" flow which is described by a single, low dimension, chaotic attractor. In small aspect ratio² Rayleigh-Bénard systems, the primary routes to chaos are period doubling and intermittency (Behringer, 1985); see the following section for definitions of the different routes to chaos.

In large aspect ratio Rayleigh-Bénard systems, chaos is generated by competition between different unstable modes, each of which can be described

¹ Bonetti and Boon (1989), p3322.

² The aspect ratio is defined as the ratio of the horizontal dimension to the depth.

by a localized chaotic attractor (Walden et al., 1985). The turbulence in these systems is "spatio-temporal" which results in a loss of spatial coherence in the flow. Behringer (1985) feels the precise route to chaos is still unclear.

Libchaber et al. (1983) studied the route to chaos for Rayleigh-Bénard convection in the presence of a magnetic field as a function of two control parameters, the Rayleigh number R_d and the Chandrasekhar number Q ; Q is defined as

$$Q \equiv \frac{\sigma B_0^2 d^2}{\rho \nu}, \quad (2.1)$$

where σ is the electrical conductivity, B_0 is the magnitude of the horizontal magnetic field, d is the depth of the fluid, ρ is the fluid density and ν is the kinematic viscosity. The magnetic field tends to "stiffen" the fluid allowing Rayleigh numbers higher than the normal critical values to be investigated; thus, larger nonlinearities in the convection can be examined. Libchaber et al. (1983) found period doubling and frequency locking to be the routes to chaotic behavior for low Rayleigh numbers and low magnetic fields. Libchaber et al. (1983) found quasi-periodicity and soft mode instability (i.e., the interaction between oscillatory instability and stationary instability) as the routes to chaos for high Rayleigh numbers.

2.1.1.2 Couette-Taylor Flow

Brandstätter and Swinney (1987) examined chaotic behavior in Couette-Taylor flow. For values of $R/R_c < 11.7$, where R and R_c are the Reynolds and critical Reynolds number for the system, the dimension of the system is 2 for modulated, wavy vortex flow. When the ratio of Reynolds numbers exceeds that threshold, the dimension of the system becomes non-integer and slightly greater than 2. This threshold also marks the first appearance of broadband

noise in the power spectrum. Brandstätter and Swinney (1987) note that the exponential decay in the power spectrum provided further evidence of non-periodic behavior corresponding to a low dimension chaotic attractor rather than stochastic processes. The dimension of the system increased as the ratio of Reynolds numbers (R/R_c) increased above the critical threshold (Brandstätter et al., 1983; Brandstätter and Swinney, 1987).

Brandstätter and Swinney (1987) found that the attractor dimension characterized flow over the entire annulus. The dimension was the same (within the error limits of the calculation) for measurements made at a number of different locations in the flow. Thus, the attractor characterized the entire flow in the annulus rather than a specific location in the fluid. This result will not be true of open systems.

Brandstätter and Swinney (1987) found that none of the well established routes to chaos, e.g., period doubling, intermittency, described the transition to chaos in this system for the conditions they investigated. They speculate that their experiment revealed another route to chaos which requires further study.

2.1.2 Open Systems

The transition to fully developed turbulence is generally investigated in open systems whereas the transition to weakly developed turbulence is studied in closed systems. The excited jet provides an example of chaotic behavior in an open system (Bonetti and Boon, 1989). The excited jet is of interest to us because of similarities to shear flows in the atmosphere.

Bonetti and Boon (1989) observe that the region of growth of the most unstable mode in open systems is followed by nonlinear saturation of those modes which generate advected coherent structures. This process leads to three dimensional destabilization and breakdown of these coherent structures. Bonetti and Boon (1989) investigated this highly transitional region in open

flow as exemplified by the excited jet in an effort to examine the spatial destabilization of "coherent structures" in the flow.

The excited jet is a stream of air that is emitted under pressure from a pipe. The flow is axially symmetric and has a Poiseuille velocity profile as a function of radial distance from the center of the flow. The jet is excited by applying a perturbation to the flow (i.e., by vibrating the end of the pipe from which the flow emerges).

The excited jet has three distinct regions downstream: the laminar region, the weakly turbulent zone and the turbulent zone. (Bonetti and Boon, 1989). The laminar region, nearest the source of the flow, is characterized by stationary macroscopic structures. This region is followed by a weakly turbulent zone where the macroscopic structures are no longer steady in time. Farther downstream is the turbulent zone where the macroscopic structures have disappeared and flow is essentially random; mixing occurs in this zone. Bonetti and Boon (1989) note that the appearance of these regions was independent of the excitation frequency, although varying the frequency did alter their length. They sampled over 8000 periods of the attractor making between 10 and 30 measurements per period.

Although they could not accurately determine the Kolmogorov entropy, Bonetti and Boon (1989) did determine that it had a finite non-zero value which is indicative of chaotic behavior (Grassberger and Procaccia, 1983). Bonetti and Boon (1989) found that the flow was characterized by a non-integer dimension which had an initial value of less than 3 but increased farther downstream to between 3 and 4. The increase in attractor dimension downstream was associated with a corresponding growth in broadband noise in the power spectrum. The turbulent region was characterized by a continuous growth in the correlation dimension downstream; the attractor in this region was not saturated due to an inadequate number of points. This was most likely because the flow became essentially random although the limited number of points in the data set makes this conclusion tenuous.

Unlike closed systems where the attractor characterized the flow in the entire system, the attractor dimension in open systems only characterized the flow over a local length scale (Bonetti and Boon, 1989). The local length scale is defined as the distance to the first zero in the spatial autocorrelation or the distance to the first local minimum in the spatial mutual information. Intuitively, this makes sense. The attractor dimension in closed systems increases as an external stability criteria decreases; the change in stability characterizes the entire system. The instability in the open jet amplifies downstream corresponding to a continuum of stability changes in the downstream direction. Consequently, the attractor dimension grows downstream as the instability amplifies. Each downstream location in open flow is analogous to a different external stability criterion in closed flow. Since each stability criterion in closed flow had a characteristic attractor dimension, so will each downstream location in open flow (to within the local length scale) have its characteristic dimension.

2.1.3 Routes to Chaos

There are several well established routes to chaotic behavior: intermittency, frequency locking, period doubling and the periodic-quasi-periodic-chaotic sequence. Each has been observed in experiments conducted on different types of fluid flows. Behringer (1985) notes that the origins of turbulence in convecting layers are usually due to the nonlinear interaction of macroscopic modes rather than microscopic fluctuations. He goes on to observe that "a strange attractor is a very complex region of phase space, now commonly associated with the onset of turbulence".³

³Behringer (1985) p672.

2.1.3.1 Intermittency

Some systems exhibit a transition from periodic behavior ($R < R_T$, where R is some transition parameter and R_T is some critical value) to chaotic behavior ($R > R_T$) which is characterized by occasional bursts of noise. For R only slightly greater than R_T , there are long intervals of periodic behavior interrupted by short bursts of noise. With increasing values of R , the interval between bursts of noise decreases until it eventually becomes impossible to distinguish the original underlying periodic state. Behringer (1985) notes that intermittency occurs when a stable and unstable attractor merge.

Intermittency as a route to chaotic behavior has been observed in convection experiments (Swinney, 1983) and Rayleigh-Bénard convection (Behringer, 1985).

2.1.3.2 Frequency Locking

Frequency locking is defined as the transition from a quasi-periodic state to a frequency locked (periodic) state for some increasing value of a control parameter. The quasi-periodic state persists over a wide range of the control parameter, followed by a well defined transition to a chaotic state.

Frequency locking has been observed as a route to chaos in Rayleigh-Bénard convection (Swinney, 1983).

2.1.3.3 Period Doubling

Period doubling occurs when a single stable solution bifurcates into alternating between two stable solutions once a critical threshold is reached. The solutions bifurcate again as the critical parameter further increases. The ratio between successive bifurcations is given by Feigenbaum's number.

Period doubling has been observed as a route chaotic to behavior in Rayleigh-Bénard convection (Swinney, 1983; Behringer, 1985; Libchaber et al., 1983) and shallow water waves (Swinney, 1983).

2.1.3.4 Periodic-Quasi-Periodic-Chaotic Sequence

The periodic-quasi-periodic-chaotic sequence is defined as the transition of a system which is periodic (i.e., characterized by only one frequency) to quasi-periodic (i.e., a system characterized by two incommensurate frequencies) to one which is chaotic (i.e., a system characterized by three or more incommensurate frequencies).

This route to chaotic behavior has been observed in Couette-Taylor flow (Swinney, 1983).

2.2 Chaos in the Atmosphere

There have been a number of studies of strange attractors in meteorological data. Most of these have focused on the longer time scales of the synoptic and climatic range. Much of the work on the longer time scales has been prompted by Lorenz's pioneering identification of a strange attractor in a model of the general circulation (Lorenz, 1963). Very little work has been done on the time scales over which waves decay to turbulence.

2.2.1 Short Time Scales

Tsonis and Elsner (1988) searched for an attractor over very short time scales in vertical velocity data from the boundary layer. They estimated a dimension of ~ 7.3 for vertical winds measured at 10 m height during the day in Boulder, Colorado. The data consisted of 10 second averages of 10 m vertical winds measured over an 11 hour period from 1330 - 0030 GMT, totalling 3960 points.

The estimate of the system dimension by Tsonis and Elsner (1988) is flawed for several different reasons. Smith (1989) showed that over 2.3×10^{11} points would be required to accurately obtain a dimension of 7.3, while earlier

estimates of the number of points required to obtain the attractor dimension (i.e., 10^{d^2} - 100^{d^2}) suggest that over 10^7 points would be needed to accurately obtain an attractor dimension of 7.3! It is unlikely that one could specify the dimension of a system with eight degrees of freedom from an analysis of only 3960 data points.

Tsonis and Elsner (1988) had no initial hypothesis as to why there would be an attractor in the data set. They speculated that the attractor was connected with a convective system described by at least eight differential equations and might be related to the Lorenz system. In addition, this data set was certainly non-stationary, a fact not considered by Tsonis and Elsner (1988). Any estimate of an attractor dimension must consider stationarity, else the data suggest the presence of a finite dimension strange attractor where there is none (see Chapter III for a more thorough discussion).

Henderson and Wells (1988) also used vertical velocity data from the boundary layer to estimate the dimension of an attractor. Their data consisted of the vertical velocities at 10 m above the ground measured by a sonic anemometer during the passage of a thunderstorm gust front over an ~ 10 minute period. Henderson and Wells (1988) found evidence of an attractor with dimensions between 4.0 and 5.5. To accurately obtain a dimension of 4 or greater would have required more than 3×10^6 points! While Henderson and Wells (1988) did not specify the number of points they used in their analysis, the number of points required for an accurate dimension estimate implies a minimum sampling rate of 5000 Hz. It is unlikely that there were a sufficient number of points to determine the attractor dimension.

2.2.2 Long Time Scales

Most studies looking for attractors in atmospheric data consider longer time scales. Fraedrich (1986) used the Grassberger-Procaccia algorithm to determine the dimension of an attractor in surface pressure data, sunshine duration data and 500 mb zonal wave amplitude data. In a later study

(Fraedrich, 1987), he examined similar data to determine the dimension of the systems under consideration and also investigated the predictability.

The surface pressure data consisted of 15 years (5475 points) of surface pressure measurements made at 0600 GMT in Berlin, West Germany. Fraedrich considered two cases: 15 years of the annual cycle, and seasonal data sets made over 14 winter and 15 summer seasons. Fraedrich (1986) found no evidence of an attractor with a finite dimension for the continuous data set. In contrast, Fraedrich (1986) calculated dimensions of 3.2 and 3.9 for the winter and summer seasons, respectively. However, in another study of the same data set published a year later, Fraedrich (1987) found a dimension of ≥ 6.8 -7.1. He gave no reason for the difference in the latter finding.

Fraedrich (1986) repeated these calculations for a 30 year record of the number of daily sunshine hours. Again, the data set was considered as two separate cases: a 30 year continuous record and separate winter (29) and summer seasons (30). As for the surface pressure data, Fraedrich (1986) found no evidence for an attractor with a finite dimension in the continuous record, but estimated dimensions of 3.1 and 4.3 for the winter and summer seasons, respectively.

Fraedrich (1986) repeated the analysis for 10 years of 500 mb zonal wind data at 50°N. The continuous record did not support evidence of a finite dimension attractor. Fraedrich (1986) calculated dimensions of 3 and 3.6 for the winter and summer cases, respectively.

On the climactic scale, Fraedrich (1987) used an oxygen isotope record from deep sea core analysis to obtain a dimension of 4.4-4.8 for an attractor. The predictability of this attractor was between 10000-15000 years.

Grassberger (1986) also searched for evidence of a climactic attractor in oxygen isotope ratios from deep sea cores. He found no evidence of a finite dimensional attractor in the data set. The small number of data points used in the study prevented attributing a dimension less than 10 to the system.

Keppenne and Nicolis (1989) applied the Grassberger-Procaccia algorithm to 9000 days of 500 mb geopotential height records from 5 stations over western Europe. They calculated a dimension of 7.5 with a dispersion of 10% for the attractor in this data. They discovered fractal dimensions in the data from each station as well as the average of the five stations. Keppenne and Nicolis (1989) used empirical orthogonal functions to support their findings.

These studies suffered from the same shortcomings that plagued the shorter time scale investigations. In all cases, it is difficult to support evidence of an attractor given a limited number of points in the calculation of the dimension. In a later section we will describe the number of points necessary to accurately estimate the dimension of an attractor.

Fraedrich's studies (Fraedrich, 1986) of the different synoptic scale data would have required at least 74,088 points, a number far greater than the 7300 actually used. The revised dimension for the surface pressure attractor, $d \geq 6.8 - 7.1$ (Fraedrich, 1987), would have required 5,489,031,744 points, an even larger figure! The dimension estimate for the climactic scale attractor obtained from the oxygen isotope data is similarly flawed. To support evidence of a dimension of 7.5, Keppenne and Nicolis (1989) would have needed more than 2.3×10^{11} points instead of the 18,000 they used. However, their dimension estimate was supported by a similar finding using a completely independent technique and thus can be given more credence.

Unlike those for short time scales, large scale studies have a stronger theoretical basis; the work of Lorenz (1963) shows the presence of a strange attractor for the synoptic or climactic time scales. The shorter time scales lack this theoretical underpinning.

2.3 Gravity Waves and Gravity Wave Breaking

Internal atmospheric gravity waves (sometimes referred to as buoyancy waves) were first proposed by Hines (1960) as a mechanism for describing observations of travelling ionospheric disturbances (TID's). The gravity wave mechanism satisfied some important characteristics of the observations: upward propagation of the wave and the increase of the wave amplitude with height⁴.

Gravity waves have frequencies in the range: $f \ll \omega \ll N$, where f is the Coriolis parameter, $f = 2\Omega \sin\phi = 1.1 \times 10^{-4} \text{ s}^{-1}$ for the latitude of the data (57° N) to be used in this study, and N is the Brunt-Väisälä frequency, defined as

$$N^2 = \frac{g}{\bar{\theta}} \frac{\partial \bar{\theta}}{\partial z}, \quad (2.2)$$

where g is the acceleration due to gravity and $\bar{\theta}$ is the mean potential temperature. This frequency is equivalent to a period of ~ 5 minutes in the mesosphere (Andrews et al., 1987).

There are many mechanisms which lead to the saturation and dissipation of atmospheric gravity waves. The primary mechanisms are thought to be dynamic and convective instabilities although there are competing mechanisms. Other mechanisms which limit wave growth are wave dissipation by turbulence, molecular diffusion, radiative damping, inertial instability, wave transience and the cascade of wave energy to small scales via nonlinear wave-wave interaction (Fritts and Rastogi, 1985). Fritts and Rastogi

⁴ Conservation of energy requires the amplitude of upward propagating waves to grow at a rate proportional to $[\rho(z)]^{-1/2}$. In the atmosphere, density decreases approximately exponentially with height, i.e. at a rate proportional to $e^{-z/H}$, where H is the atmospheric scale height. Thus, upward propagating waves grow at a rate of approximately $e^{z/2H}$.

(1985) note that wave-wave interaction is the most efficient of these mechanisms.

In the turbulence theory of gravity wave saturation, the wave amplitude is limited by the turbulent eddy diffusivity which originates from the convective instability of the wave itself, with convective overturning hypothesized not to occur. Walterscheid and Schubert (1990) object to this theory of gravity wave saturation on two points. First, their model, which contains no assumptions about the eddy diffusivity, shows that overturning does indeed occur. The upward propagating wave is not limited to neutral stability, but instead develops highly unstable regions over certain phases of the wave. The overturning causes localized convection which restores neutral stability. Second, the turbulence generated by the breakdown of the wave does not act to limit growth of the wave, but is a consequence of the nonlinear overturning. As Walterscheid and Schubert (1990) point out, overturning and wave saturation can occur even in the absence of turbulence. Upward propagating waves overturn when the lapse rate of the mean potential temperature plus wave potential temperature becomes unstable, i.e.,

$$\frac{\partial(\bar{\theta} + \theta')}{\partial z} < 0 \quad (2.3)$$

The unstable lapse rate is equivalent to the condition where the wave plus the mean horizontal velocity exceeds the phase speed of the wave, i. e.,

$$u' + \bar{u} > c. \quad (2.4)$$

Rearranging this expression yields a measure of the degree of nonlinearity of the wave, i.e.,

$$\frac{|u'|}{|c - \bar{u}|} \approx 1 \quad (2.5)$$

when overturning occurs. Thus, gravity waves are highly nonlinear when saturation takes place.

Dynamical or shear instability occurs when the wave amplitude becomes large enough that the wave plus the mean velocity has a Richardson⁵ (Ri) number less than 1/4. Fritts (1982) showed that regions of dynamic and convective instability are essentially the same, but that convective instability should occur first and preempt shear instability. Walterscheid and Schubert (1990) show that convective instability does occur first and preempts shear instability by limiting the growth of the wave amplitude with height. However, Chimonas (1986) showed that waves can be dynamically unstable for any Richardson number if the flow is tilted. The previous studies have all assumed that the flow is horizontally stratified.

Transient effects occur when wave breakdown modifies the mean flow and can cause self acceleration of the wave. This can then lower the height at which the wave breaks. Walterscheid and Schubert (1990) believe wave transience introduces important considerations in the wave breaking process but that it is not the principle mechanism behind gravity wave saturation.

⁵ The Richardson number is defined as:

$$Ri \equiv \frac{\frac{g}{\bar{\theta}} \frac{\partial \bar{\theta}}{\partial z}}{\left[\frac{\partial \bar{v}}{\partial z} \right]^2} \equiv \frac{N^2}{\left[\frac{\partial \bar{v}}{\partial z} \right]^2},$$

where \bar{v} is the velocity and the other variables retain their previous definitions.

2.3.1 Conventional Saturation Theory

The term gravity wave saturation refers to any process that acts to limit or maintain constant wave amplitudes with altitude. The process occurs via instabilities or interactions arising from large amplitude wave motions. Gravity wave saturation plays an important role in maintaining the mesospheric circulation and temperature gradient; gravity wave saturation provides the drag necessary to explain the mean zonal wind reversals observed in the upper mesosphere and lower thermosphere (see for example, Fritts, 1984; Holton, 1982, 1983; Dunkerton 1982; Lindzen, 1981).

Here, we provide a brief review of linear saturation theory as proposed by Lindzen (1981). Linear saturation theory assumes that the growth of the amplitude of monochromatic gravity waves in a horizontally stratified flow would be limited by the appearance of convective instability. This would result in the production of turbulence and a level of eddy diffusion that is just sufficient to restrain wave amplitudes to the unsaturated limit. This theory assumes that the gravity wave saturation does not affect wave propagation or the wave characteristics.

The basic equations in Cartesian coordinates for an inviscid atmosphere are:

$$\begin{aligned}\rho \frac{d\vec{v}}{dt} + \nabla p - \rho \vec{g} &= 0 \\ \frac{dp}{dt} - \frac{\rho_0 N^2}{g} w &= 0 \\ \nabla \cdot \vec{v} &= 0\end{aligned}\tag{2.6}$$

where ρ is the atmospheric density, \vec{v} is the vector velocity, w the vertical component of the velocity, g the acceleration due to gravity, p is the pressure and N^2 is the Brunt-Väisälä frequency. The equations in 2.6 are Euler's equation, a modified form of the thermodynamic equation and the continuity

equation, respectively. The Boussinesq approximation is implicit in this set of equations, i.e., the atmosphere will be considered as an incompressible fluid except in the buoyancy term. This approximation is not especially valid for the atmosphere as a whole, but may be valid for the region near the level of gravity wave saturation.

Let us apply the following perturbations to an incompressible, inviscid and adiabatic atmosphere. The background is assumed to be hydrostatic with a zonal wind that varies with height, i.e.,

$$\begin{aligned} u &= u_0(z) + u'(x,z,t) \\ w &= w'(x,z,t) \\ p &= p_0(z) + p'(x,z,t) \\ \rho &= \rho_0(z) + \rho'(x,z,t), \end{aligned} \tag{2.7}$$

where the primes indicate the perturbation quantities, u_0 is the basic state zonal wind, and p_0, ρ_0 are the basic state density and pressure. The basic state pressure and density vary with height as

$$\begin{aligned} p_0(z) &= p_0(0) e^{-z/H} \\ \rho_0(z) &= \rho_0(0) e^{-z/H}, \end{aligned} \tag{2.8}$$

where $p_0(0)$ and $\rho_0(0)$ are the pressure and density at the surface and H is the scale height of the atmosphere.

Applying the perturbations (2.7) to the set of equations in (2.6) and neglecting second and higher order terms yields the set of perturbation equations

$$\begin{aligned}
\rho_0 \frac{\partial u'}{\partial t} + \rho_0 u_0 \frac{\partial u'}{\partial x} + \rho_0 w' \frac{\partial u_0}{\partial z} &= -\frac{\partial p'}{\partial x} \\
\rho_0 \frac{\partial w'}{\partial t} + \rho_0 u_0 \frac{\partial w'}{\partial x} &= -\frac{\partial p'}{\partial z} - \rho' g \\
\frac{\partial \rho'}{\partial t} + u_0 \frac{\partial \rho'}{\partial x} - \frac{\rho_0 N^2}{g} w' &= 0 \\
\frac{\partial u'}{\partial x} + \frac{\partial w'}{\partial z} &= 0
\end{aligned}
\tag{2.9}$$

We can solve for w' first by assuming solutions of the form

$$\begin{aligned}
u' &= \hat{u}(z) e^{i(\omega t - kx)} \\
w' &= \hat{w}(z) e^{i(\omega t - kx)} \\
p' &= \hat{p}(z) e^{i(\omega t - kx)} \\
\rho' &= \hat{\rho}(z) e^{i(\omega t - kx)}
\end{aligned}
\tag{2.10}$$

and by substituting these into the perturbation equations (2.9). Cancelling out the exponential terms yields the set of perturbation equations:

$$\begin{aligned}
i\rho_0[\omega - ku_0]\hat{u} + \rho_0 \frac{\partial u_0}{\partial z} \hat{w} &= ik\hat{p} \\
i\rho_0[\omega - ku_0]\hat{w} &= -\frac{\partial \hat{p}}{\partial z} \hat{w} - \hat{\rho} g \\
ik\hat{u} + \frac{\partial \hat{w}}{\partial z} &= 0 \\
i[\omega - ku_0]\hat{\rho} - \frac{\rho_0 N^2}{g} \hat{w} &= 0
\end{aligned}
\tag{2.11}$$

Solving this for w yields the Taylor-Goldstein equation (Fritts, 1984):

$$\frac{\partial^2 \hat{w}}{\partial z^2} + \left[\frac{N^2}{(\omega - ku_0)^2} - \frac{1}{(\omega - ku_0)} \frac{\partial^2 u_0}{\partial z^2} - k^2 - \frac{1}{H(\omega - ku_0)} \frac{\partial u_0}{\partial z} - \frac{1}{4H^2} \right] \hat{w} = 0
\tag{2.12}$$

Lindzen (1981) notes that for cases of gravity wave saturation, we can assume that

$$\frac{1}{4H^2} \ll \frac{N^2}{(\omega - kU_0)^2} \quad (2.13)$$

which allows us to drop the last term on the left hand side of equation 2.12. The $\partial^2 u_0 / \partial z^2$ and $\partial u_0 / \partial z$ terms can also be dropped because the basic state zonal wind is assumed to be a slowly varying function of height. Scaling arguments also allow us to neglect the k^2 term. This reduces equation 2.10 to

$$\frac{\partial^2 \hat{w}}{\partial z^2} + \left[\frac{N^2 k^2}{(\omega - kU_0)^2} \right] \hat{w} = 0 \quad (2.14)$$

Near the critical level, the denominator, $(\omega - kU_0)$, goes to zero because the absolute value of the horizontal component of the phase speed (ω/k) approaches the background zonal wind speed. This zero creates a singularity at the critical level, making solution of equation 2.14 difficult.

The WKBJ approximation is used to solve an equation of the form of 2.14. The WKBJ method is described as follows (Mathews and Walker, 1970). Given an equation of the form

$$\frac{\partial^2 y}{\partial x^2} + f(x)y = 0 \quad (2.15)$$

where $f(x)$ is a slowly varying function of x and does not pass through a zero or other singularity, then solutions to equation 2.15 are of the form

$$y(x) = \frac{1}{[f(x)]^{1/4}} \left[c_+ e^{i \int \sqrt{f(x)} dx} + c_- e^{-i \int \sqrt{f(x)} dx} \right] \quad (2.16)$$

If we define the following quantity,

$$\lambda^2 \equiv \frac{N^2}{(\omega - kU_0)^2}, \quad (2.17)$$

then the solution to equation 2.15 becomes

$$\hat{w} \approx A \lambda^{-1/2} e^{i \int \lambda dz} \quad (2.18)$$

and is depicted in Figure 2.1.

Lindzen (1981) uses this result to show that the condition for the convective saturation of gravity waves is

$$\left| \frac{dT'}{dz} \right| = \Gamma, \quad (2.19)$$

where T' is the perturbation temperature and Γ is the dry adiabatic lapse rate. Other commonly used conditions for convective gravity wave saturation are:

$$|p_0 + p'| = 0, \quad (2.20)$$

$$|\rho_0 + \rho'| = 0, \quad (2.21)$$

$$\left| \frac{d(\theta_o + \theta')}{dz} \right| = 0, \quad (2.22)$$

$$\text{and } |u_o + u'| = 0. \quad (2.23)$$

Saturation conditions in 2.20 and 2.21 occur because you can not have negative pressures or densities. Condition 2.22 is the same as 2.19; it is the condition for ordinary convective instability. The last condition, 2.23, relates to the phase speed of the wave "catching" up to the basic state wind speed.

The gravity wave saturation model of Walterscheid and Schubert (1990) provides some interesting insights into the mechanism behind gravity wave saturation. Two dimensional and fully nonlinear, the model makes no significant assumptions about the gravity wave saturation mechanism; the atmosphere in the model is compressible and non-hydrostatic. Most importantly, the model indicates that nonlinear growth of the gravity wave creates regions of overturning prior to saturation. The large unstable potential temperature gradients allow the development of small scale cellular convection which causes the breakdown of the gravity wave. Turbulence is an end product of the wave breakdown via the decay of the cellular convection rather than the cause of the wave breakdown. Walterscheid and Schubert (1990) cite the laboratory work of Delisi and Corcos (1973) as support for this conclusion from their model.

2.3.2 Slantwise Static Instability Theory

Hines (1988) objects to the linear saturation mechanism proposed by Lindzen (1981) on two points: the spectrum of waves and the vertical gradients. In raising these objections, Hines suggests that slantwise static instability is a less demanding mechanism for gravity wave breaking.

Waves in the middle atmosphere are not represented by a single dominant wave number but instead by a spectrum of wave numbers. Hines

(1988) notes that this does not affect the linear saturation theory of wave breaking per se, but it "does open the way to patchiness rather than a laminar deposition of turbulence"⁶. The instability criterion for a single wave mode, i.e., where the phase speed of the perturbation equals that of the background flow, does not impose nonlinearity on the system. It would impose large nonlinearities when two waves have similar amplitudes but different wave vectors. Hines (1988) states that the nonlinear interaction may leach away wave energy before the wave becomes unstable.

Hines (1988) also objects to the conventional saturation theory because it assumes the background flow is strictly horizontally stratified and only considers vertical gradients in the evaluation of the stability. Hines notes that this restriction is more mathematical in nature but is not justified physically. Hines (1988) examines the stability criteria for gradients which are no longer strictly vertical.

Hines (1988) notes that the criterion for the onset of instability in a horizontally stratified atmosphere is given by

$$\tau_z^2 \equiv \frac{-g}{\bar{\theta}} \frac{\partial \bar{\theta}}{\partial z} > 0 \quad (2.24)$$

where g is the acceleration due to gravity, $\bar{\theta}$ is the mean potential temperature. This is the negative of the Brunt-Väisälä frequency ω_b^2 (defined as N^2 in the previous section) and as such would appear in the form

$$e^{i\omega_b t} \quad (2.25)$$

⁶ Hines (1988), p1269.

in the solution of the relevant linearized equations. If equation 2.25 were negative, i.e., unstable conditions, then the solutions would take the form

$$e^{t/\tau_z} \quad (2.26)$$

where τ_z is the e-folding time for the growth of any instabilities. This mechanism will be referred to hereafter as vertical static instability. If the atmosphere is not horizontally stratified, i.e., the gradient of the potential temperature is no longer constrained to the vertical, the new criterion for instability is given by

$$\tau_s^{-2} \equiv \frac{-g}{\theta} \frac{\partial \bar{\theta}}{\partial s} \cos \zeta > 0 \quad (2.27)$$

where ζ is the angle off the vertical for any parcel motion oriented along the s axis as shown in Figure 2.2. Any parcel motion confined to the shaded region in the figure would be unstable. By analogy, the e-folding time for growth of an instability for this type of stratified atmosphere would be given by

$$e^{t/\tau_s} \quad (2.28)$$

The e-folding time for growth of the instability may be long for certain values of ζ .

Hines (1988) concludes that turbulence is far more likely to develop from slantwise static instability than for vertical static instability, even though it may be a slower mechanism. Since gravity waves produce potential temperature gradients that are not necessarily constrained to the vertical

plane, this mode of instability is the more likely to generate turbulence. Under most conditions, the normalized wave amplitude necessary for the development of turbulence from slantwise static instability is $\ll 1$; the normalized wave amplitude necessary for the development of turbulence for vertical static instability is defined as 1.

Hines also concludes that the turbulence spectrum from slantwise static instability would be highly anisotropic, with much stronger horizontal motions than vertical motions. This might approach two dimensional turbulence in the limit. The production of turbulence from slantwise static instability is more likely for "short" vertical wavelengths than from vertical static instability. Hines (1988) notes that for vertical wavelengths of 6 km and a buoyancy period of 5 minutes, vertical static instability requires vertical velocities of 20 m s^{-1} for saturation to occur. This is not consistent with observations. However, because slantwise static instability requires much smaller wave amplitudes for saturation, this mechanism can produce saturation consistent with observations of vertical wind velocities in the mesosphere.

The one difficulty with finding a strange attractor associated with the slantwise static instability mechanism is that the smaller wave amplitudes which produce saturation and turbulence may allow the gravity wave to remain fairly linear. The analysis by Hines (1988) was done for a monochromatic wave to simplify the mathematics and is limited by this assumption. Nonlinear wave-wave interaction will affect both saturation mechanisms equally. Without nonlinear wave-wave interaction, the slantwise static instability mechanism reduces the probability of finding an attractor in the saturation of gravity waves. However, the "patchiness" of the turbulence created by saturation of gravity waves with a spectrum of wave numbers opens the way for the investigation of the fractal structure of turbulence.

2.3.3 Nonlinear Mechanisms

There are three "resonant triad" interactions which act on gravity waves: elastic scattering, induced diffusion and parametric subharmonic instability (Fritts and Rastogi, 1985). Of these mechanisms, Fritts and Rastogi feel parametric subharmonic instability acts most efficiently in transferring wave energy between waves of very different scales. Parametric subharmonic instability transfers energy from large scale waves to two small scale waves at half the frequency of the larger wave. Elastic scattering converts the incident wave into a reflected wave by scattering off a vertical shear in the wind and tends to make the vertical wave spectrum symmetric. Elastic scattering can be rapid, depending on the vertical wave number (Yeh and Liu, 1985). In induced diffusion, the wave action density diffuses in wave space if two waves with nearly identical wave vectors interact with the vertical shear of a smaller wave. Ibrahim (1987) suggests that induced diffusion can be sufficient for gravity wave saturation.

Fritts and Rastogi (1985) note that parametric subharmonic instability acts on waves of all amplitudes and may exchange energy among waves at amplitudes less than that required for convective or dynamic instability. However, it works best at high vertical wave numbers and small intrinsic frequencies. Fritts and Rastogi do not believe that parametric subharmonic instability competes effectively with convective or dynamic instability among higher frequency, larger scale gravity wave motions as a mechanism explaining gravity wave saturation.

Parametric subharmonic instability transfers the energy in moderate-to-large scale waves to small scale waves at one half the frequency. Yeh and Liu (1985) note that conservation of wave number and conservation of frequency restrict this mechanism to those waves with an elevation angle of 60° or greater. The time scale for parametric subharmonic instability varies with the inverse square of the vertical wavenumber.

Yeh and Liu (1985) state that if wave growth occurs over an amount of time equal to a few periods or less, the nonlinear interactions are no longer considered "weak" and other processes, such as convective or dynamic instability, may become important. Furthermore, the interactions in their study only considered the energy transferred in the vertical plane and neglected energy transferred in the horizontal plane.

Nonlinear wave-wave interaction can act to limit the growth of gravity waves by transferring energy from larger amplitude waves to smaller waves. This mechanism will not necessarily lead to gravity wave breaking. There may be no transition from a laminar state to a turbulent one and therefore no potential strange attractor in the flow. There may be a strange attractor associated with nonlinear wave-wave interaction, but it may be a function of the underlying spectrum of waves instead of a function of the transition from laminar to turbulent flow. The latter is more likely to be a universal and repeatable behavior, whereas the former will only describe a particular packet of gravity waves and may not be found again.

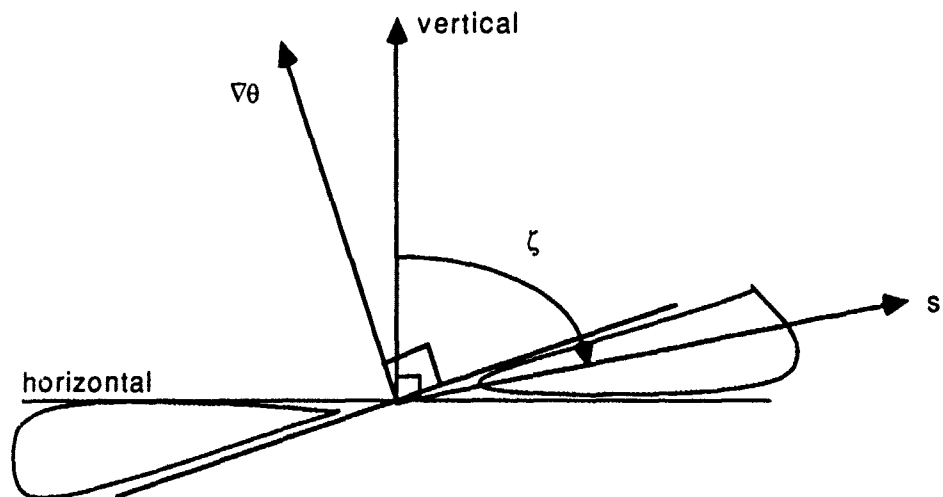


Figure 2.1 Nonvertical orientation for the potential temperature gradient. Interchanges of air parcels along axes within the shaded regions such as the s axis are unstable (adapted from Hines, 1988).

CHAPTER III

THE METHODS OF ANALYSIS

This chapter describes the methods that will be used to analyze the data. The bulk of the chapter is devoted to a description and derivation of the Grassberger-Procaccia correlation integral algorithm, since this technique is not commonly used on meteorological data. A discussion of the strengths, weaknesses and difficulties that arise in employing this algorithm follows the derivation. The remainder of the chapter provides a brief overview of the more conventional analysis tools (autocorrelation and power spectrum) that will be used to support the analysis of the system dimension.

3.1 The Grassberger-Procaccia Correlation Integral Algorithm

There are a number of techniques described in the literature for estimating the dimension of a strange attractor. Box counting algorithms yield an estimate of the capacity dimension, commonly referred to as the fractal dimension (see, for example, Liebovitch and Tibor, 1989). The nearest neighbor method developed by Badii and Politi (1987) is another approach to estimating the dimension of a system. Yet another dimension estimate can be obtained from singular systems analysis (see Broomhead and King, 1986; Albano et al., 1988; Vautard and Ghil, 1989). The spectrum of Lyapunov (or characteristic) exponents for an attractor can be calculated and related to the dimension of the system (see Packard et al., 1980; Froehling et al., 1981; Roux et al., 1983; Wolf et al., 1985). However, the most frequently used method to

calculate the dimension of a system is the correlation integral algorithm (Grassberger and Procaccia, 1983; Grassberger and Procaccia, 1984).

Each technique has its strengths and weaknesses. The box counting technique is computationally intensive although Liebovitch and Tibor (1989) developed a faster and more efficient algorithm. The singular systems approach is difficult to implement although it is often used as a check on the other methods (Broomhead and King, 1986; Albano et al., 1988; Vautard and Ghil, 1989). The nearest neighbor approach is relatively new and has not been widely used; its strengths and weaknesses have yet to be thoroughly examined in the literature. Calculating the spectrum of Lyapunov exponents often presupposes some knowledge of the attractor. The Grassberger-Procaccia algorithm has the advantage of being easily implemented and calculated. Because of its frequent use, the limitations of the Grassberger-Procaccia algorithm have been widely investigated and described in the literature.

The Grassberger-Procaccia algorithm (along with subsequently developed variations) will be used in this study. It is easy to understand and program. It makes no assumptions about the presence of a strange attractor in the signal and requires no a priori knowledge of its nature or structure. Somewhat computationally intensive (the computer time increases as the square of the number of points in the data set), the Grassberger-Procaccia algorithm is less demanding than the box counting algorithm. Despite these advantages, this algorithm has several drawbacks which will be discussed in detail later in the chapter.

Before deriving the Grassberger-Procaccia algorithm and discussing some of its advantages and disadvantages, let us define the different concepts of dimension and the method for building a phase space portrait from a single data set.

3.1.1 Concepts of Dimension

Three different dimensions are often used to describe a set¹: the capacity dimension, the Hausdorff dimension and the information dimension. These are summarized in Table 3.1 (adapted from Farmer et al., 1983). The Hausdorff and capacity dimension are metric dimensions, a concept of dimension on which a sense of distance is defined. The information dimension is a probabilistic dimension based on the natural measure - the relative probability of different regions of the attractor as obtained from time averages (Farmer et al., 1983).

Table 3.1 Dimension definitions.

Name	Symbol	Generic name
Capacity dimension	d_c	fractal
Hausdorff dimension	d_h	
Information dimension	d_I	

The capacity dimension is defined as

$$d_c \equiv \lim_{\epsilon \rightarrow 0} \frac{\log N(\epsilon)}{\log(1/\epsilon)} \quad (3.1)$$

where $N(\epsilon)$ is the number of cubes with sides of length ϵ needed to cover the set of points (Barnsley, 1988). This definition of dimension is the basis of the box counting algorithm.

The Hausdorff dimension is more complicated than the capacity dimension. Its definition is similar to that of the capacity dimension but the cubes used to cover the set can be of variable length. We will not give a more

¹ A set can be a collection of points, a geometric object or a time series of data.

precise definition but note instead that for most attractors the Hausdorff dimension is equal to the capacity dimension (Farmer et al., 1983).

The information dimension is a generalization of the capacity dimension; it takes into account the relative probability of the cubes used to cover the set. It is defined as

$$d_I \equiv \lim_{\epsilon \rightarrow 0} \frac{I(\epsilon)}{\log(1/\epsilon)} \quad (3.2)$$

where $I(\epsilon)$ is the information for length scale ϵ defined as

$$I(\epsilon) = - \sum_{i=1}^{N(\epsilon)} p_i \log p_i \quad (3.3)$$

and p_i is the probability that the attractor trajectory visits the i th cube. If all the cubes are visited with equal frequency then the probability that the i th cube is visited is given by

$$p_i = \frac{1}{N(\epsilon)} \quad (3.4)$$

and therefore the information can be written as

$$I(\epsilon) = \log N(\epsilon) \quad (3.5)$$

Thus, the capacity dimension is equal to the information dimension for a completely homogeneous attractor. In general, attractors are not homogeneous and the cubes are not visited with equal frequency. Thus, for an inhomogeneous attractor,

$$I(\epsilon) < \log N(\epsilon) \quad (3.6)$$

and consequently the capacity dimension is always greater or equal to the information dimension, i.e.,

$$d_c \geq d_I \quad (3.7)$$

Information theory gives a very specific meaning to $I(\epsilon)$. It is the amount of information necessary to specify a system to within accuracy ϵ ($\epsilon > 0$). Alternately, it can be thought of as the amount of information obtained by making a new measurement with an uncertainty ϵ .

2.1.2 Building Phase Space Vectors

Originally, there was no universally accepted method for constructing phase space vectors from a time series. Packard et al., (1980) pointed out, "...there is no universally applicable method of phase space construction, though the nature of the phenomenon might suggest possible alternatives."² However, Brandstätter et al., (1983) suggested that phase space portraits can be constructed by lagging the original time series by an arbitrary amount to obtain the second phase space dimension. This technique of constructing a phase space representation of the data is often referred to as Taken's method of delays and is now almost universally used.

Fraser and Swinney (1986) provide a clear explanation of building a multi-dimensional phase portrait from a single time series. A scalar time series $s(t)$ can be expanded into a m dimensional phase space vector $x(t)$ by using time delays τ , as follows

² Packard et al. (1980), p713.

$$\mathbf{x}(t) = \{x_0(t), x_1(t), \dots, x_{m-1}(t)\}, \quad (3.8)$$

where

$$x_n(t) = s(t + n\tau); \quad n=0,1,2, \dots, m-1.$$

Here s is the original time series, τ the specified time lag and x_0, x_1, \dots, x_{m-1} are the individual components of an m dimensional phase space vector \mathbf{x} . Fraser and Swinney (1986) note that for an infinite amount of noise free data, the time delay τ can be arbitrary. However, for noisy or limited data, a small time delay τ may make the components $x_0(t)$ and $x_1(t)$ indistinguishable and all trajectories appear to be on a line $x_0=x_1$. To avoid this problem, the time delay τ must be chosen to make the vectors $x_0(t)$ and $x_1(t)$ as independent as possible. Techniques in determining the proper choice for the time delay will be discussed in later sections.

3.1.3 Trajectories in Phase Space

The trajectory in phase space is said to follow an attractor if its orbits rapidly return to this subset (i.e. the attractor) after finite perturbations (Swinney, 1983). Large perturbations could send the orbit out of the basin of attraction. An attractor is labelled strange if nearby orbits diverge exponentially on average. This condition is sometimes referred to as "sensitive dependence on initial conditions" (Swinney, 1983).

3.1.4 Derivation of the Grassberger-Procaccia Algorithm

Grassberger and Procaccia (1984) note that "two of the most basic properties of dissipative chaotic systems are related to information: the

Kolmogorov (or 'metric') entropy K and the Renyi-Balaton information dimension σ .³ Both K and σ relate to the information $I(\epsilon, T)$ gained by observing the trajectory of a system with precision ϵ during a finite amount of time T . Grassberger and Procaccia (1984) define the precision ϵ as the uncertainty in the measurements of any of the coordinates of the vector \mathbf{x} .

The Kolmogorov entropy is defined as

$$K \equiv \lim_{\epsilon \rightarrow 0} \lim_{T \rightarrow \infty} \frac{I(\epsilon, T)}{T} \quad (3.9)$$

The definition of the Kolmogorov entropy requires making a very long series of observations as can be seen from the limit placed on time. Grassberger and Procaccia (1984) show that since the time limit is taken first, equation 3.9 implies that the information for a given precision ϵ increases linearly with time and that the rate of increase tends towards a finite constant for infinite precision (i.e., infinitely small error).

Furthermore, Grassberger and Procaccia (1984) compare this to an ordered system where

$$\lim_{T \rightarrow \infty} \frac{I(\epsilon, T)}{T} = 0 \quad (3.10)$$

and systems with random noise where

$$\lim_{T \rightarrow \infty} \frac{I(\epsilon, T)}{T} \propto \ln(1/\epsilon) \xrightarrow{\epsilon \rightarrow 0} \infty \quad (3.11)$$

³ Grassberger and Procaccia (1984), p35. Note that σ is the same as the previously defined information dimension d_I .

This leaves us with the following definitions for the behavior of the Kolmogorov entropy:

1. $K = 0$ for ordered systems,
2. $K = \infty$ for random systems, and
3. $K =$ a finite constant for systems characterized by a strange attractor.

To extend this concept to a time series of data, Grassberger and Procaccia (1983) introduce a new quantity K_2 which has the following properties:

1. $K_2 \geq 0$,
2. $K_2 \leq K$,
3. $K_2 = \infty$ for random systems, and
4. $K_2 \neq 0$ for chaotic systems.

Grassberger and Procaccia (1983) note that $K_2 > 0$ is a sufficient condition for chaos. The quantity K_2 can be calculated in the following manner.

Grassberger and Procaccia (1983) define a new quantity, $C(\epsilon)$, which is total probability that a random pair of points on the attractor will fall into the same cube of size ϵ in phase space. Grassberger and Procaccia (1984) note that this probability scales as

$$C(\epsilon) \underset{\epsilon \rightarrow 0}{\approx} \epsilon^v \quad (3.12)$$

where v is called the correlation exponent. Furthermore, v also approximates the fractal dimension, d_c , of the attractor (Grassberger and Procaccia, 1983).

For a time series of data $\{\vec{X}_i\}_{i=1}^N$, where $\vec{X}_i = \vec{X}(t=i\tau)$, the correlation integral, $C_m(\epsilon)$, can be calculated from the following (Grassberger and Procaccia, 1983):

$$C_m(\epsilon) = \lim_{N \rightarrow \infty} \frac{1}{N^2} \times \left\{ \text{number of pairs of points } (n,k) \text{ with } |\vec{X}_n - \vec{X}_k| \leq \epsilon \right\} \quad (3.13)$$

Here N is the total number of points in the time series and the time delay τ equals $\lambda \Delta t$ for some lag λ . The subscript m is the embedding dimension and must be greater than or equal to F , the number of degrees of freedom of the attractor. The Whitney embedding theorem states that it is possible to embed an m dimensional geometric object arbitrarily in a $2m+1$ dimensional space.

Equation 3.13 may be rewritten more precisely by replacing the norm with an explicit expression for the Euclidean norm in a m dimensional phase space:

$$C_m(\epsilon) = \lim_{N \rightarrow \infty} \frac{1}{N^2} \times \left\{ \text{number of pairs } (n,k) \text{ with } \left[\sum_{i=0}^{m-1} |\vec{X}_{n+i} - \vec{X}_{k+i}|^2 \right]^{1/2} \leq \epsilon \right\} \quad (3.14)$$

This should be the same as (Grassberger and Procaccia, 1983)

$$C_m(\epsilon) \underset{\substack{m \rightarrow \infty \\ \epsilon \rightarrow 0}}{\approx} \epsilon^v \exp(-m\tau K_2) \quad (3.15)$$

This now gives us a simple way to calculate the fractal dimension as well as estimating the lower bound on the Kolmogorov entropy. If we plot the natural logarithm of $C_m(\epsilon)$ as a function of the natural logarithm of ϵ for increasing values of embedding dimension m , we should get a series of straight lines whose slope is v , the fractal dimension of the attractor and which are displaced from one another by the factor $-m\tau K_2$. An example of the

correlation integral is shown in Figure 3.1. Calculating a value for K_2 will quickly tell us whether the data is ordered, chaotic or random.

In practice, the region of constant slope will only be valid over a limited range of ϵ which is often called the "scaling" region. This gives equation 3.15 the form

$$C(\epsilon) \approx \chi(\epsilon) \epsilon^\nu \quad (3.16)$$

where $\chi(\epsilon)$ is a possibly oscillatory function of $O(1)$ (Smith, 1988). The structure of $\chi(\epsilon)$ is generated by the sparse or empty regions (lacunae) of the set. Some of the oscillations in $\chi(\epsilon)$ are also generated from noise and fluctuations due to a finite number of points.

The Kolmogorov entropy of the attractor can be approximated by examining the following

$$K_{2,m}(\epsilon) = \frac{1}{\tau} \ln \left[\frac{C_m(\epsilon)}{C_{m+1}(\epsilon)} \right] \quad (3.17)$$

and then

$$\lim_{\substack{m \rightarrow \infty \\ \epsilon \rightarrow 0}} K_{2,m}(\epsilon) \approx K_2 \quad (3.18)$$

The Kolmogorov entropy, along with the correlation dimension, can be used to test for strange attractors in a set of data. An example of using the Grassberger-Procaccia approximation of the Kolmogorov entropy to determine the type of behavior of a system is shown in Figure 3.2.

Grassberger and Procaccia (1983) demonstrated this technique on the Mackey-Glass delay differential equation and the Henon attractor and found

that this technique works for fractal dimensions as large as 7.5 with ~ 30000 data points. However, later research with the correlation integral suggests that its only practical for determining the dimension of systems with dimensions on the order of 4 or less (Smith, 1988).

3.1.5 Generalized Correlation Integral

The technique developed by Grassberger and Procaccia (1983; 1984) has been extended to determine the generalized entropy and generalized dimension (Hentschel et al., 1983; Pawelzik and Schuster, 1987; Grassberger, 1985). Such generalized quantities reveal important information on the structure of the attractor.

Atmanspacher et al., (1988) notes that the quantity for characterizing an attractor as a metric structure is its dimension. Traditionally, the concept of dimension has been limited to purely integer values. However, the dimension can take on non-integer values for chaotic (or strange) attractors. Attractors with purely integer dimensions correspond to regular (i.e. stationary, and/or periodic) processes. The concept of a fractal (i.e. non-integer) dimension, $d < m$, of an attractor in a m dimension phase space can be derived from information theory. The information dimension, d_I , describes how information $I(\epsilon)$ scales with varying spatial resolution ϵ as previously defined in equation 3.2.

One way to obtain the information I is to break the attractor up into m boxes of size ϵ . The probability that a point on the attractor falls into the i th box is given by

$$p_i = \frac{N_i}{N} \tag{3.19}$$

where N_i is the number of points in the i th box and N is the total number of points on the attractor.

Pawelzik and Schuster (1987) define the generalized information of order q as

$$I^{(q)} = \frac{1}{1-q} \log \sum_{i=1}^m p_i^q \quad (3.20)$$

A continuous spectrum of dimensions of order q can be defined by substituting $I^{(q)}$ into the original definition of the information dimension (equation 3.2),

$$\begin{aligned} d^{(q)} &= \lim_{\epsilon \rightarrow 0} \frac{1}{1-q} \frac{\log \sum_{i=1}^m p_i^q}{\log \left(\frac{1}{\epsilon} \right)} \\ &= \frac{1}{q-1} \frac{\log \sum_{i=1}^m p_i^q}{\log(\epsilon)} \end{aligned} \quad (3.21)$$

Some of the most frequently encountered dimensions are: $d^{(0)}$, the Hausdorff dimension (previously referred to as d_H); $d^{(1)}$, the information dimension (previously referred to as d_I); and $d^{(2)}$, the correlation dimension (Atmanspacher et al., 1988). Furthermore, Atmanspacher et al. (1988) observe that

$$d^{(q)} \leq d^{(q')} \text{ if } q' \leq q \quad (3.22)$$

The equality holds only for completely homogeneous probability distributions, i.e., $p_i = 1/N$. The more an attractor "bunches" up (i.e. spends more time

visiting a particular region of phase space), the less homogeneous the probability distribution. Differences arise between dimensions of different order q because of the degree of inhomogeneity of the attractor, i.e., the degree to which the boxes are visited with unequal frequency.

The correlation integral method proposed by Grassberger and Procaccia (1983) is based on the correlation dimension v . This has been extended to a dimension of arbitrary order q as follows

$$C^{(q)}(\epsilon, N) = \lim_{\epsilon \rightarrow 0} \left[\frac{1}{N} \sum_{i=1}^N \left[\frac{1}{N} \sum_{j=1}^N H[\epsilon - |\bar{x}_i - \bar{x}_j|] \right]^{q-1} \right]^{\frac{1}{q-1}}, \quad (3.23)$$

where H is the Heaviside step function ($H(x)=0$ if $x<0$, $H(x) = 1$ if $x \geq 0$), and ϵ is the size of the box (Hentschel et al., 1983; Pawelzik and Schuster, 1987; Grassberger, 1985). Notice that this reduces to the original expression of Grassberger and Procaccia (1983) for order $q=2$. By analogy, the generalized entropy of order q may now be written as

$$K^{(q)} = \lim_{\epsilon \rightarrow 0} \lim_{n \rightarrow \infty} \left\{ \frac{-1}{n} \ln C^{(q)}(\epsilon, N) \right\} \quad (3.24)$$

These results can be used for a series of single observations evenly spaced in time by use of Taken's method of delays. This lets us write the generalized correlation integral as

$$C_m^{(q)}(\epsilon, N) = \lim_{\epsilon \rightarrow 0} \left[\frac{1}{N} \sum_{i=1}^N \left[\frac{1}{N} \sum_{j=1}^N H \left[\epsilon - \left[\sum_{k=0}^{m-1} (x_{i+k} - x_{j+k})^2 \right]^{\frac{1}{2}} \right] \right]^{q-1} \right]^{\frac{1}{q-1}} \quad (3.25)$$

Pawelzik and Schuster (1987) point out that this technique is only slightly more computationally intensive than the original correlation algorithm proposed by Grassberger and Procaccia (1983). Most of the computational effort is spent in counting the number of the pairs of points; raising the interior sums to the various powers represents only a small additional burden.

Once a spectrum of generalized entropies have been generated for a time series, we can determine the spectrum of dynamical fluctuations around the Kolmogorov entropy. This spectrum can be used to deduce properties and structure of the attractor (Atmanspacher et al., 1988) or applied to a description of turbulence (Chhabra et al., 1989; Meneveau and Nelkin, 1989).

3.2 Limitations of the Grassberger-Procaccia Algorithm

The Grassberger-Procaccia algorithm does have a number of weaknesses which must be addressed. First, noise in the signal can yield misleading estimates of the dimension. Second, an inappropriate choice of the time delay in constructing the phase space vectors can also yield incorrect estimates of the attractor dimension and may suggest the presence of a chaotic attractor where there is not one. Furthermore, a limited or non-stationary data set can introduce errors and require the use of different norms in calculating the distances between pairs of points.

3.2.1 Noise

Noise affects length scales over a range on the order of magnitude of the standard deviation of the noise (Ben-Mizrachi et al., 1984). This leads to a noise length scale region where noise scales as the embedding dimension (Ben-Mizrachi et al., 1984; Theiler, 1987; Franaszek, 1987). Thus, noise is proportional to ϵ^m and has a slope on the $\ln C(\epsilon, N)$ vs $\ln \epsilon$ plots that equals m , the embedding dimension. The presence of noise reduces the scaling region of other signals; in systems with a low signal to noise ratio, the scaling region

may even disappear. The magnitude or amount of noise in the signal can be determined from the break in the slopes in the $\ln\text{--}\ln$ plots of the correlation integral; this break is often referred to as a "knee". The presence of noise in the signal violates the limit in equation 3.12; you can not take the limit as ϵ goes to zero because the attractor is not clearly defined for length scales on the order of the magnitude of the noise.

Furthermore, a limited number of data points has much the same effect as noise on the slopes from the correlation integral. This occurs because random noise never completely saturates an infinite dimensional phase space; a limited data set may not cover the attractor well enough to allow it to be sufficiently embedded in a $2d+1$ phase space.

Certain types of noise make it possible to mistake a data set with a finite correlation dimension as having an attractor. Certain sets of stochastic data can yield finite correlation dimensions yet are not strange attractors. For instance, the "random walk" yields a correlation dimension of 1.1 (Ramsey and Yuan, 1989). Even more disconcerting (especially to those meteorologists who live and die by the $-5/3$ power law) is that "colored" random noise characterized by a power law spectrum can yield a finite correlation dimension (Osborne and Provenzale, 1989). White noise which has a flat power spectrum does yield an infinite correlation dimension as indicated originally by Grassberger and Procaccia (1983, 1984). Osborne and Provenzale (1989) showed that white noise gives infinite correlation dimensions because the random noise acts as a fractal path in phase space, leading to self similarity.

3.2.2 Filtering and Digitizing Errors

Filtering and digitizing the data can yield inaccurate estimates of the dimension of an attractor. Filtering leads to inaccurate dimension estimates in much the same manner as noise. Data is often filtered to reduce the amount of noise in a signal, but doing so can lead to an overestimate of the dimension of an attractor (Badii et al., 1988). On the other hand, digitizing the signal creates

errors which underestimate the dimension; in this regard it acts in an opposite manner to noise (Möller et al., 1987). Random noise combined with errors introduced during digitizing can create a "false" scaling region which could in turn suggest the presence of an attractor where there was none.

Möller et al., (1987) suggest that adding Gaussian noise with a standard deviation equal to 0.4 times the least significant bit before digitizing reduces the error in the dimension estimate in signals where most of the error is attributed to digitizing. For signals primarily distorted by noise, adding Gaussian noise with a standard deviation on the order of the least significant bit provides the best improvement in the dimension estimate. Tests run by Möller et al., (1987) for both cases show the error in the dimension estimate can be reduced by a factor up to 80%.

3.2.3 Number of Points

A limited data series (i.e. limited in the total number of points or amount of the attractor that is covered) leads to a downward bias in the dimension of random variables and an upward bias in the the estimate of a dimension of an attractor (Ramsey and Yuan, 1989). Small data sets also lead to conditions where the correlation integral does not saturate at increasing embedding dimension. Ramsey and Yuan (1989) suggest a method of non-linear curve fitting that will allow one to test for the presence of an attractor in a limited data set.

Obviously, there must be some minimum number of points for which the Grassberger-Procaccia algorithm will yield accurate estimates of the attractor dimension. The most commonly quoted limits on the number of points to adequately implement this algorithm is

$$10^{d_2} - 100^{d_2} \tag{3.26}$$

where d_2 is the correlation dimension (see, for example, Henderson and Wells, 1988).

Smith (1989) provides a more rigorous and detailed formulation of the minimum number of points needed to obtain an accurate dimension estimate. Smith gives the number of points necessary to estimate the correlation dimension of a non-lacunar set to within 5% of its true dimension as

$$N_{\min} \geq 42^M \quad (3.27)$$

where M is the greatest integer less than the dimension. For example, the value of M would be 2 for an attractor with a dimension of 2.3.

Abraham et al. (1988) showed promising results in examining the dimensions of small data sets contaminated by noise. They were able to obtain the dimension of the Henon attractor for data sets with as few as 500 points. Note that this fits Smith's minimum criteria; the dimension of the Henon attractor is 1.24 - hence the minimum number of points needed to estimate its dimension could be as low as 42! While it was difficult to accurately determine the dimension from small data sets, Abraham et al. (1988) still felt it was possible to distinguish between chaotic, periodic and random behavior.

3.2.4 Time Delay

A single time series may not properly fill out phase space if the wrong time delay for the embedding dimension is chosen. Often, the time to the first zero in the autocorrelation is chosen as the delay time in constructing the higher dimension vectors from the time series. Fraser and Swinney (1986) points out this practice as being "naive"; it may grossly underestimate the correlation dimension of the attractor in the data. Too small a time delay in the case of highly autocorrelated data may yield pairs of points that lie close together because they are closely related in time rather than their lying

"accidentally" close together because they are on the attractor. Highly autocorrelated data restricts the trajectories of a signal from "filling" out phase space, thus restricting the information that may be gained by examining the distances between them. Figure 3.3 shows an example of a function with two choices of time delay, one of which fills the phase space and one of which does not.

Fraser and Swinney (1986) suggest that a better choice of the proper time delay can be made on the basis of mutual information theory. The mutual information, I , is defined as

$$I = \iint P(X, Y) \log_2 \left[\frac{P(X, Y)}{P(X)P(Y)} \right] dX dY \quad (3.28)$$

where X is the measurement at time t , Y is the measurement at time $t+\tau$, $P(X, Y)$ is joint probability density and $P(X)$ and $P(Y)$ are the respective X and Y probability densities. For logarithms taken to base 2, the units of the mutual information is in bits. The mutual information measures the relationship between two signals in a more general manner than the autocorrelation, which measures the linear dependence. Normally, the first zero in the autocorrelation between two data vectors implies that the two are linearly independent. However, data characterized by a strange attractor are usually highly nonlinear, thus making the first zero in the autocorrelation a poor choice for the time delay. For nonlinearly related data, Fraser and Swinney suggest that first local minimum in the mutual information provides the best choice of time delay in construction of higher dimension data vectors. However, calculating the mutual information is computationally very

expensive (Fraser and Swinney, 1986) and often not as enlightening as repeating the correlation integral calculations for different time delays⁴.

Liebart and Schuster (1989) show the first local minimum in the mutual information is the best choice for time delay as opposed to some other local minimum (say the second or third). Their tests show that the first local minimum in the mutual information helps preserve the small scale structure of the attractor in the phase space reconstruction. They also point out that this criterion for the time delay is not "that the reconstructed orbit in phase space is closest to the true one but that the dimensions and entropies from the reconstructed orbit are closest to their true values".⁵

3.2.5 The Norm

Additional error can be introduced by an improper choice of norm used in the Grassberger-Procaccia method. While all norms are theoretically equivalent, Havstad and Ehlers (1989) found differences between the dimensions calculated from using the Euclidean norm and the maximum norm. The Euclidean norm counts points that fall within spheres while the maximum norm counts points that fall within cubes. Havstad and Ehlers (1989) found the maximum norm underestimated the dimension of the Mackey-Glass attractor whereas the Euclidean norm yielded a value for the dimension that was very close to the true one. They believe that the difference occurs because the diagonals of the cubes are aligned with the surfaces of the attractor. While the maximum norm is attractive because it is computationally less intensive, only the more computationally expensive Euclidean norm will be used in this study.

⁴ Glenn James, personal communication (1989). Glenn James is a fellow AF Ph.D. type who just recently graduated from Georgia Tech (Winter quarter, 1990). He also noted that the mutual information calculations were too much trouble and "a pain in the".

⁵Liebart and Schuster (1989), p108.

3.2.6 Non-Stationary Data Sets

Implicit in this analysis is the assumption that the data set is stationary, an assumption common to most signal analysis. However, Havstad and Ehlers (1989) have shown the Grassberger-Procaccia method is acceptable (with some modifications) for data sets that are not stationary. The dimension for small, non-stationary data sets can be calculated from small overlapping groups with reasonable accuracy if the dimension is not more than 10 (Havstad and Ehlers, 1989). However, the number of points in each overlapping segment still must be the minimum number necessary to implement the correlation integral algorithm.

Given some of the errors and uncertainties discussed above (small data sets, noise, a certain degree of autocorrelation, non-stationary data sets), one of the most difficult problems is defining the scaling region. In many experimental results, the scaling region is quite small and poorly defined for limited sets of noisy data. Ellner (1988) has developed an alternate method of calculating the generalized dimension of an attractor that improves the discrimination of the scaling region as well as providing an estimate of the errors. This technique is based on a maximum likelihood method. Unfortunately, the maximum likelihood method is even more computationally demanding than the Grassberger-Procaccia algorithm.

Ellner (1988) notes that the maximum likelihood technique offers several advantages over the technique of Grassberger and Procaccia. For small data sets, the scaling region is better defined and freer of distortions that occur because of the finite sample effect. This yields a larger apparent scaling region and, in turn, gives a more accurate estimate of the dimension. Furthermore, the maximum likelihood technique yields a dimension estimate accompanied by confidence intervals which give the error due to finite sample size.

3.3 Extension of the Grassberger-Procaccia Correlation Integral

Additional research has been done examining the strengths and weaknesses of this technique. One of the biggest disadvantages of the technique proposed by Grassberger and Procaccia (1983) is the limits in equations 3.15 and 3.18. These limits impose a requirement for a lengthy time series and, as pointed out by Theiler (1986), can lead to spurious dimensions if the number of data points is too small and the data are too highly autocorrelated. However, Theiler proposes a modification to the technique of Grassberger and Procaccia (1983) which improves the convergence of the integral towards its infinite limit for autocorrelated data.

Theiler redefines the correlation integral of Grassberger and Procaccia (1983) as:

$$C(\epsilon, N) = \frac{2}{N^2} \sum_{n=1}^N \sum_{i=1}^{N-n} H(\epsilon - |x_{i+n} - x_i|) \quad (3.29)$$

where $H(x)$ is the Heaviside step function, N the total number of points in the data set and the phase space vector x_i is defined as

$x_i = (s_i, s_{i+\tau}, s_{i+2\tau}, \dots, s_{i+(m-1)\tau})$ where s_i is the original signal at time t and τ the time delay. Theiler notes that for typical conditions ($\tau, m \ll N$), there are as almost as many vectors x_i as there are data points s_i . The correlation dimension, v , can be defined by the limit

$$v = \lim_{\epsilon \rightarrow 0} \lim_{N \rightarrow \infty} \frac{\log C(\epsilon, N)}{\log \epsilon} \quad (3.30)$$

or where the derivative exists

$$\nu = \lim_{\epsilon \rightarrow 0} \lim_{N \rightarrow \infty} \frac{d[\log C(\epsilon, N)]}{\frac{d\epsilon}{d \log \epsilon}} \quad (3.31)$$

The limits in the two expressions above provide problems in implementing this technique in practice.

Theiler (1986) shows that the Grassberger-Procaccia correlation integral redefined in equation 3.29 can be better served by a more generalized version

$$C(\epsilon, N, W) = \frac{2}{N^2} \sum_{n=W}^N \sum_{i=1}^{N-n} H(\epsilon - |x_{i+n} - x_i|) \quad (3.32)$$

W is the number of autocorrelated points to exclude from the counting statistics. Note that $W=1$ yields the original definition of the correlation integral proposed by Grassberger and Procaccia (1983). Essentially, this algorithm doesn't count the first W autocorrelated points that lie nearby. Skipping these points in the summation improves the convergence of the algorithm in both limits. Theiler notes that the key to this modification lies in choosing the right value of W .

Theiler (1986) demonstrated the validity of this modification in examining uncorrelated and autocorrelated noise. As previously mentioned, autocorrelation restricts the trajectories of a function from "filling" out phase space, thus restricting the information that may be gained from examining the distances between pairs of data points. Highly autocorrelated data may yield pairs of points that lie close together because they are closely related in time rather than their lying "accidentally" close together because they are on an attractor.

Noise has a slope on the $C(\epsilon, N)$ vs ϵ plots equal to m since noise scales as ϵ^m where m is the embedding dimension (Theiler, 1986). Noise has an effect similar to that for autocorrelation. Autocorrelation and a limited number of points may unnecessarily restrict the range over which this slope occurs, creating a "knee" in the plot of $\ln C(\epsilon, N)$ vs. $\ln \epsilon$ at higher embedding dimensions. Theiler (1986) shows that the usable range of $C(\epsilon, N, W)$, i.e. that range over which $C(\epsilon, N, W)$ is proportional to ϵ^m , will be between

- a. Uncorrelated limit - $2/N^2$ and 1, and
- b. Autocorrelated limit - $2/N^2$ and $2/N$.

As the number of data points approaches infinity, the autocorrelated range may approach the uncorrelated limit.

Given this, Theiler suggests a minimum value for W which extends the usable range for the slope:

$$W > \tau \left(\frac{2}{N} \right)^{2/m} \quad (3.33)$$

where τ is the first zero in the autocorrelation, N the number of data points and m is the embedding dimension. This is equivalent to dropping the first W terms in the summation series in the correlation integral. By dropping the first W terms, the summation neglects the points that are nearby because they are correlated in time and thus approaches its true limit.

There are two different time scales which must be considered in employing the Grassberger-Procaccia algorithm. The time scale of the first minimum of the mutual information determines the best lag for the reconstruction of phase space vectors from the original data. The time to the first zero in the autocorrelation determines the number of autocorrelated data points to exclude from the summation in the correlation integral.

3.3.1 The Normalization Factor

There is some question about the normalization factor used in the correlation integral algorithm and its variations. In the original definition by Grassberger and Procaccia (1983, 1984), the normalization factor was $1/N^2$. However, it was seen that the number of calculations could be halved by only determining the distances for the upper half of the matrix which held the pairs of points (i.e., the distance between point i and point j is the same as the distance between point j and point i -- why repeat the calculation?). The normalization factor was further modified by Henderson and Wells (1988) to $2/N(N-1)$ by not calculating the identity (sometimes called "self pair") terms (i.e., those terms for which $i=j$). Smith (1988) noted that the "self pair" terms must be calculated explicitly and included in the full double summation. This is required to distinguish the scaling of true noise from fluctuations due to a finite number of points N . When the "self pair" ($i=j$) terms are omitted, the correlation integral is not necessarily bounded in the limit as ϵ approaches zero.

3.4 Autocorrelation Analysis

The autocorrelation analysis is based on the correlation function which is defined as follows (Walpole and Meyers, 1989):

$$r = \frac{S_{xy}}{\sqrt{S_{xx} S_{yy}}} \quad (3.34)$$

where S_{xx} , S_{yy} and S_{xy} are given by

$$\begin{aligned}
S_{xx} &= \sum_{i=1}^N x_i^2 - \frac{1}{N} \left[\sum_{i=1}^N x_i \right]^2 \\
S_{yy} &= \sum_{i=1}^N y_i^2 - \frac{1}{N} \left[\sum_{i=1}^N y_i \right]^2 \\
S_{xy} &= \sum_{i=1}^N x_i y_i - \frac{1}{N} \sum_{i=1}^N x_i \sum_{i=1}^N y_i
\end{aligned}
\tag{3.35}$$

The individual components in the summation are defined as

$$\begin{aligned}
x_i &= x(i \Delta t) \\
y_i &= x((i + \lambda) \Delta t)
\end{aligned}
\tag{3.36}$$

where x_i is an element of the original time series x , Δt is the sampling interval and y_i is an element of the original time series x lagged by some factor λ .

The correlation was calculated for each lag λ . The error of the autocorrelation is defined as

$$E(\lambda) = \left[\frac{N - \lambda}{N(N + 2)} \right]
\tag{3.37}$$

The errors were calculated but are not displayed on the figures shown in this study simply to render the figures more readable. The number of points in the autocorrelation were chosen to minimize the error.

3.5 Power Spectrum Analysis

We will use the method of calculating the power spectrum as described by Press et al., (1986). The "power" calculated in this study is the mean squared power defined as

$$P \equiv \frac{1}{T} \int_0^T |c(t)|^2 dt \approx \frac{1}{N} \sum_{j=0}^{N-1} |c_j|^2 \quad (3.38)$$

where Δ is the sampling interval, N the number of points and $T=(N-1)\Delta$. The power (P) is defined as a function of frequency (f) at $N/2+1$ discrete frequencies by

$$\begin{aligned} P(0) &= \frac{1}{N^2} |c_0|^2 \\ P(f_k) &= \frac{1}{N^2} [|c_k|^2 + |c_{N-k}|^2] ; \quad k=1, 2, \dots, \left(\frac{N}{2} - 1\right) \\ P(f_c) &= \frac{1}{N^2} |c_{N/2}|^2 \end{aligned} \quad (3.39)$$

where the frequencies f_k and f_c are defined as

$$\begin{aligned} f_c &= \frac{1}{2\Delta} \\ f_k &= \frac{k}{N\Delta} = 2f_c \frac{k}{N} ; \quad k=0, 1, \dots, \frac{N}{2} \end{aligned} \quad (3.40)$$

and the Fourier coefficients c_k are defined by the following

$$c_k = \sum_{j=0}^{N-1} c_j e^{2\pi i j k / N} ; \quad k=0, 1, \dots, N-1$$

(3.41)

The "Welch" window was used on the data when applying the Fourier transform (Press et al., 1986). The data was segmented to obtain the smallest variance of the power for the number of data points in the transform. The segments were overlapped by half their length M and the variance was reduced by a factor of $9k/11$ where k is the number of segments. The number of data points required by the transform is $(2k+1)M$.

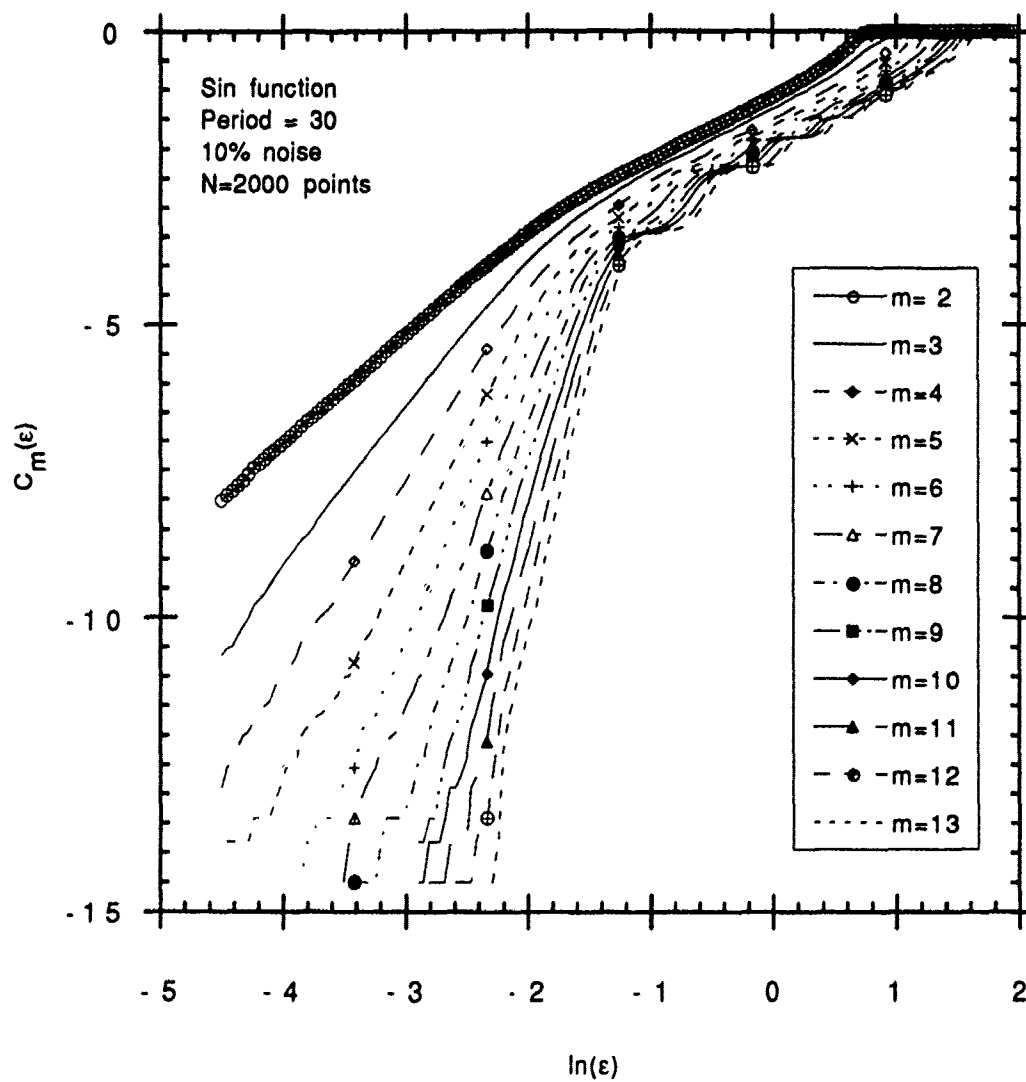


Figure 3.1 Correlation integral of the sine function with period equal to thirty with 10% external noise. The total number of points is 2000.

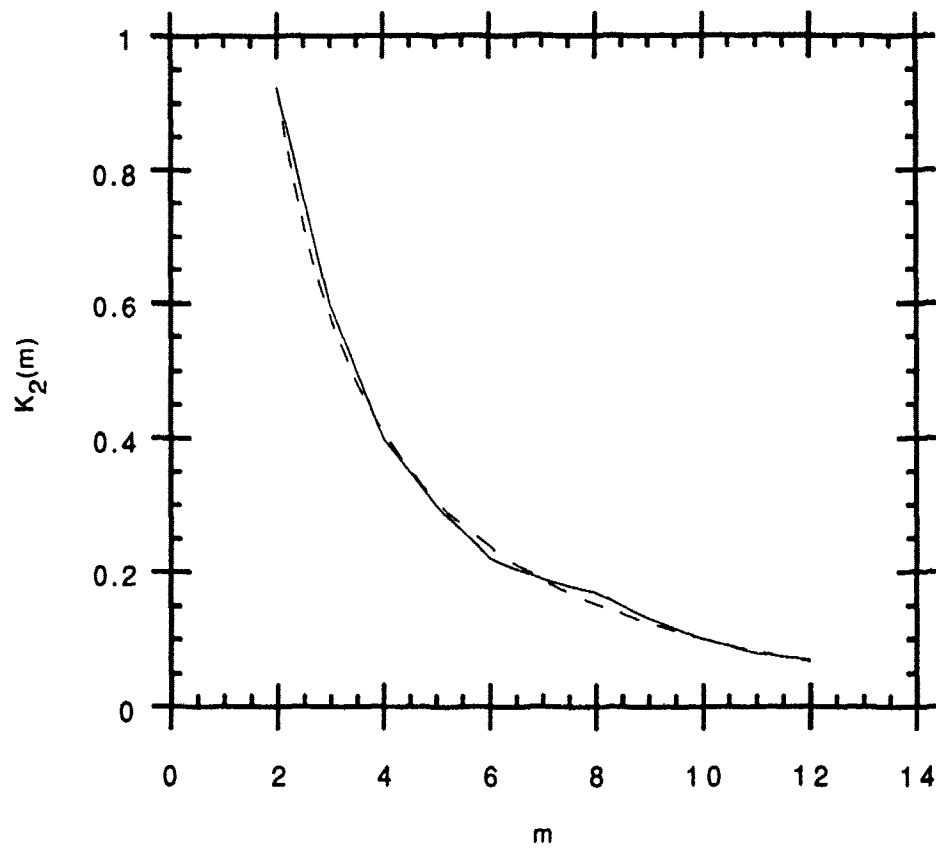


Figure 3.2 Kolmogorov entropy (K_2) for the correlation integral of the sine function shown in Figure 3.1 plotted as a function of increasing embedding dimension. The curve asymptotically approaches the value of 0, indicating periodic behavior.

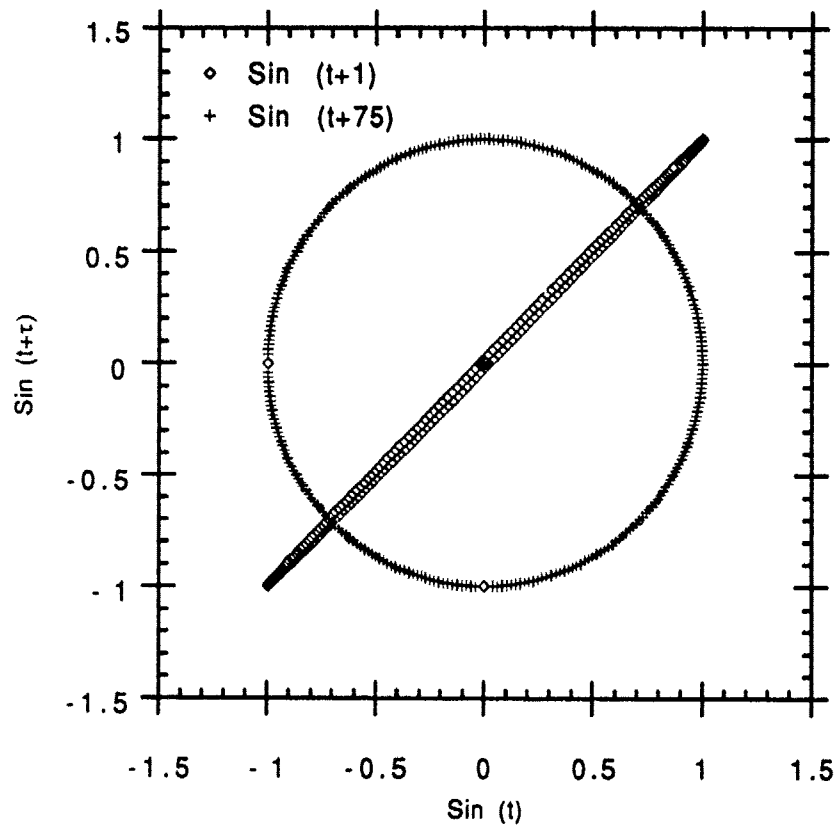


Figure 3.3 Phase space portrait of a sine function with period of 300 for a time delay of $\tau=1$ and a time delay equal to the first zero in the autocorrelation, i.e. $\tau=75$.

CHAPTER IV

OVERVIEW OF THE DATA

This chapter gives an overview of the data used in this study. It first describes the theory behind the partial reflection radar from which the data was obtained. This is followed by a description of the Saskatoon partial reflection radar itself. The chapter concludes with a description of the data from the Saskatoon radar used in this study.

4.1 Theory of Partial Reflection Radars

Partial reflection radars transmit an electro-magnetic pulse which is both partially and totally reflected in the middle atmosphere. The reflected signal creates a diffraction pattern on the ground which moves at a rate twice the speed of the wind in the scattering layer at which the reflection occurred (see Figure 4.1). This induces an e.m.f. in a stationary antenna. As the pattern moves past the antenna, the induced e.m.f. varies in amplitude; this is called radiowave fading. Normal signal analysis of partial reflection radar data revolves around cross correlation of the signal peaks between antennas to deduce the direction and speed of the wind. Comparisons of the fading rates from at least three antennas give an estimate of the horizontal pattern velocity and hence the velocity of the reflecting/scattering region.

The mechanisms causing the echoes range from reflections from sharply bounded irregularities in the refractive index to scattering (i.e., "partial reflections") from quasi-isotropic irregularities ("turbulent blobs") whose scales are on the order of half the radar wavelength. At the altitudes

measured by partial reflection radars (typically 50 - 120 km, depending on the design and sensitivity of the radar), irregularities in the refractive index can be created by free electrons carried along by the neutral wind as well as variations in potential temperature and moisture content (Hocking, 1985). Short wavelength solar radiation ionizes the air in the upper atmosphere and generates free electrons; concentrations of these free electrons typically vary from less than $\sim 10^2 \text{ cm}^{-3}$ at 60 km to $\sim 10^4 \text{ cm}^{-3}$ at 100 km (Gregory and Stephenson, 1972).

The refractive index varies primarily in the vertical, a consequence of the increase in the free electron density with height as well as changes in the potential temperature with height. The signal strength generally increases with height because of the vertical gradient in the refractive index. However, there are horizontal variations in the refractive index which modulate the transmitted pulse wave front so that the scattered/reflected wave is equivalent to an angular spectrum of plane waves. The horizontal variations in the refractive index can be either a result of horizontal variations in the potential temperature caused by turbulence or wave activity or horizontal variations in the free electron density or a combination of both. This spectrum of plane waves creates the diffraction pattern on the ground which is measured by the receiving antennas (Fraser, 1984).

Echoes can be obtained from minimum heights of 50-60 km to heights where the signal is totally reflected in the E or F region of the ionosphere¹. The lower altitude limit is essentially a function of the sensitivity of the system to signals that are only partially reflected in the lower mesosphere. The spatial characteristics of the partial reflection regions vary from thin, stratified layer to thick, turbulent layers. The thin, stratified layers are often less than 1 km thick (Fraser, 1984). Measurements made near local solar noon can be influenced by the D region of the ionosphere which extends further down into

¹The E region spans the altitude range 90 - 150 km. The F region encompasses 150 - 500 km (Kelley, 1989).

the mesosphere². The effects of the geomagnetic field on the motions of the free electrons must be considered at heights where the electron-neutral collision frequency is low. This effect does not appear to be significant at heights below 95–100 km (Fraser, 1984).

4.2 Saskatoon Partial Reflection Radar

The data used in this study came from the partial reflection radar located at 52° N, 107° W in Saskatoon, Canada. This radar operates at an average frequency of 2.2 MHz with an equivalent wavelength of 135 m. It emits an approximately trapezoidal pulse with a width of 20 μ s; this is equivalent to a 3 km height resolution (Manson et al., 1974; Gregory and Stephenson, 1972; Manson and Meek, 1987; Meek and Manson, 1987). Data are recorded for 23 height levels ranging from 52 km to 118 km in 3 km increments. The pulse repetition rate used for this data set is 15 s⁻¹. Data below 70 km is considered unreliable (Meek, 1989, private communication).

The radar consists of a transmitter and four receiving antennas. The receiving antenna array is laid out in a "Y" pattern with a separation between antennas 1, 2 and 3 of 2λ (270 m), twice the wavelength of the radar. The receiving antenna array is depicted in Figure 4.2. Measurements are taken at each of the four antennas as the recording system cycles around the antenna array at a rate of 15 Hz; this yields the 0.2666 second measurement separation between measurements at each antenna.

4.3 Overview of the Data

The data set was taken on 2 August (day of year 214) 1985 starting at 18:31:00 GMT and covers approximately one and a half hours (a total of 17910

²The D region is less than 90 km altitude.

points). The data set has been described previously in the literature by Manson and Meek (1987). Manson and Meek (1987) found several "glints" or regions of focused turbulence in the data set to be used in this study.

The data were broken down into three separate files. There is a time gap between the files due to data recording considerations. The first file started at 18:31:00 GMT, ended at 19:01:12 GMT and consisted of 6705 points. There was a 2 minute 16 second gap between the first file and the second file which is equivalent to 510 points. The second file began at 19:03:28 GMT and ended at 19:29:36 GMT for a total of 5895 points. There is a gap of approximately 40 seconds between the second and the third files which is equivalent to 146 points. The third file began at 19:30:15 GMT and ended at 19:53:50 GMT for a total of 5310 points. The total number of points, not counting the breaks between files, is 17910.

A careful examination of the raw data record seemed to reveal an undocumented change of gain between the first and remaining files. The apparent change in gain was signalled by a 20 second dropout in signal just prior to the end of the first file (i.e., at point 6610). We calculated the variance of the data for the first 6000 points and compared that to the variance of the remaining points for the seven levels between 76 and 94 km. The results of these calculations are summarized in Table 4.1. The average ratio of the variances over all seven levels was 3.08 which is very close to what you would expect from a 10 db (i.e., a ratio of 3.16) change in gain.

We used the F test (Walpole and Meyers, 1989) to determine whether the variances were indeed the same. We were able to reject the hypothesis that the variances were the same for each level at the 99.995% confidence level. Thus, it is safe to conclude that there was an undocumented gain change between the first and the remaining files.

Table 4.1 Summary of mean and variance changes in the data.

Level (km)	1 < n < 6000		7000 < n < 17900		Ratio of two variances
	Mean	Variance	Mean	Variance	
76	101.4	306.4	103.8	99.8	3.07
79	100.4	969.7	104.4	680.3	1.43
82	99.0	1569.8	102.6	401.3	3.91
85	100.3	1052.6	102.9	413.3	2.55
88	98.1	1024.2	102.3	288.7	3.55
91	111.8	2341.9	108.4	400.9	5.84
94	115.4	958.0	113.9	774.8	1.24

There is also a difference in the mean signal strength for each of the seven levels between the first file and the last two files. We used the Student t test to determine whether the means belonged to the same population. We were able to reject the hypothesis that the mean from the first file and the mean from the second and third files at each level belonged to the same population at the 99.95% level. The change in mean over the approximate hour and a half that is spanned by the data set is most likely due to receiver drift. Meek (personal communication, 1989) reports that the data should be corrected for receiver drift for observation periods longer than an hour.

The variance is low for the 76 km data compared to that for the other levels above 76 km. In general, the signal strength increases with height. There was very little variation in the signal for levels below 76 km which is why data from these levels were not even considered beyond some preliminary examination.

We tested for receiver drift over the length of the first file by calculating the mean and variance in 500 point groups from point number one to point number 6500 for each of the seven levels (76 through 94 km). The hypothesis that the means for each level belonged to the same population was accepted at the 95% confidence level. While this hypothesis was not accepted at

a more rigorous confidence level (i.e., one $> 95\%$), it seems reasonable to assume that any receiver drift over the first data file (a period of approximately 30 minutes) was minimal.

These two problems, receiver drift and change in signal gain, could be corrected. The drift in the mean could be easily remedied by detrending the data. The change in the gain could be eliminated by subtracting out the detrended mean, multiplying by the ratio of the variances and adding back the mean. While making any changes to the original data increases the risk of rendering any dimension estimates inaccurate, these changes represent the least significant risk. However, there was one additional problem that eliminated almost two thirds of the data from consideration.

In addition to the gain change, the data in the second and third files appeared to be contaminated by a high frequency oscillation. This was almost certainly due to a folding back of some portion of the long range signal into the lower height gates. The oscillation can be seen clearly in the autocorrelation (see Figure 4.3) and power spectrum (see Figure 4.4) of data from the second and third files. The oscillation was present in the signal at all of the heights (76-94 km) to be used in this study, but it was strongest in the data from 91 and 94 km. The oscillation occurred with a period of .867 s, which is slightly greater than every third point.

Filtering the data could easily remove this high frequency signal. However, doing so would increase the uncertainty in any estimate of the dimension of the system and possibly suggest the presence of an attractor where there was none. Because of this, we decided to eliminate data from the second and third data files from further analysis. Only data from the first file (6705 points - 18:31:00 to 19:01:12 GMT) was considered in further analysis.

The data for each of the four antennas and seven levels from 76 to 94 km is shown in Figures 4.5 - 4.8. The data shown in the figures was averaged over 3.5 s and only every thirteenth point was plotted in order to improve legibility.

Several features are immediately obvious from examining the data. The variation in the signal for levels 76 and 79 km is generally much less than for the upper levels for all antennas. In addition, the variation in signal strength is slightly less at all levels for antenna #4 than for the other three antennas.

Meek and Manson (1987) found a strong scattering layer to be located at 82 km in a previous study of this data set. The variation in signal strength then increases again for 91 and 94 km. This phenomena can be most easily seen in the data from antenna #4 shown in Figure 4.8. The presence of a strong scattering layer near 82 km is often seen in the summer mesosphere (Fraser, 1984).

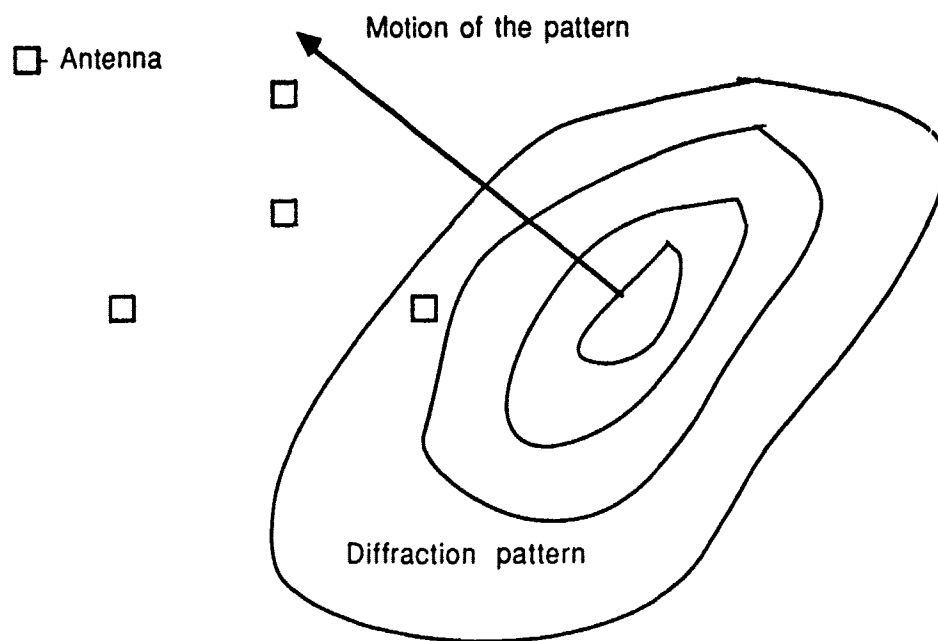


Figure 4.1 Depiction of a diffraction pattern on the ground moving past the antenna array. The antennas are shown by the squares and the direction of motion of the pattern is indicated by the arrow.

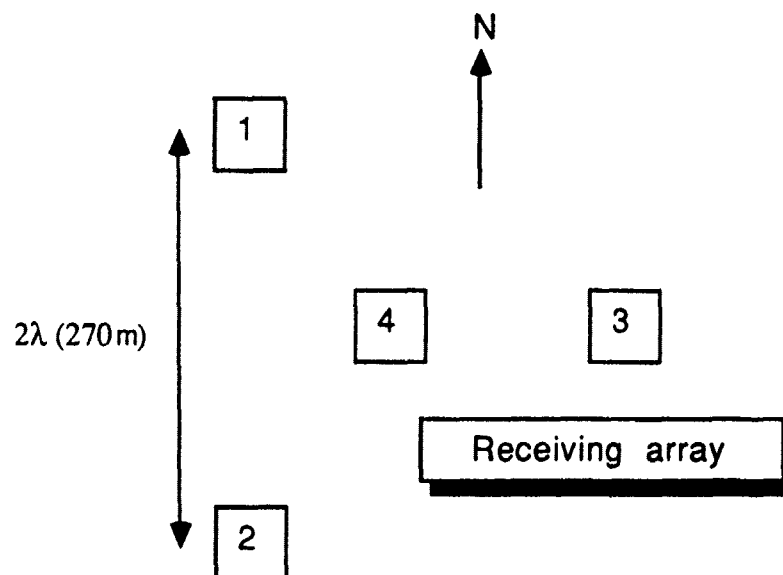


Figure 4.2. Receiving array of Saskatoon radar in the Y configuration, (adapted from Meek and Manson, 1987)

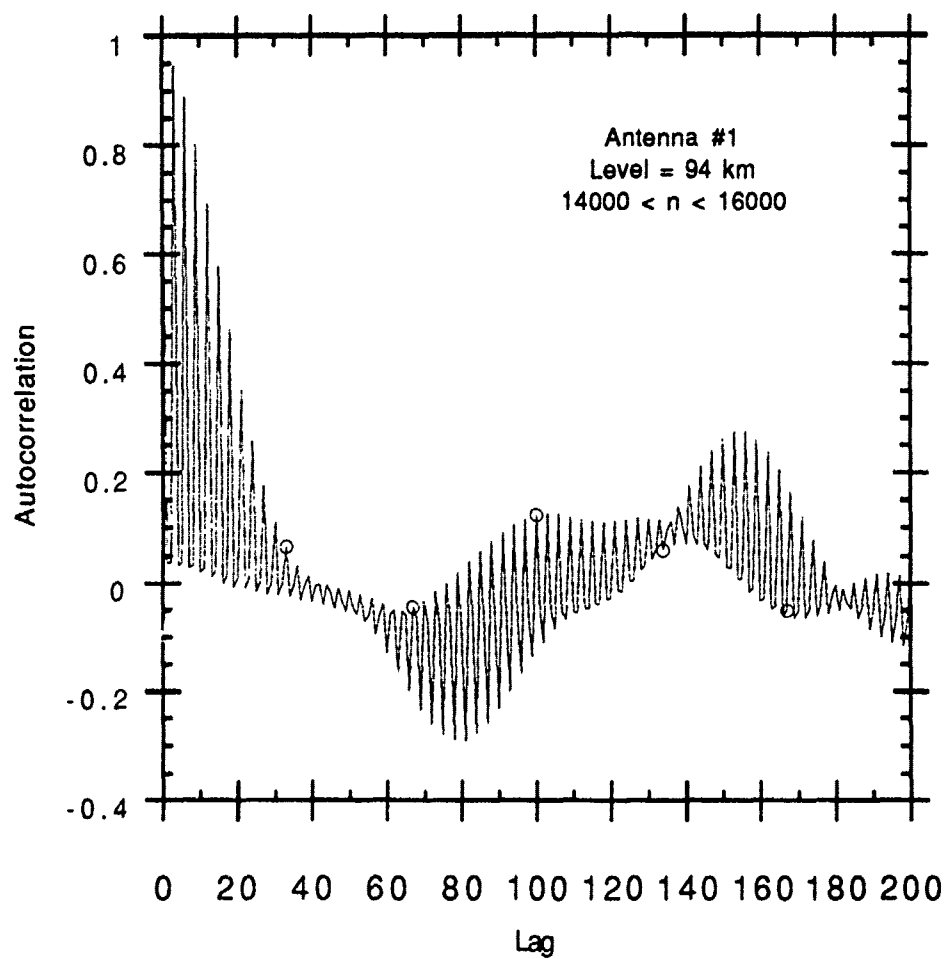


Figure 4.3 Autocorrelation for antenna #1 at 94 km for points 14000 through 16000 (i.e., data from the contaminated third file).

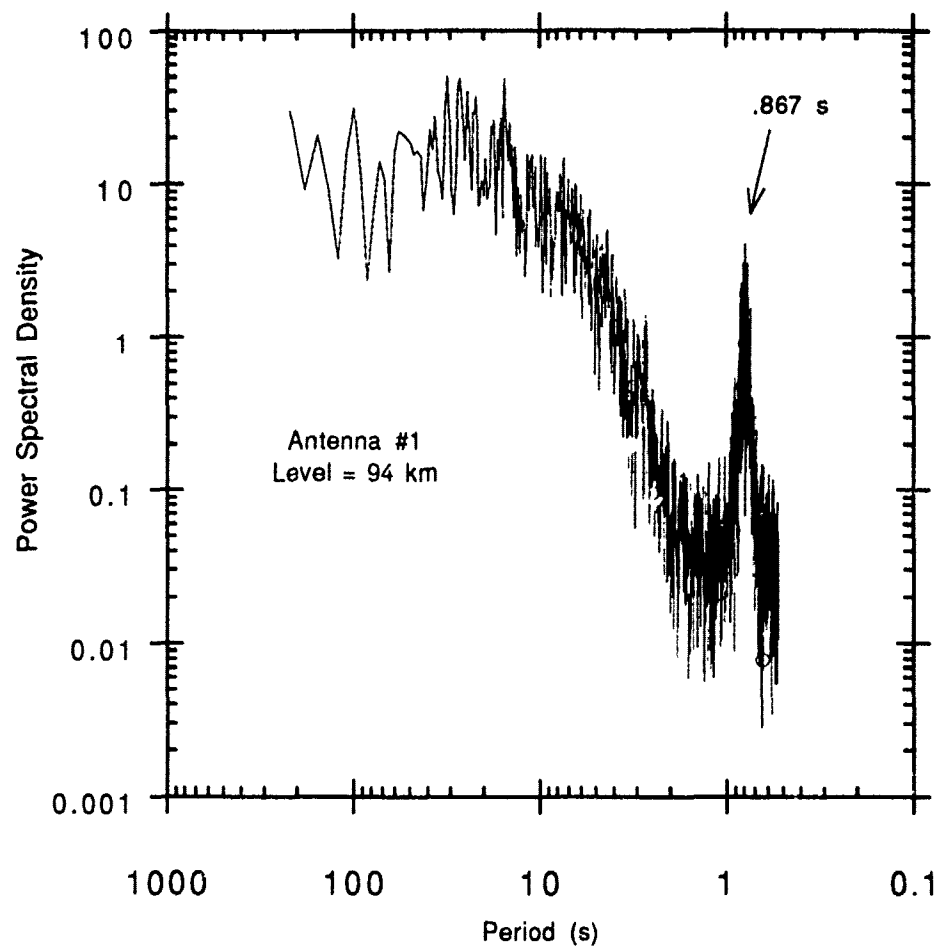


Figure 4.4 Power spectrum for antenna #1 at 94 km This includes the data from the contaminated second and third files.

Figure 4.5 Data from antenna #1 for (a) 76 km; (b) 79 km; (c) 82 km; (d) 85 km; (e) 88 km; (f) 91 km; and (g) 94 km. The data starts at 18:31:00 GMT. The figure is on the following pages.

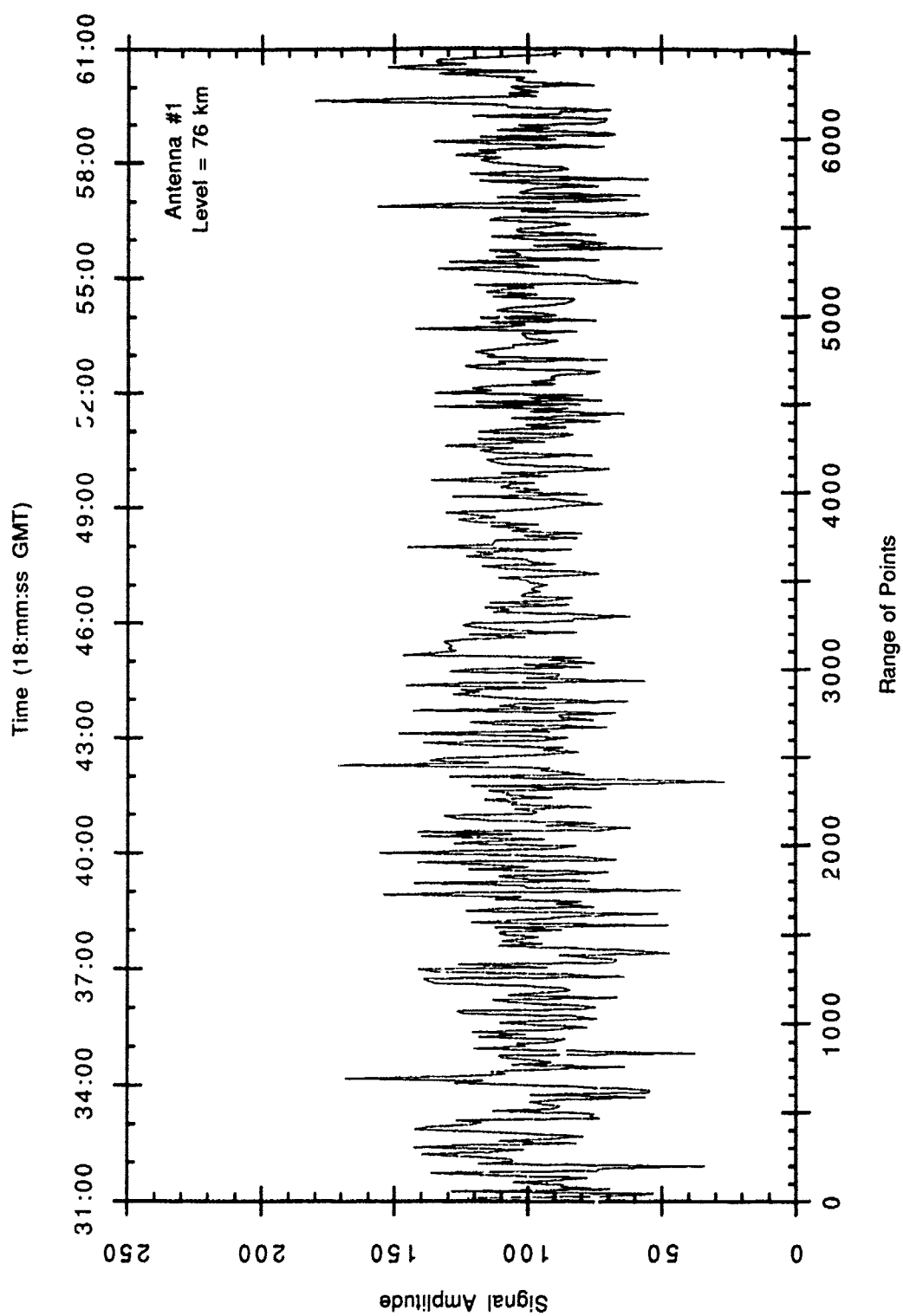


Figure 4.5 (a)

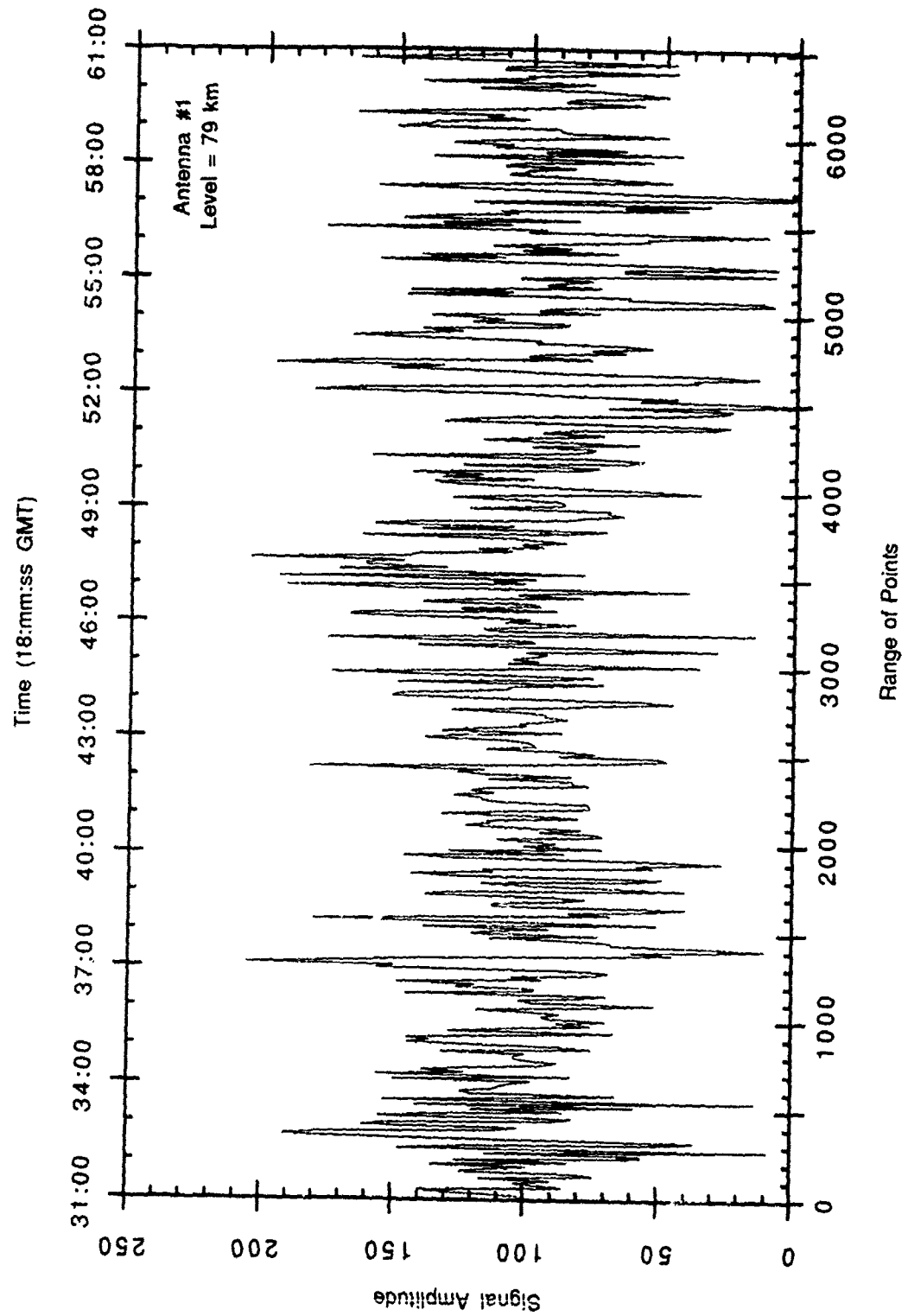


Figure 4.5 (b)

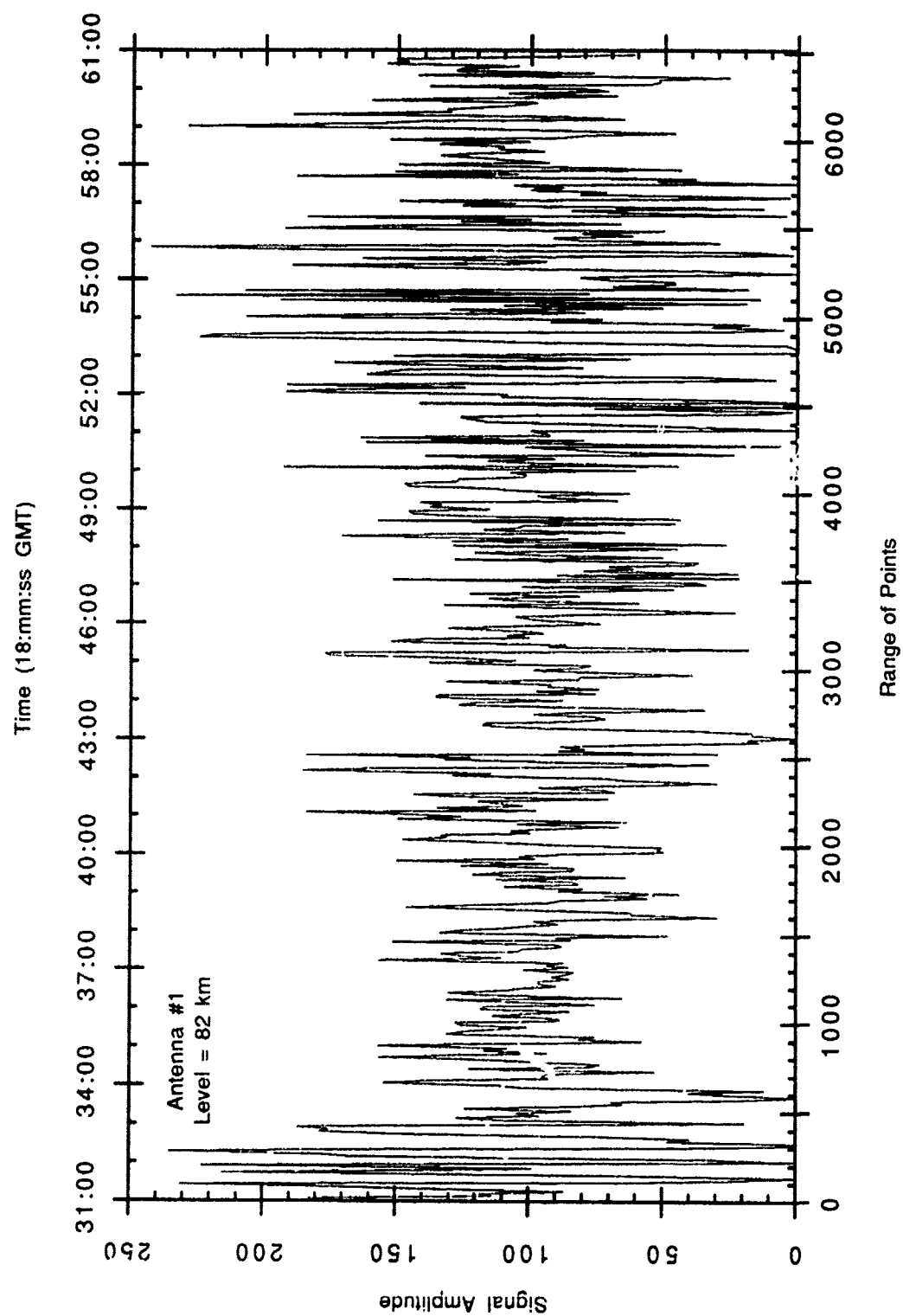


Figure 4.5 (c)

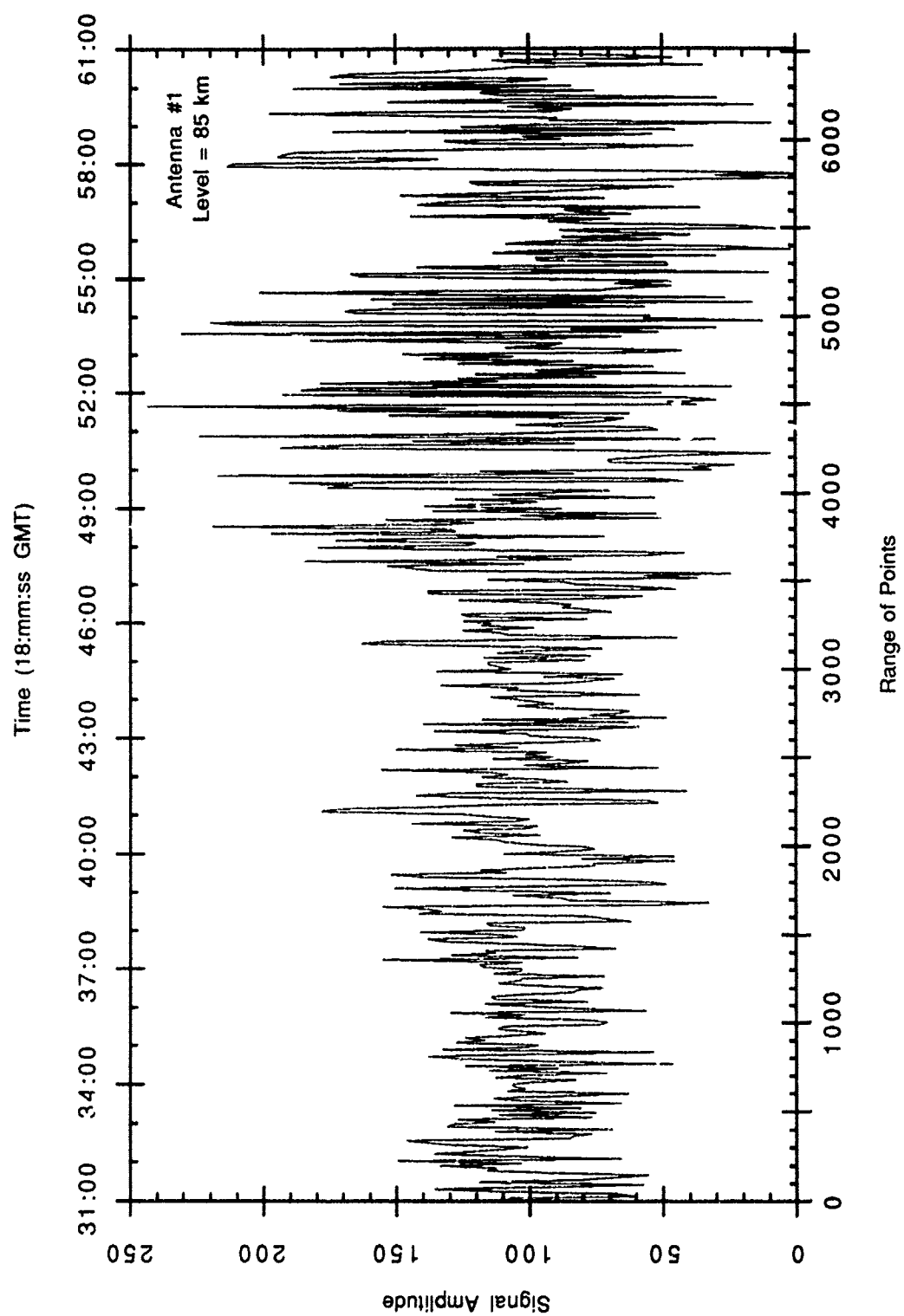


Figure 4.5 (d)

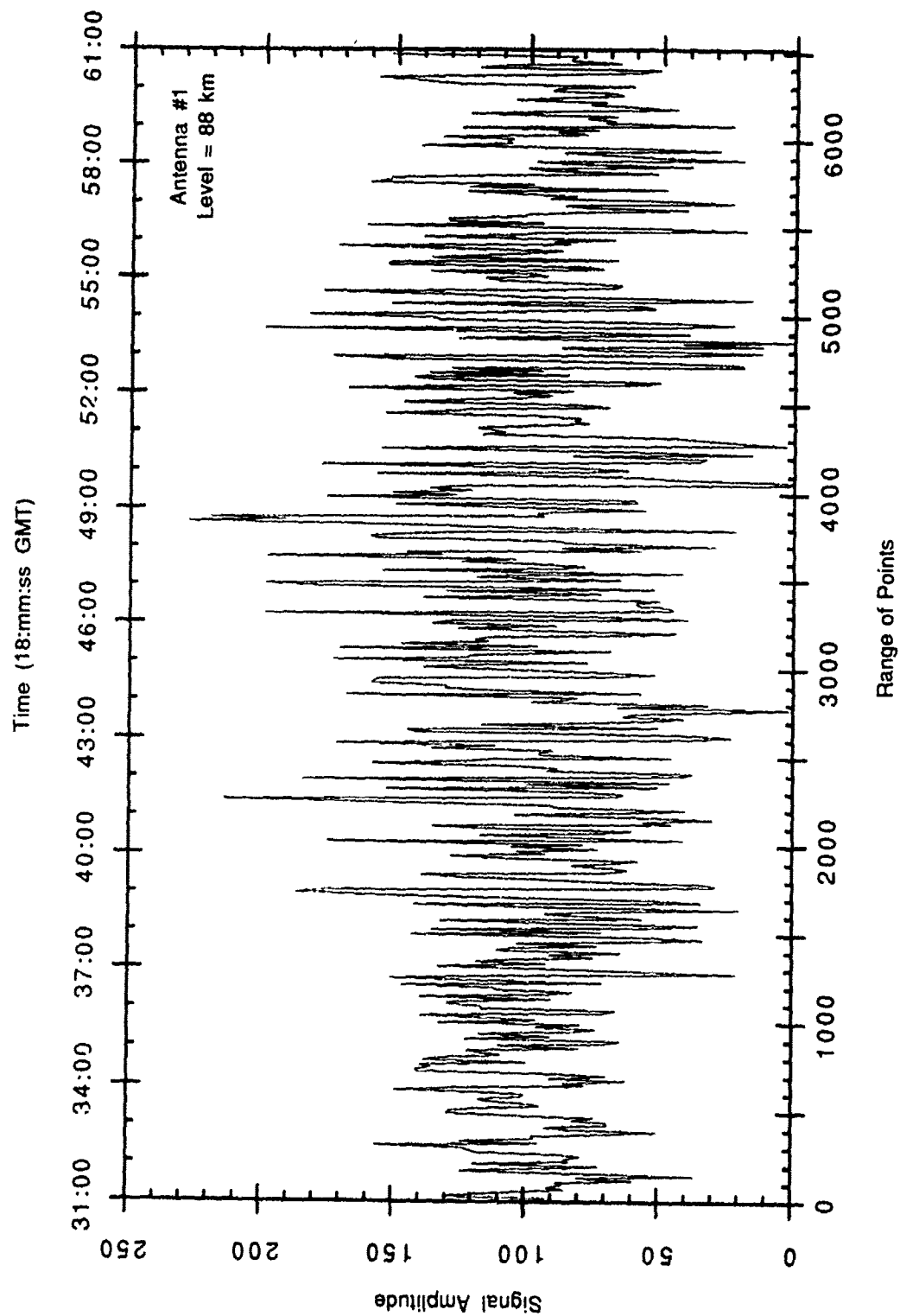


Figure 4 5 (e)

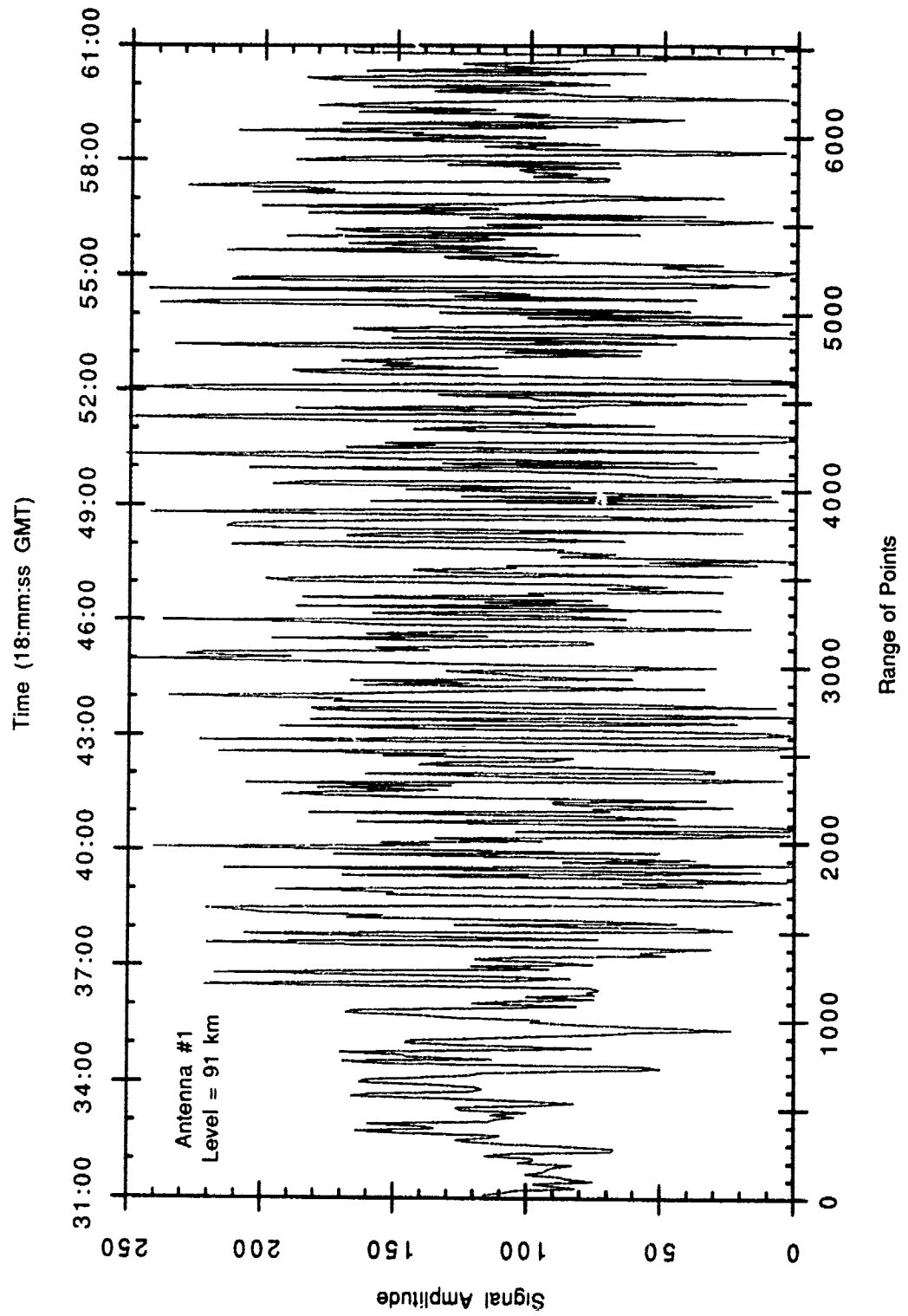


Figure 4.5 (f)

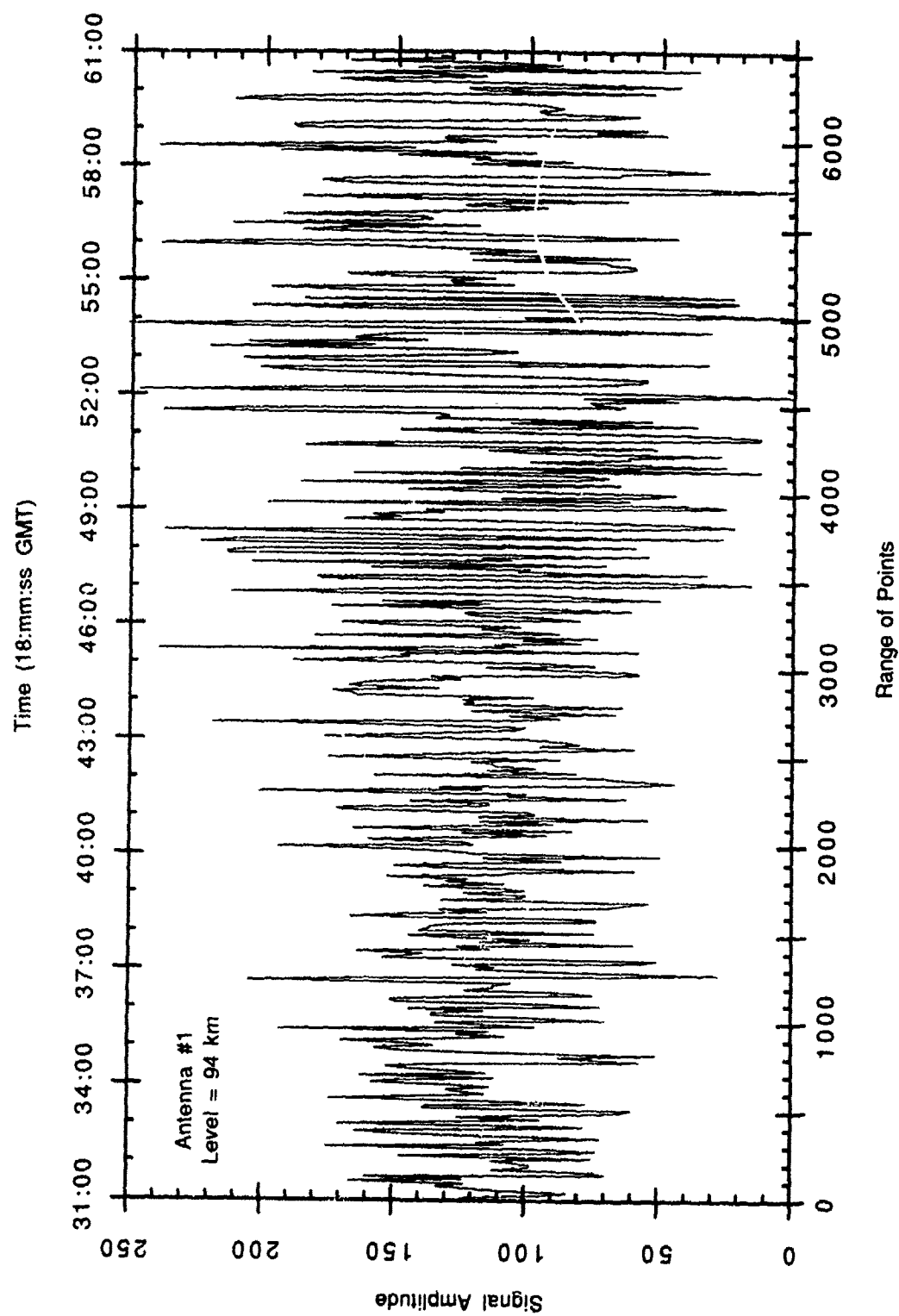


Figure 4.5 (g)

Figure 4.6 Data from antenna #2 for (a) 76 km; (b) 79 km; (c) 82 km; (d) 85 km; (e) 88 km; (f) 91 km; and (g) 94 km. The data starts at 18:31:00 GMT. The figure is on the following pages.

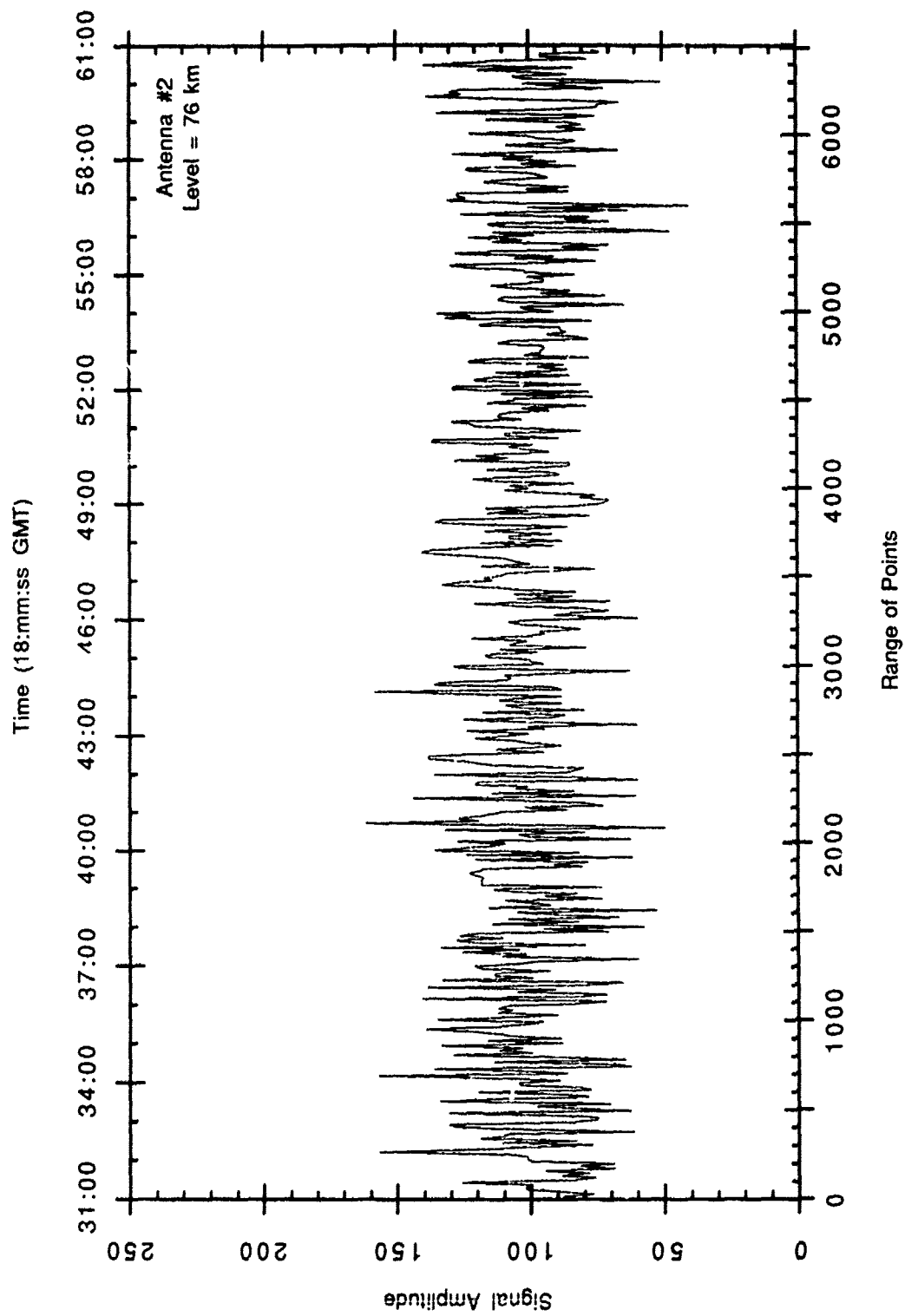


Figure 4.6 (a)

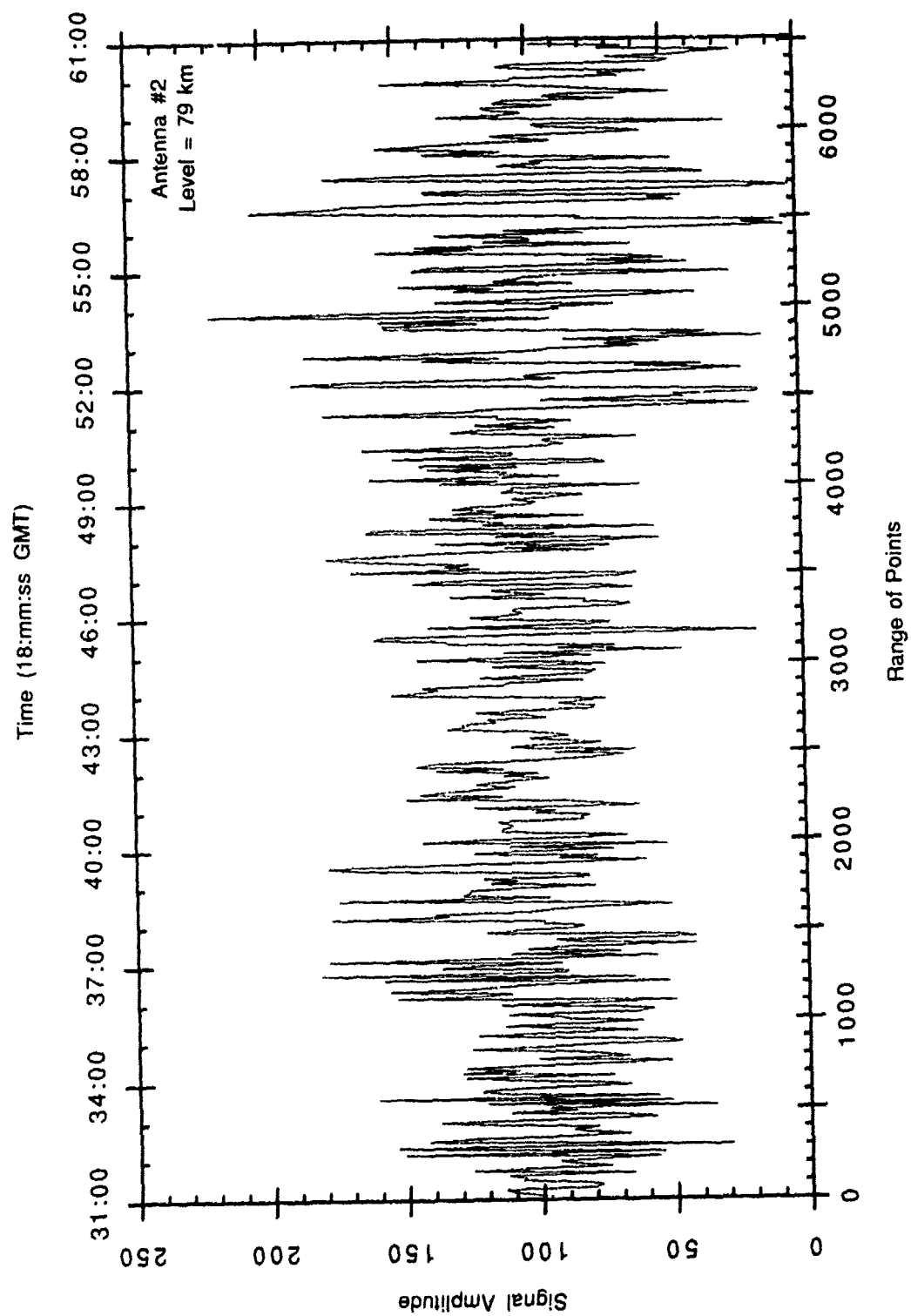


Figure 4.6 (b)

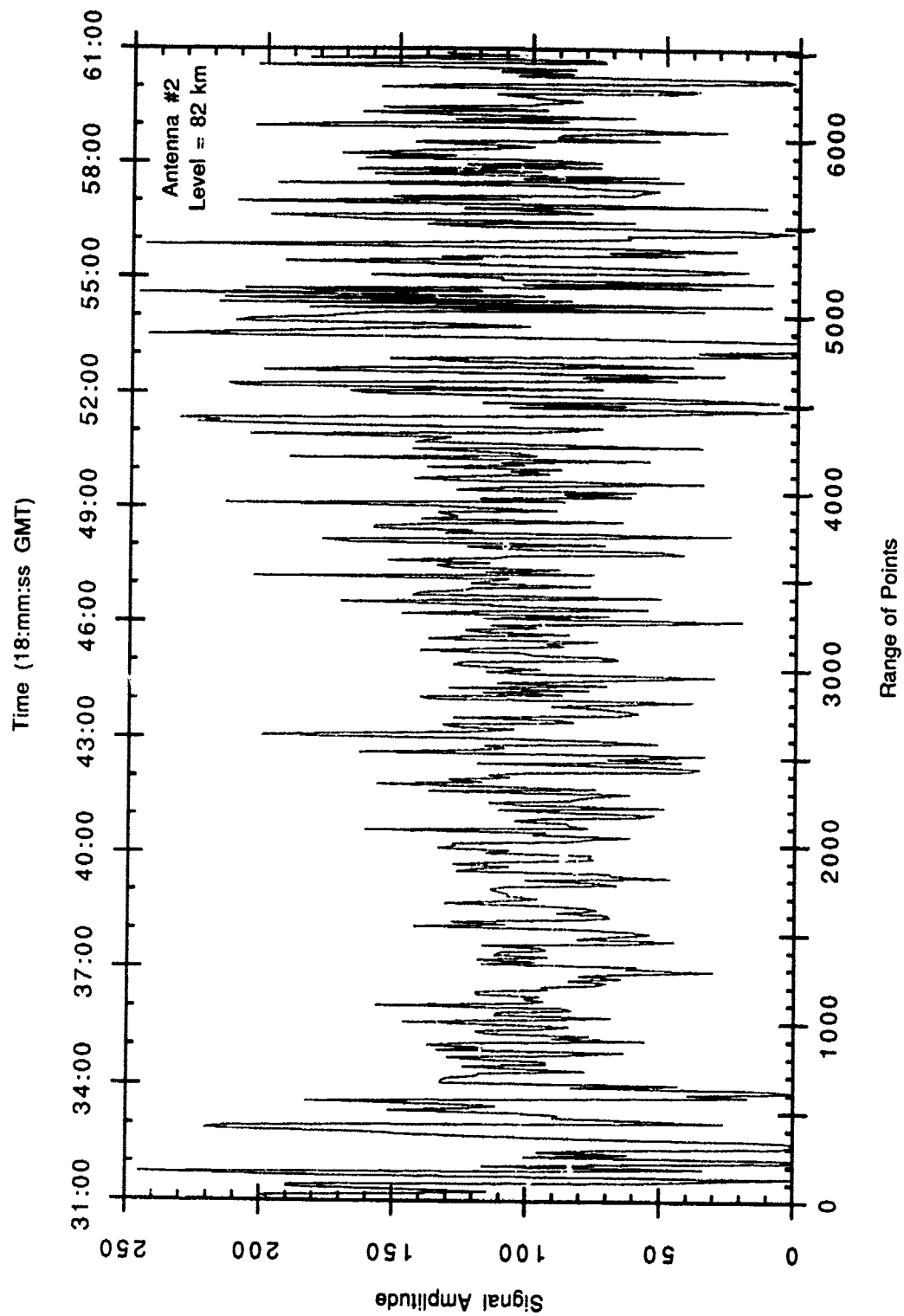


Figure 4.6 (c)

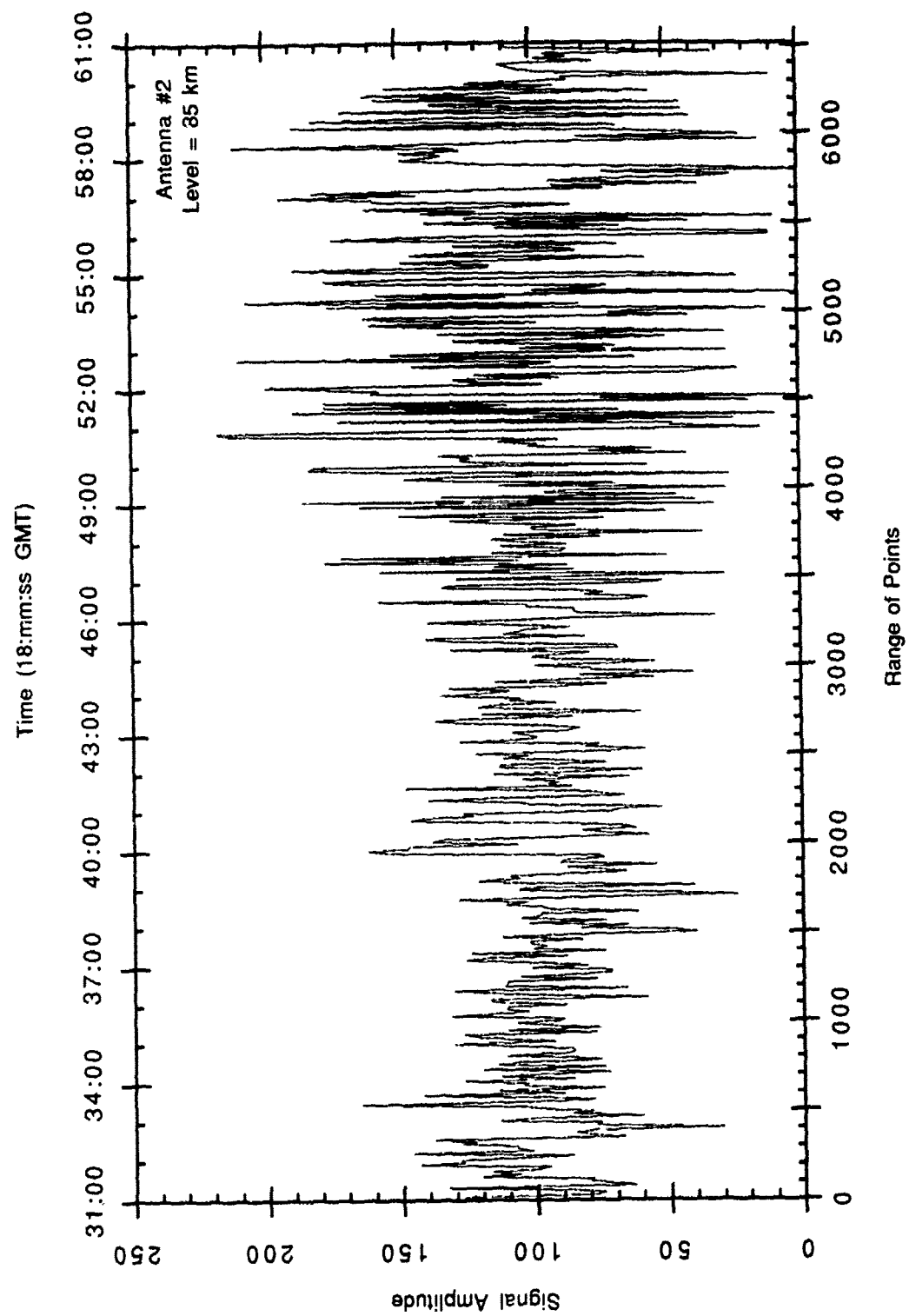


Figure 4.6 (d)

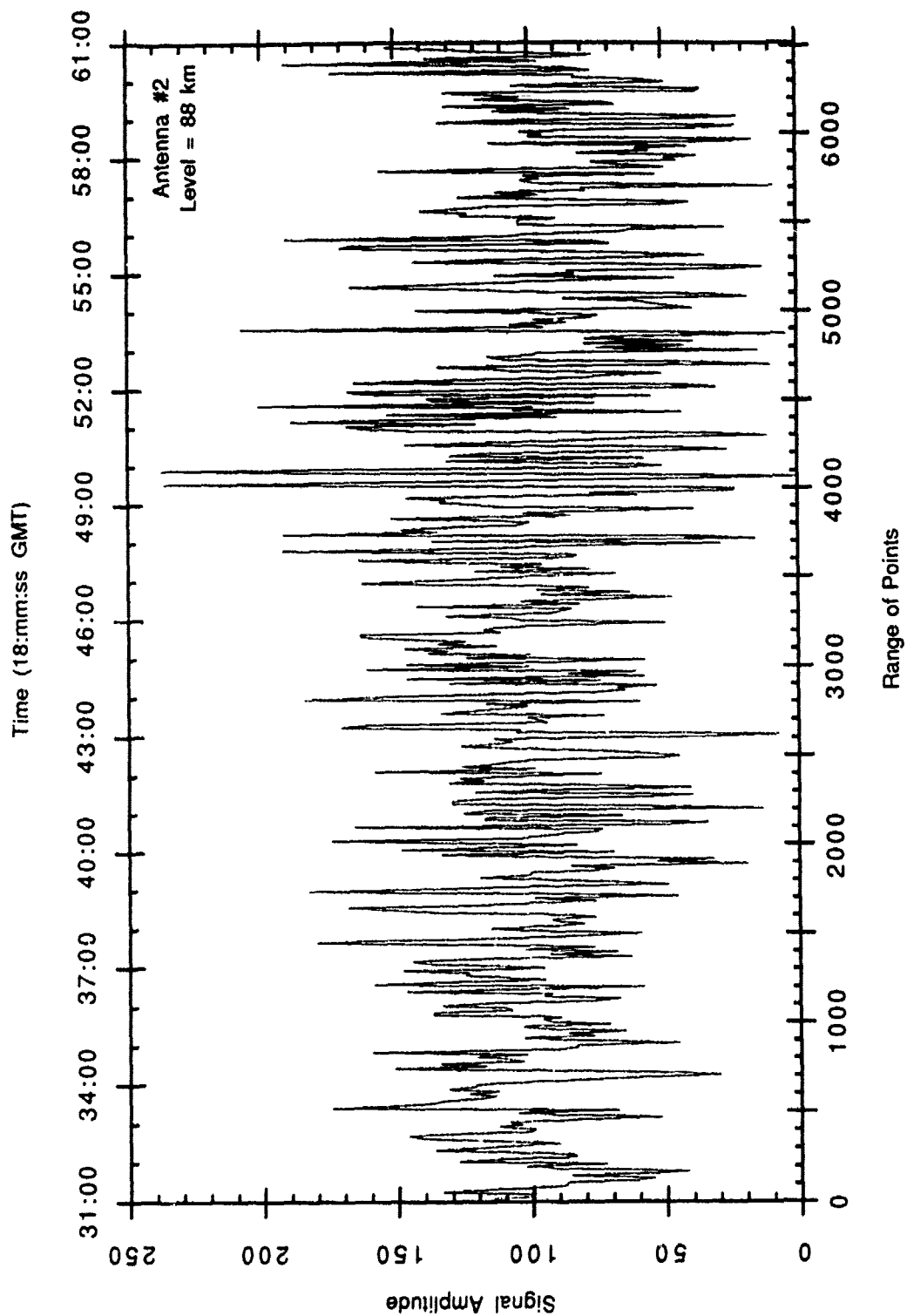


Figure 4.6 (e)

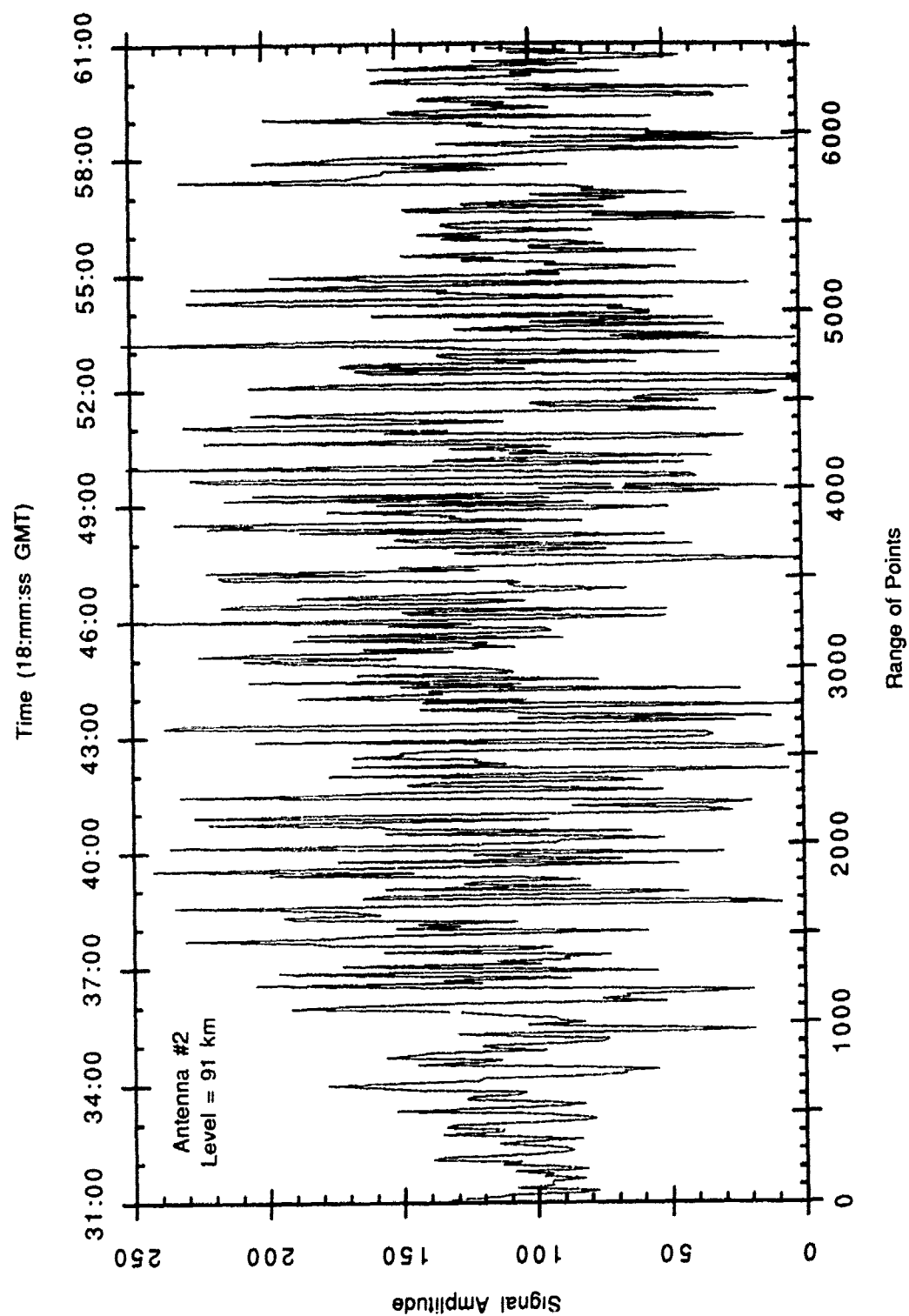


Figure 4.6 (f)

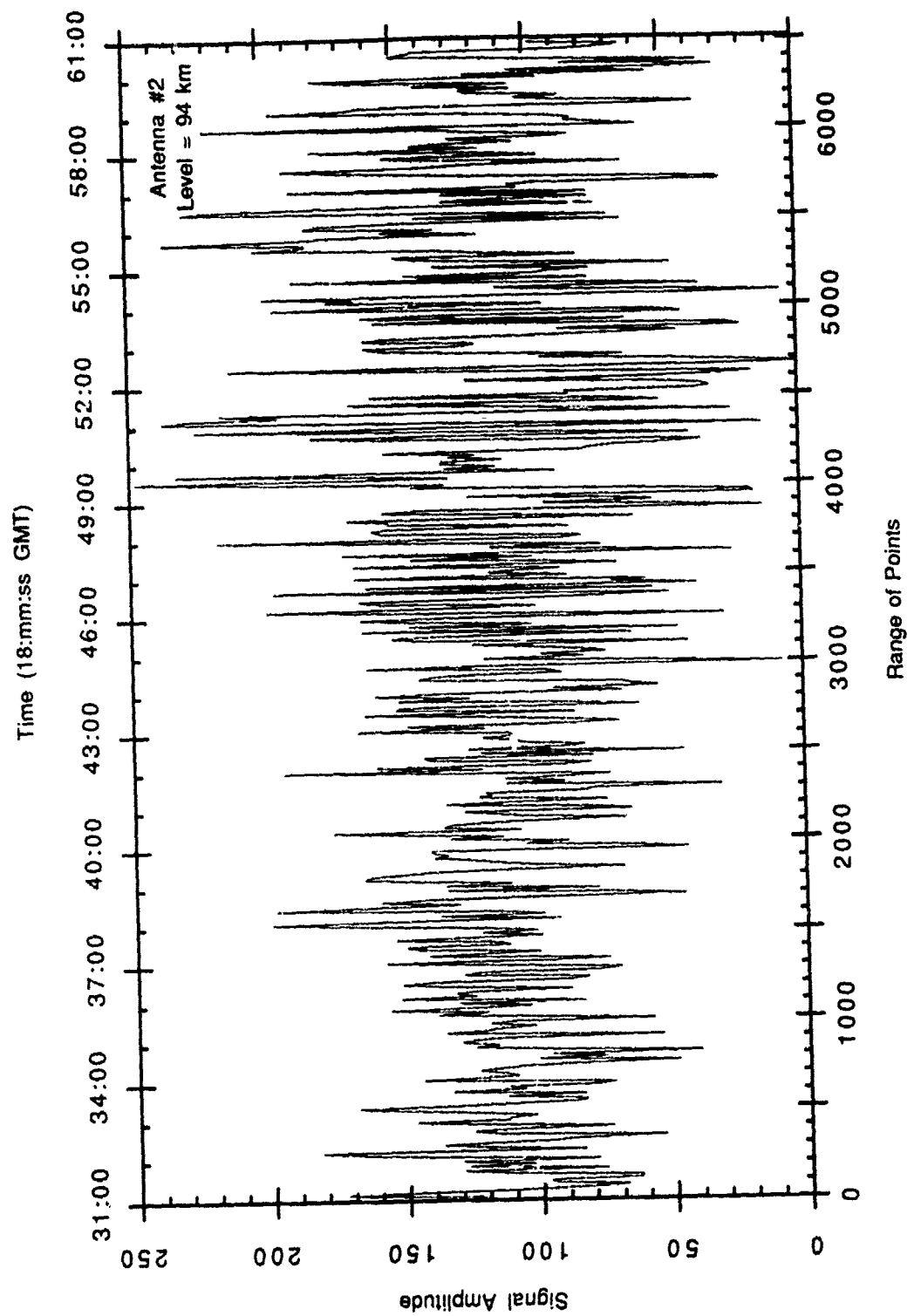


Figure 4.6 (g)

Figure 4.7 Data from antenna #3 for (a) 76 km; (b) 79 km; (c) 82 km; (d) 85 km; (e) 88 km; (f) 91 km; and (g) 94 km. The data starts at 18:31:00 GMT. The figure is on the following pages.

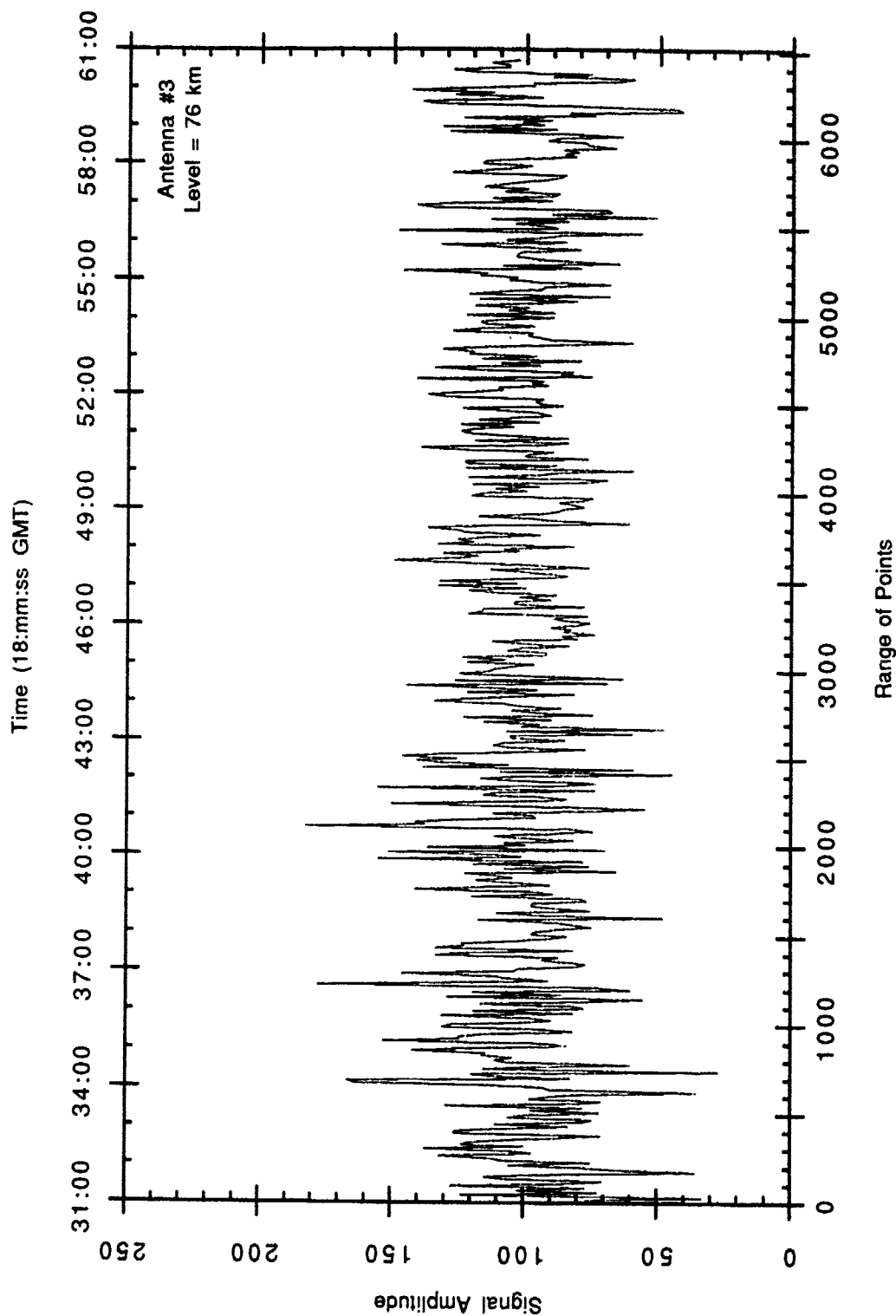


Figure 4.7 (a)

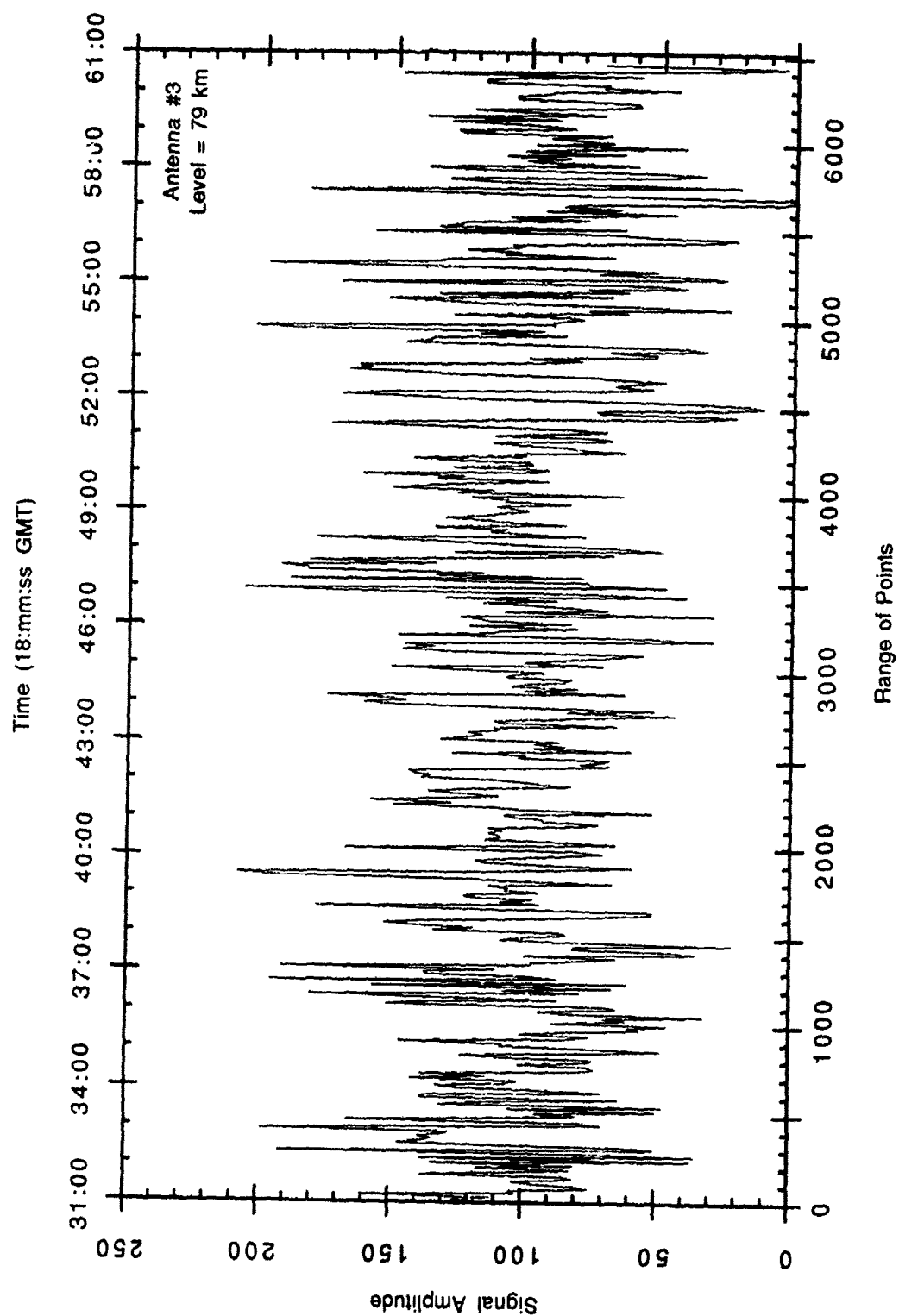


Figure 4.7 (b)

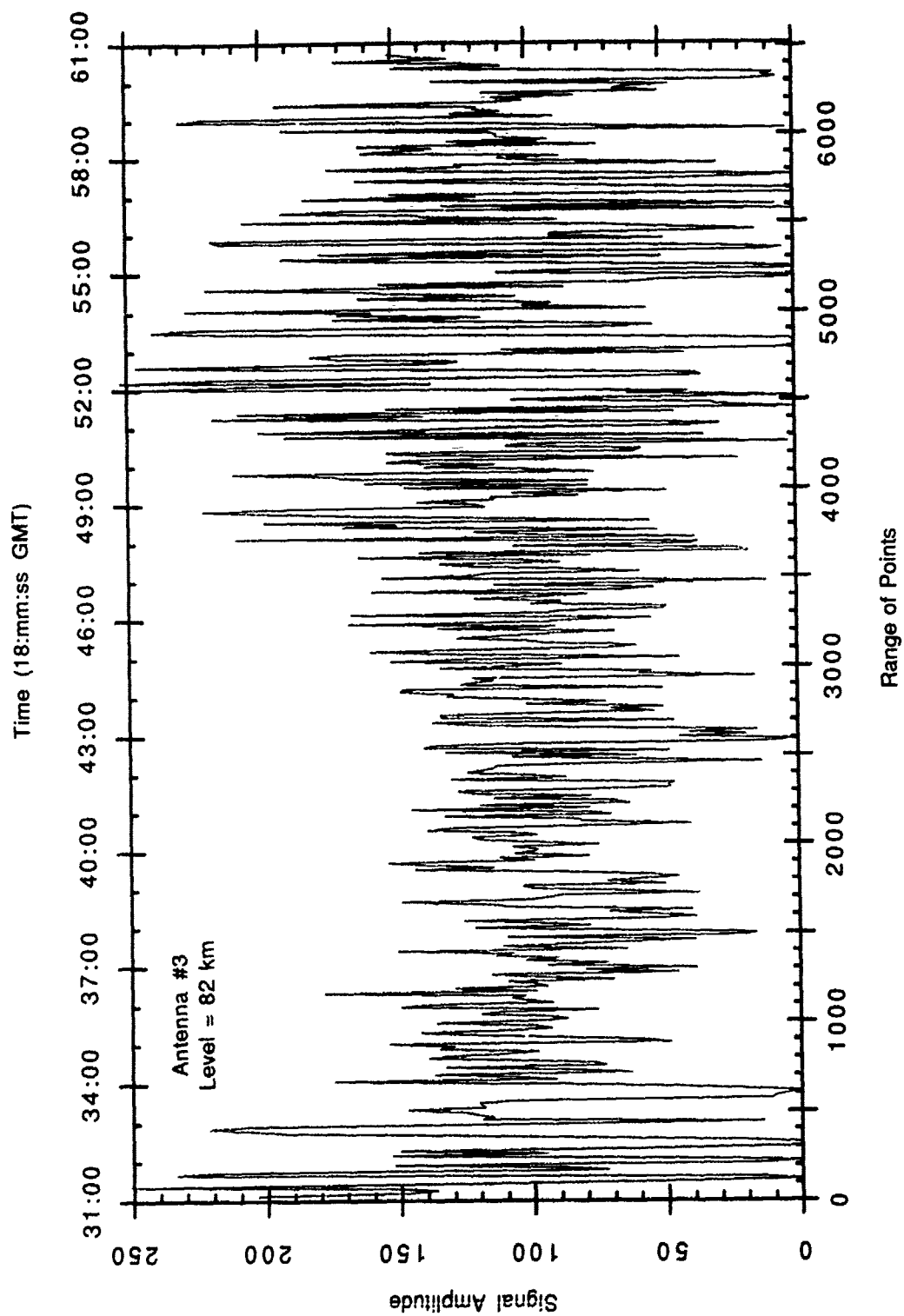


Figure 4.7 (c)

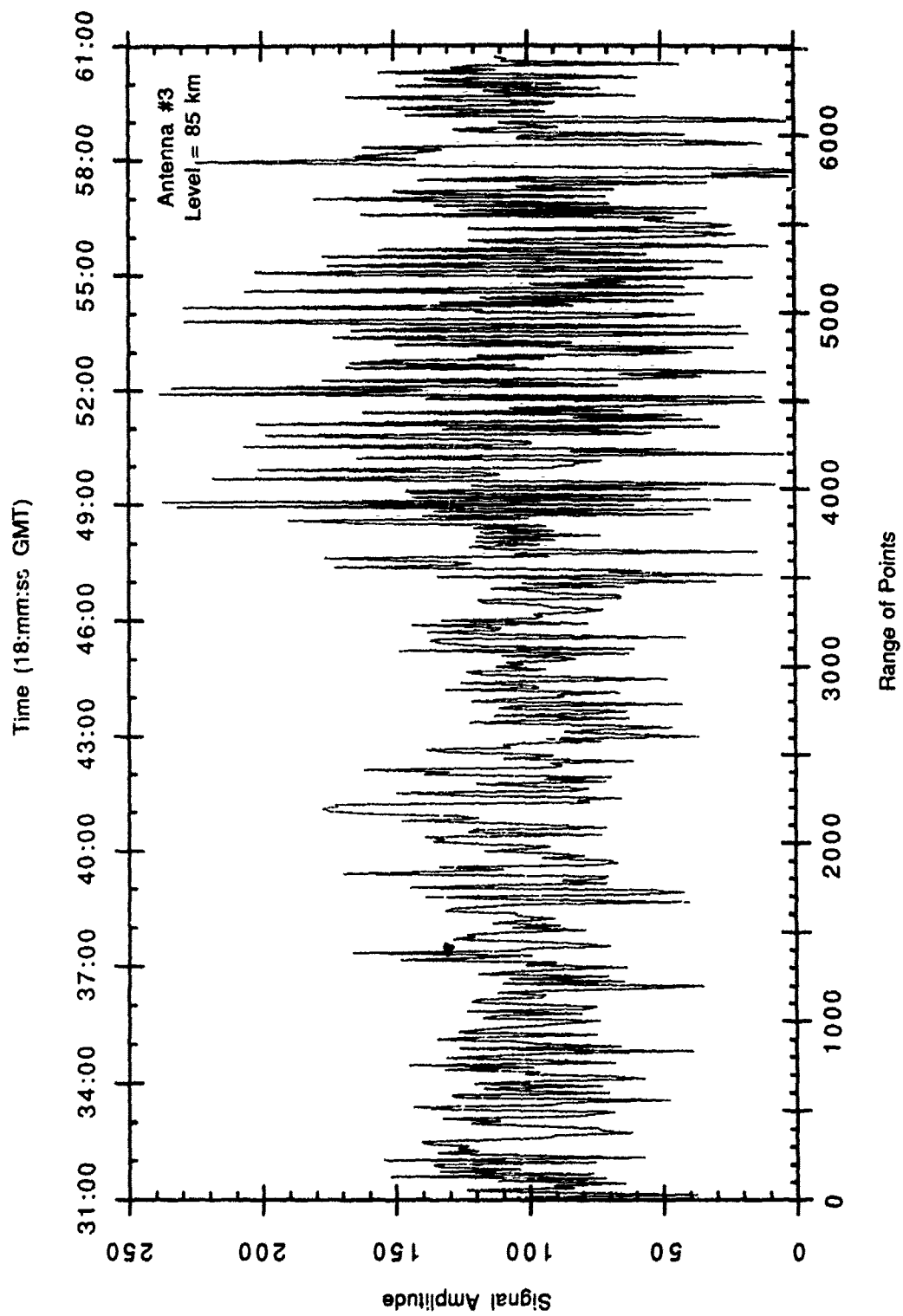


Figure 4.7 (d)

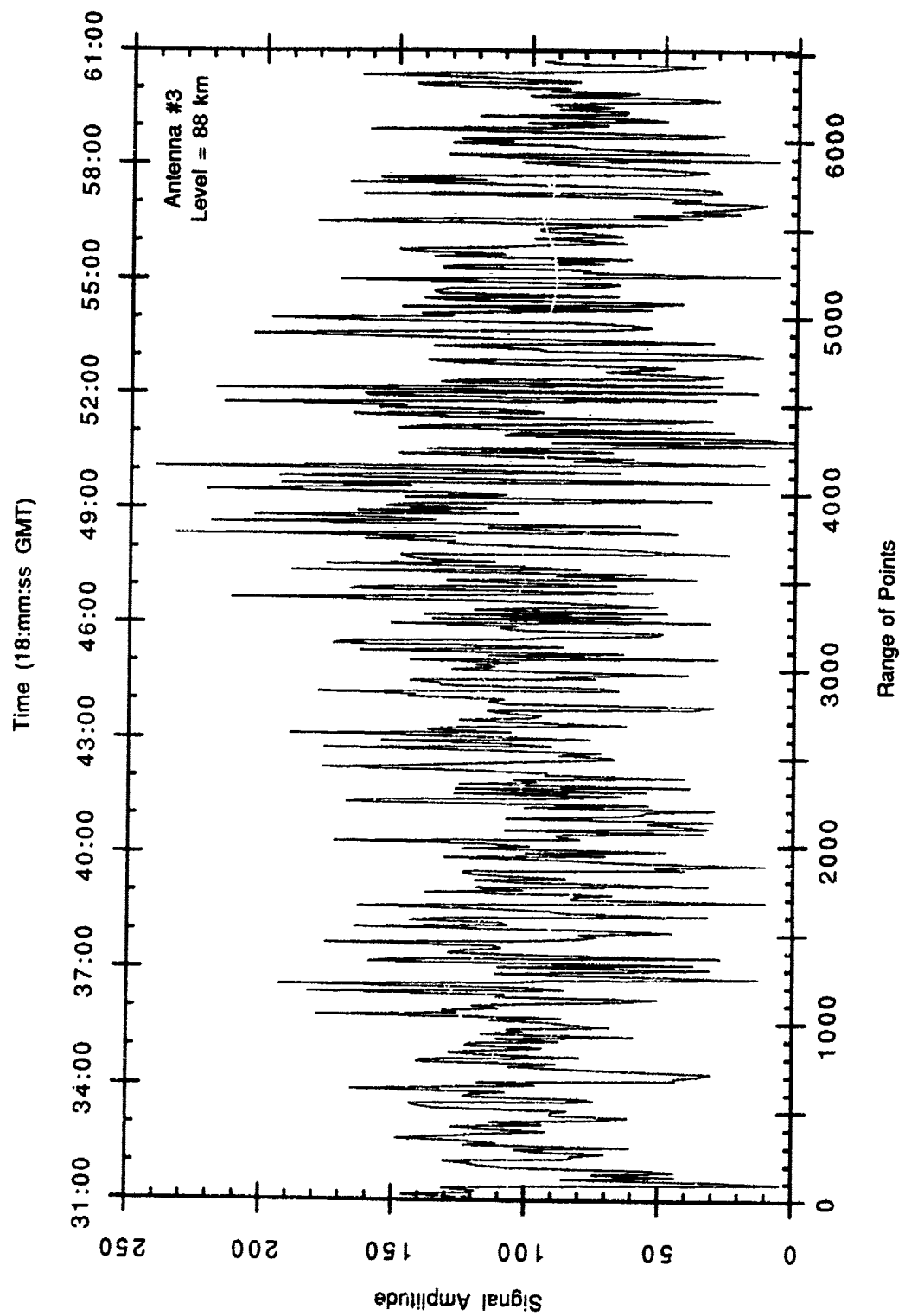


Figure 4.7 (e)

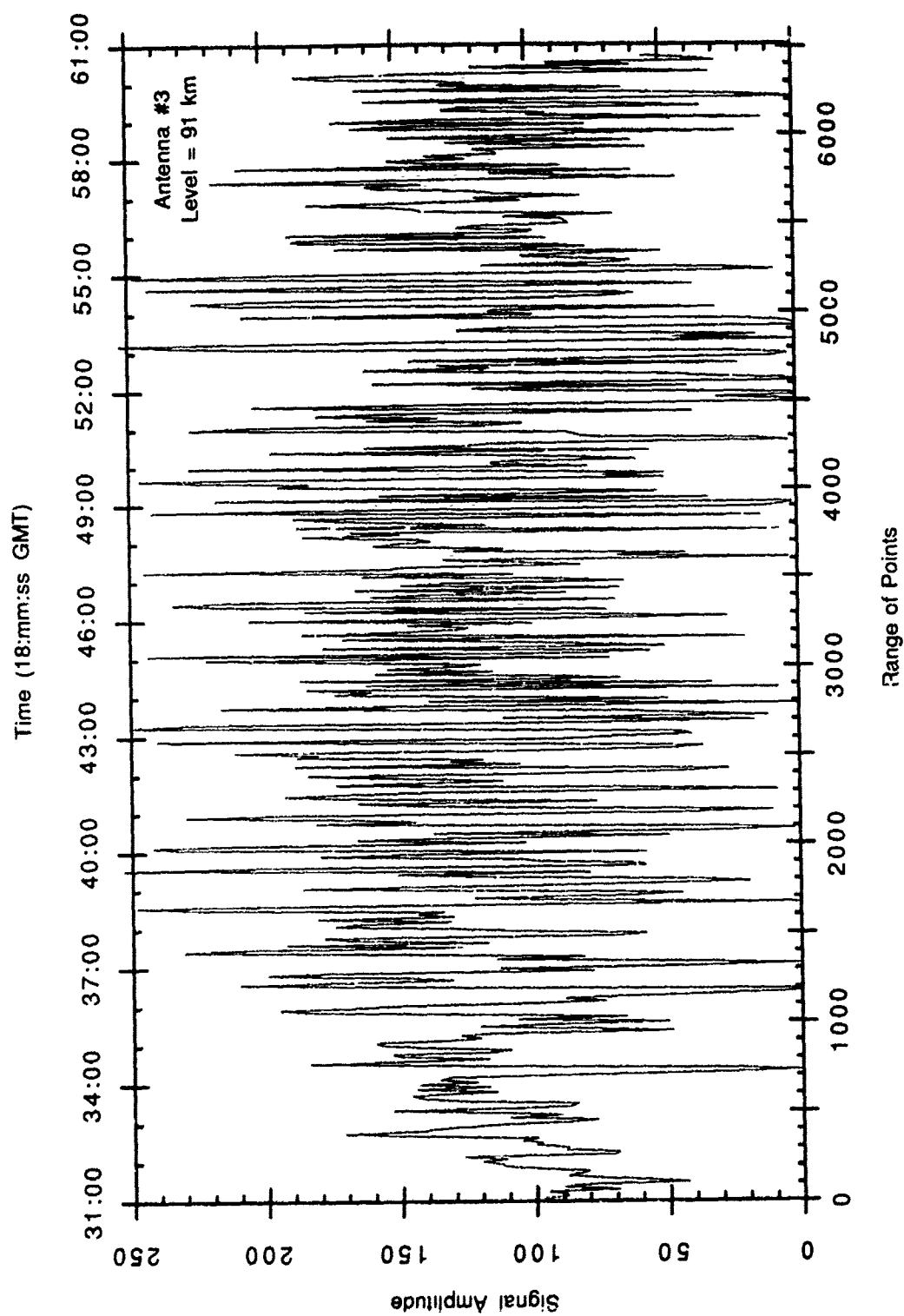


Figure 4.7 (f)

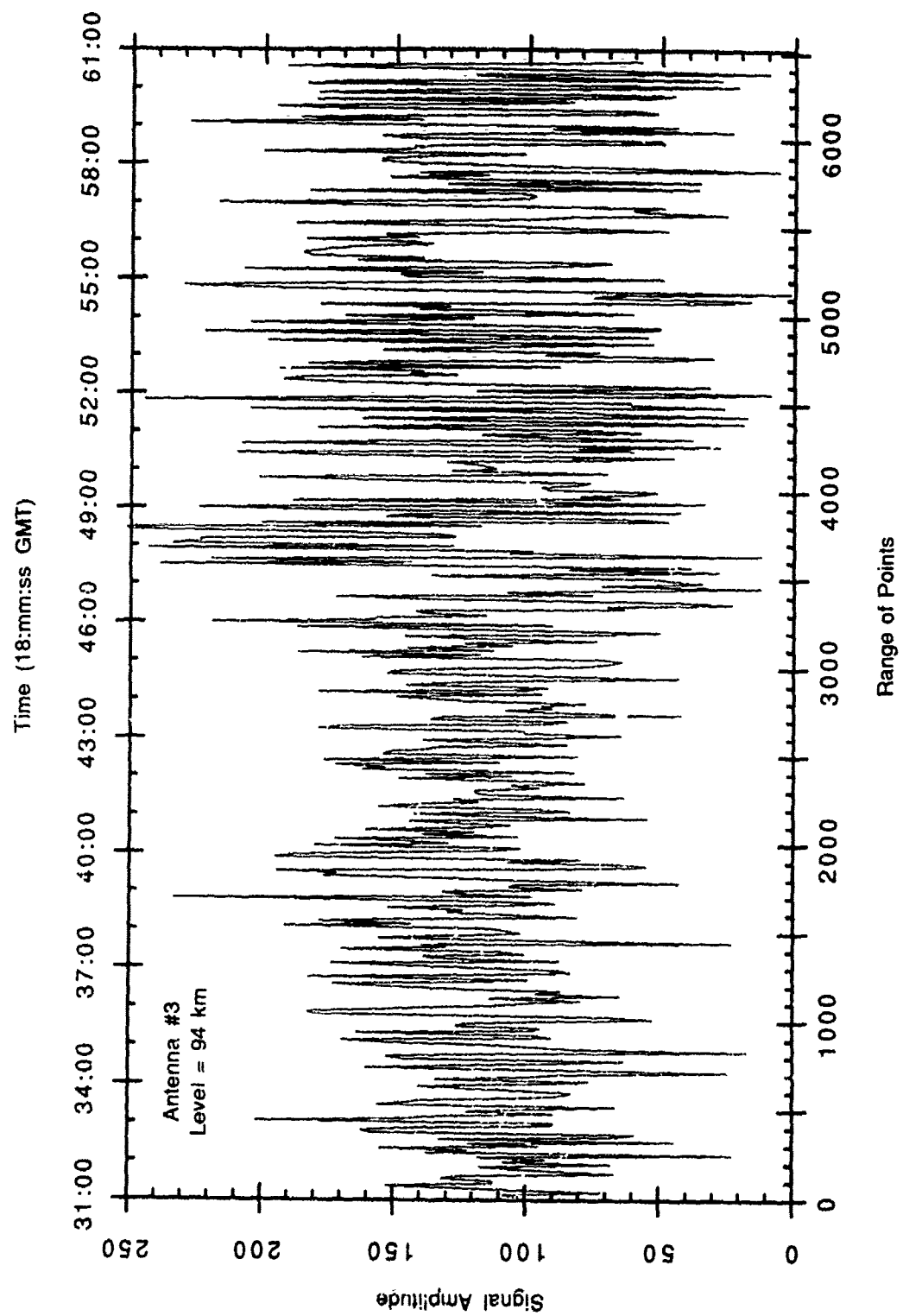


Figure 4.7 (g)

Figure 4.8 Data from antenna #4 for (a) 76 km; (b) 79 km; (c) 82 km; (d) 85 km; (e) 88 km; (f) 91 km; and (g) 94 km. The data starts at 18:31:00 GMT. The figure is on the following pages.

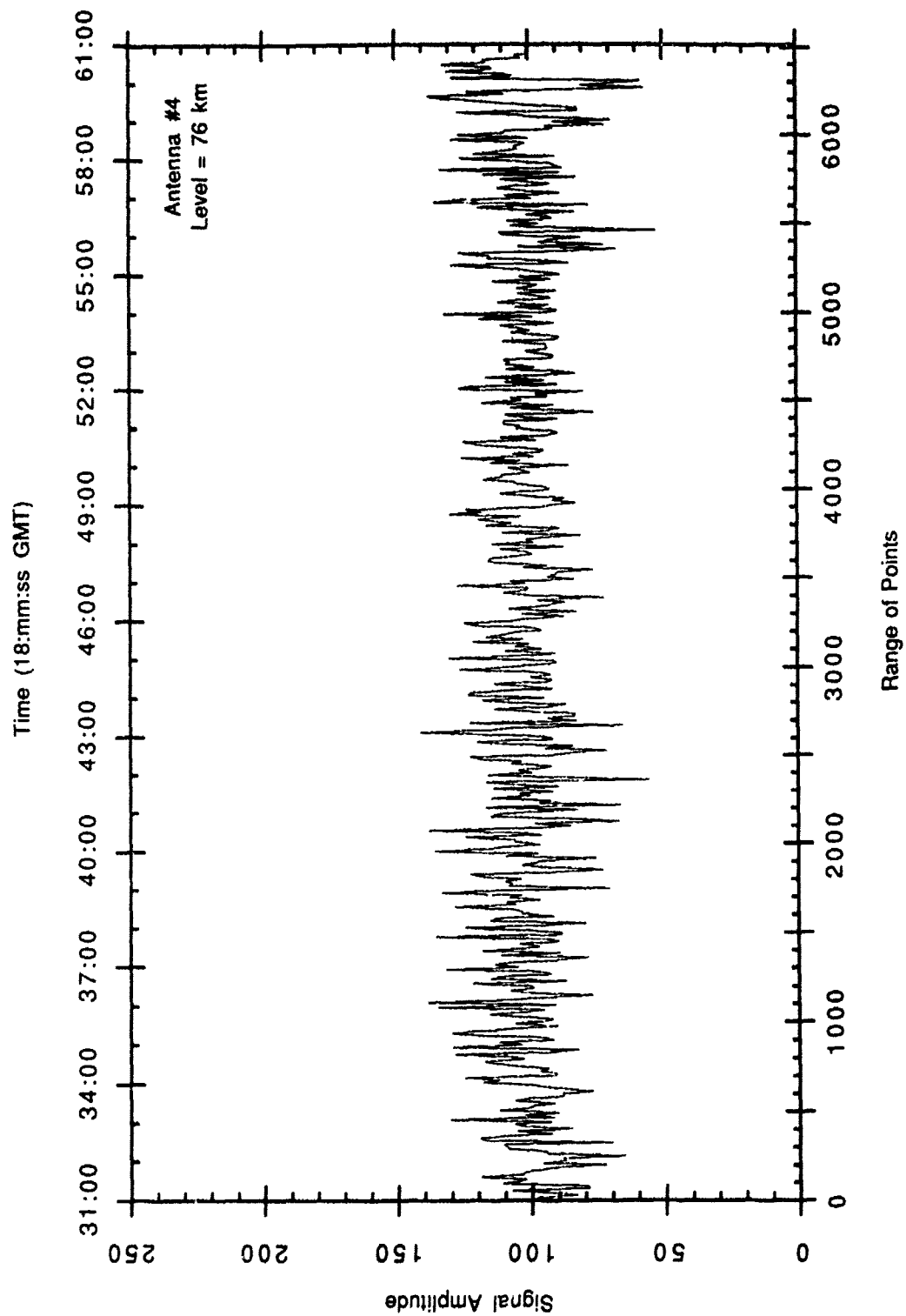


Figure 4.8 (a)

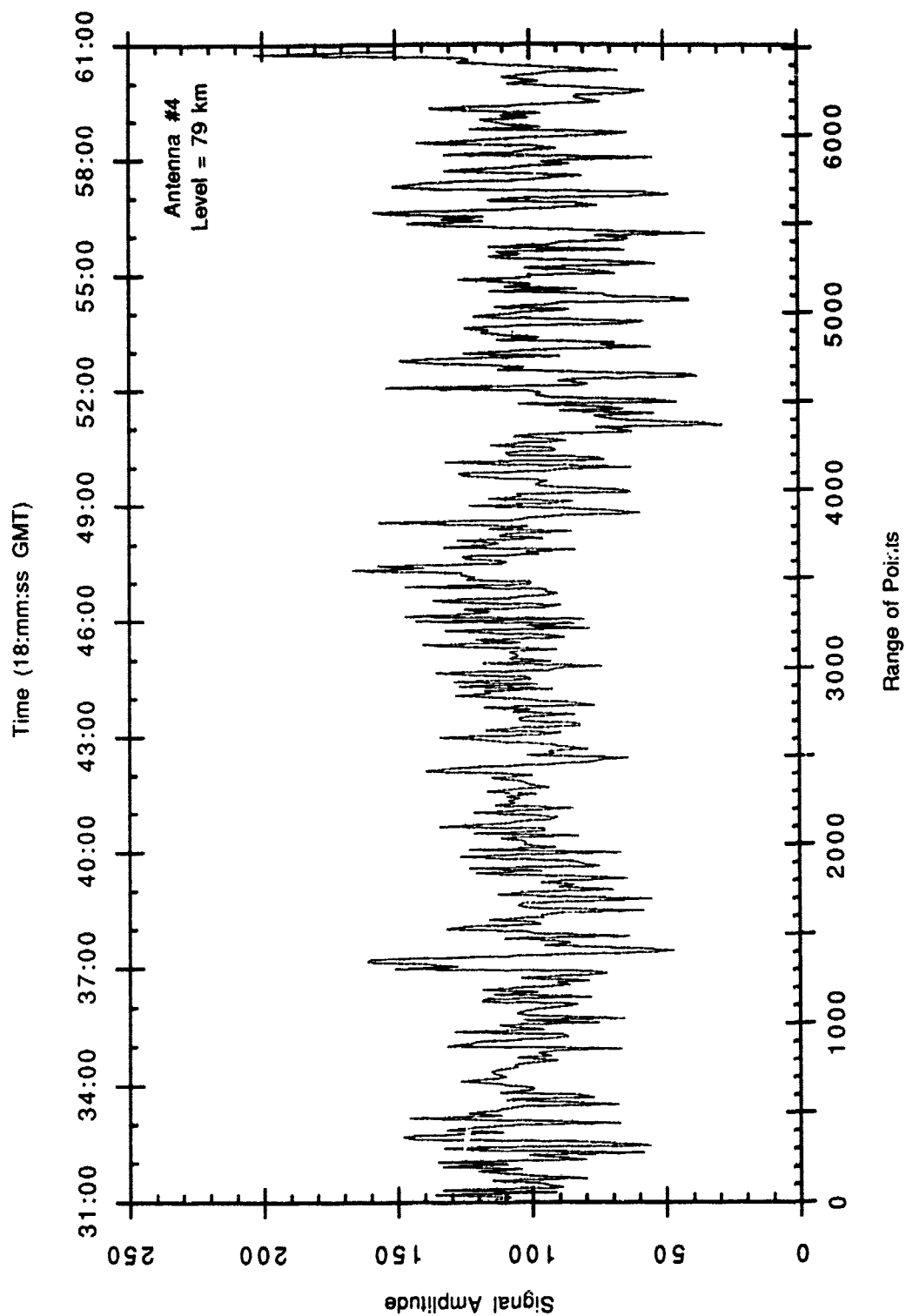


Figure 4.8 (b)

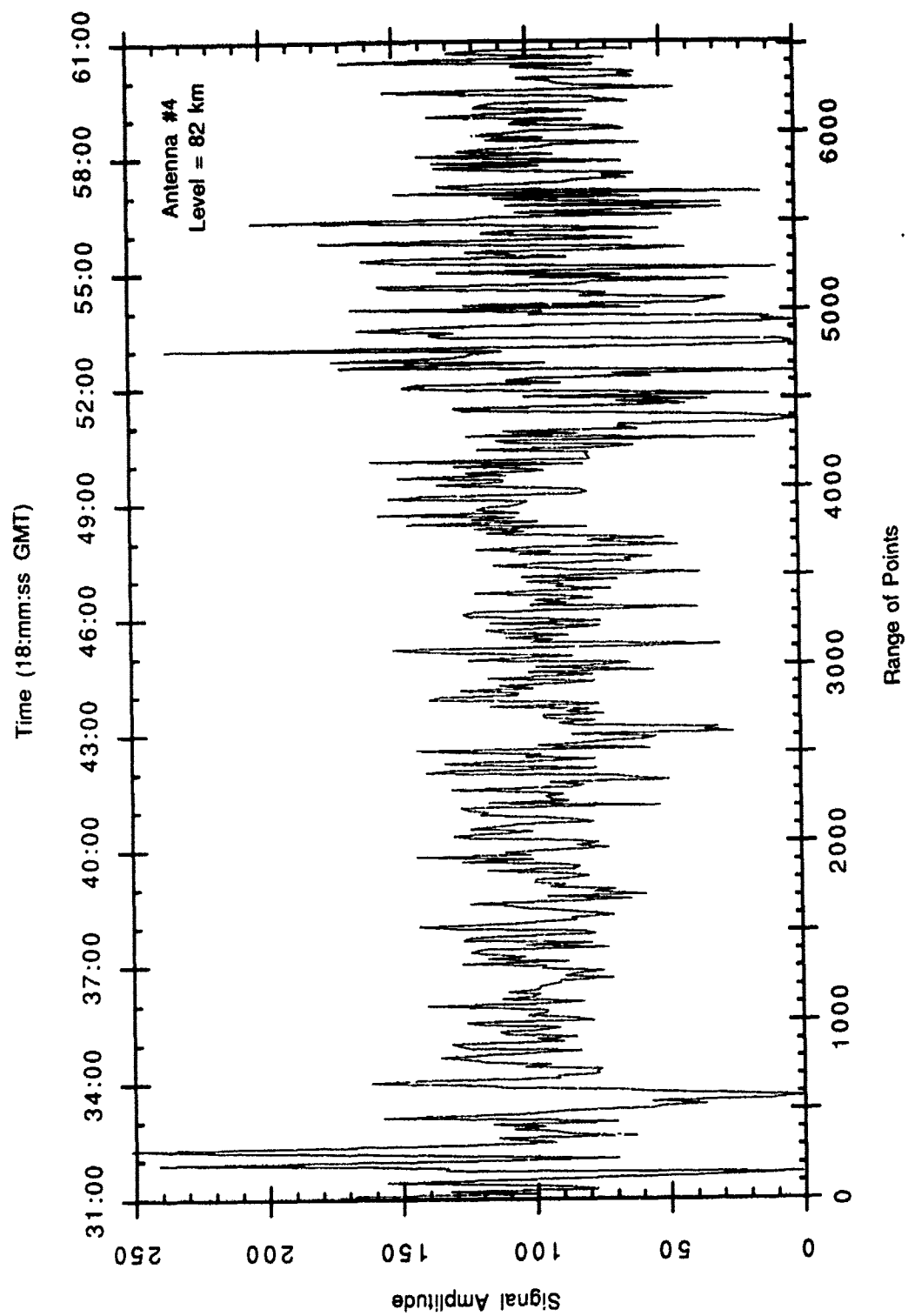


Figure 4.8 (c)

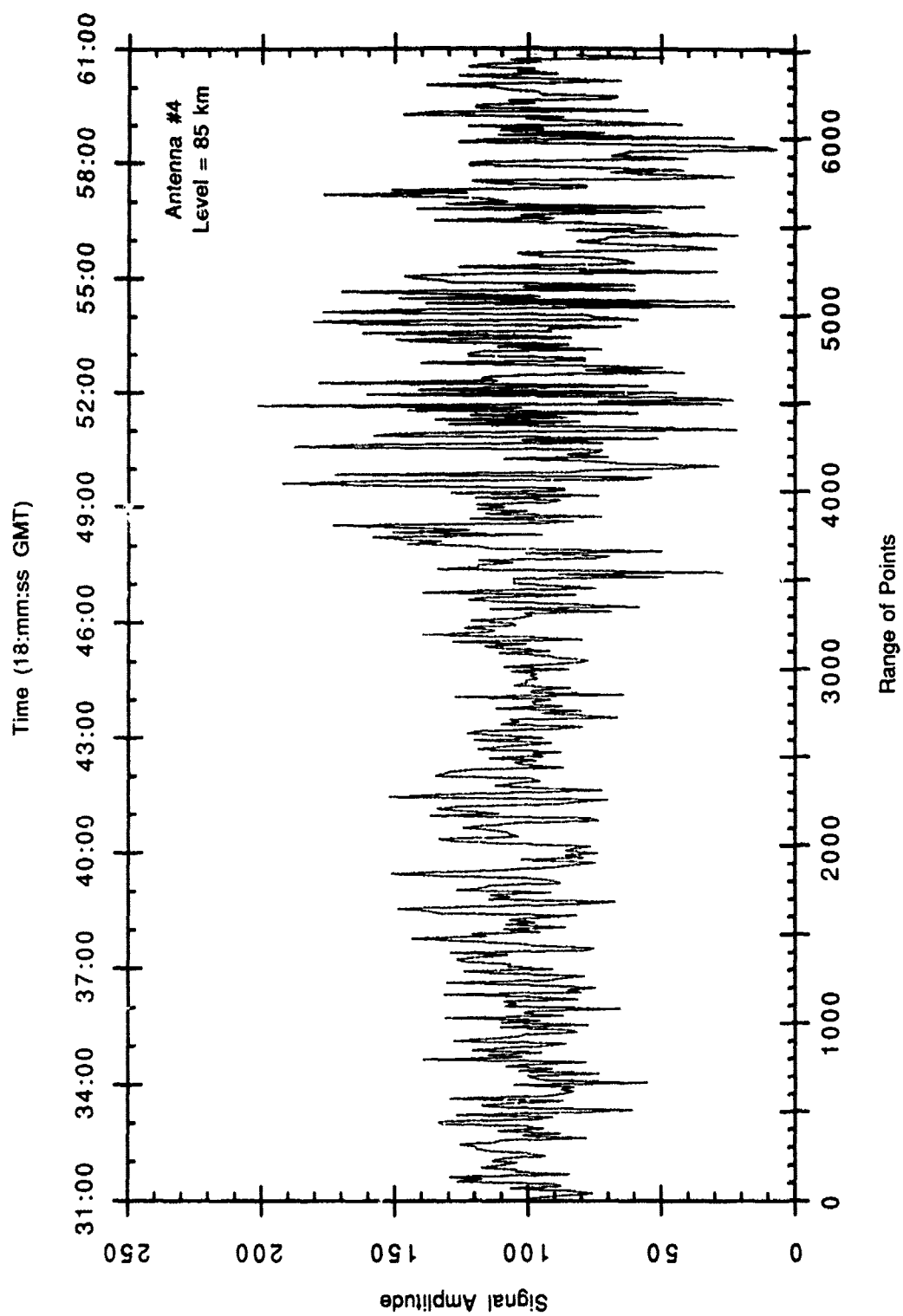


Figure 4.8 (d)

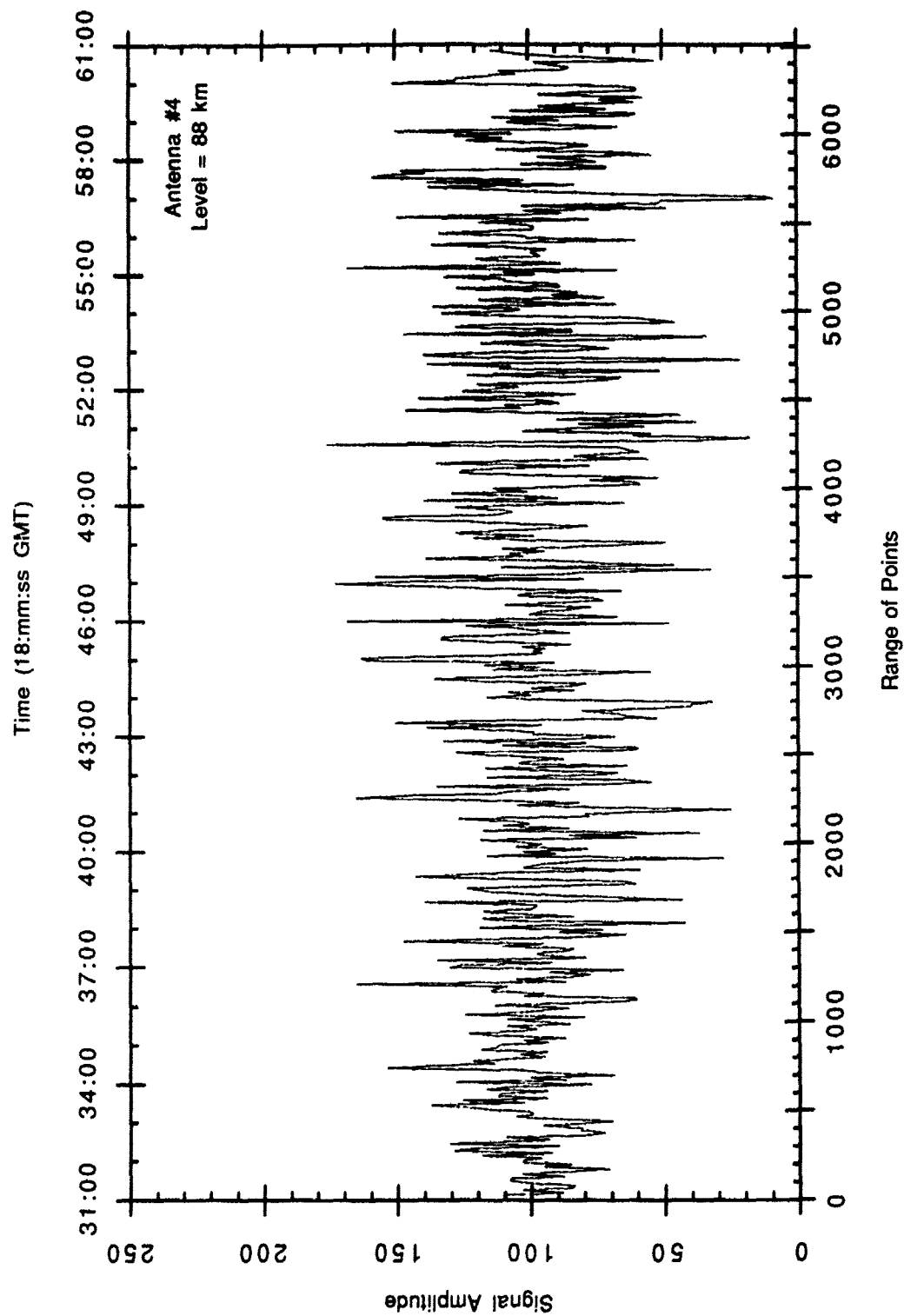


Figure 4.8 (e)

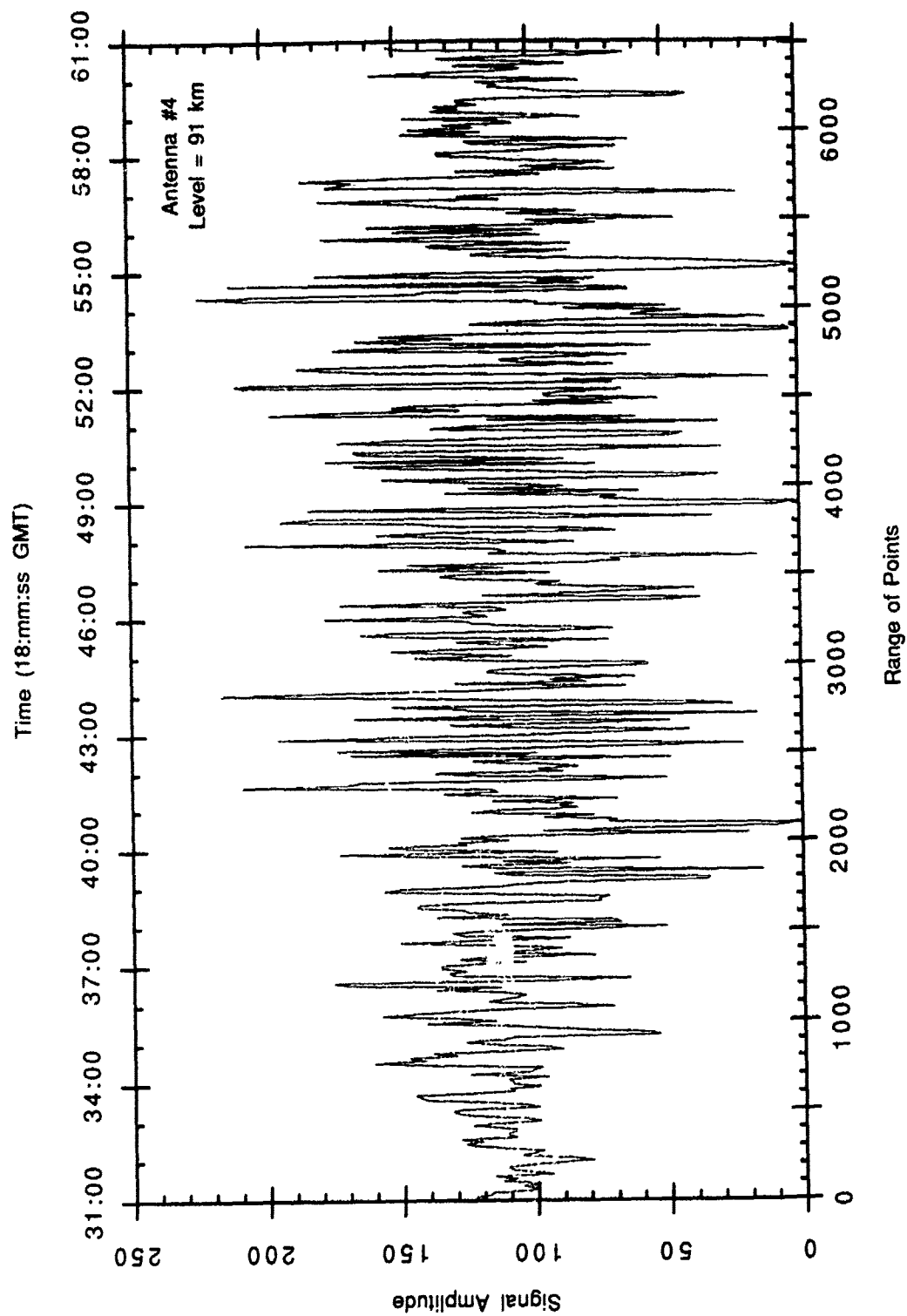


Figure 4.8 (f)

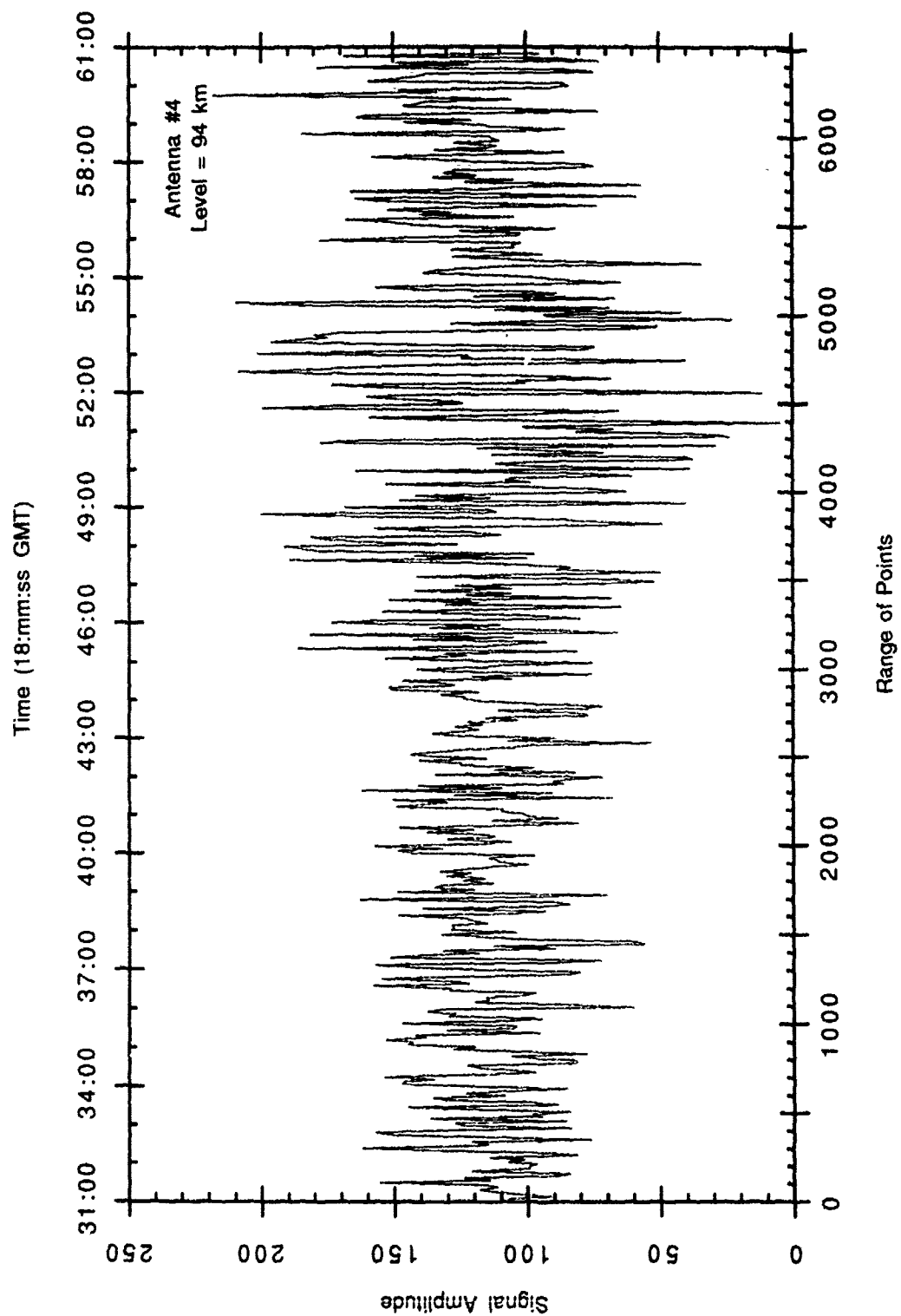


Figure 4.8 (g)

CHAPTER V

ANALYSIS AND INTERPRETATION

This chapter contains the results of the analysis of the data and the interpretation of those results. It first describes how the Grassberger-Procaccia algorithm was applied to the data, followed by the results of that analysis. Analysis of the power spectra of the echo data from the partial reflection radar follows. The chapter concludes with the interpretation of results from the implementation of the Grassberger-Procaccia algorithm.

5.1 Analysis

Determining the optimum time delay for building the phase space reconstruction of the attractor is the first step in applying the Grassberger-Procaccia algorithm. We will use the first local minimum in the mutual information as the best time delay and the first zero in the autocorrelation to determine the number of autocorrelated vectors to exclude from the summation in the correlation integral, i.e., the value of W from equation 3.32.

5.1.1 Calculating the best choice for time delay

The mutual information was calculated from equation 3.28 with up to 200 lags. The radar data ranges from a minimum value of 0 to a maximum value of 255; the integral was divided into boxes with sides ΔX and ΔY of length 10. This box size was chosen to provide the best convergence for the integral over the entire range of lags. The mutual information was calculated using the first 6000 points of the data from each of the four antennas. It was not possible to

calculate the mutual information for a smaller number of points because the probabilities would not be statistically valid. An even larger number of points would have been desirable.

The results of the mutual information calculation are depicted in Figures 5.1 - 5.4. In general, the mutual information drops off very quickly with increasing values of lag. There are some oscillatory characteristics at larger lags but they are small in amplitude. The lag for which the first minima in the mutual information occurs is summarized for each level in Table 5.1; the subscripts indicate the antenna for which the calculations were performed.

Table 5.1 Lag for the first local minimum in the mutual information.

Level (km)	τ_1	τ_2	τ_3	τ_4
76	12	10	9	12
79	18	20	19	18
82	17	19	18	19
85	15	19	18	15
88	14	17	16	16
91	22	19	17	17
94	13	17	14	18

5.1.2 Autocorrelation

The autocorrelation was calculated up to a maximum of 200 lags using equation 3.35. The maximum error according to equation 3.37 was less than 0.05% at the two hundredth lag. The data for each level and antenna was divided into three 2000 point groups ($1 < n \leq 2000$, $2000 < n \leq 4000$, $4000 < n \leq 6000$) and the autocorrelation was calculated separately for each group.

The autocorrelations for each antenna and level are shown in Figures 5.5 - 5.8. As with the mutual information, the autocorrelation exhibited some

oscillatory behavior as a function of lag. In general, the autocorrelation was smoother and not as noisy as the mutual information.

The average lag (λ) at which the first zero in the autocorrelation occurs for each level and antenna is summarized in Table 5.2. The average lag is the average of the first zero of the three 2000 point groups. The subscript of λ indicates the antenna.

Table 5.2 Lag (λ) for the first zero in the autocorrelation.

Level (km)	λ_1	λ_2	λ_3	λ_4
76	24	9	8	8
79	20	18	17	20
82	22	22	28	28
85	11	10	10	11
88	15	16	13	18
91	18	18	18	18
94	15	15	17	18

5.1.3 Calculating W

Since we intend to use Theiler's modification of the Grassberger-Procaccia algorithm, we must use the information from Tables 5.1 and 5.2 to calculate the value of W (see equation 3.33), the number of autocorrelated vectors to skip in the summation. The value of W for each antenna and level is summarized in Table 5.3. The subscript again indicates the antenna. The calculation is based on a total of 1500 points and a maximum embedding dimension of 13. The values have been rounded up to the next greatest integer since Theiler's modification of the Grassberger-Procaccia algorithm employs integer values of the time step in the summation.

Table 5.3 The value of W for each antenna and level (N=1500, m=13).

Level (km)	W ₁	W ₂	W ₃	W ₄
76	9	4	3	3
79	8	7	7	8
82	8	8	11	11
85	4	4	4	4
88	6	6	5	7
91	7	7	7	7
94	6	6	7	7

5.1.4 Implementing the Grassberger-Procaccia algorithm

We will use Theiler's (1986) modification of the Grassberger-Procaccia algorithm to calculate the base statistics necessary to estimate the dimension of the system. The exact algorithm implemented in this analysis is given by

$$C_m(\epsilon, N) = \frac{2}{N(N-1)} \sum_{i=1}^N \sum_{j=i+W}^N H \left[\epsilon - \left[\sum_{k=0}^{m-1} (x_{i+k} - x_{j+k})^2 \right]^{\frac{1}{2}} \right] \quad (5.1)$$

where N is the number of points in the data series, x is the reconstructed phase space vector, ϵ is the "search" radius, H is the Heaviside function and W the number of autocorrelated vectors to skip (see preceding section for the values of W).

We used the normalization factor, $(2/N(N-1))$, which did not include the calculation of the "self pair" terms nor did we perform the summation over the full range of indices. Both of these decisions were based on the desire to reduce the number of calculations since the amount of computer time required by the algorithm grows by the square of the number of points. Tests run on known attractors, strange and periodic, and noise (i.e., the Henon attractor, a sine

function of known period and Gaussian noise) with a limited number of points (<1000) revealed no convergence problems in the correlation algorithm as described by equation 5.1. Since the Grassberger-Procaccia algorithm is widely used by experimenters without calculating the full double summation or the "self pair" terms and our tests showed no decrease in convergence, we decided to use the computationally less demanding form given by equation 5.1.

The algorithm was optimized for the data set. The correlation integral was calculated for 150 values of ϵ evenly spaced logarithmically over the interval from $\ln \epsilon=1$ to $\ln \epsilon=7$. This was repeated for 12 different values of embedding dimension from 2 through 13. Because of the likelihood of the data set being non-stationary, the algorithm was applied to overlapping 1500 point groups. Each group overlapped the previous group by half the number of data points in the analysis. Thus, the calculations were repeated for the following seven groups of points: $1 < n \leq 1500$; $750 < n \leq 2250$; $1500 < n \leq 3000$; $2250 < n \leq 3750$; $3000 < n \leq 4500$; $3750 < n \leq 5250$ and $4500 < n \leq 6000$. A limited number of runs were done for 5000 points. Each set of calculations was repeated for each level (76 through 94 km) of each antenna. This resulted in over 196 separate sets of calculations.

All the calculations were performed on either a Macintosh IIcx or Macintosh IIfx computer. FORTRAN was used for all computer programs.

A representative set of plots of the correlation integral for each level is shown in Figure 5.9. The set of points was chosen arbitrarily as was the antenna. This set of figures is entirely representative of all the overlapping segments for all levels for each of the antennas. The entire set of calculations is represented by the graphs shown in Appendix A.

5.2 Power Spectrum Analysis

The power spectrum was implemented upon the basis of equations 3.39-3.41. The Fast Fourier Transform (FFT) from Press et al. (1986) required the

number of points analyzed to be a power of 2. To obtain a power spectrum which extended out to the buoyancy period (~5 min) required a total of 8192 points. This exceeded the total number of points in the first file. Consequently, some data (a total of 1487 points -- approximately 6 min 36 s) from the second file were included in the power spectrum calculations. We did not correct for the gap between the first and second file.

We performed tests on data with a known period to determine the degree of aliasing introduced by the time gap between the files. Tests showed that there was some aliasing but also that it was not expected to be a major source of error. Any errors introduced by not correcting for the time gap are on the order of errors introduced by the change in variance of the data from the second file.

The power spectra for antennas 1 through 4 at all levels are shown in Figure 5.10-5.13, respectively. Note that the x axis represents the period and is depicted in reverse order. This was done to give the figures the more common appearance of power spectra as a function of frequency. Interpreting the power spectra as a function of period is the same for frequency as long as one bears in mind that the slope of any power law behavior will be the negative of what you would normally expect.

The power spectra exhibited the same general characteristics for all levels and antennas. Each power spectrum had three (sometimes four) distinct regions. The power spectra were flat for periods less than 1-2 seconds. In general, the spectra were flat for periods less than 2 seconds for 76 km; this region decreased to periods less than approximately 1 s at 94 km. The flat region was followed by a region that clearly exhibited power law behavior (i.e., constant slope on a log-log plot); this usually occurred in the period range between 1-2 and approximately 6-10 s. Weaker power law behavior (i.e., the slope on the log-log plot was not well defined) occurred in the region between approximately 10 and 200 s. Each power spectrum contained the peak energy in the longest period, near the Brunt-Väisälä period for the

mesosphere. Power spectra for antenna #4 were qualitatively similar to those for the other three antennas except that the power over the entire spectrum was less. This is most likely due to the reduced variance in the data from antenna #4 described in Chapter IV.

To further understand the behavior described by the power spectra, we fit different portions of the power spectra to a power law. These results are shown in Figures 5.14–5.17. The fitted power slopes for the stronger power law behavior (i.e., between 1–2 s and 6–10 s) are summarized in Table 5.4.

Table 5.4 Slope for power law curve fits between 1–2 and 6–10 s.

Level (km)	Antenna # 1	Antenna # 2	Antenna # 3	Antenna # 4	Average Slope
76	7.0	5.3	5.7	5.2	5.8
79	5.0	6.6	5.5	-	5.7
82	2.7	2.3	2.7	1.9	2.4
85	3.0	2.9	3.0	2.4	2.8
88	3.4	1.5*	3.1	3.0	2.8*
91	2.9	1.5*	3.5	2.4	2.6*
94	3.7	2.1*	4.2	4.0	3.5*

*These slopes are distinctly different than those for the other antennas. The average includes these values.

We must be careful in interpreting the apparent power law behavior. There has been almost no work done on interpretation of power spectrum analysis of echo data from partial reflection radars and we should be cautious in treating it in the same manner as that for horizontal and vertical winds.

Hocking (1985) defines the length scale for the viscous region in the mesosphere as less than 3–6 m at 70 km and less than 20–30 m at 90 km. In the viscous region, the kinetic energy of turbulent eddies is diminished by viscous effects and dissipated as heat.

The length scale for the buoyancy region in the mesosphere is greater than 60–1000 m (Hocking, 1985). At large scales, the buoyancy effects become important. In the buoyancy region, the turbulent eddies take on a "pancake" like appearance (Hocking, 1985) and consequently, the horizontal length scales are much greater than the vertical length scales.

The inertial region lies between the viscous and buoyancy regions. Hocking (1985) notes that the break in the slope of power spectra between the viscous and inertial regions occurs at length scales two to four times the length scale of the viscous region.

The flat region in the power spectra corresponds to the amount of time it takes the smallest size eddy that can be detected by the radar (i.e., approximately 70 m) to be advected past the radar. The maximum period of the flat region decreases at higher levels because of the general increase in the wind speed with height. Meek and Manson (1987) give the wind speed at 76 km as approximately 30 m s^{-1} , increasing to approximately 60 m s^{-1} near 94 km for this time period at Saskatoon.

The region between 1–2 and 6–10 s is most likely the viscous region. While the radar can not detect turbulent eddies small enough to be in the viscous region, it can detect variations in the motion of the echo patterns that occur on time scales which correspond to the viscous region. The power spectra length scales for the viscous region can be calculated from the period using the multiplicative factor from Hocking (1985), the wind speed and a factor of 2π ; they correspond to those given by Hocking (1985). This interpretation assumes the Taylor hypothesis, i.e., the eddies causing the diffraction pattern are "frozen" and do not evolve with time as they pass over the receiver array. Power law behavior in the viscous region is commonly described by

$$E(k) \propto k^{-7}, \quad (5.2)$$

where k is the horizontal wave number. The region over which the power law behavior is valid increases with height because so does the length scale for the viscous region. Note that the slopes for the power law behavior (see Table 5.4) for 76 and 79 km are almost as large as -7. This behavior does not hold for altitudes above 79 km.

The region between approximately 10 and 200 s is the inertial region. This region exhibits much weaker power law behavior than the viscous region. Some power law curve fits for this region are shown in Figures 5.14 - 5.17. The radar does directly detect eddies on the length scales of the inertial region. This, combined with fluctuations of the wind speeds on time scales equivalent to the inertial region length scales, may explain the departure of the power law curve fit from the commonly expected -5/3 behavior.

5.3 Interpretation

The first step in interpreting the output of the correlation integral algorithm lies in determining the slope as a function of ϵ . Once the slope has been calculated, we can determine if there is an attractor present and its dimension. First, let us discuss how to interpret the slope as a function of ϵ .

5.3.1 Interpreting the Slope as a Function of ϵ

The slope of the lines from the correlation integral algorithm should equal the fractal dimension of the attractor when plotted on a ln-ln graph. The plot of the slope of the natural logarithm of the correlation integral against the natural logarithm of the radius ϵ can be divided into four distinct regions.

Each region yields information on the algorithm and the underlying attractor. Figure 5.18 shows a idealized diagram of such a plot.

Region A in Figure 5.18 is the section where the statistics are limited by the number of points in the data set. The slope in this region starts out near zero and often is characterized by some oscillatory behavior. The slope is zero because the number of points in a "ball" of radius ϵ approaches zero as ϵ approaches zero. Oscillatory behavior is the result of fluctuations in the counting statistics because of the limited number of data points.

Region B is dominated by instrumental and external noise. The slope is proportional to the embedding dimension. In this region, the "balls" are smaller than the smallest temporal and spatial scale of the attractor. Often, the slope will only approach the embedding dimension; this occurs primarily at the higher embedding dimensions because there aren't enough points to adequately saturate higher dimensional spaces.

There will always be a transition between regions A and B for data sets where there are a finite number of points. As the number of points increases this transition would occur at increasingly smaller values of ϵ .

Region C is the "scaling" region. This region is characterized by constant slope which, at high enough embedding dimension, should equal the fractal dimension of the attractor. The slopes should converge to a common value for embedding dimensions equal or greater than $2d+1$ since this dimension phase space will completely embed the attractor. The width of the scaling region is vital. The limits imposed on the original definition of the correlation integral necessitate a scaling region which spans several orders of magnitude. Noise reduces the width of the scaling region and may make it difficult to discern. A high signal-to-noise ratio yields a larger scaling region whereas signals characterized by a low signal-to-noise ratio will have a very small scaling region or may not have one at all.

There may be multiple scaling regions present in region C if there are attractors of different length scales present in the data. Multiple attractors in the data would lead to distinct plateaus in the slope diagram.

Region D is characterized by the slope converging to zero. As ϵ increases and approaches the size of the attractor, the "balls" contain nearly the total number of points in the system. Thus the slope approaches zero. In some systems, the transition from region C to D is characterized by a small "hump" or region of higher slopes. This "hump" occurs because of edge effects of the "balls" used to count the points and curvature of the attractor (Brandstätter and Swinney, 1987).

5.3.2 Calculating the Slope

The slope of the lines in Figure 5.9 was calculated using a seven point least squares fit (the algorithm was taken from Press et al., 1986). The slope calculated for each point was the least squares fit of the point extending three points on either side. The errors of the least squares fit were calculated but not displayed so as to render the figures more legible.

The results of this analysis are shown in Figure 5.19. Examination of the figures reveals no apparent scaling region for any level. The data set seems to be characterized by noise for times scales less than 6 min 40 s (i.e., 1500 points). There may be a higher dimension attractor in the data but it can not be detected with only 1500 points and thus will appear as noise. While recognizing this possibility, we will consider the results to be noise for purposes of discussion. The slopes of the entire correlation integral analysis are given in Appendix B.

5.3.3 Why Noise?

There does not appear to be an attractor in this data set. Noise seems to be present in the signal for all time scales that were investigated. This leads us to the question -- why have we found only noise and should we have expected it?

The lack of positive results may be attributed to one or any combination of reasons. These fall into three broad categories: difficulties with the algorithm, difficulties with the data and an invalid hypothesis.

5.3.3.1 Difficulties with the algorithm

As was previously described in Chapter III, the Grassberger-Procaccia algorithm has a number of weaknesses that make it difficult to implement. Among these are the finite size of the data set, noise (both instrumental and external) and the inability of the algorithm to detect the presence of an attractor amid a wide spectrum of competing signals.

The idealized models of gravity wave breaking invoke a single monochromatic wave that becomes unstable at some point as it travels upward. This is almost certainly not the case in the atmosphere; instead of a single monochromatic gravity wave, there is an entire spectrum of gravity waves which travel in packets. As pointed out earlier, the spectrum of waves gives rise to nonlinear wave-wave interaction.

It is not known whether the Grassberger-Procaccia algorithm could pick out the presence of a strange attractor in such a sea of competing signals, some of which might have time scales on the order of the attractor. While there has been a limited investigation into the use of the algorithm in the presence of two competing signals, its use on a spectrum of signals remains largely unexplored.

The limited size of the data set could also prevent detection of an attractor, especially if the dimension is greater than 3. The 1500 point case is not adequate to accurately estimate the dimension of systems with dimensions

greater than or equal to 2. However, 1500 points should be sufficient to test for the presence of an attractor of dimension 3 or less.

We did perform a limited set of calculations using 5000 points for 82 and 85 km. The data analyzed was an average of all four antennas. Unfortunately, these calculations were performed with an incorrect value of the time delay used to reconstruct the phase space vectors; the value of the time delay was only 2 instead of the values given in Table 5.1. The results of these calculations are shown in Figure 5.20. From the plot of the slope as a function of ϵ , there doesn't appear to be an attractor in this data set for the 5000 point time scale (i.e., 22 min 13s). While it is true that these results are not as reliable as those for the 1500 point cases because of the incorrect choice of time delay, the greater number of points makes the exact choice of the time delay less crucial, especially since we found only noise. Had the 5000 point case suggested the presence of an attractor, we would be inclined to interpret the results with more caution. We look upon the 5000 point case as further support for the absence of an attractor and there only being noise in this data set.

The degree of autocorrelation and the lack of general independence as determined from the mutual information also reduces the useable size of the data set and contributes to the problems in the algorithm from a limited number of points.

The noise in the signal is the biggest problem. There may only be noise in the data on the time scales examined here or the signal-to-noise ratio may be so low as to completely obscure the scaling region of an attractor. The degree to which the noise is instrumental or external will be touched upon in a later section.

5.3.3.2 Difficulties with the Data

The problems associated with the data fall into two categories: no gravity waves in the data set and the quality of the data itself. The issue of data quality overlaps some of the limitations of the Grassberger-Procaccia

algorithm that have been discussed in previous sections. The second problem is not really a problem but a statement of fact: we found nothing but noise in the data because there really was nothing but noise in the data. First let us discuss the quality of the data itself.

The biggest problem that occurred was the high frequency "ringing" present in the data in the second and third file. This so contaminated the data that some preliminary analysis of these signals suggested the presence of an attractor with finite dimensions until the cause was discovered. (The plots of the original data set that were supplied to us indicated no such problems). As mentioned earlier, this high frequency contamination of the data precluded the use of almost an hour of data, thus severely reducing the size of the data set. This exacerbated the problems that occur with finite data sets as described in previous sections.

In addition to the "ringing", gain changes and drift in the receiver presented an additional source of error. While each of these problems could have been corrected, doing so would have introduced an additional degree of uncertainty into any dimension estimates. These problems precluded use of the last two files.

The elimination of almost two thirds of the data set emphasizes the Grassberger-Procaccia algorithm's need for lengthy data records. Data analysts always complain they could use more data, but in this case it seems to be an absolute necessity. Without a sufficient number of points, the entire algorithm is not statistically valid.

This data set may contain no evidence of gravity wave breaking. The data set was originally suggested to us as one that potentially contained evidence of gravity wave breaking.

Meek and Manson (1987) used this data set to examine "glints" in the pattern of echoes at the receiver. The "glints" were regions of strong persistent echoes that travelled in a straight line through the receiver array.

They speculate that the glints were either long lived pockets of turbulence or focusing of the signal due to favorable alignment of surfaces of the wave.

Meek and Manson (1987) found two glints in the data set from day 214 that has been examined in this study. The first glint was observed between 18:31:24 and 18:34:36 GMT as it travelled through the receiver array. The second glint was observed between 18:47:48 and 18:49:24 GMT. The velocity of a glint could be deduced by tracking the amount of time it took to cross the receiver array; Meek and Manson (1987) estimated that both glints had velocities of $\sim 50 \text{ m s}^{-1}$. If the glints were caused by focusing of the turbulence along the surface of a wave, the period of the wave can be deduced from the difference in time between the glints. The period of a wave travelling 50 m s^{-1} is approximately 5 minutes which is roughly the same as estimates of the Brunt-Väisälä period in the mesosphere.

Meek and Manson (1987) used a wave model to determine if the glints could be caused by focusing along the surface of a travelling wave. The wave model reproduced the observations of the glints well. Meek and Manson further speculated that the waves responsible for the glints were close to their critical levels since their phase velocities matched the parallel component of the background wind (an instability criterion given by Fritts and Rastogi, 1985). Thus, while Meek and Manson did not directly observe gravity waves breaking, they speculated the conditions were favorable for this occurrence.

Unfortunately, we could find no evidence of gravity wave activity in our analysis of the data set. Power spectra of the data for each level and antenna showed no evidence for wave activity near the Brunt-Väisälä frequency. To detect periods in the power spectrum out to the Brunt-Väisälä period required using data from the contaminated second and third files. The problems previously discussed in detail may have prevented us from detecting long period signals in the power spectrum.

Meek and Manson (1987) found evidence of wave activity in this data set. Furthermore, they speculated that the waves causing the glints may be

near saturation. While our analysis of the data set could not support this conclusion for the reasons described above, neither could we rule it out conclusively. This still leaves us with the unanswered question of whether or not the presence of breaking gravity waves exists in the data set.

5.3.3.3 Invalid Hypothesis

The last reason why we may not have detected anything but noise in the signal is that the hypothesis is invalid. Gravity wave breaking and the subsequent decay to turbulence may not be characterized by chaotic behavior. The analogies to laboratory studies may be incorrect or they may not extend to the real atmosphere where there is an entire spectrum of activity besides gravity waves. On the other hand, the hypothesis may be valid; the breakdown of atmospheric gravity waves may be characterized by chaotic behavior but it is of such an ephemeral nature we may not be able to detect it.

The extension of the results from laboratory experiments to the atmosphere may be invalid. In our review of some of the laboratory studies, we examined chaotic behavior which arose from convective instabilities (Rayleigh-Bénard convection) and dynamic instabilities (Couette-Taylor flow) in closed systems and dynamic instabilities in open systems (the excited jet). None of these regimes are similar to the type of flow and instabilities thought to describe gravity waves and their breakdown, although the shear instabilities present in the excited jet are somewhat similar to one type of dynamical instability that may occur in gravity waves. It may be wrong to infer chaotic behavior in breaking gravity waves on this basis.

Laboratory experiments are held under tightly controlled conditions which are very unlike those found in the atmosphere. Only one spectrum of activity is studied making it easier to detect chaotic behavior in a fluid. Gravity wave breaking in the atmosphere is accompanied by a wide range of other types of processes in the atmosphere, some of which have time scales that overlap those of gravity waves. Detecting chaotic behavior in such a welter of

potentially conflicting data may be nearly impossible. Furthermore, the interaction of gravity wave breaking and other types of atmospheric motion may eliminate any chaotic behavior that might occur otherwise.

Laboratory experiments allow for the generation of a long period of measurements. The conditions which control the instability of the fluid flow can be held constant allowing measurements to be made of the long term evolution of its chaotic behavior. The flow is "continuously unstable".

Gravity wave breaking is a transient phenomenon; gravity waves propagate upward and may become unstable and break down. A better extension of the laboratory analogy would be a continuous source of gravity waves which become unstable and break without modifying the basic state flow at some level. This scenario is unlikely to ever occur in the real atmosphere, much less at a time and place where measurements were being made.

Chaotic behavior in gravity wave breaking may be so ephemeral that we may never be able to detect it. Bonetti and Boon (1989) recommended a sampling rate of 10 to 30 measurements per pseudo-period of the orbit of the attractor. If we consider Smith's (1988) estimate of the number of points required to accurately estimate the dimension using the Grassberger-Procaccia algorithm for an attractor of dimension 2, and Bonetti and Boon's estimate of the sampling rate, we must sample approximately between 59 and 176 orbits to fully characterize the attractor! If we assume that the pseudo-period of an attractor in the breaking of gravity waves is on the order of the Brunt-Väisälä period (5 minutes) and a dimension on the order of 2, we would have to make measurements for more than 6 hours. The length of time may be even greater if the attractor were of higher dimensions which is very likely.

Six hours is practically an eternity for the phenomena we are considering in the atmosphere. The data set would not be stationary over this length of time and atmospheric flow regimes with longer time scales (tides, synoptic scale activity) would contaminate the data set. This requirement

almost certainly eliminates finding chaotic behavior in gravity wave breaking since gravity waves that break decay to turbulence at a rate much faster than 6 hours.

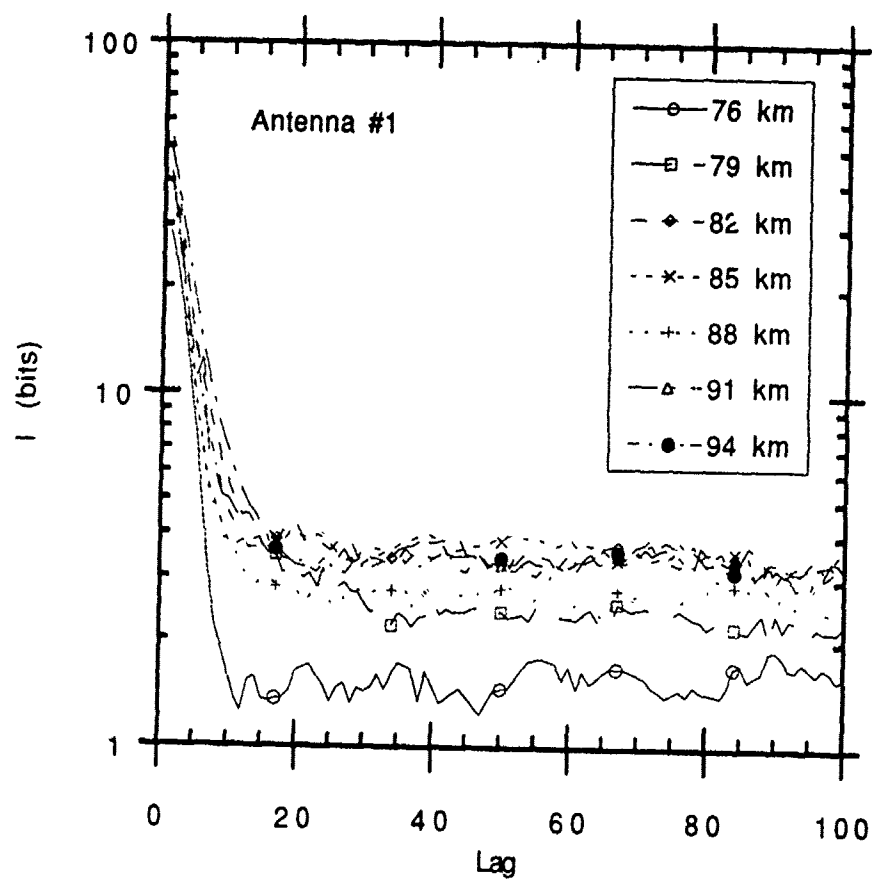


Figure 5.1 Mutual information for antenna #1 calculated from the first 6000 points for levels 76 through 94 km.

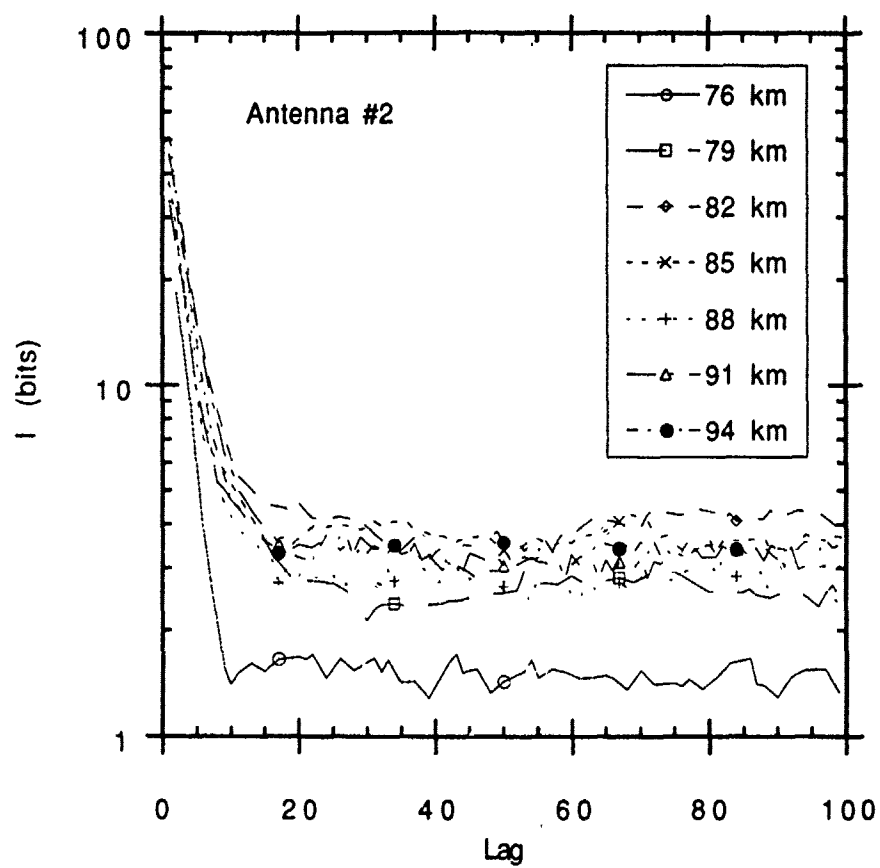


Figure 5.2 Mutual information for antenna #2 calculated from the first 6000 points for levels 76 through 94 km.

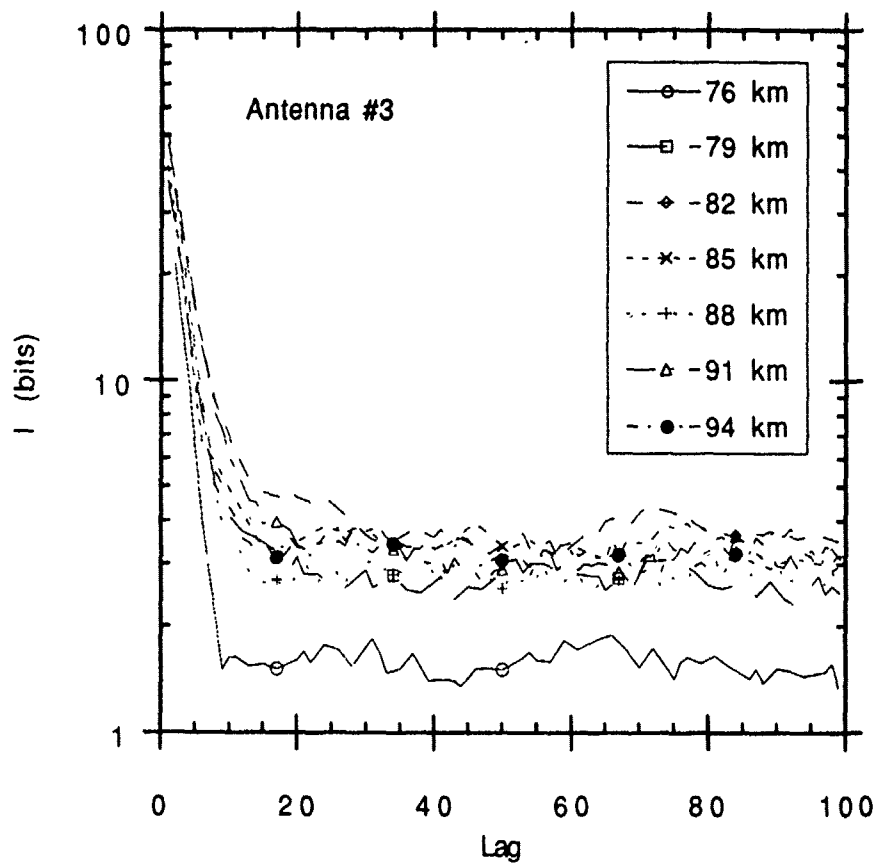


Figure 5.3 Mutual information for antenna #3 calculated from the first 6000 points for levels 76 through 94 km.

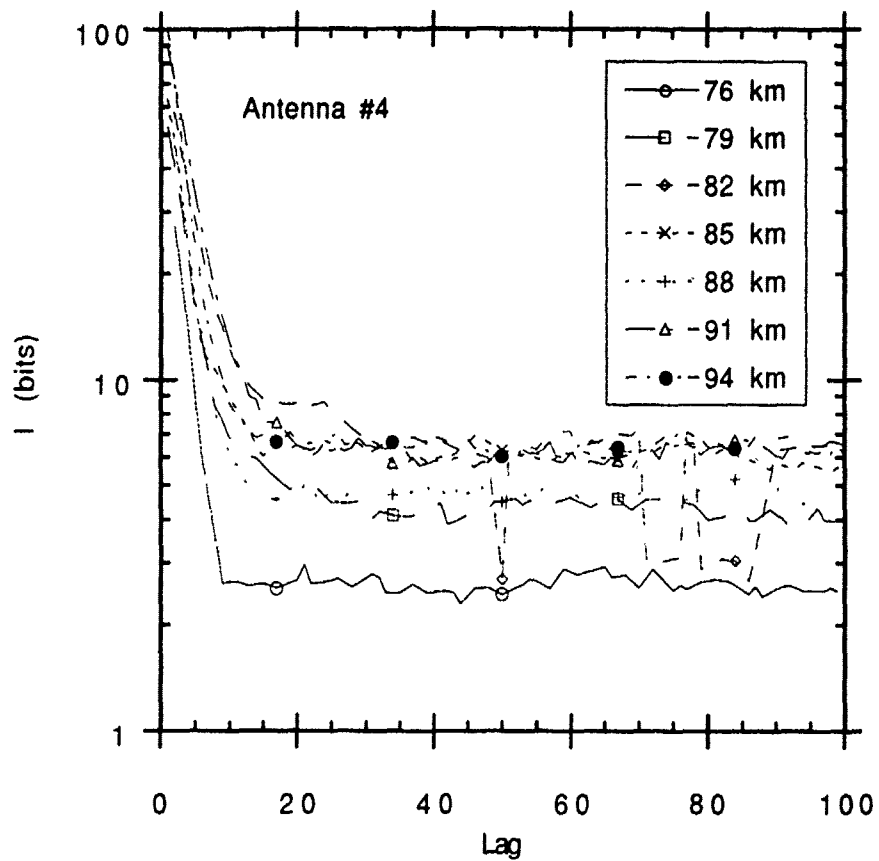


Figure 5.4 Mutual information for antenna #4 calculated from the first 6000 points for levels 76 through 94 km.

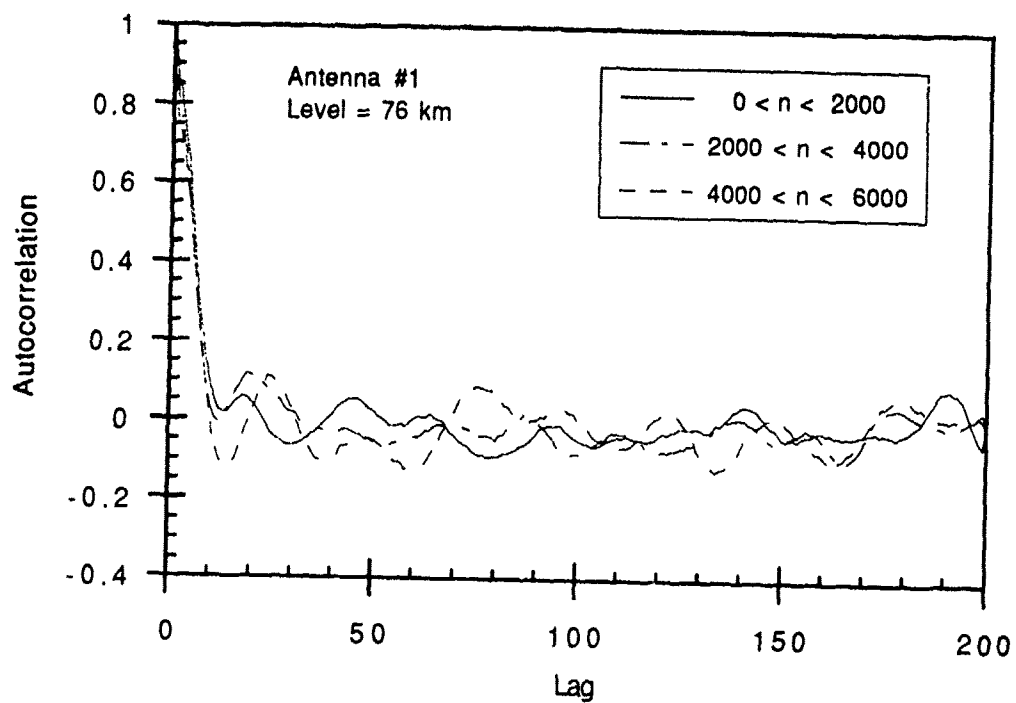


Figure 5.5(a)

Figure 5.5 Autocorrelation (2000 point groups) for antenna #1 for (a) 76 km, (b) 79 km, (c) 82 km, (d) 85 km, (e) 88 km, (f) 91 km and (g) 94 km.

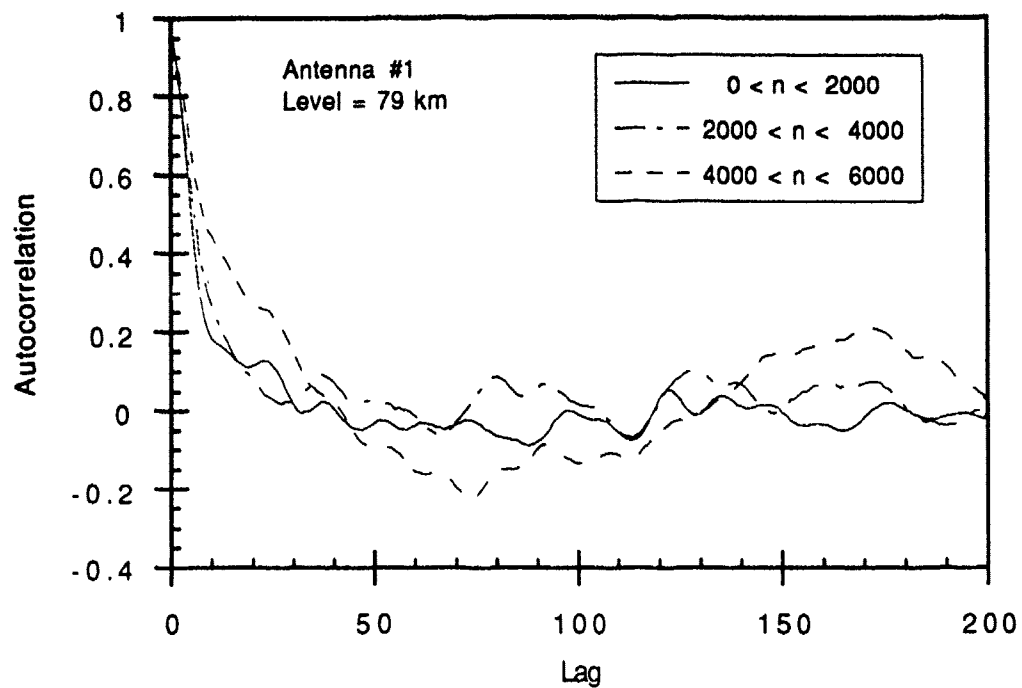


Figure 5.5(b)

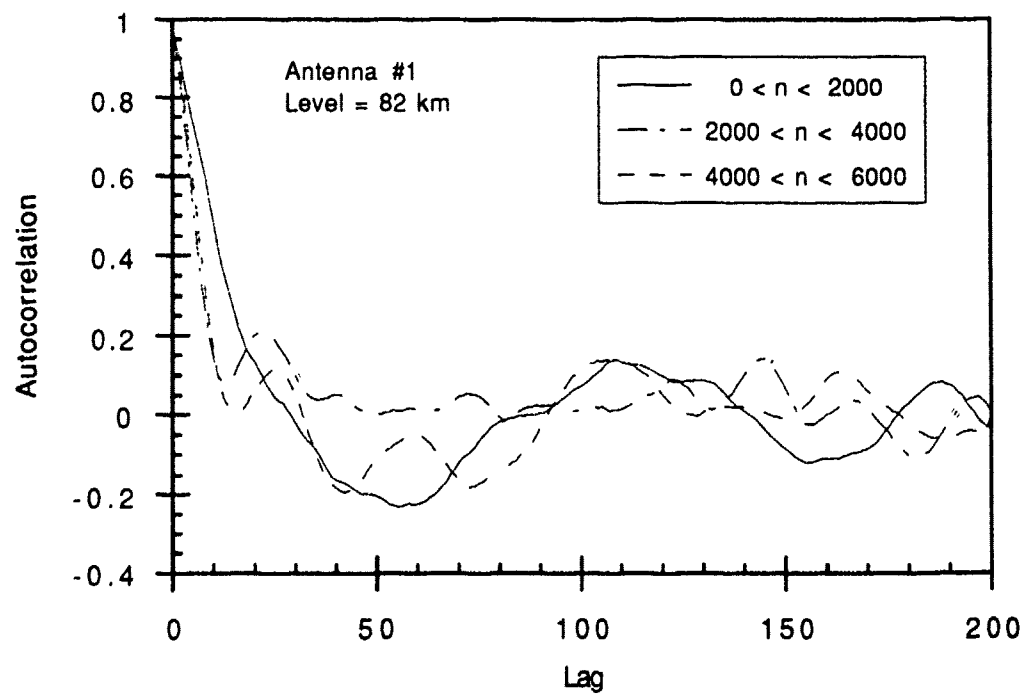


Figure 5.5 (c)

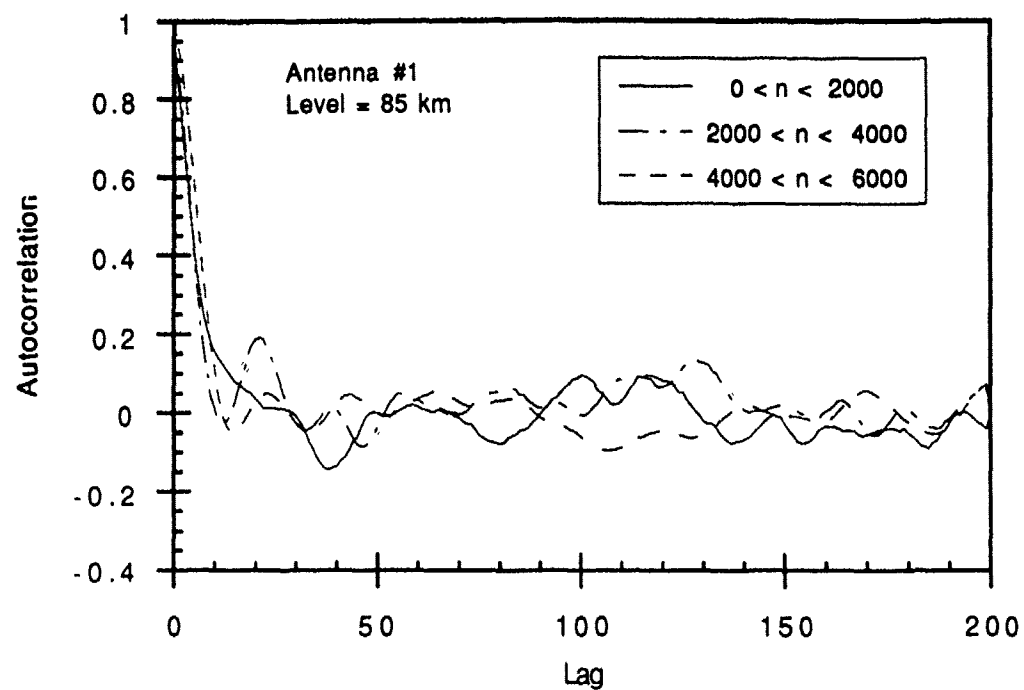


Figure 5.5 (d)

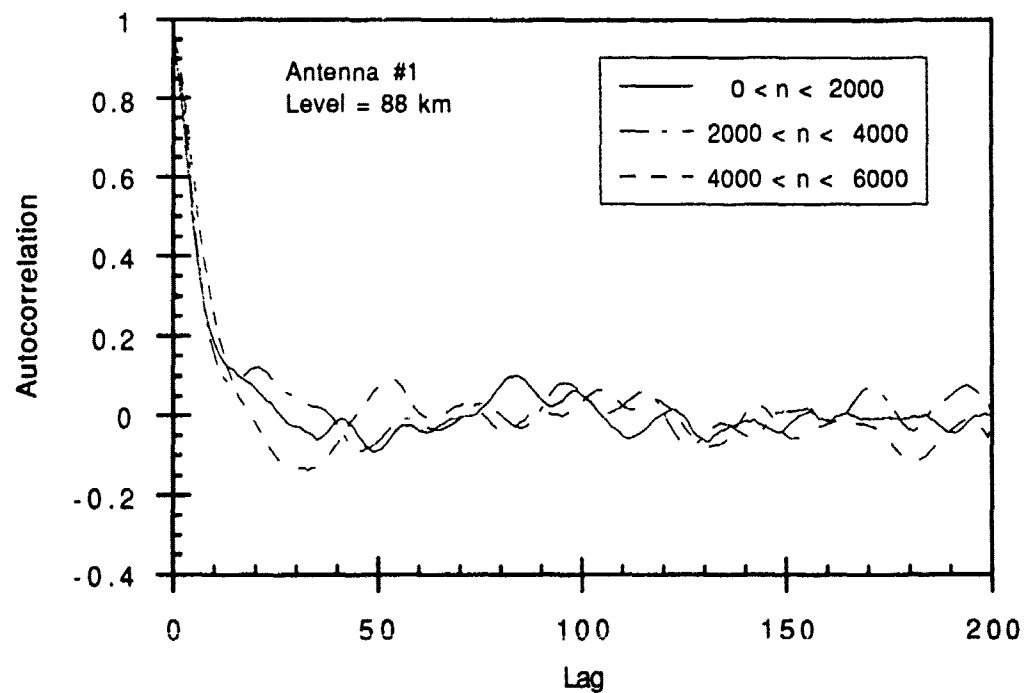


Figure 5.5 (e)

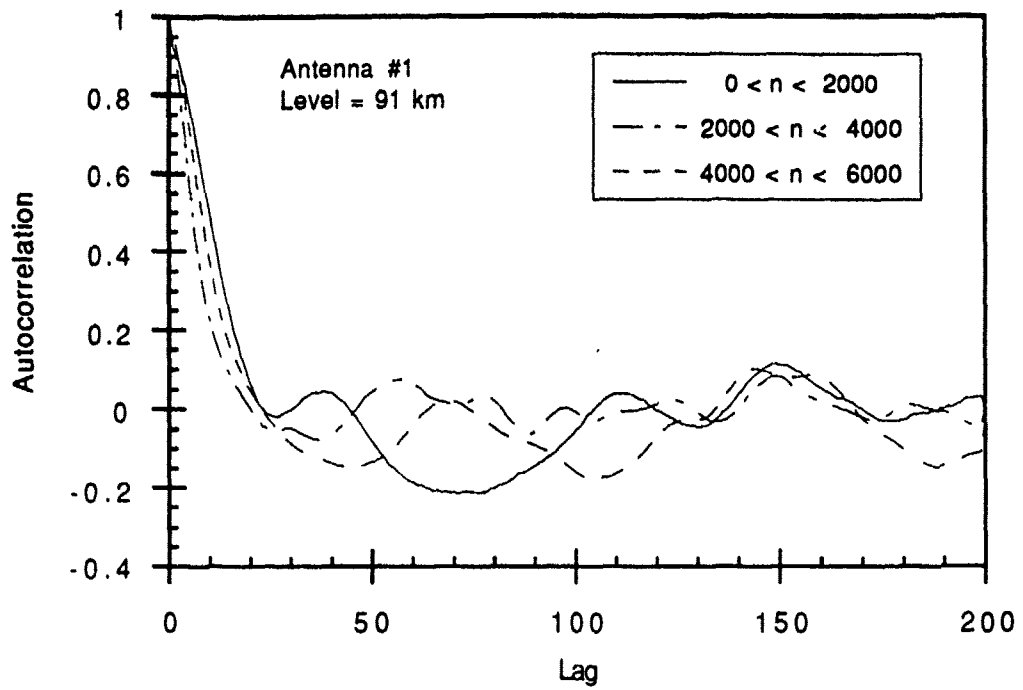


Figure 5.5 (f)

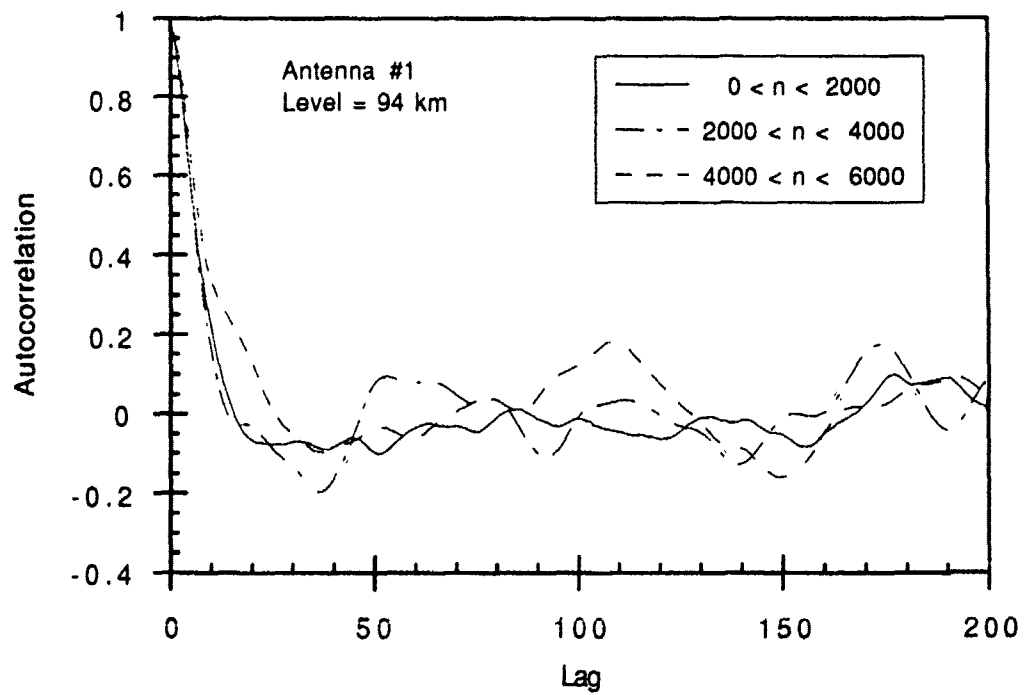


Figure 5.5 (g)

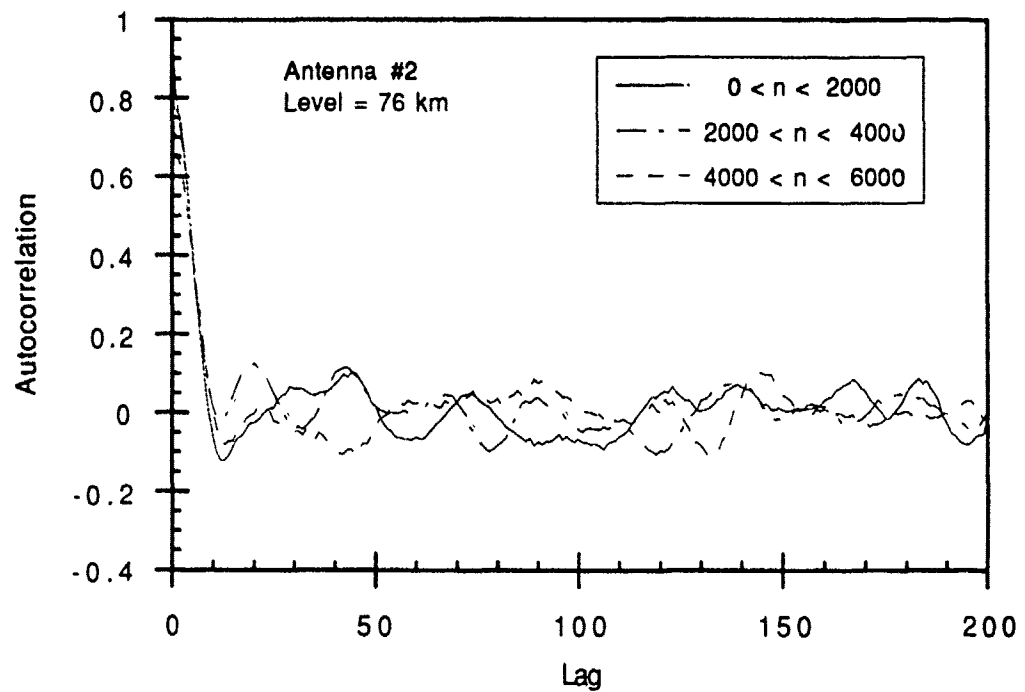


Figure 5.6(a)

Figure 5.6 Autocorrelation (2000 point groups) for antenna #2 for (a) 76 km, (b) 79 km, (c) 82 km, (d) 85 km, (e) 88 km, (f) 91 km and (g) 94 km.

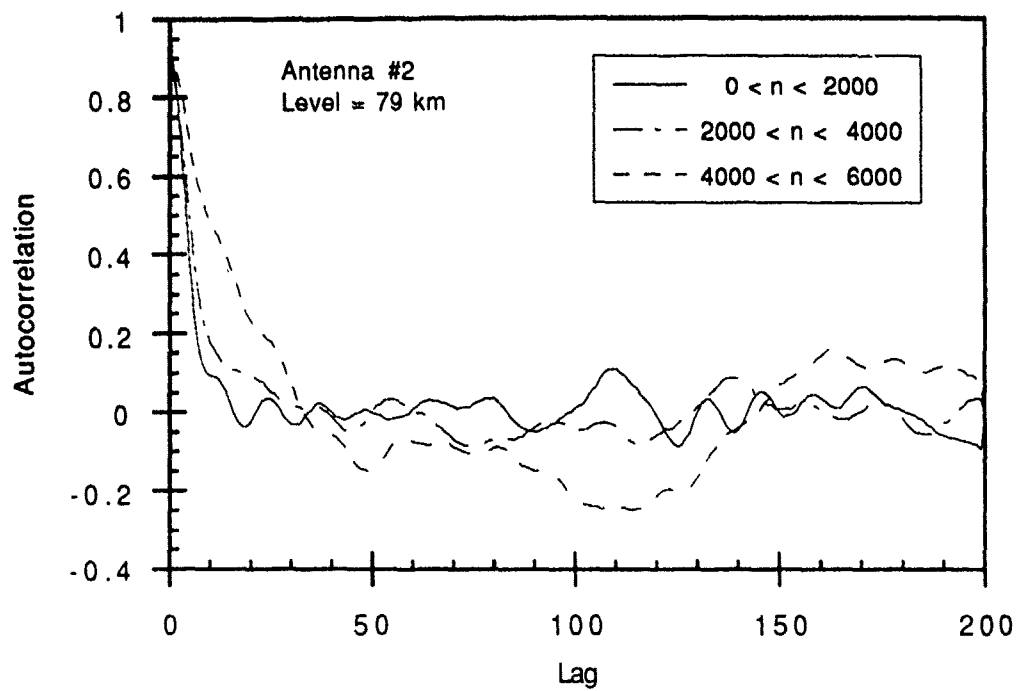


Figure 5.6(b)

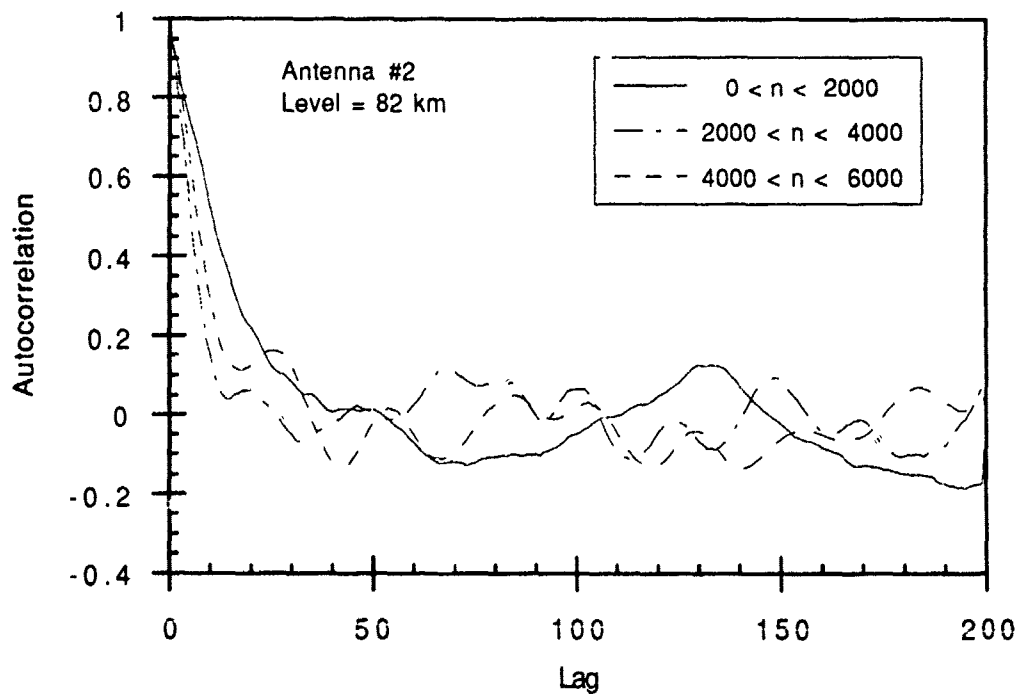


Figure 5.6 (c)

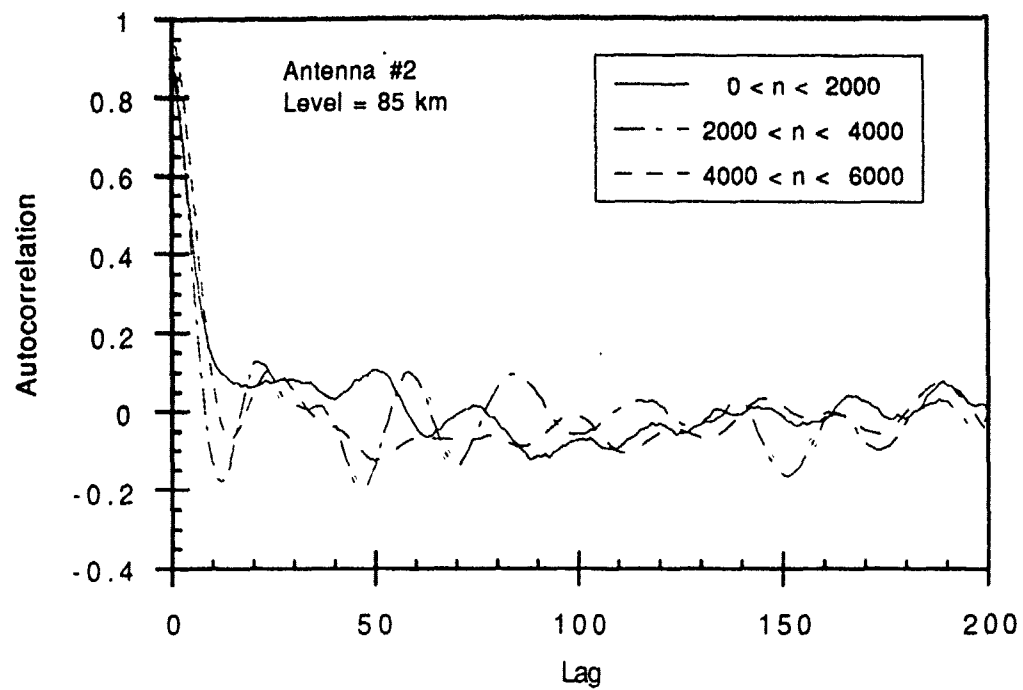


Figure 5.6 (d)

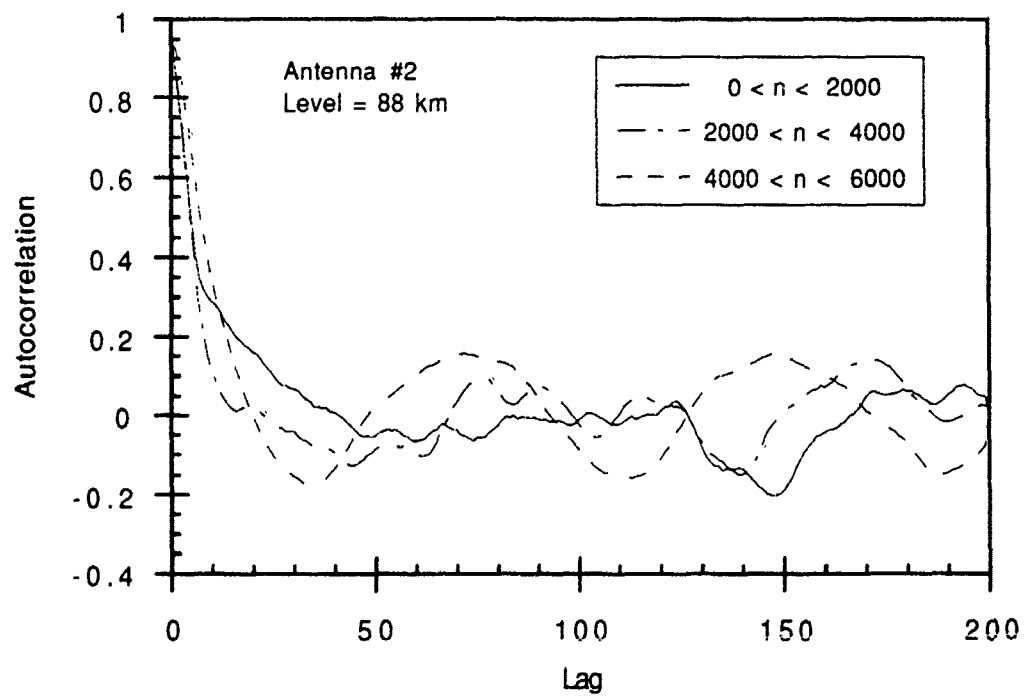


Figure 5.6 (c)

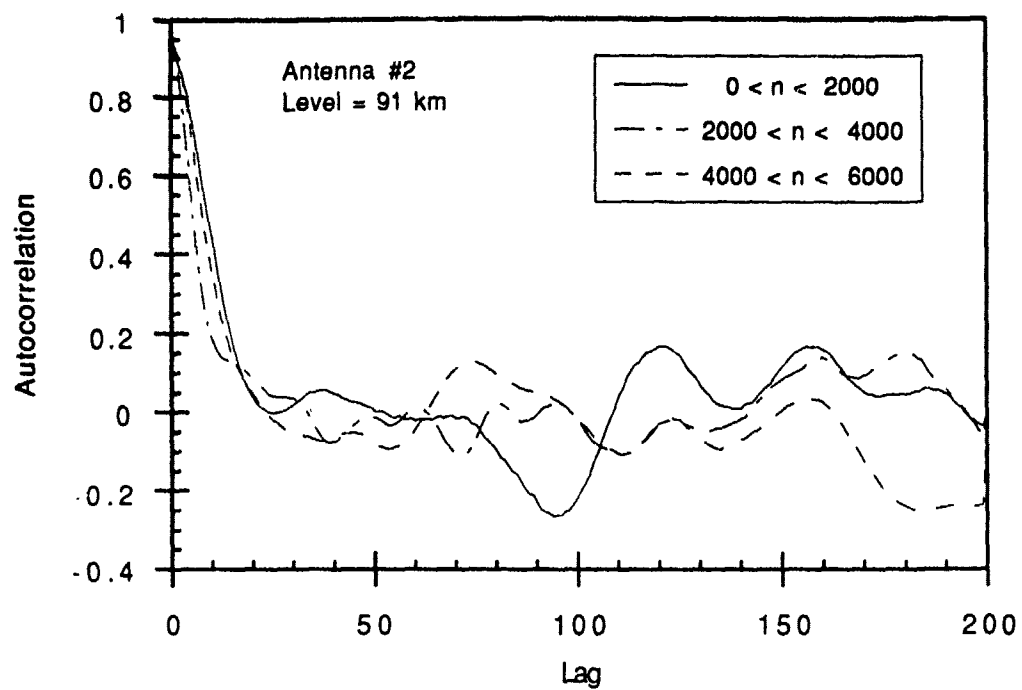


Figure 5.6 (f)

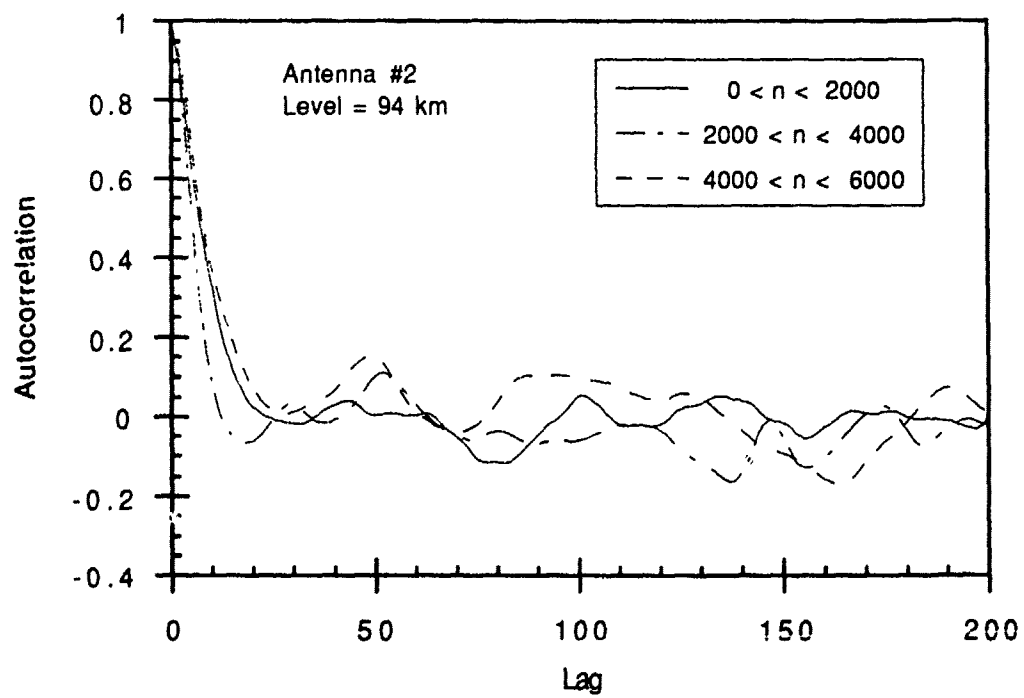


Figure 5.6 (g)

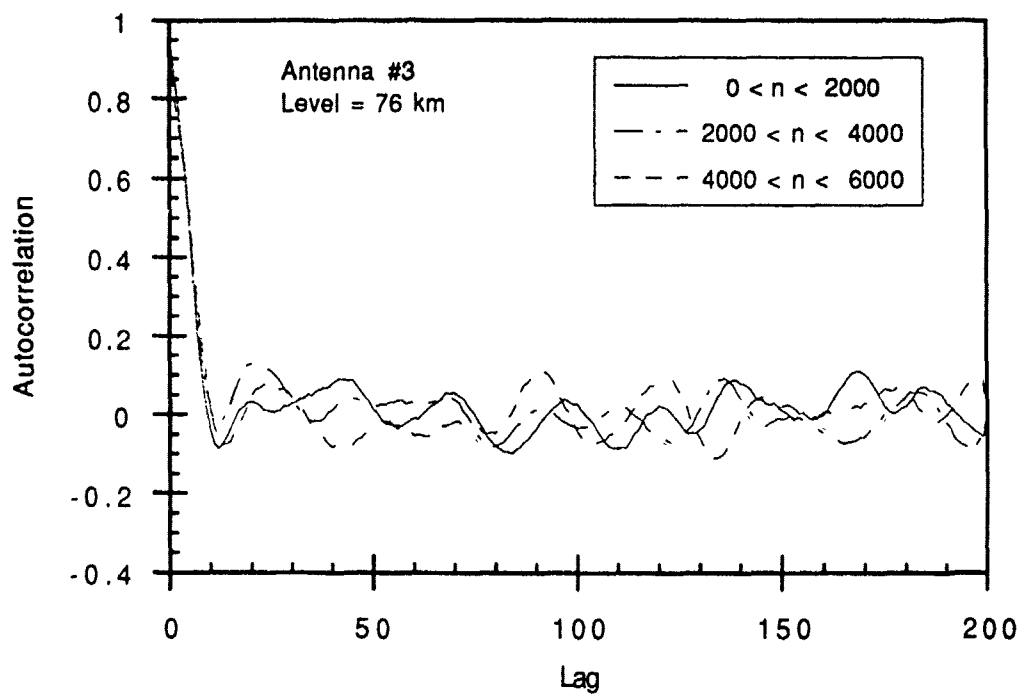


Figure 5.7(a)

Figure 5.7 Autocorrelation (2000 point groups) for antenna #3 for (a) 76 km, (b) 79 km, (c) 82 km, (d) 85 km, (e) 88 km, (f) 91 km and (g) 94 km.

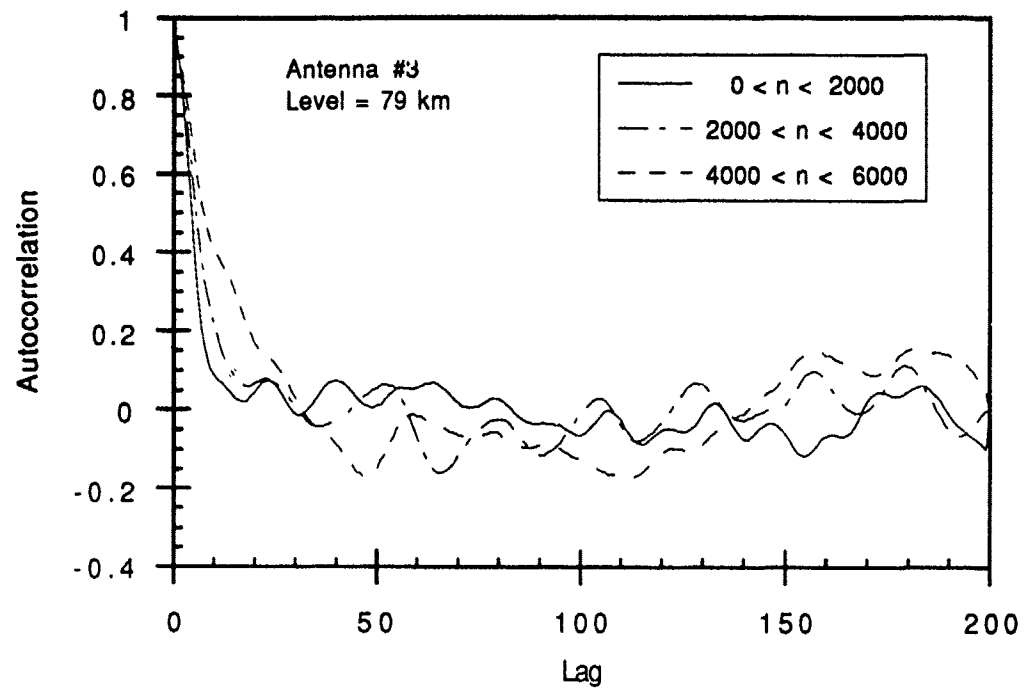


Figure 5.7(b)

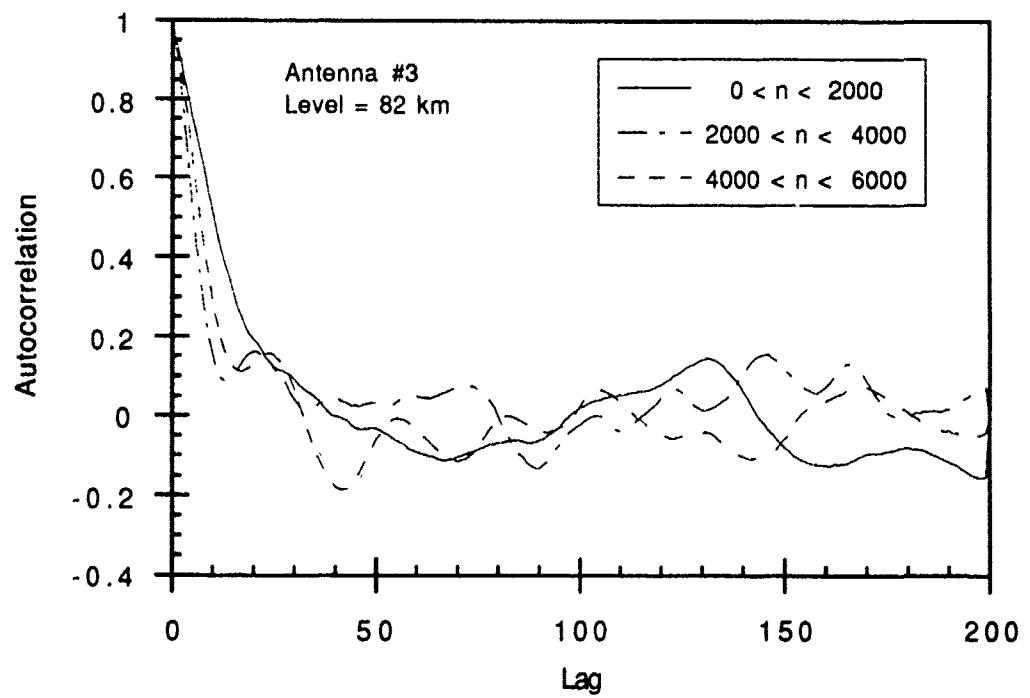


Figure 5.7 (c)

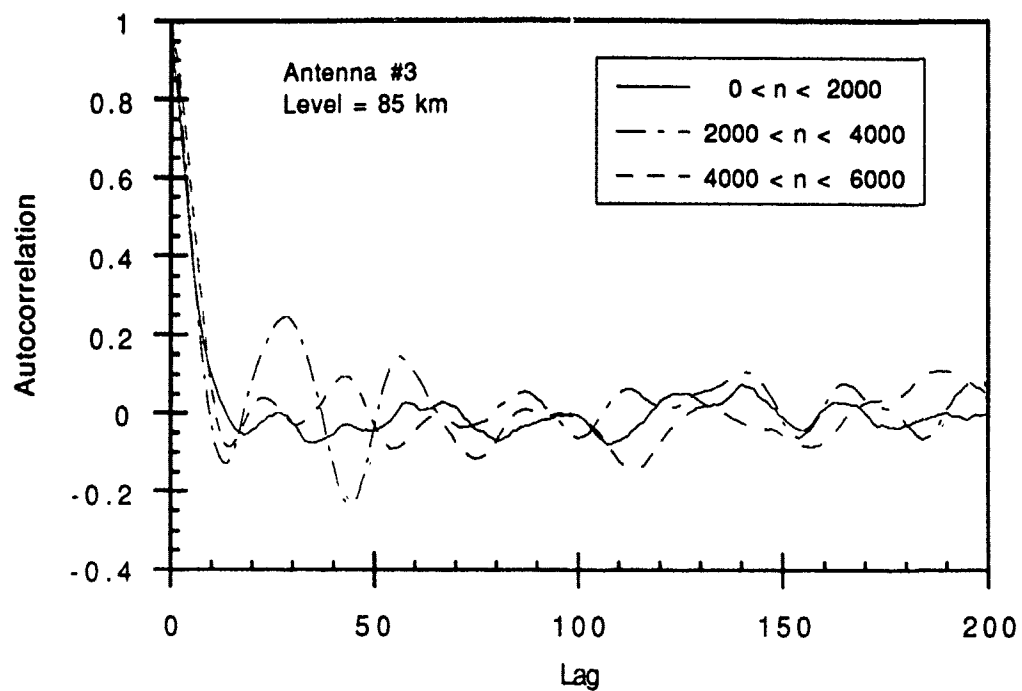


Figure 5.7 (d)

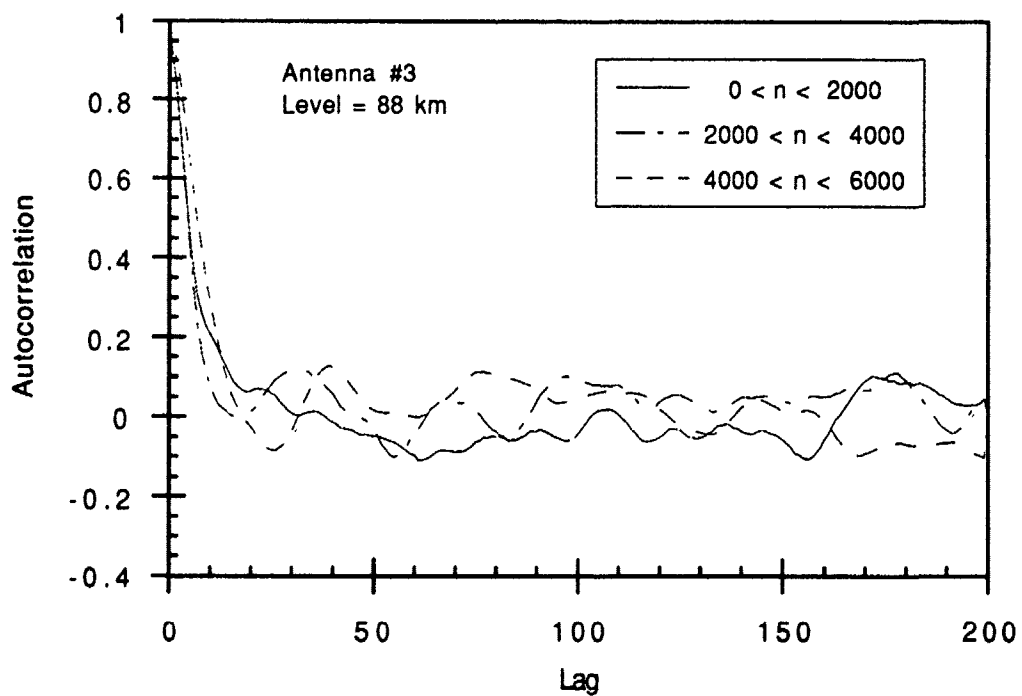


Figure 5.7 (e)

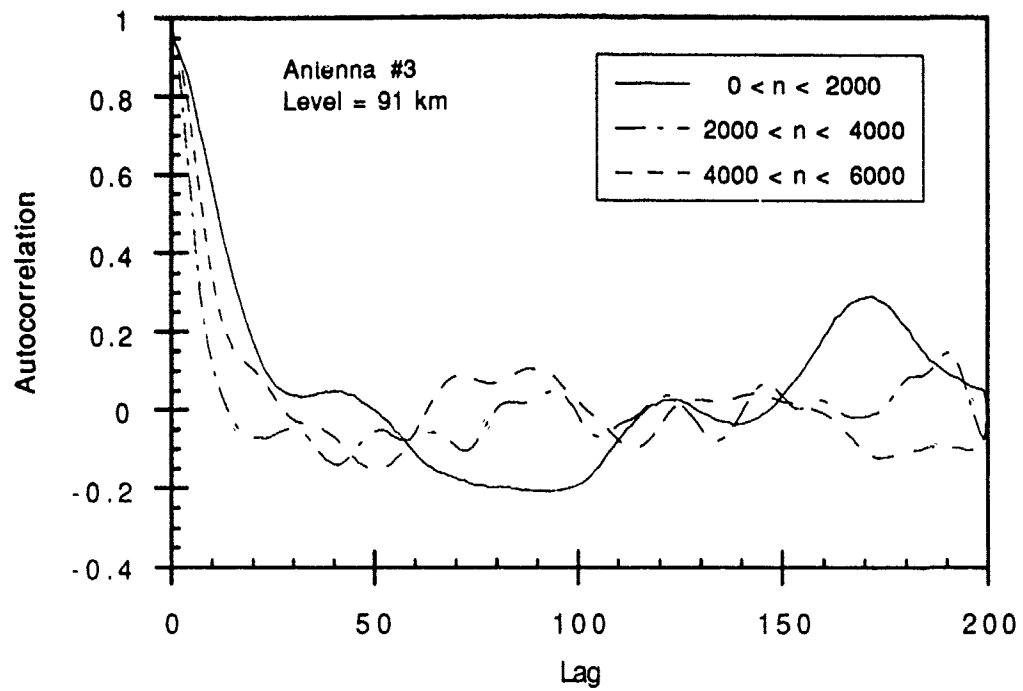


Figure 5.7 (f)

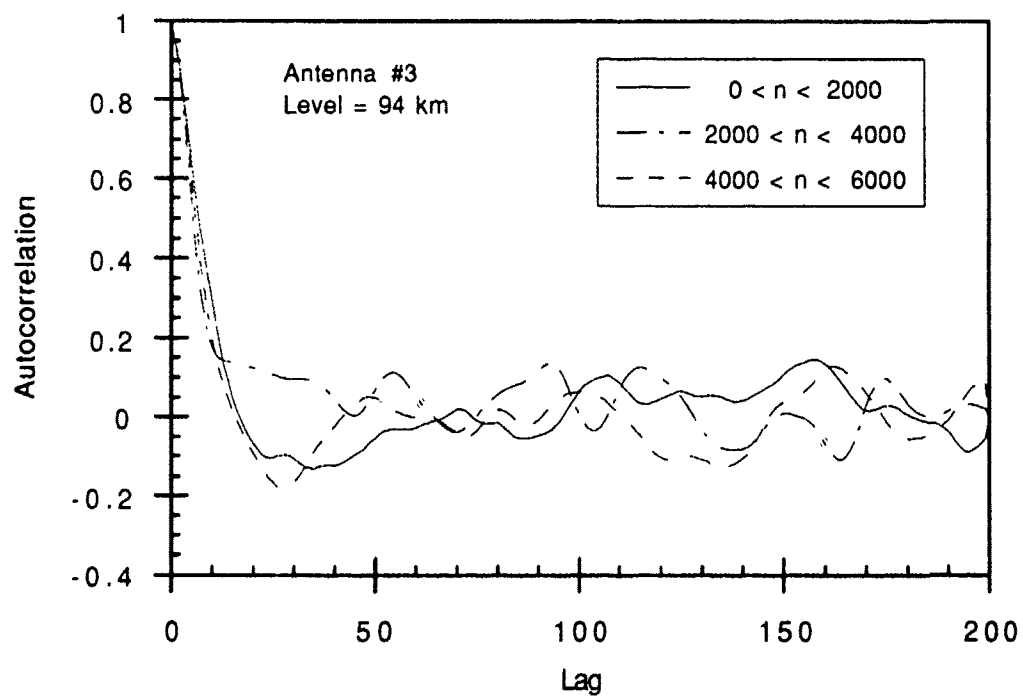


Figure 5.7 (g)

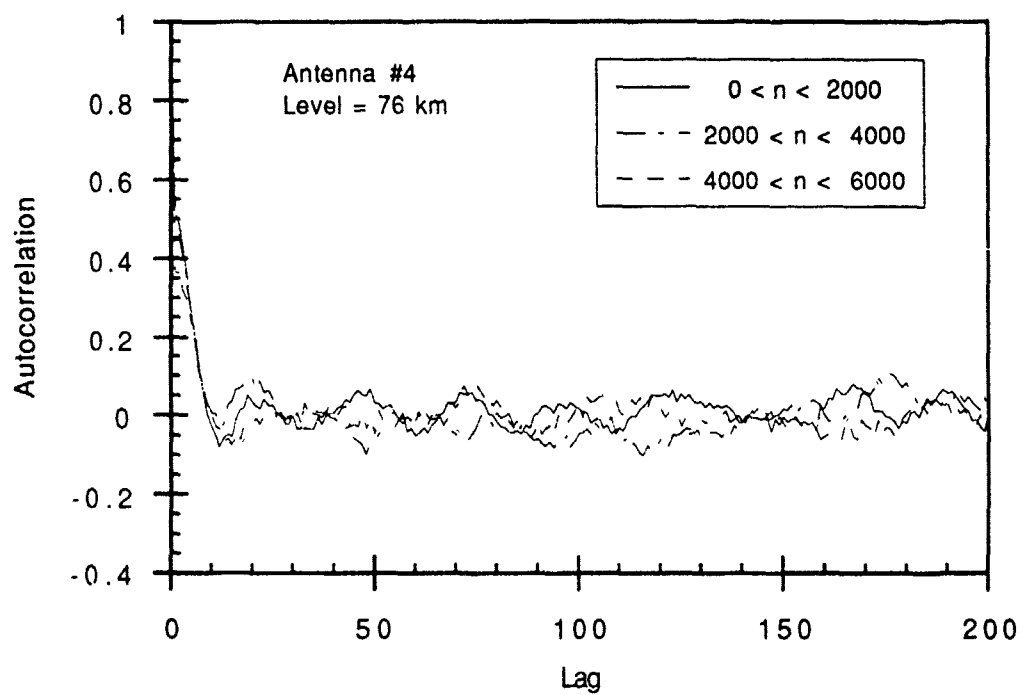


Figure 5.8(a)

Figure 5.8 Autocorrelation (2000 point groups) for antenna #4 for (a) 76 km, (b) 79 km, (c) 82 km, (d) 85 km, (e) 88 km, (f) 91 km and (g) 94 km.

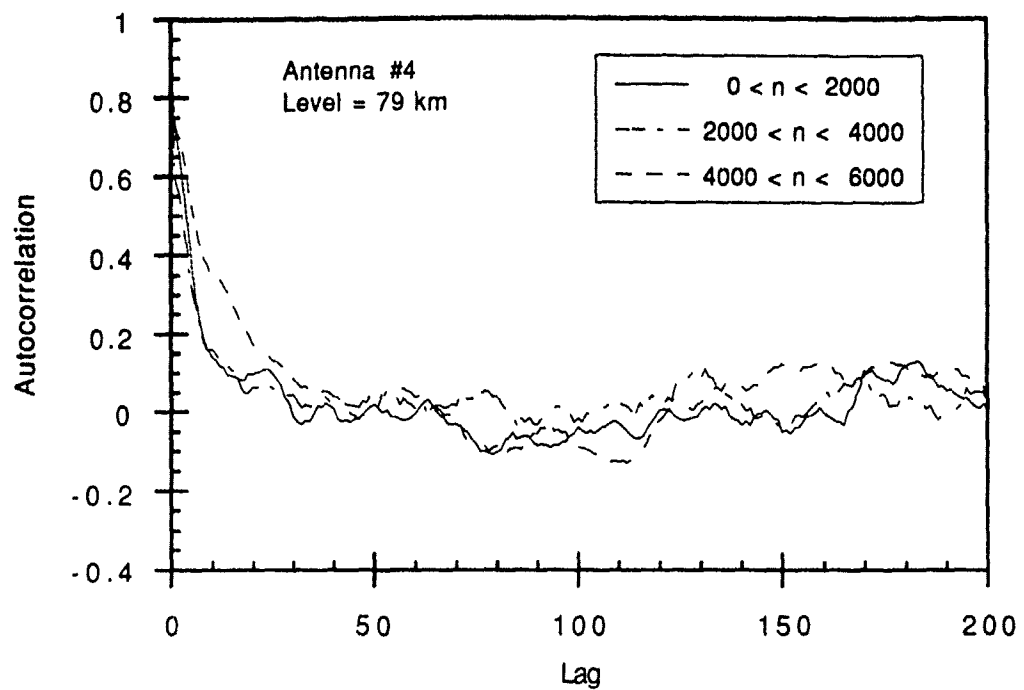


Figure 5.8(b)

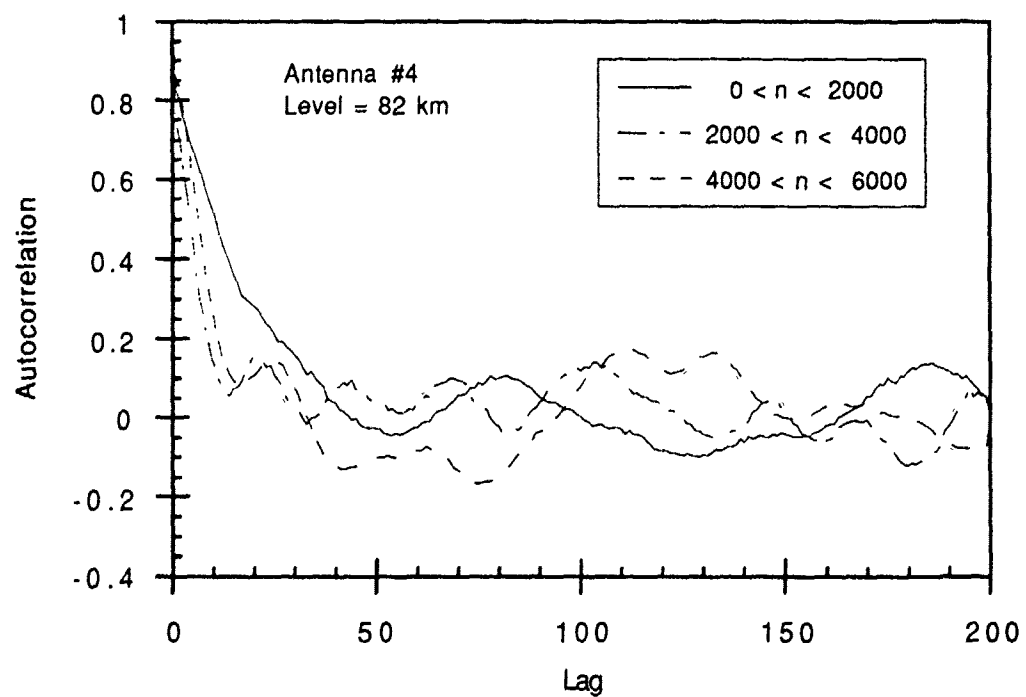


Figure 5.8 (c)

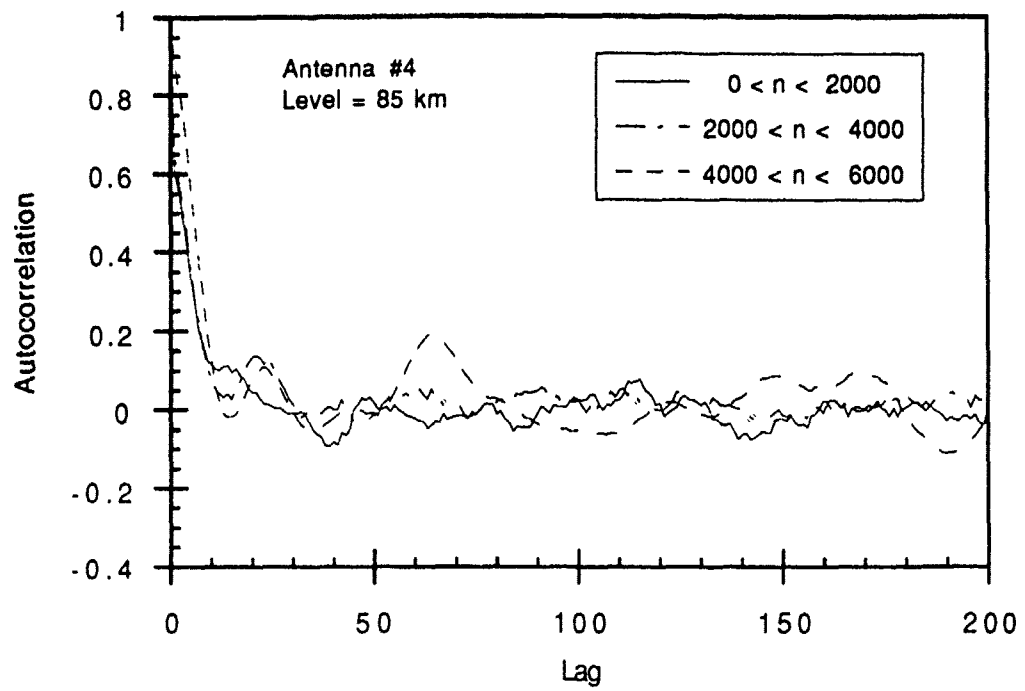


Figure 5.8 (d)

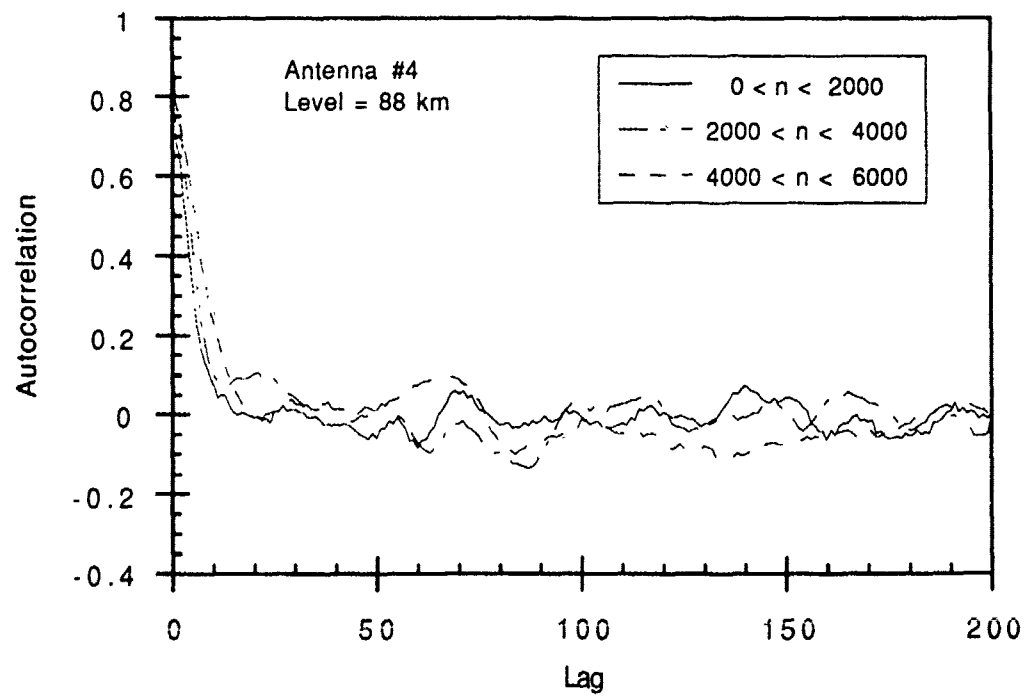


Figure 5.8 (e)

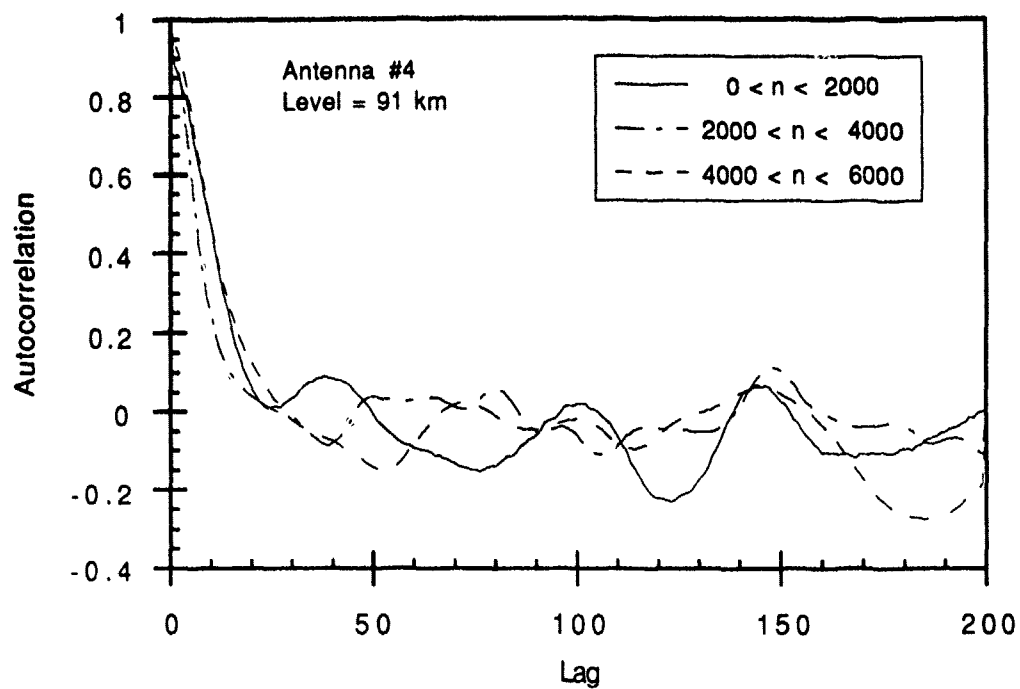


Figure 5.8 (f)

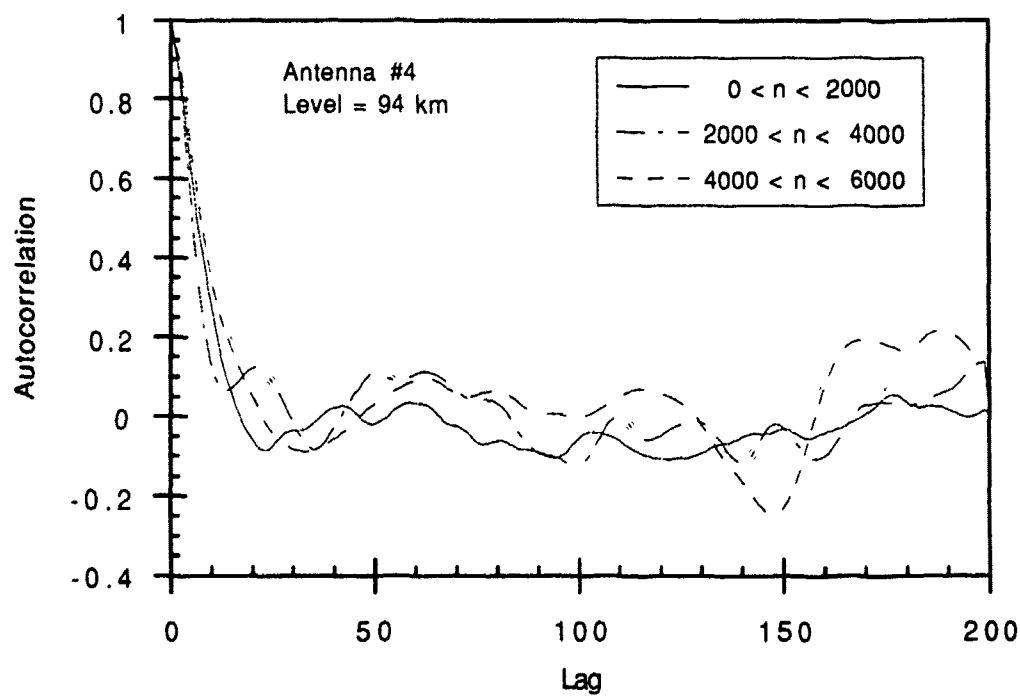


Figure 5.8 (g)

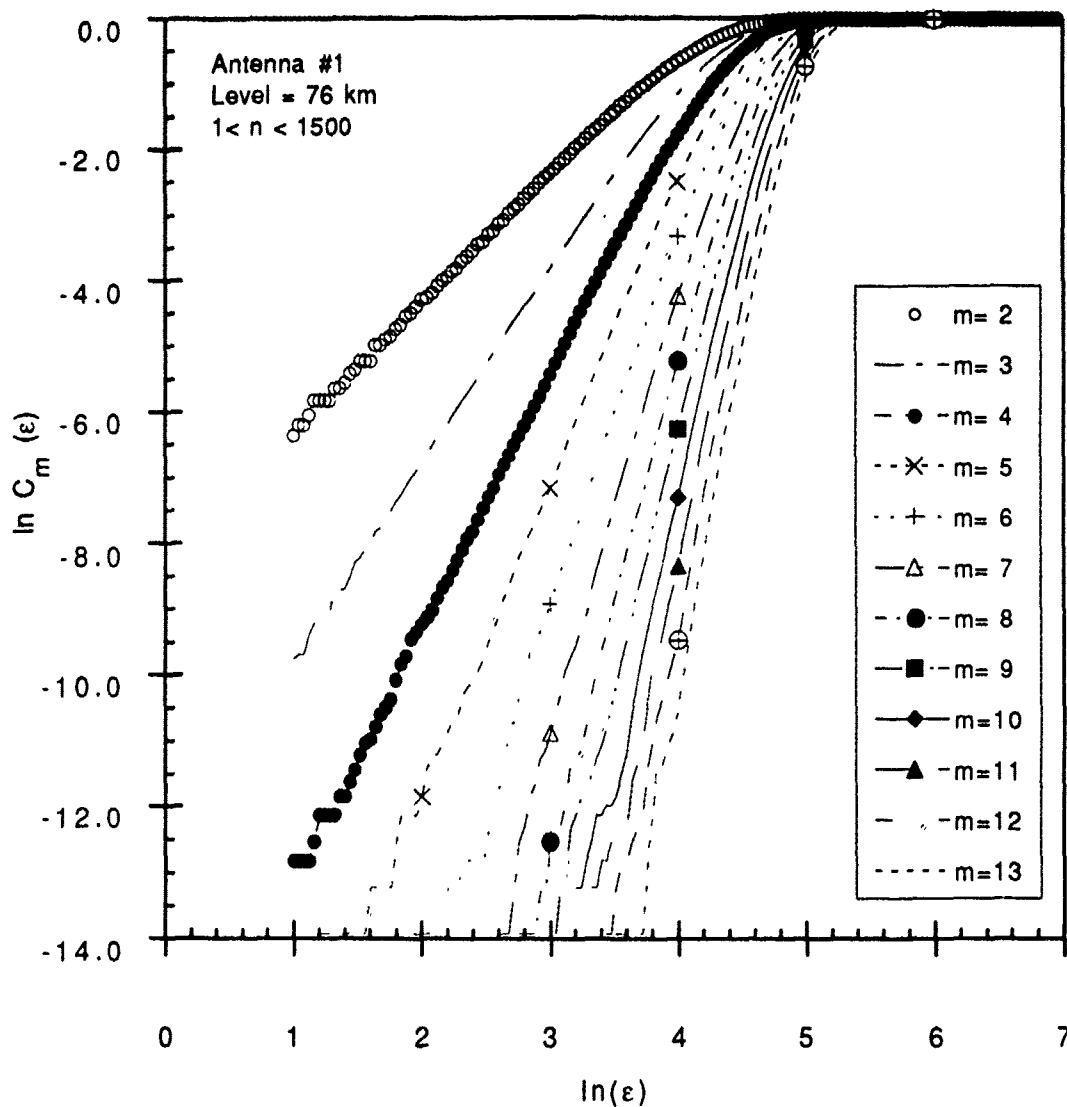


Figure 5.9(a)

Figure 5.9 Correlation integral plotted as a function of embedding dimension m for points 1 through 1500 from antenna 1 for (a) 76 km; (b) 79 km; (c) 82 km; (d) 85 km (e) 88km; (f) 91 km and (g) 94 km.

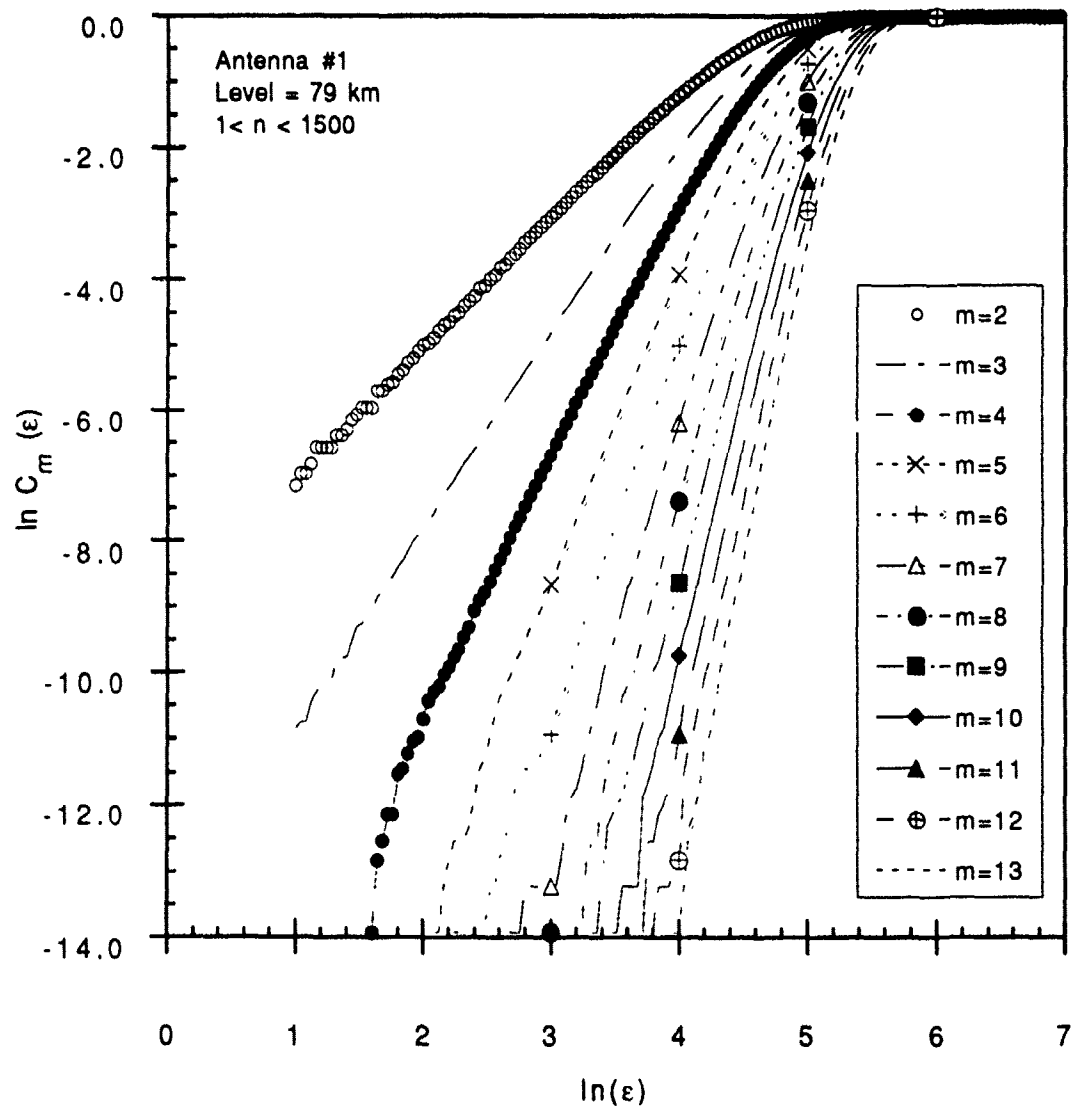


Figure 5.9(b)

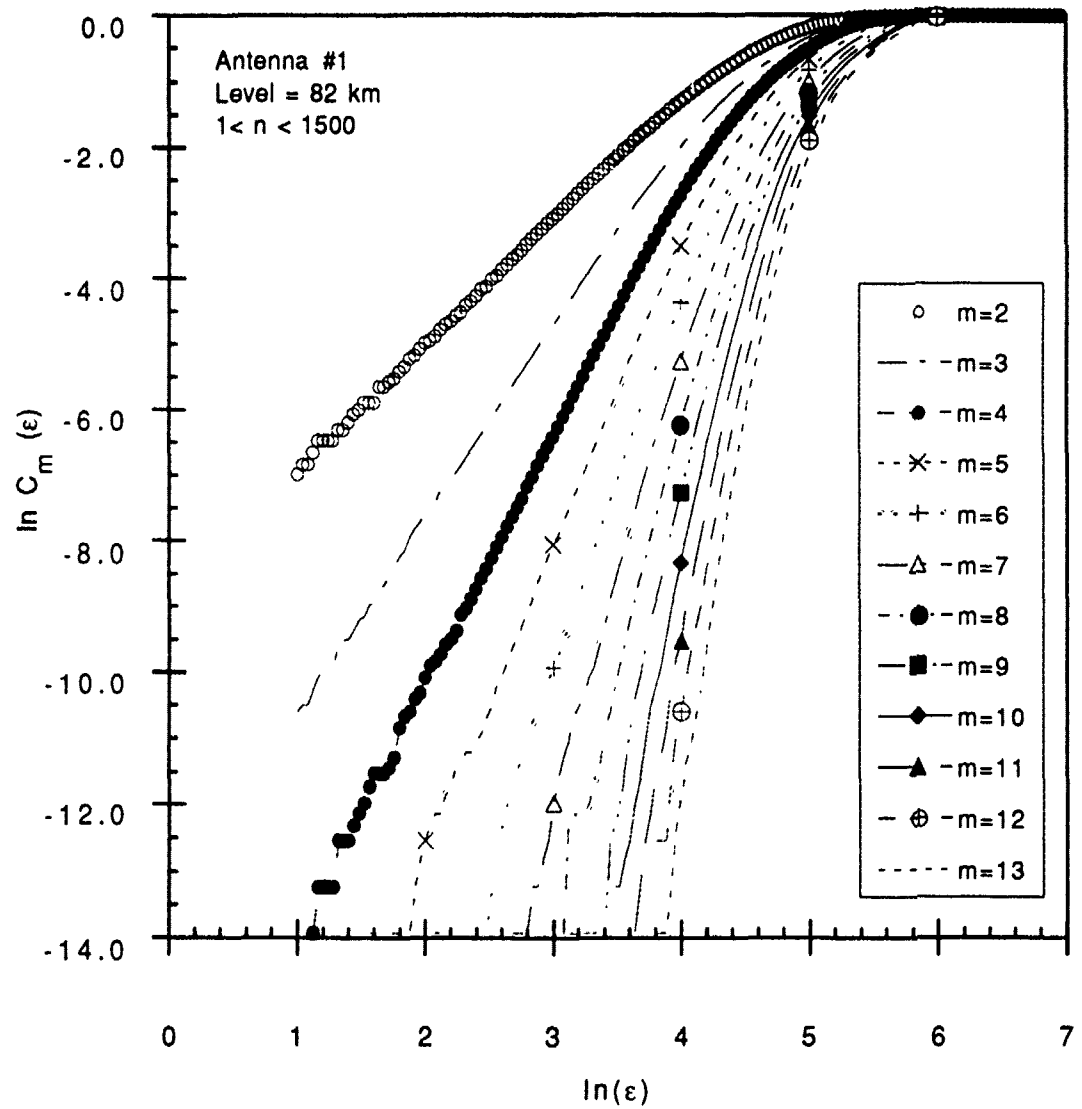


Figure 5.9 (c)

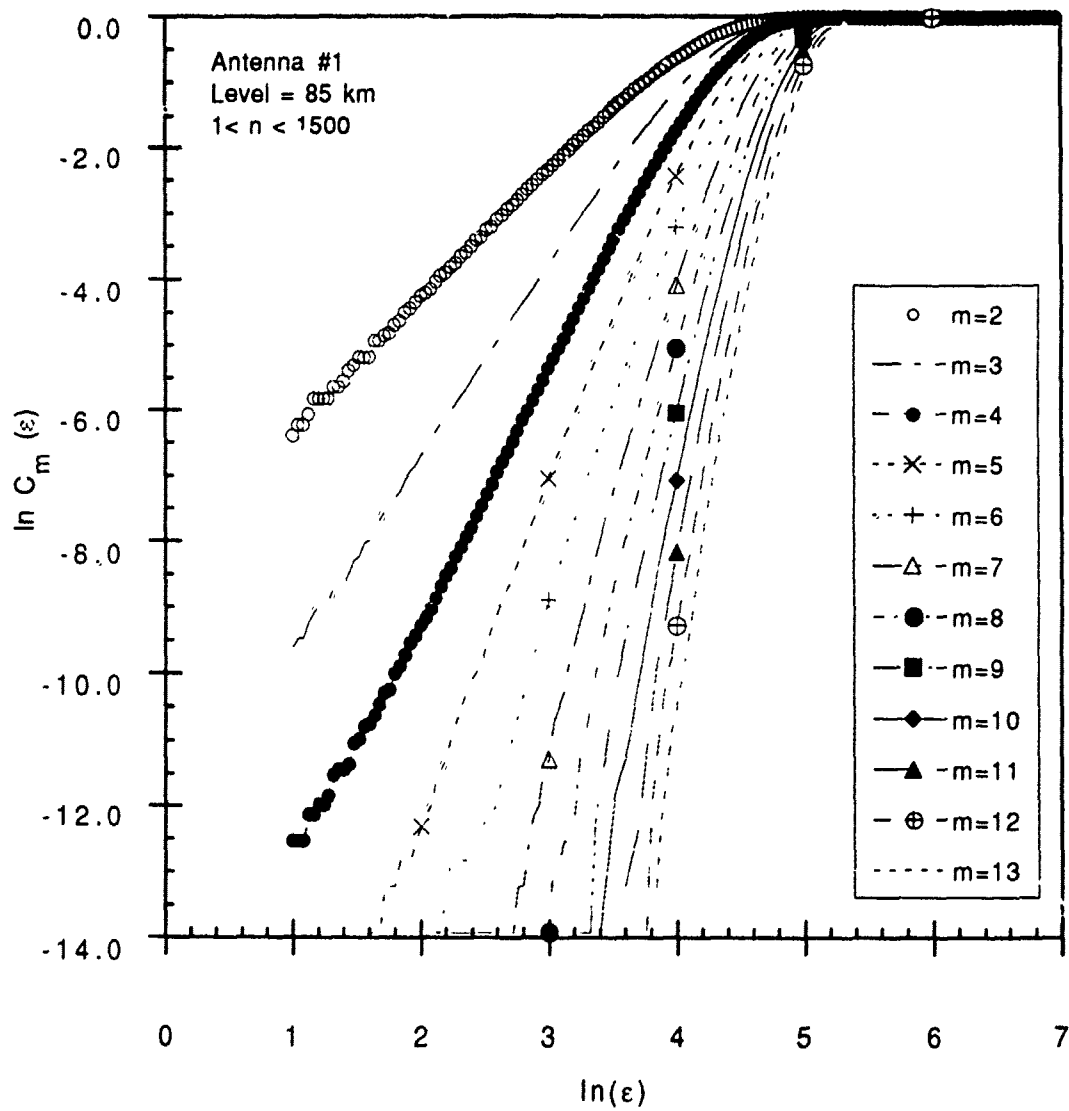


Figure 5.9(d)

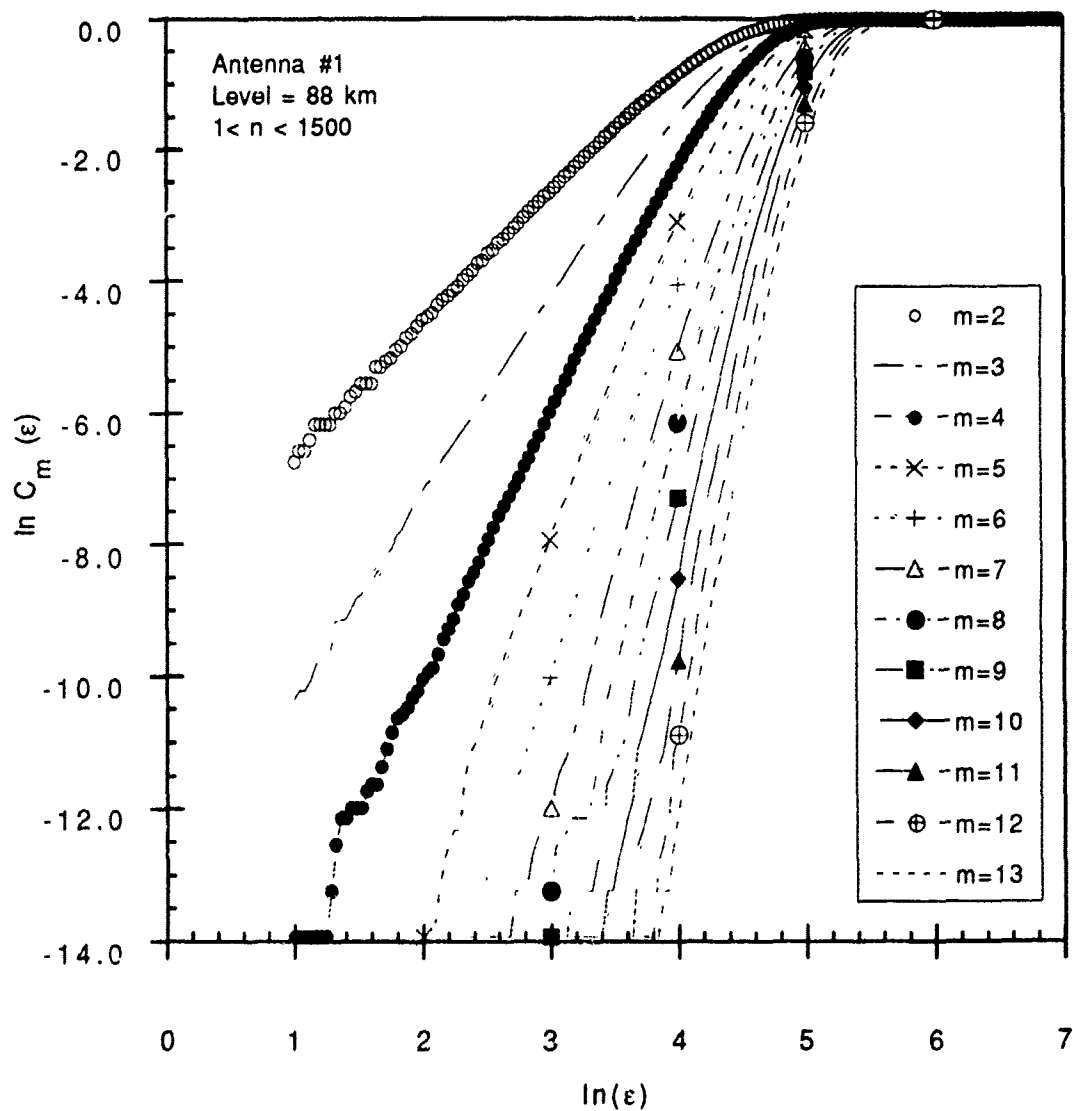


Figure 5.9(c)

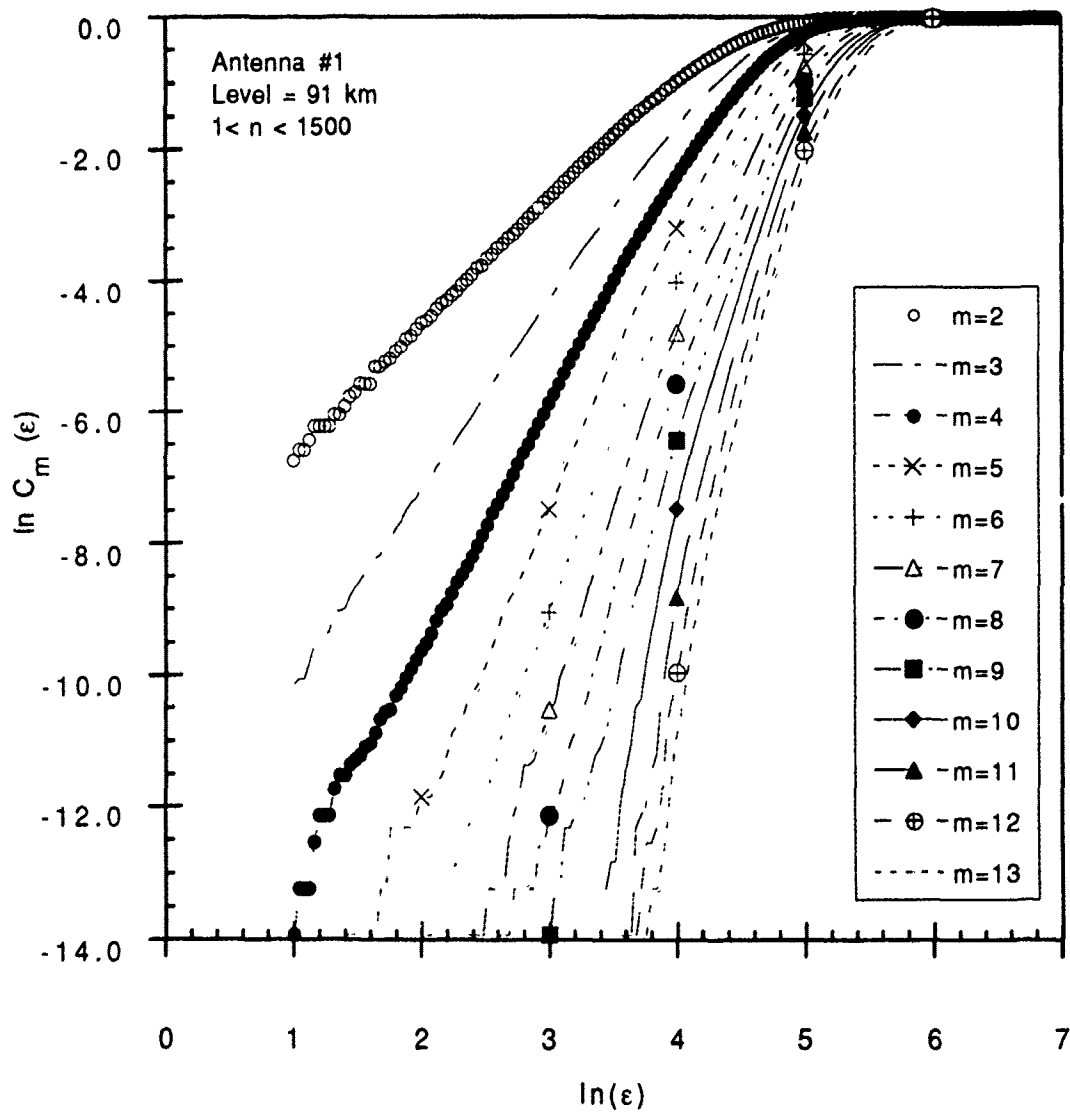


Figure 5.9(f)

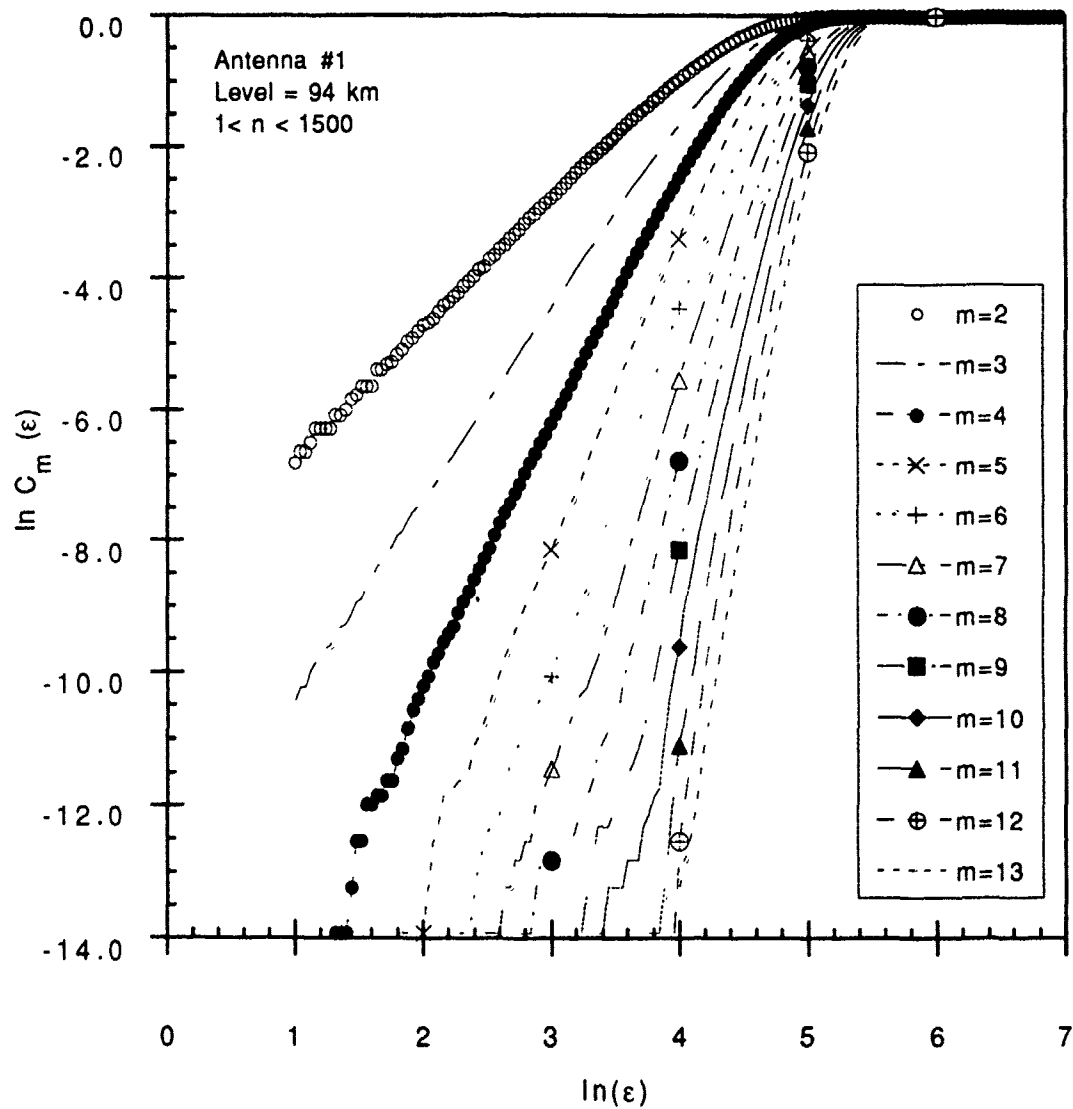


Figure 5.9(g)

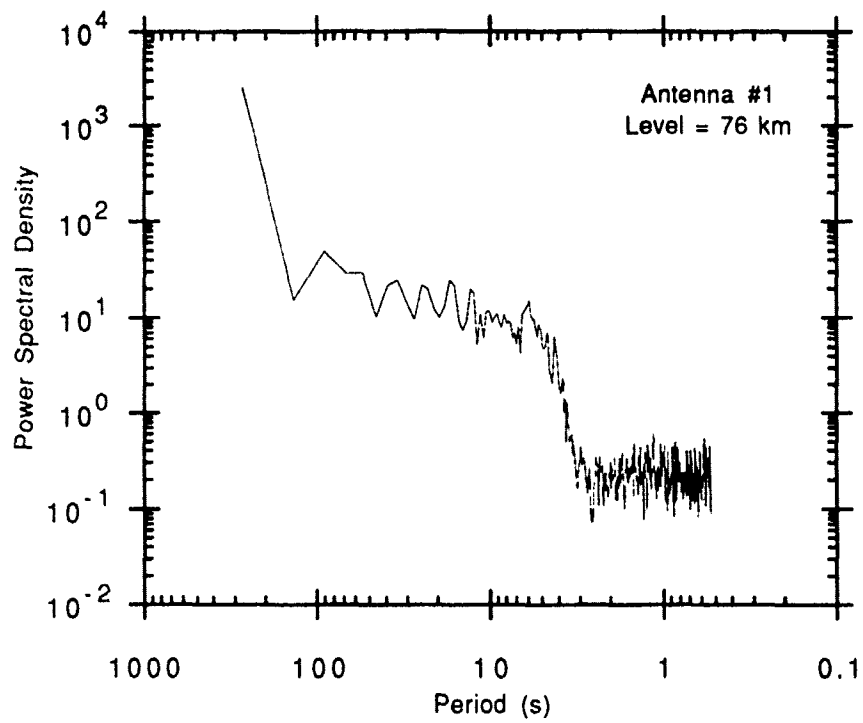


Figure 5.10(a)

Figure 5.10 Power spectral density for antenna #1 for (a) 76 km, (b) 79 km, (c) 82 km, (d) 85 km, (e) 88 km, (f) 91 km and (g) 94 km.

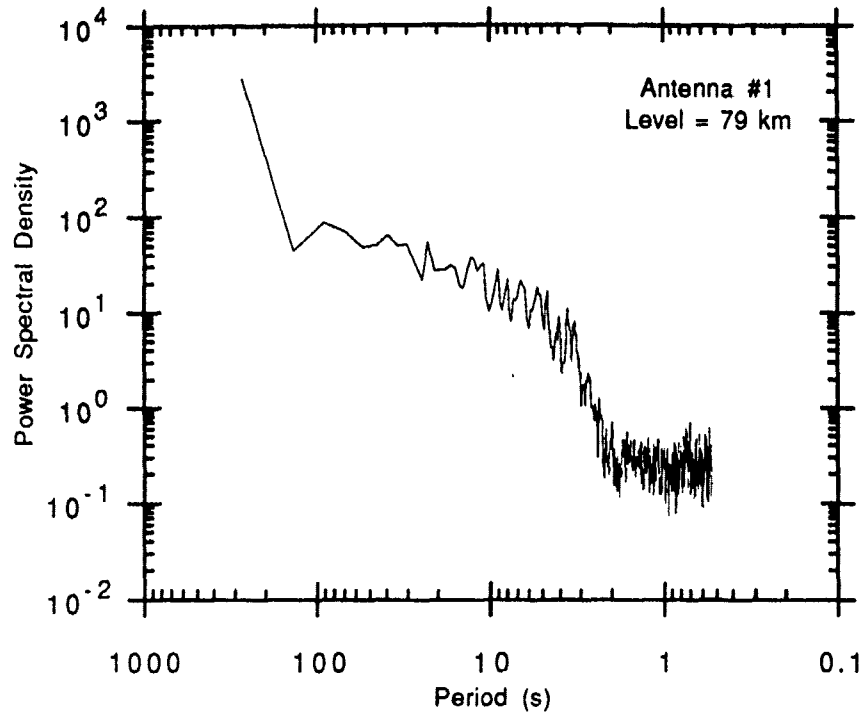


Figure 5.10(b)

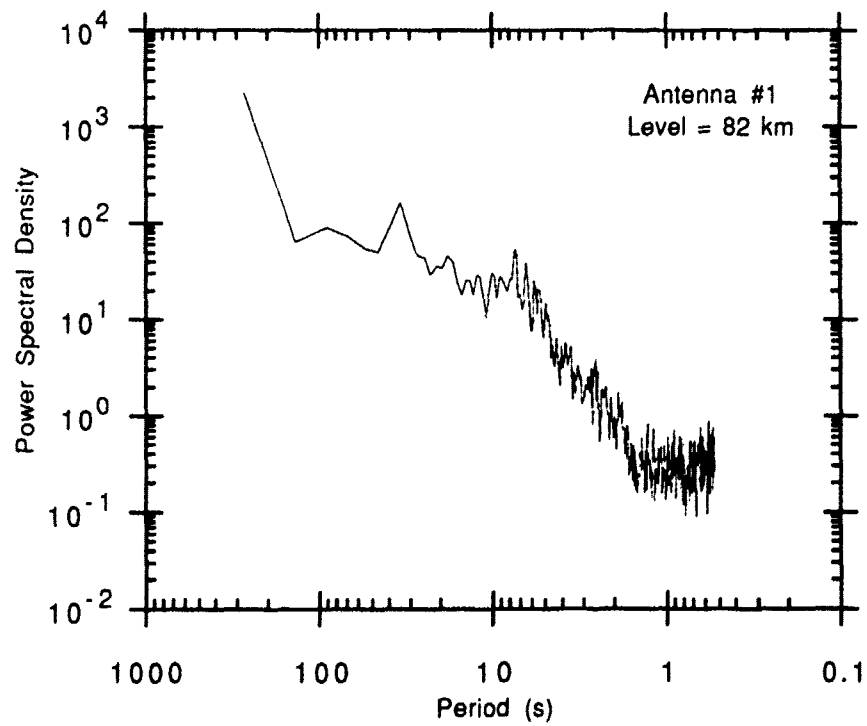


Figure 5.10 (c)

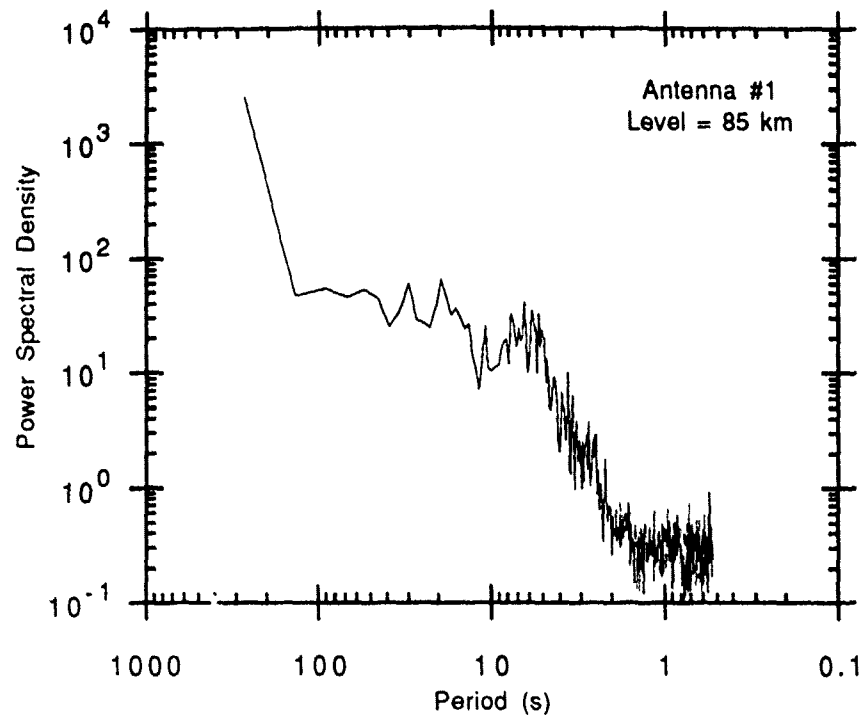


Figure 5.10 (d)

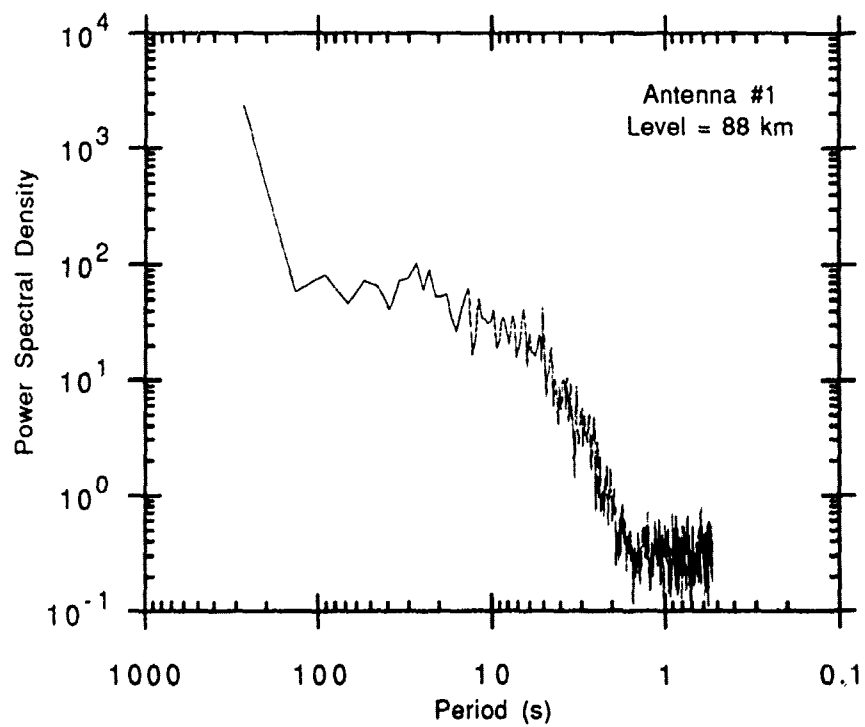


Figure 5.10 (c)

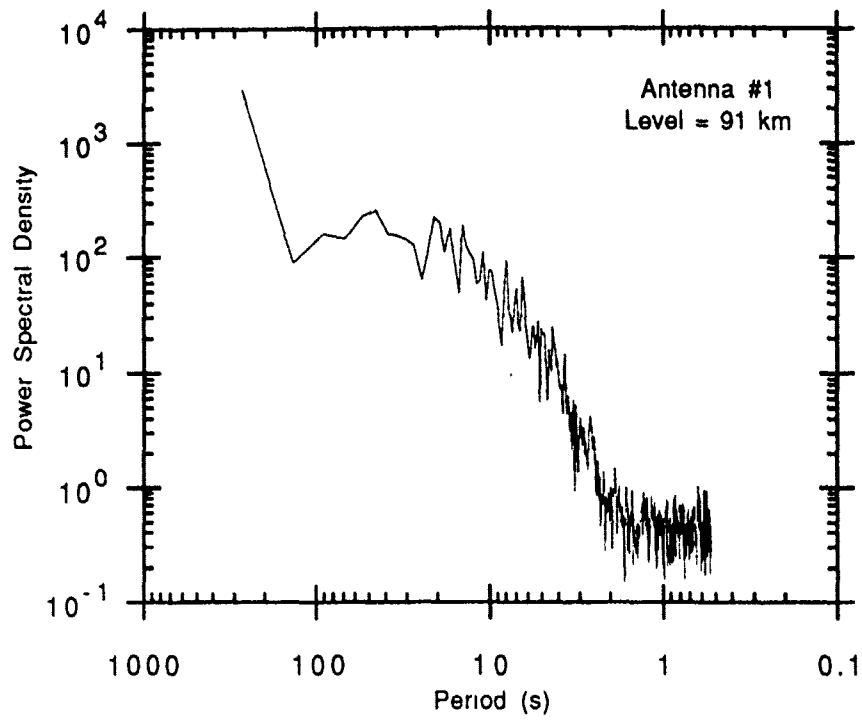


Figure 5.10 (f)

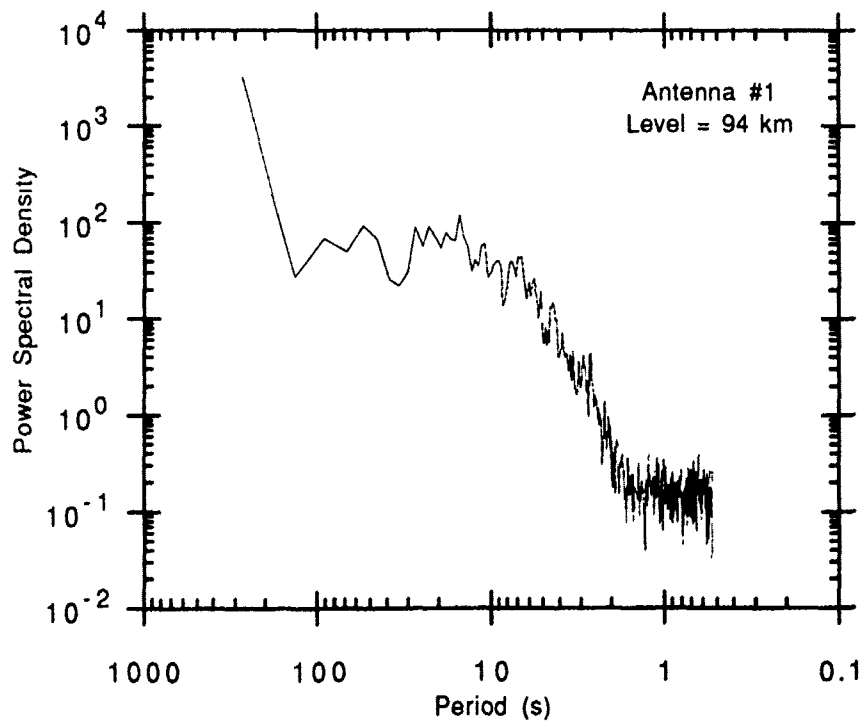


Figure 5.10 (g)

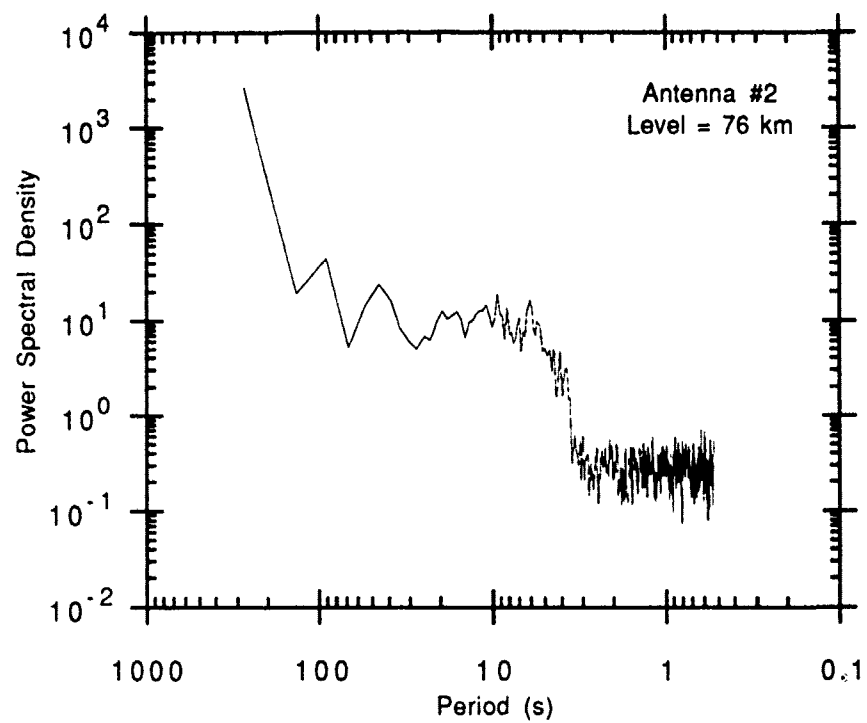


Figure 5.11(a)

Figure 5.11 Power spectral density for antenna #2 for (a) 76 km, (b) 79 km, (c) 82 km, (d) 85 km, (e) 88 km, (f) 91 km and (g) 94 km.

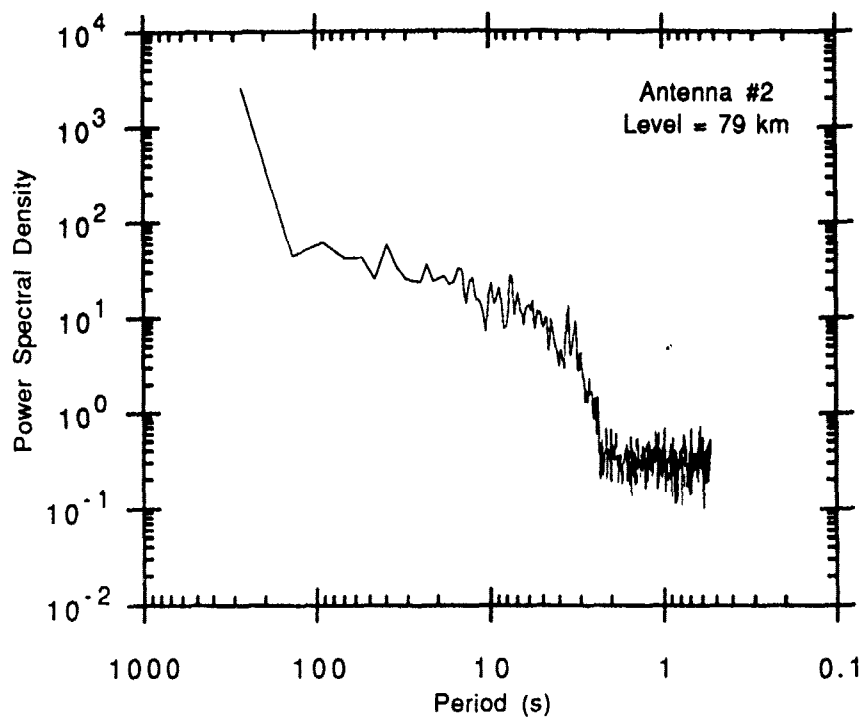


Figure 5.11(b)

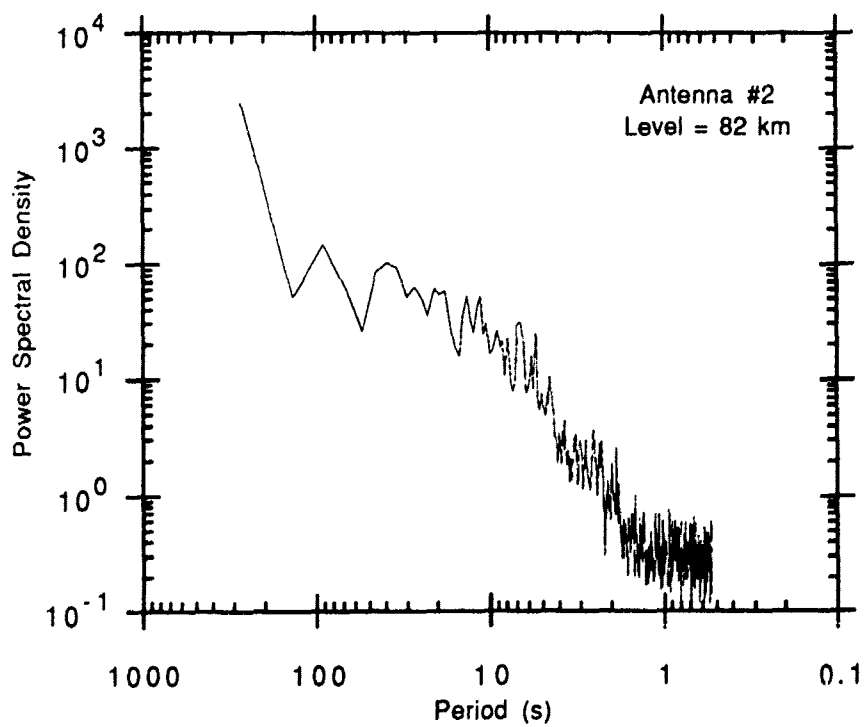


Figure 5.11 (c)

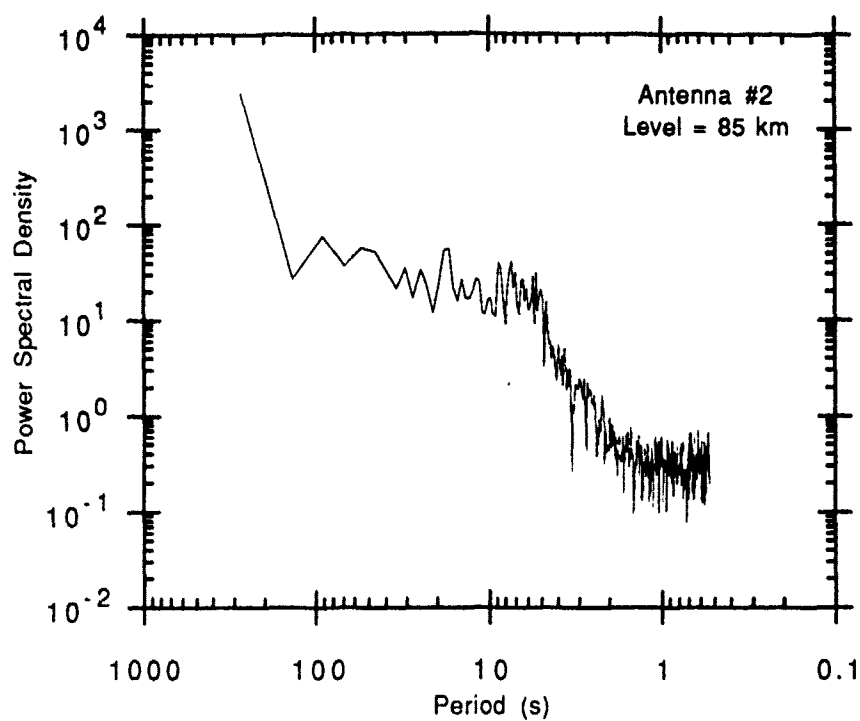


Figure 5.11 (d)

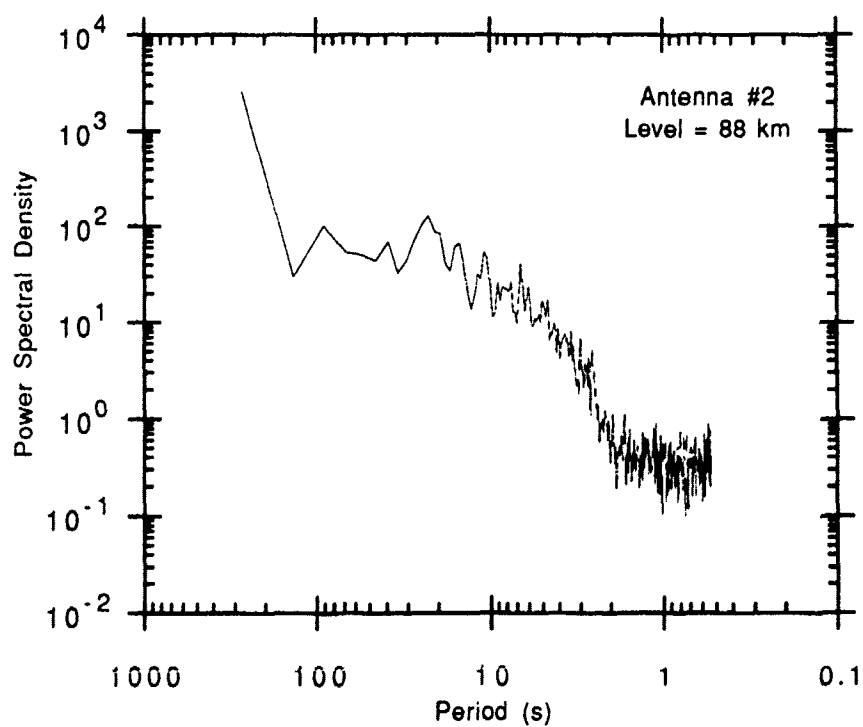


Figure 5.11 (e)

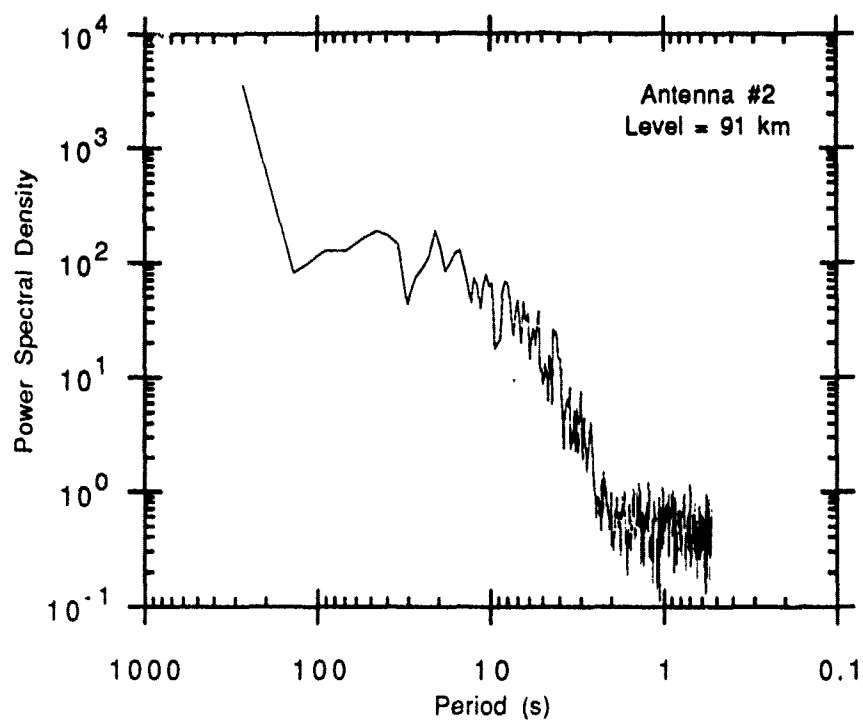


Figure 5.11 (f)

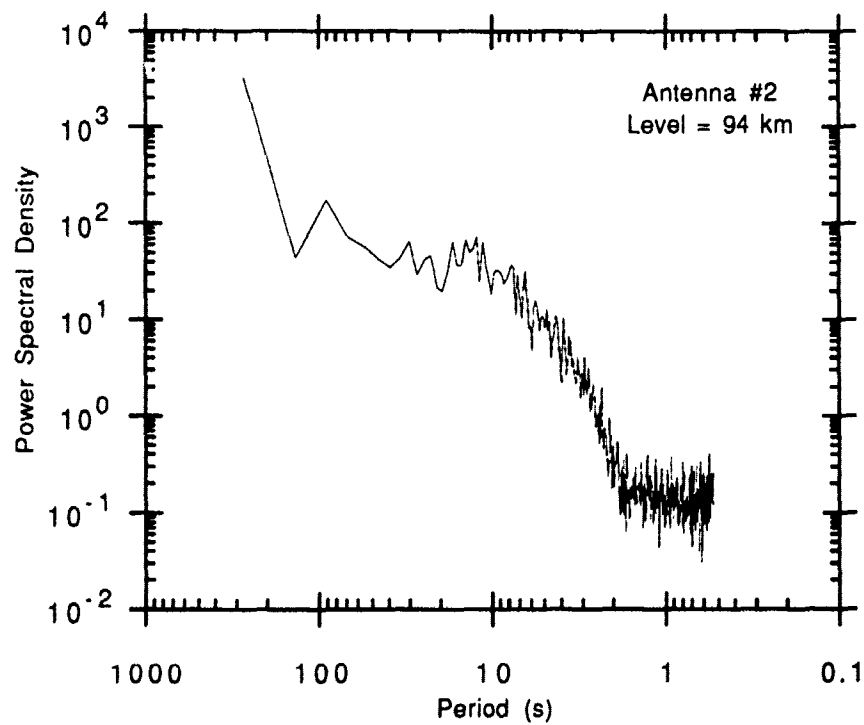


Figure 5.11 (g)

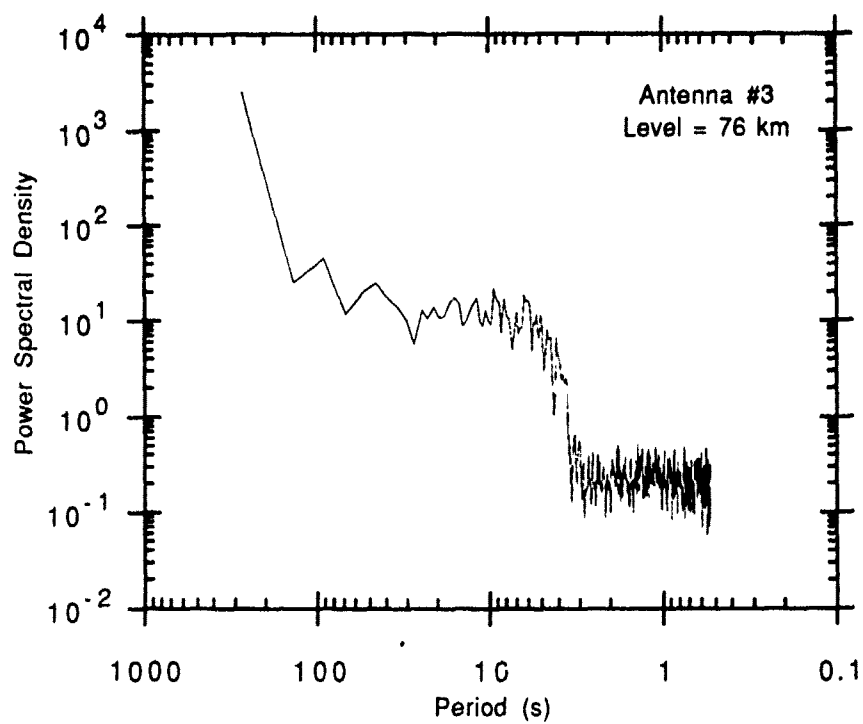


Figure 5.12(a)

Figure 5.12 Power spectral density for antenna #3 for (a) 76 km, (b) 79 km, (c) 82 km, (d) 85 km, (e) 88 km, (f) 91 km and (g) 94 km.

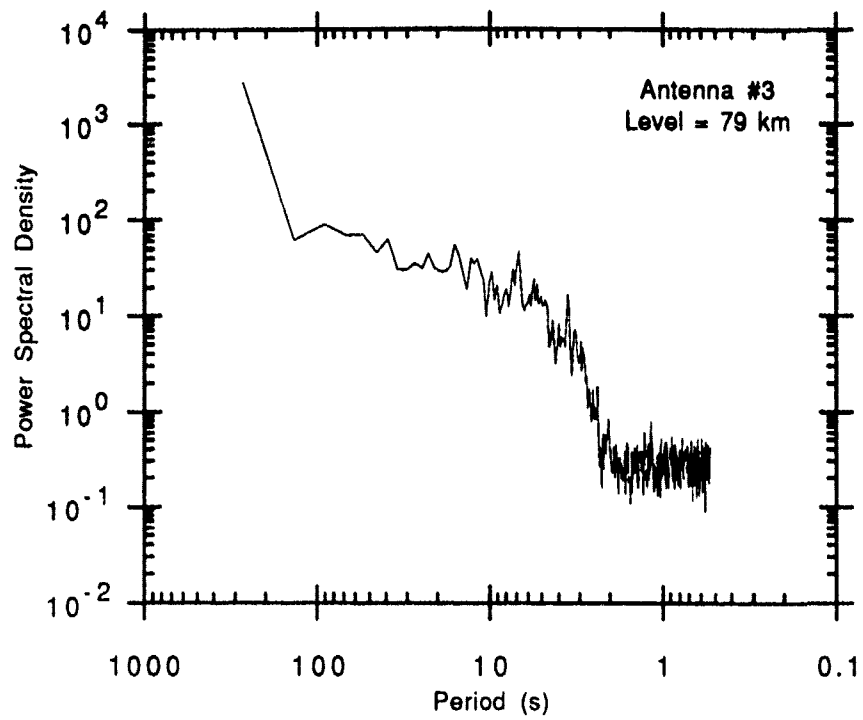


Figure 5.12(b)

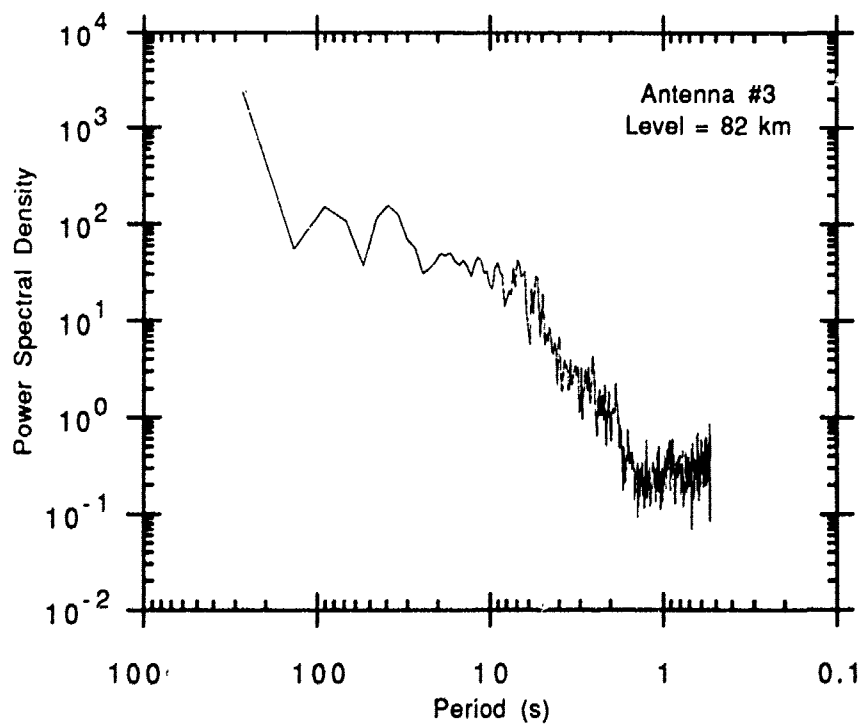


Figure 5.12 (c)

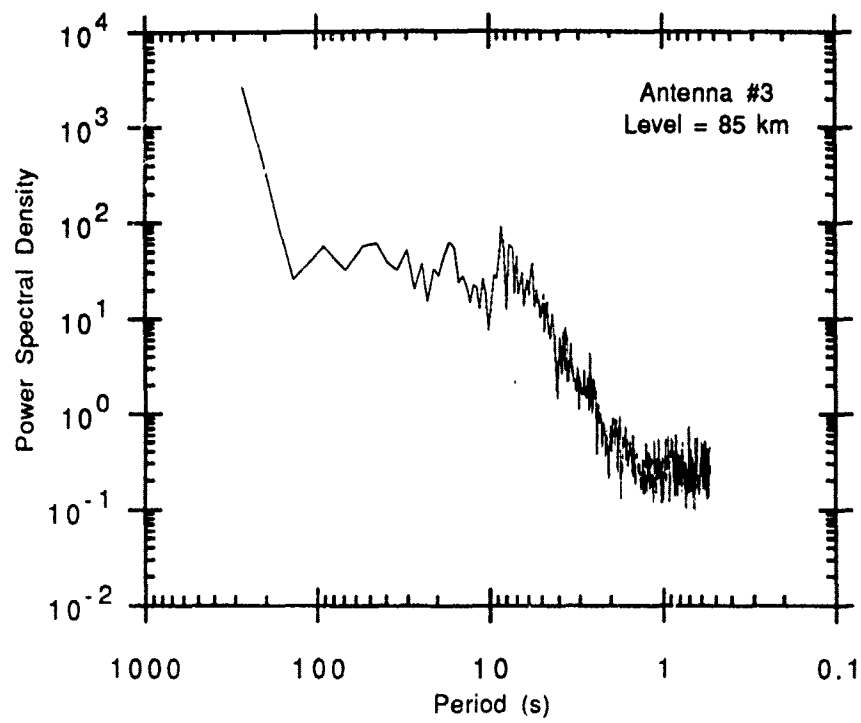


Figure 5.12 (d)

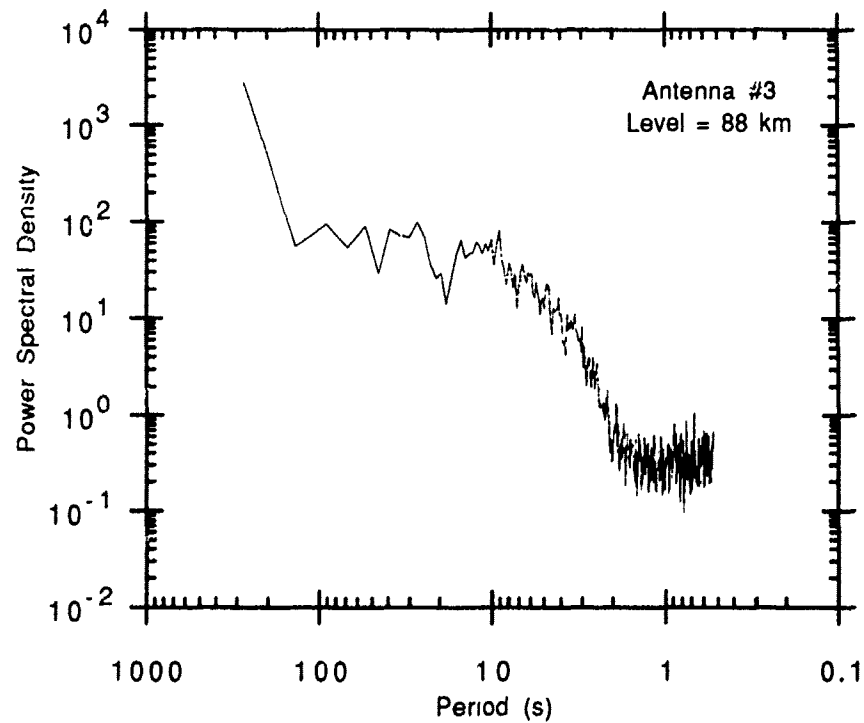


Figure 5.12 (e)

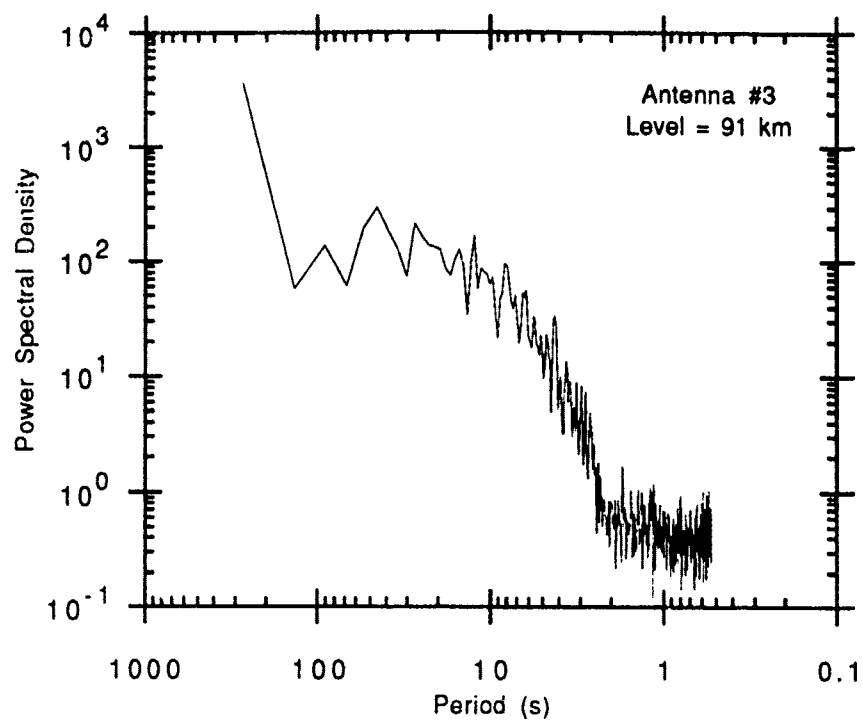


Figure 5.12 (f)

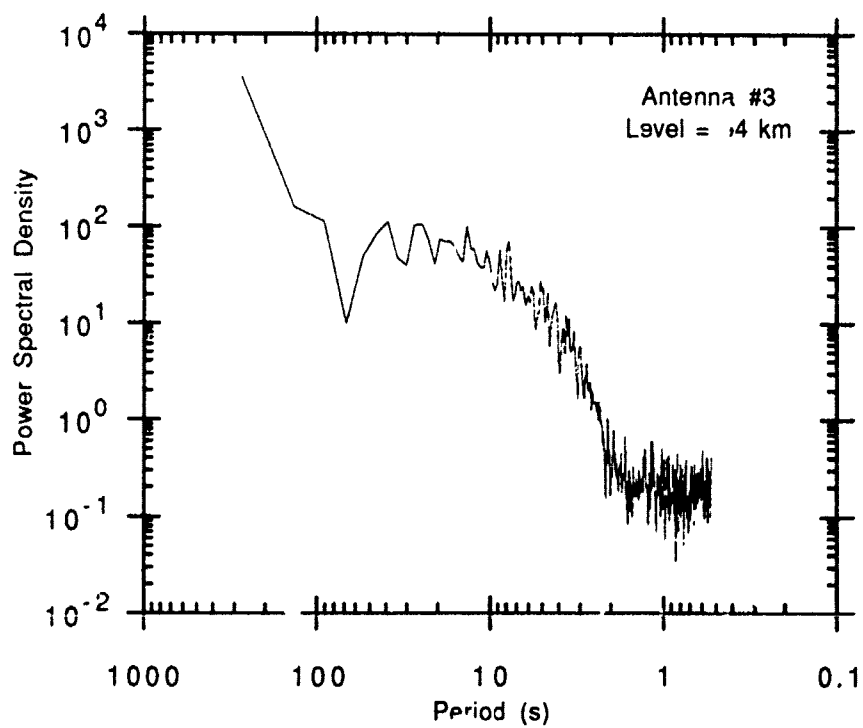


Figure 5.12 (g)

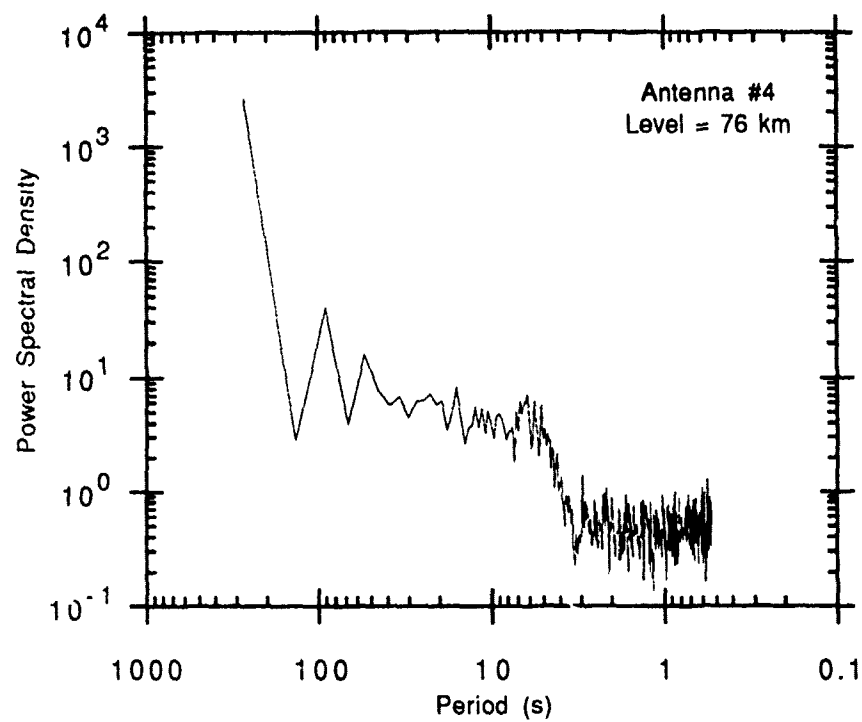


Figure 5.13(a)

Figure 5.13 Power spectral density for antenna #4 for (a) 76 km, (b) 79 km, (c) 82 km, (d) 85 km, (e) 88 km, (f) 91 km and (g) 94 km.

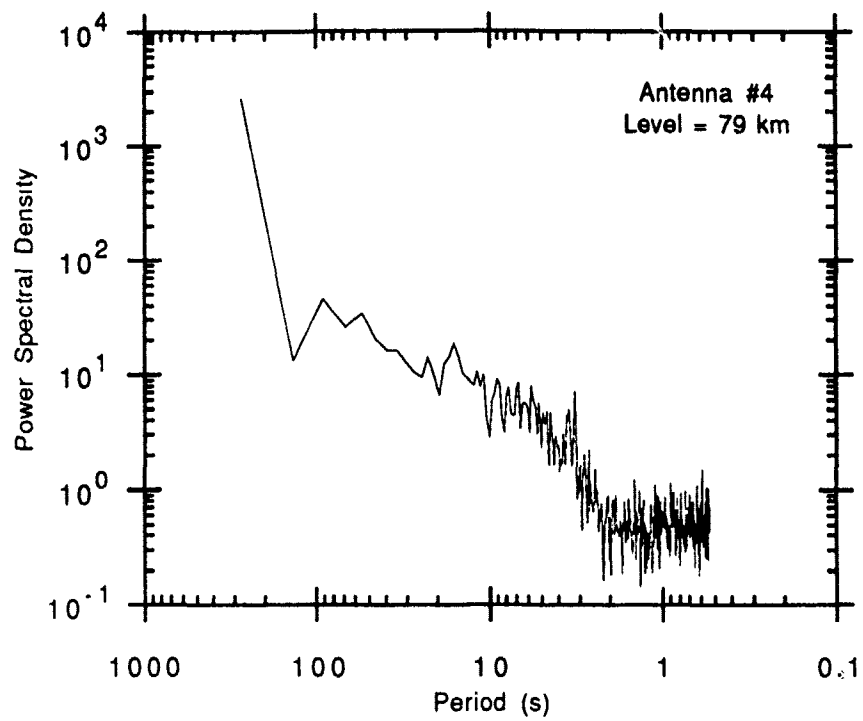


Figure 5.13(b)

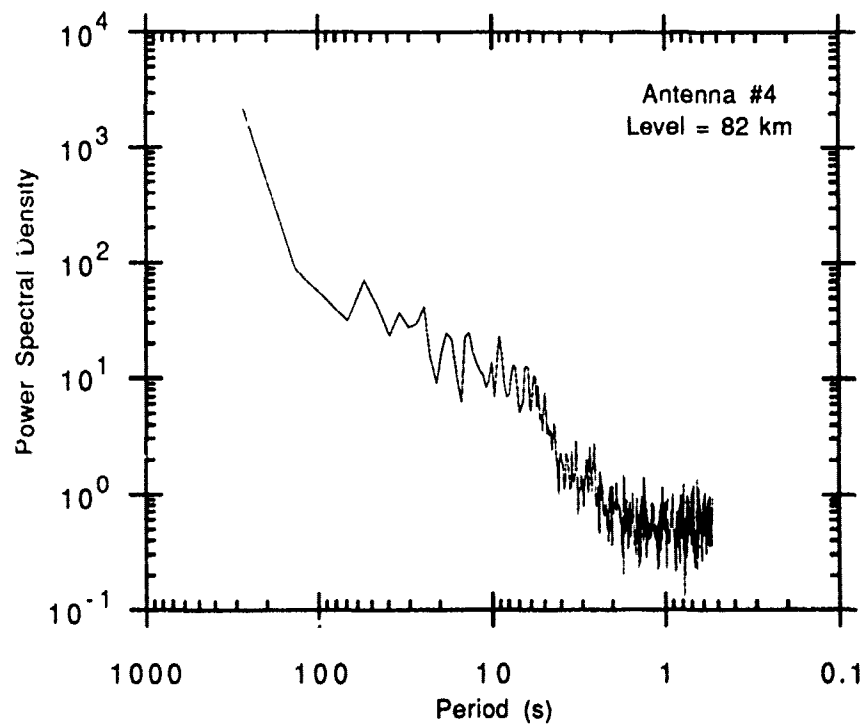


Figure 5.13 (c)

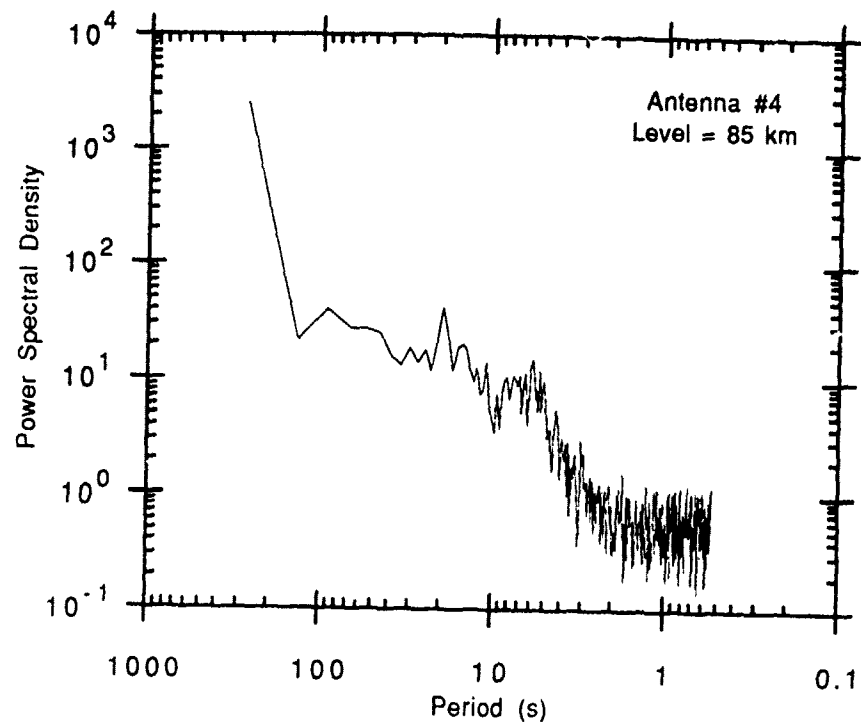


Figure 5.13 (d)

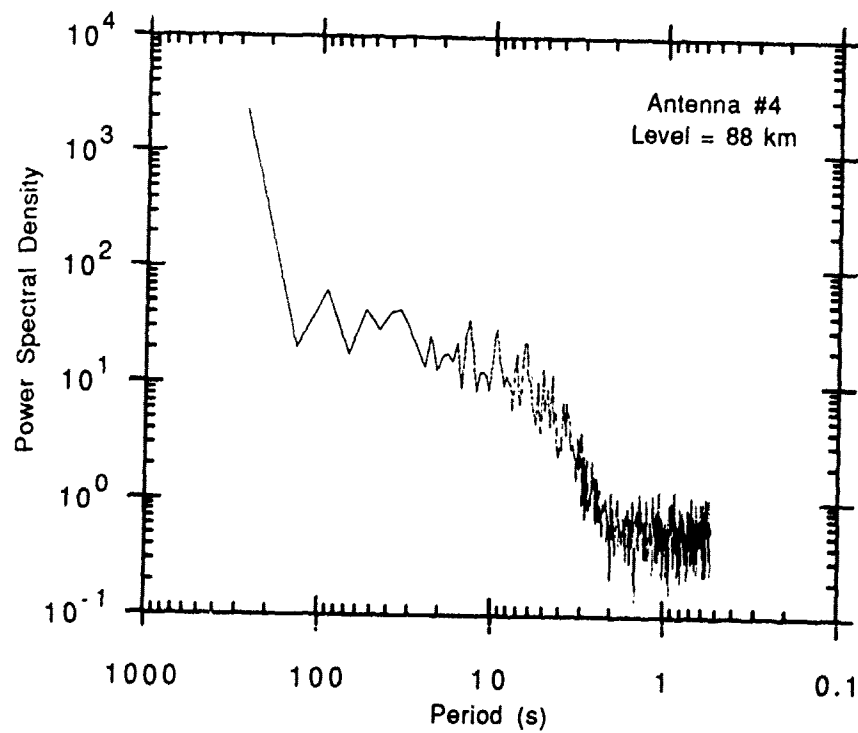


Figure 5.13 (c)

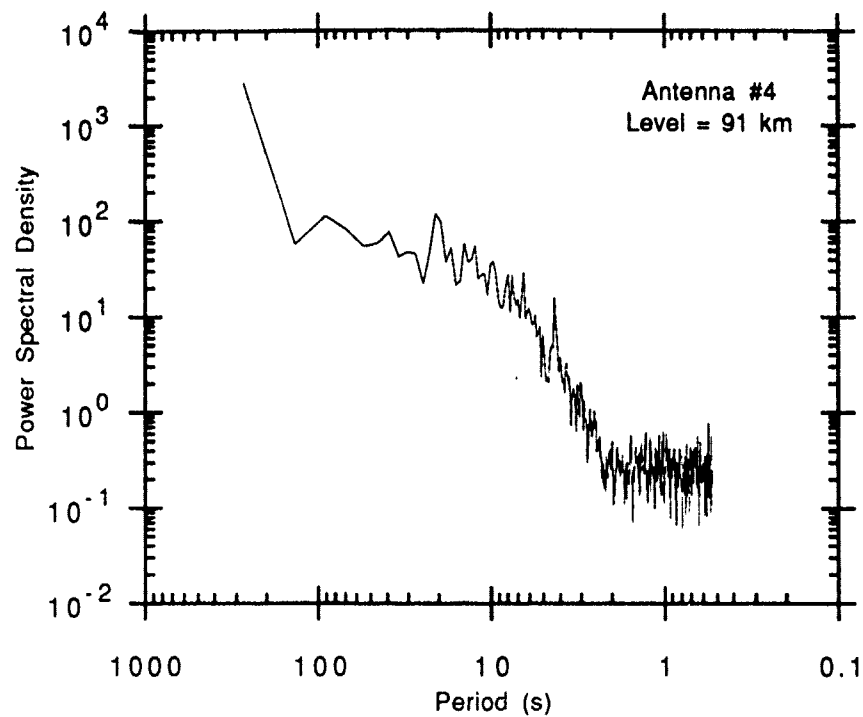


Figure 5.13 (f)

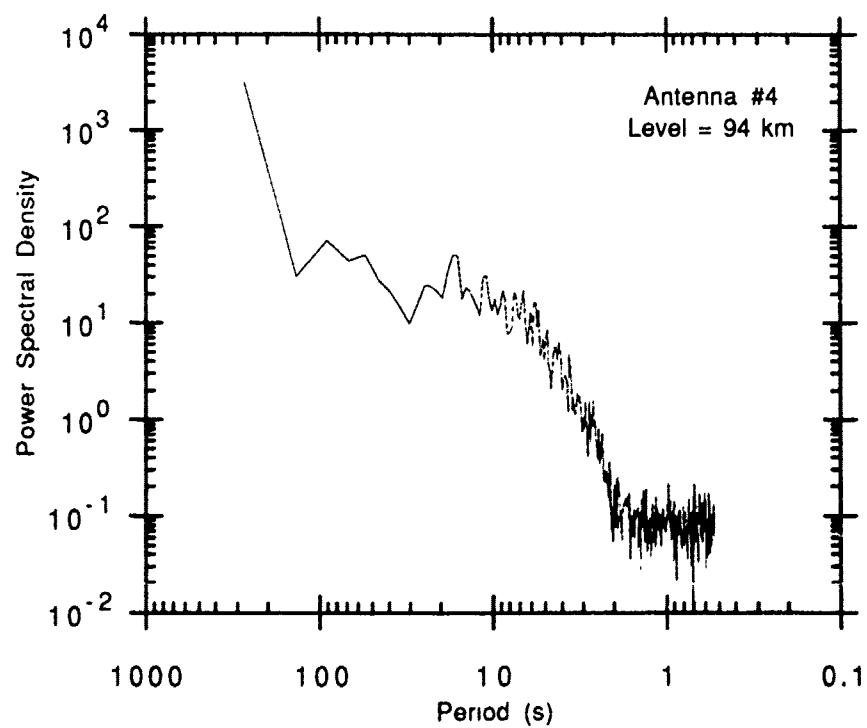


Figure 5.13 (g)

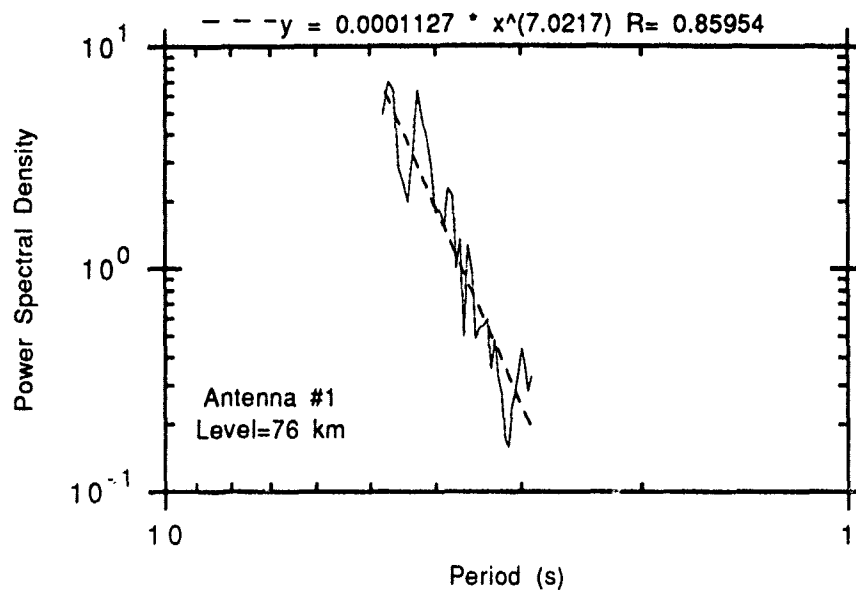


Figure 5.14 (a)

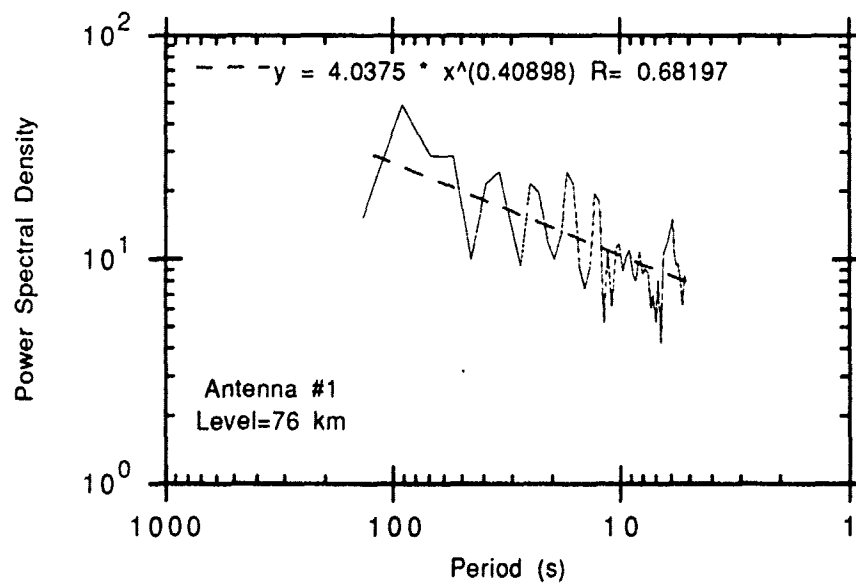


Figure 5.14(b)

Figure 5.14 Power law fits for the power spectra from antenna #1 for (a) 76 km, (b) 76 km, (c) 79 km, (d) 79 km, (e) 82 km, (f) 82 km, (g) 85 km, (h) 85 km, (i) 88 km, (j) 88 km, (k) 91 km and (l) 94 km.

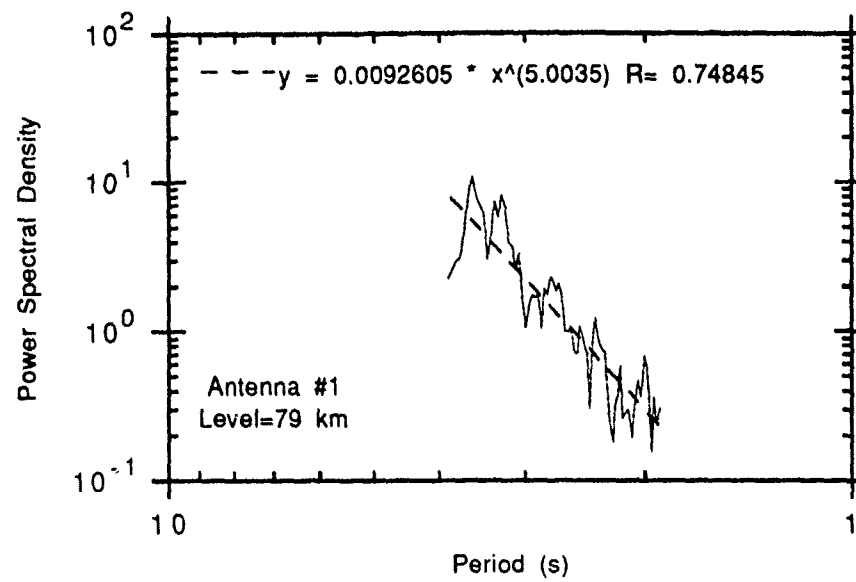


Figure 5.14 (c)

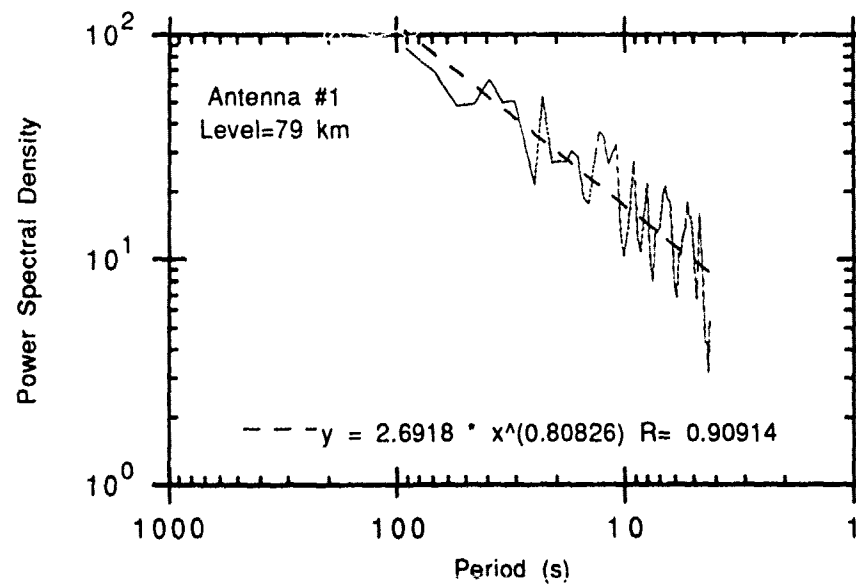


Figure 5.14 (d)

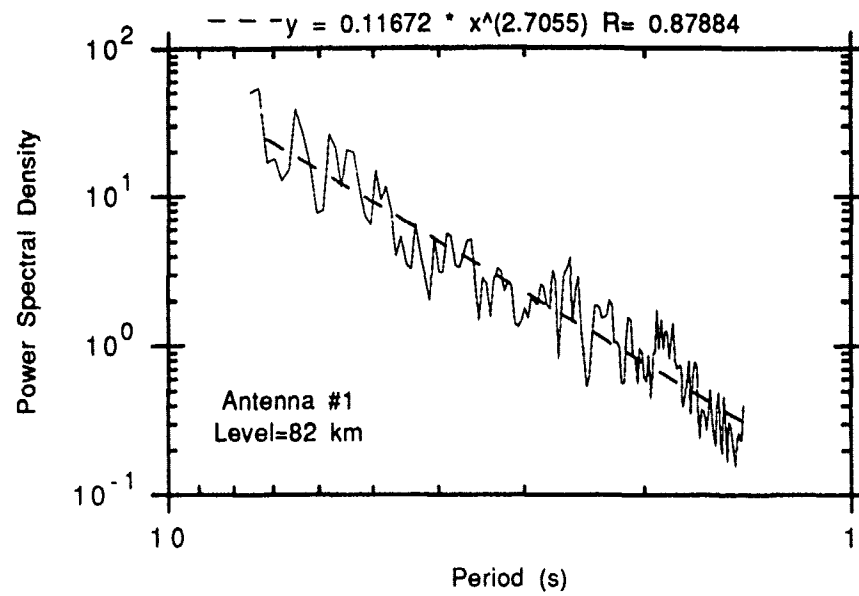


Figure 5.14 (c)

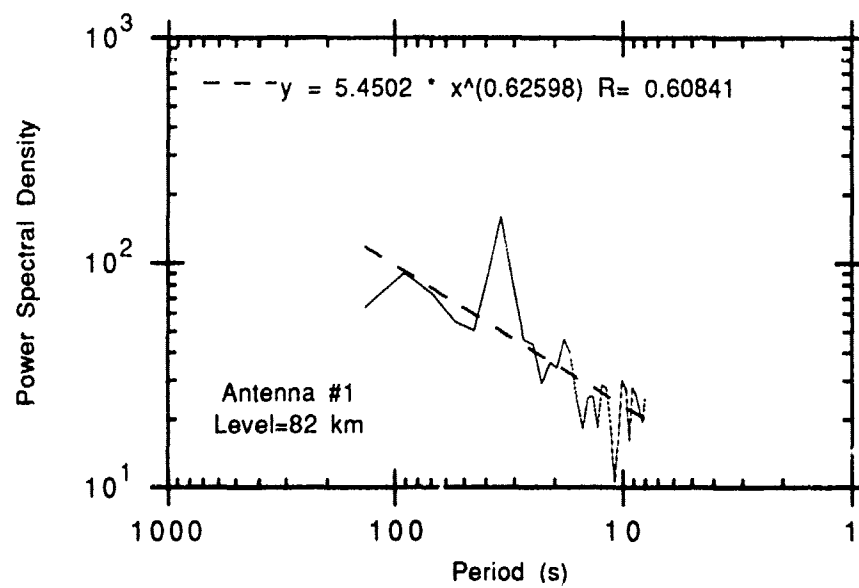


Figure 5.14 (f)

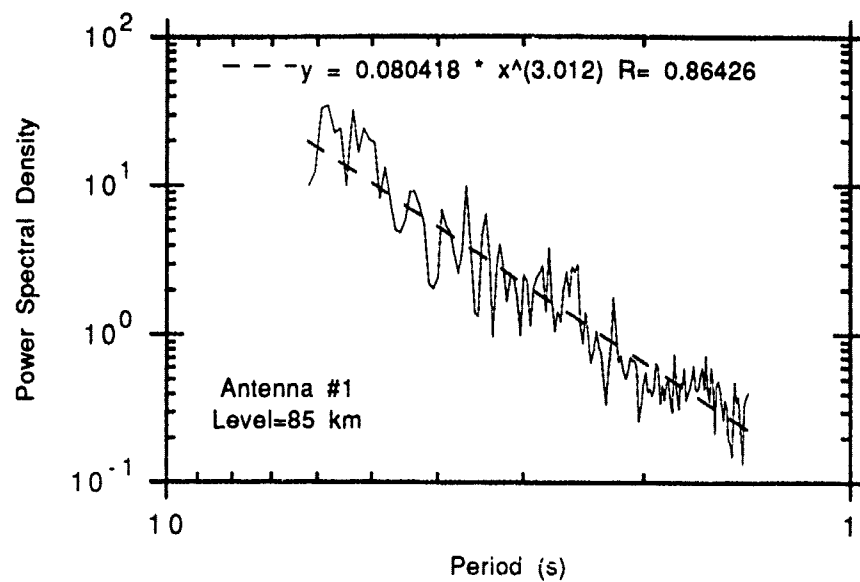


Figure 5.14 (g)

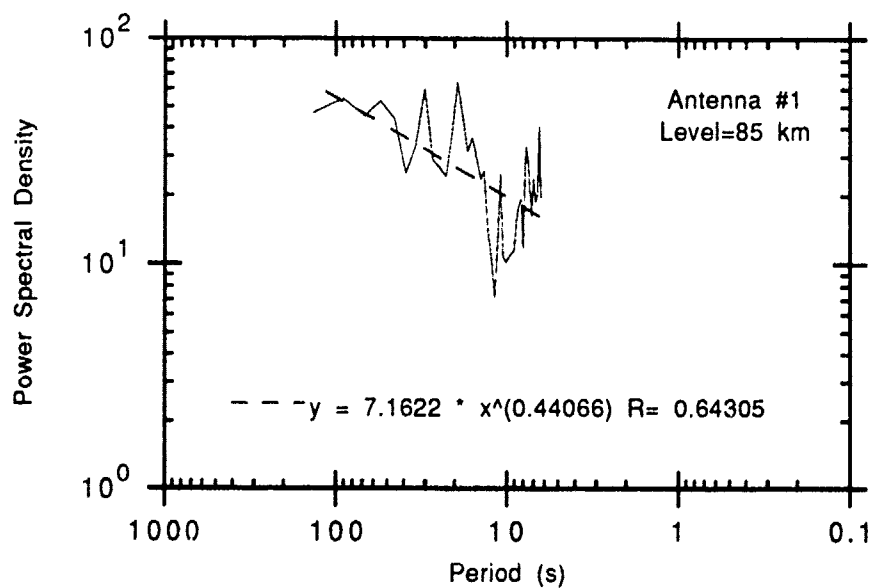


Figure 5.14 (h)

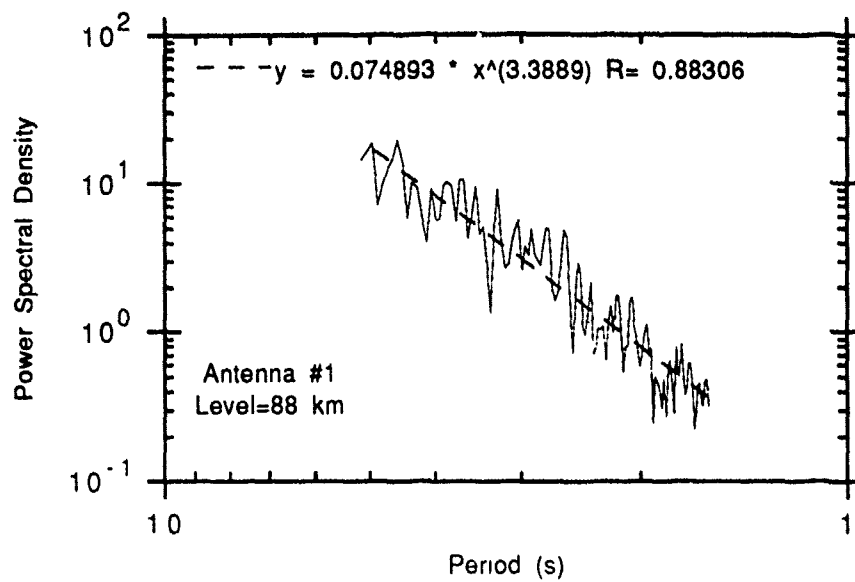


Figure 5.14 (i)

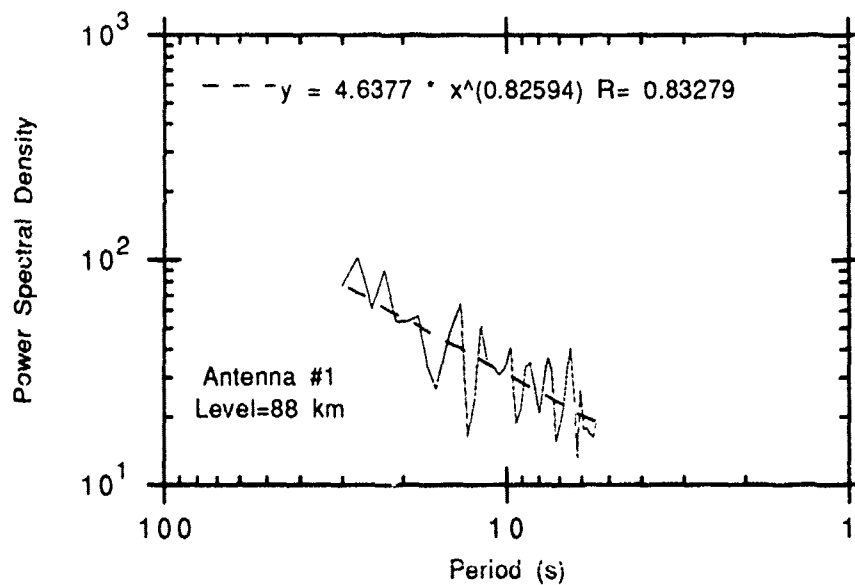


Figure 5.14 (j)

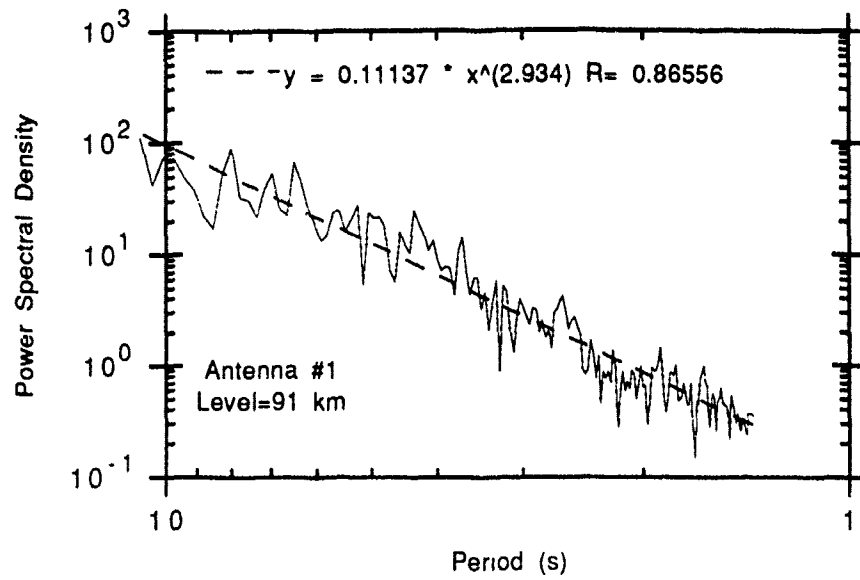


Figure 5.14 (k)

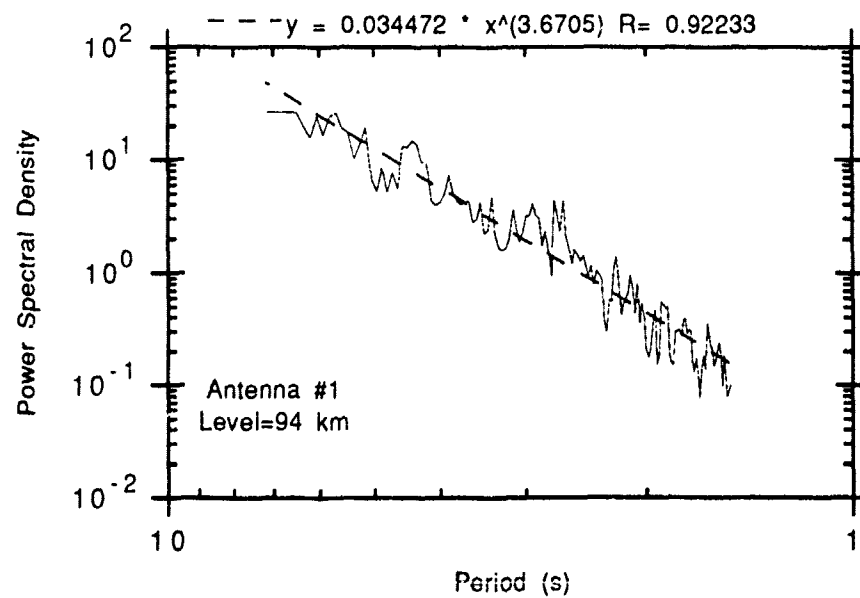


Figure 5.14 (l)

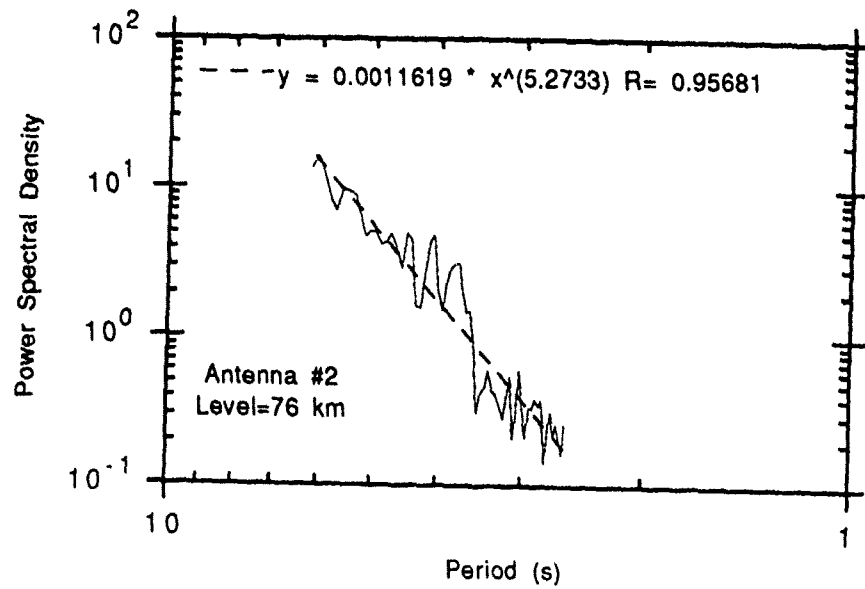


Figure 5.15 (a)

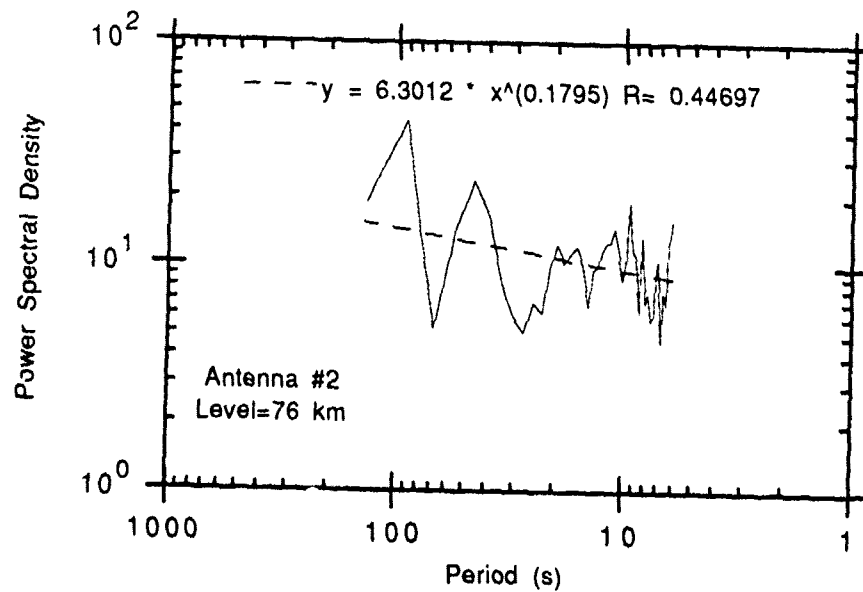


Figure 5.15(b)

Figure 5.15 Power law fits for the power spectra from antenna #2 for (a) 76 km, (b) 76 km, (c) 79 km, (d) 79 km, (e) 82 km, (f) 82 km, (g) 85 km, (h) 85 km, (i) 88 km, (j) 91 km and (k) 94 km..

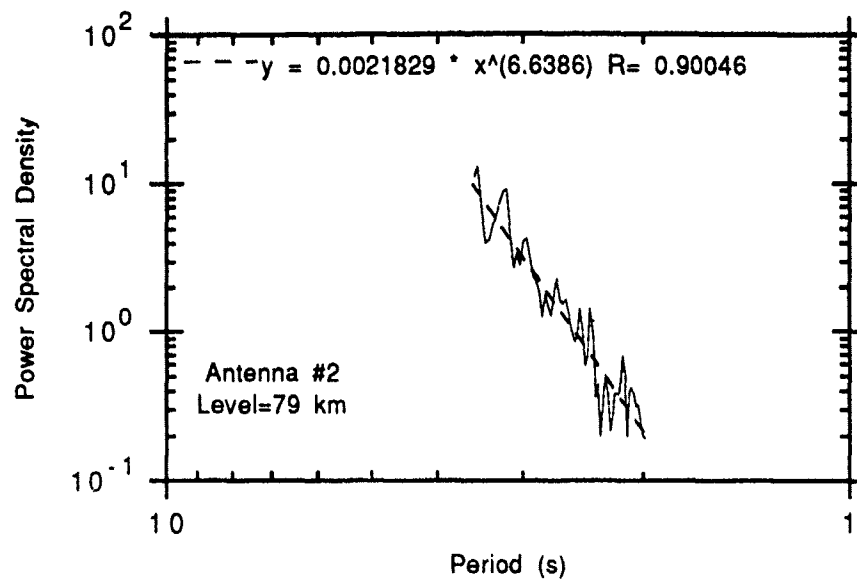


Figure 5.15 (c)

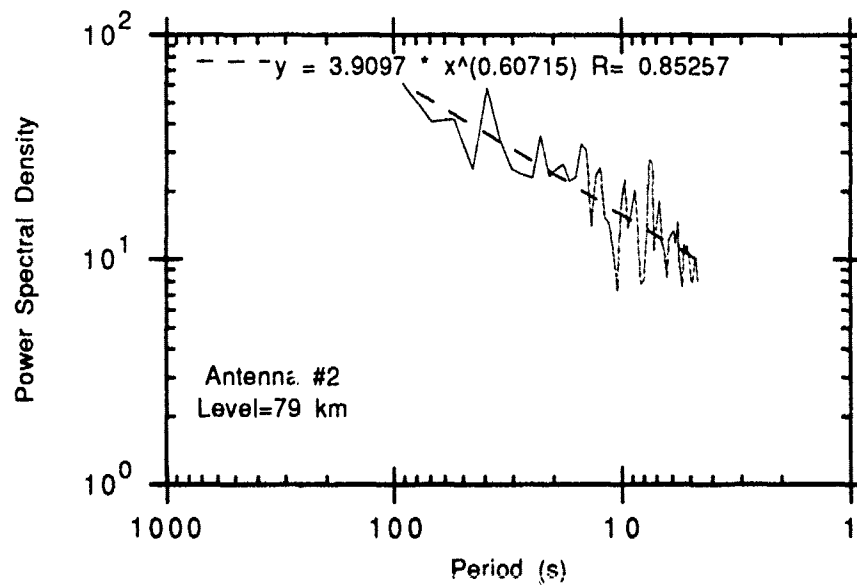


Figure 5.15 (d)

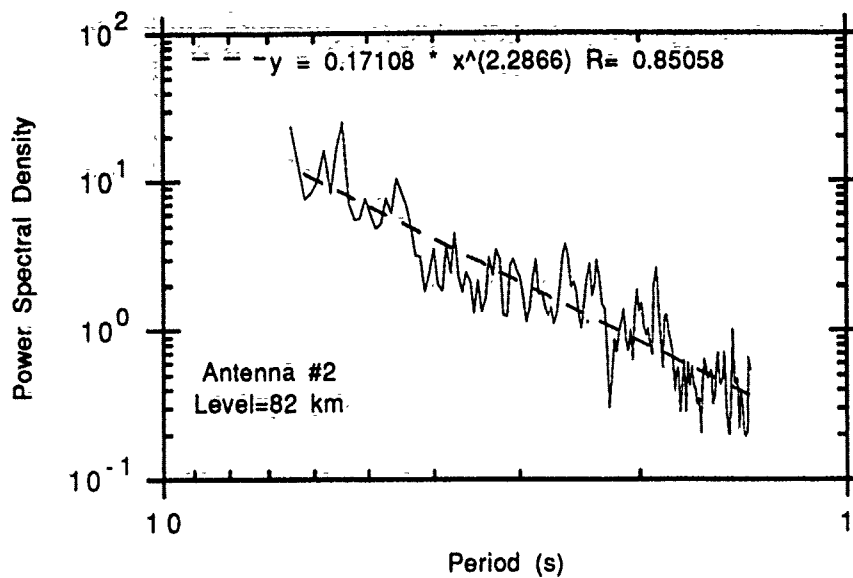


Figure 5.15 (e)

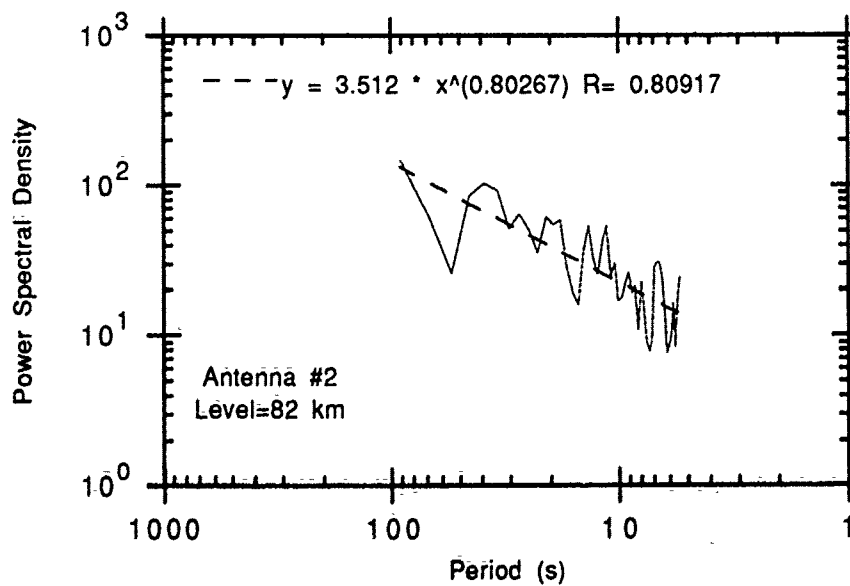


Figure 5.15 (f)

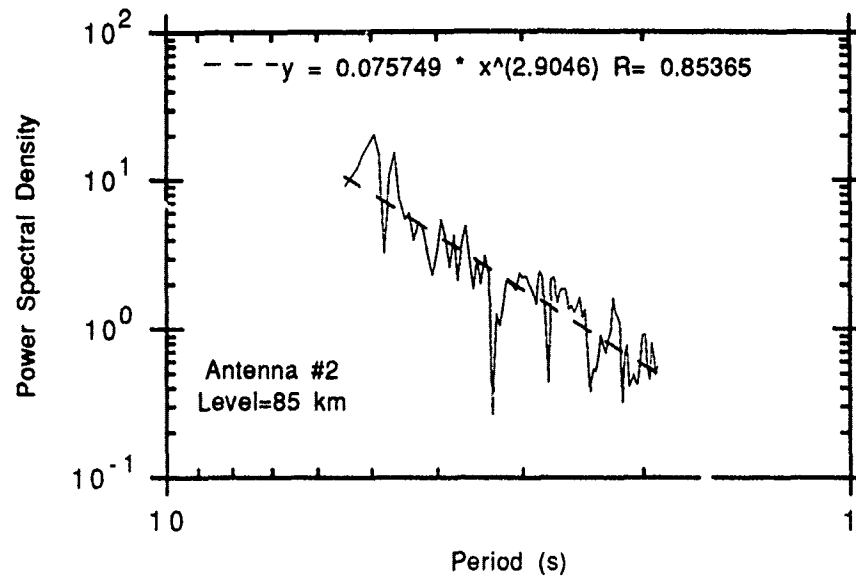


Figure 5.15 (g)

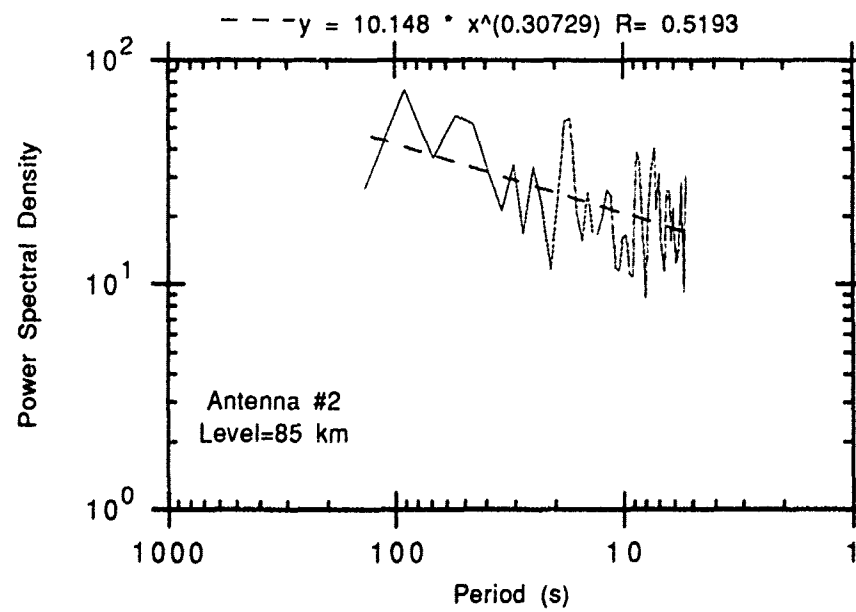


Figure 5.15 (h)

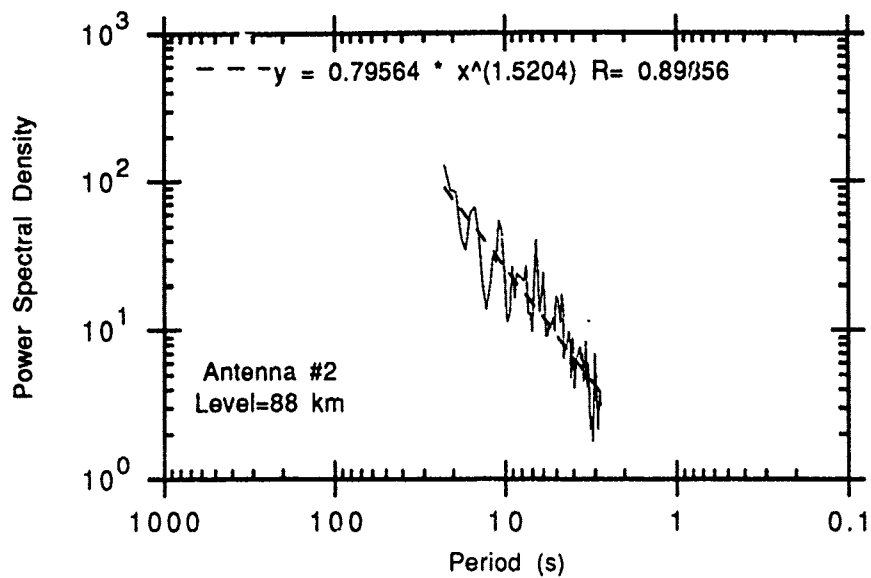


Figure 5.15 (i)

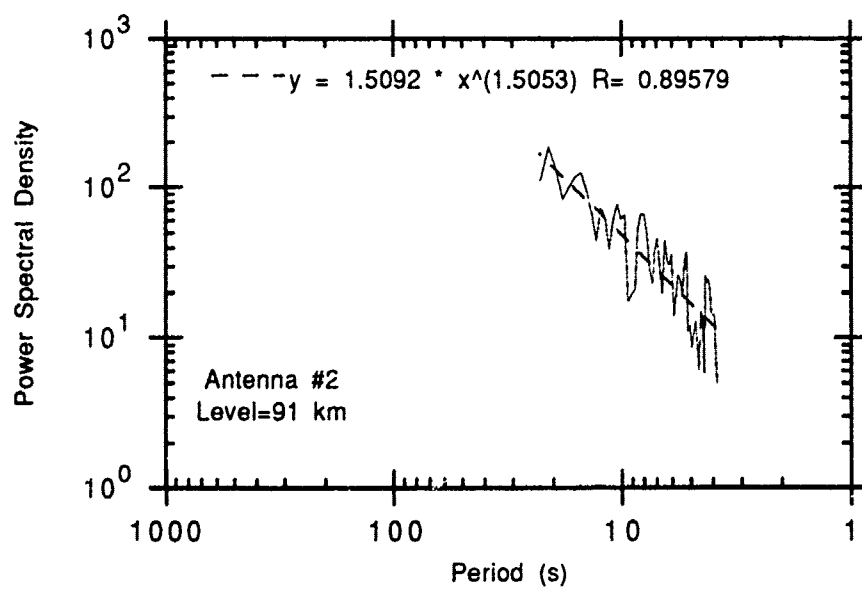


Figure 5.15 (j)

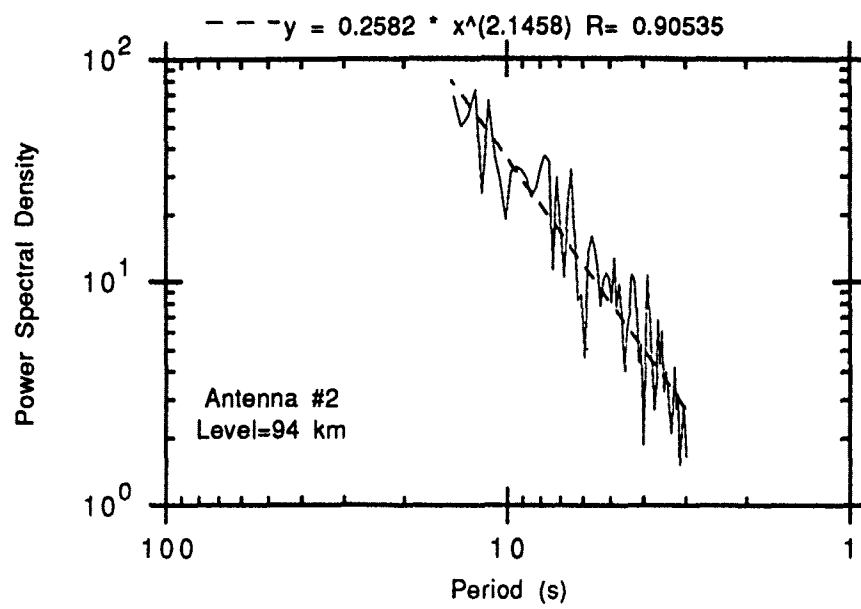


Figure 5.15 (k)

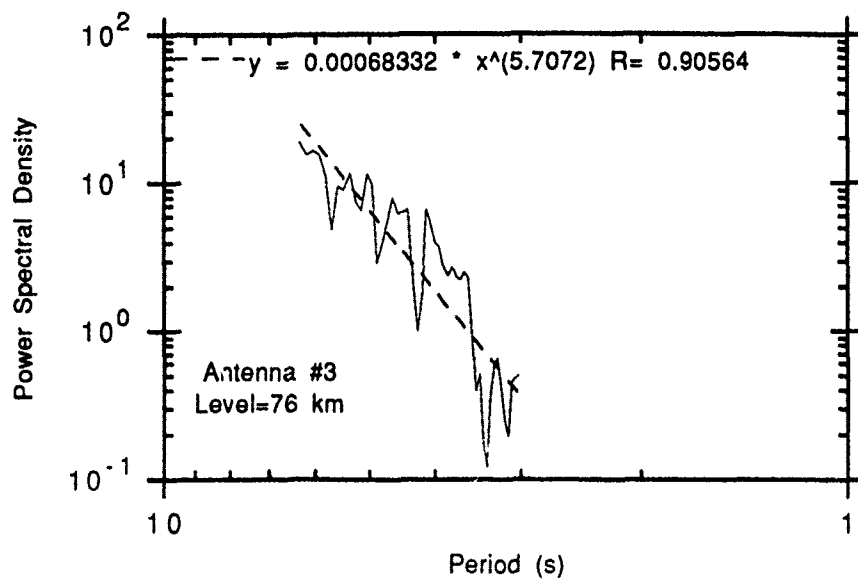


Figure 5.16 (a)

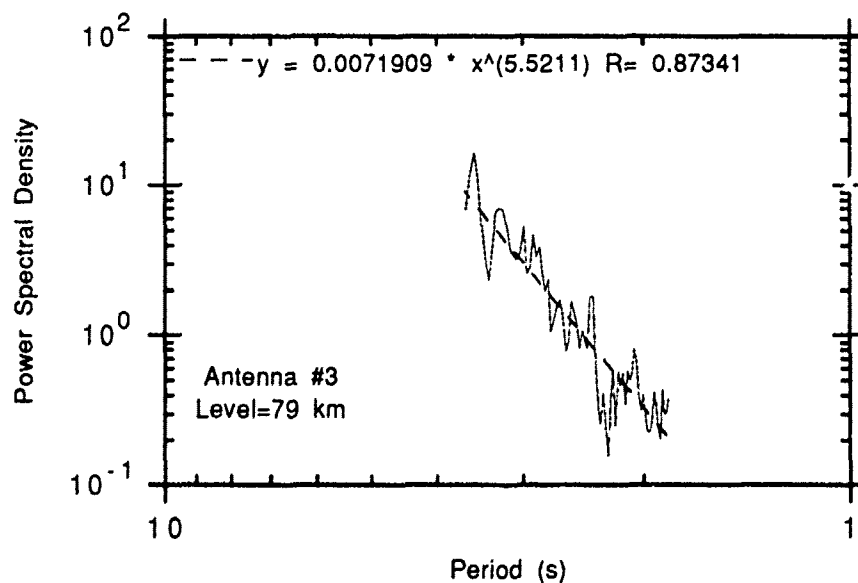


Figure 5.16(b)

Figure 5.16 Power law fits for the power spectra from antenna #3 for (a) 76 km, (b) 79 km, (c) 79 km, (d) 82 km, (e) 82 km, (f) 85 km, (g) 88 km, (h) 91 km, (i) 91 km and (j) 94 km.

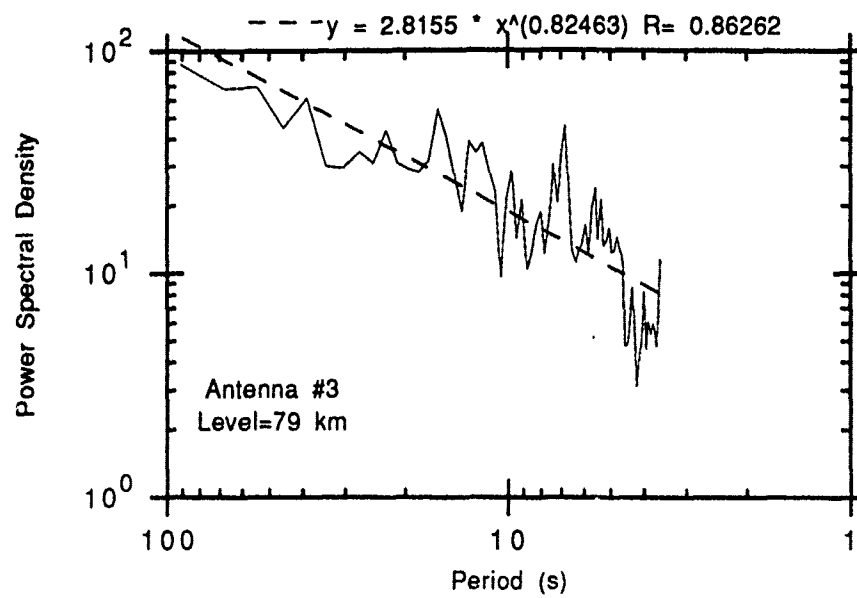


Figure 5.16 (c)

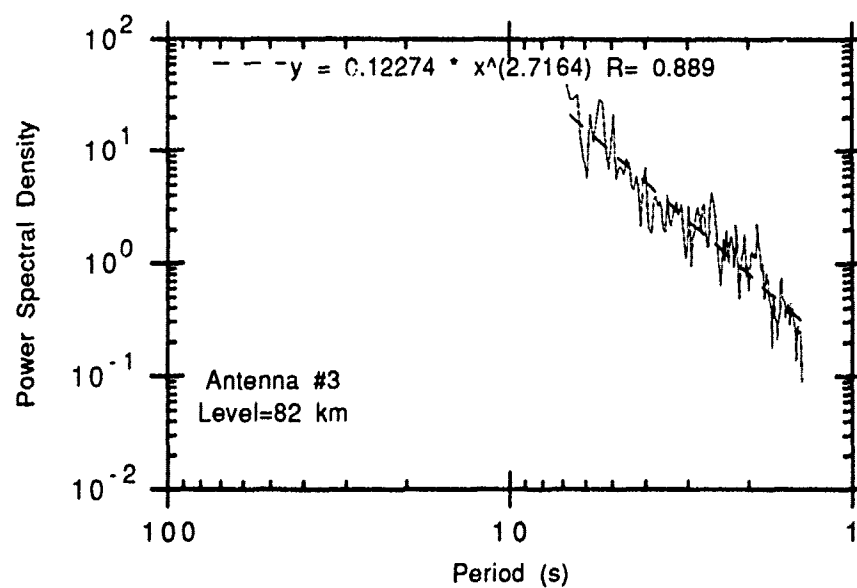


Figure 5.16 (d)

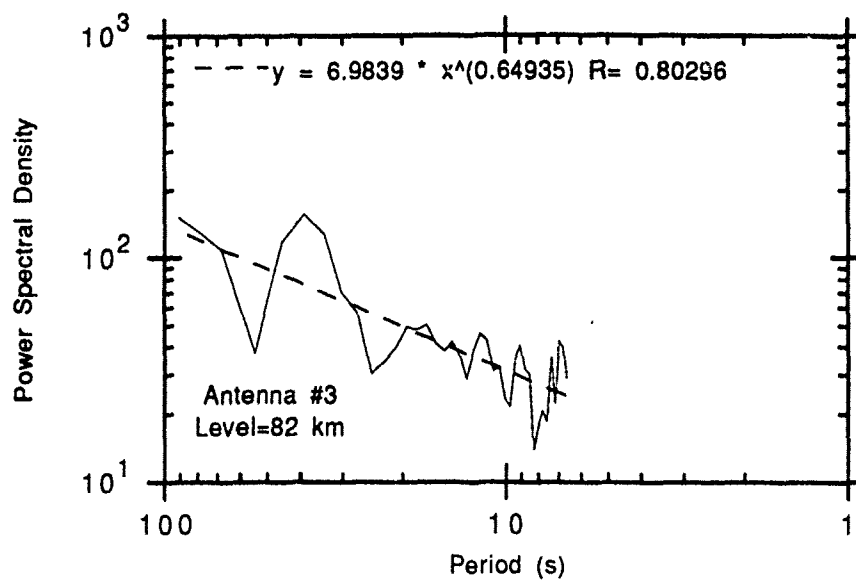


Figure 5.16 (c)

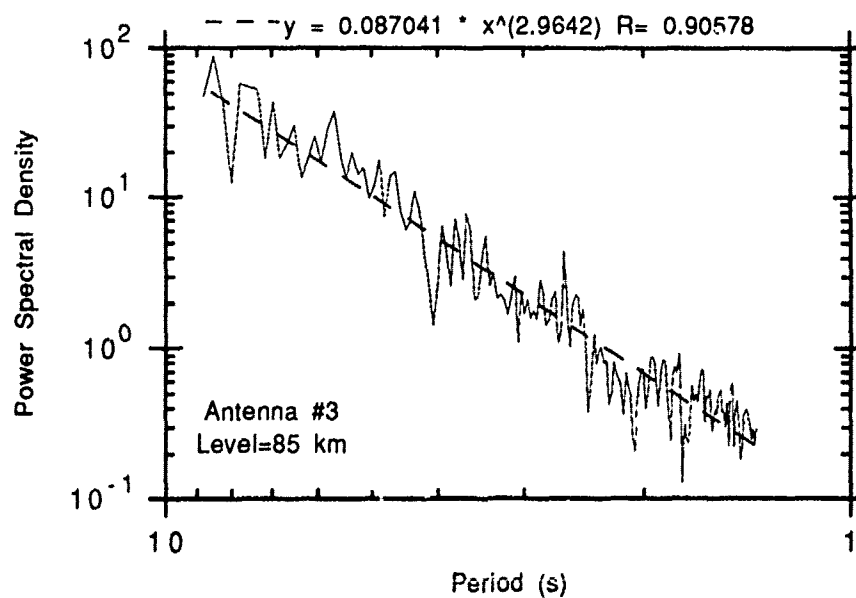


Figure 5.16 (f)

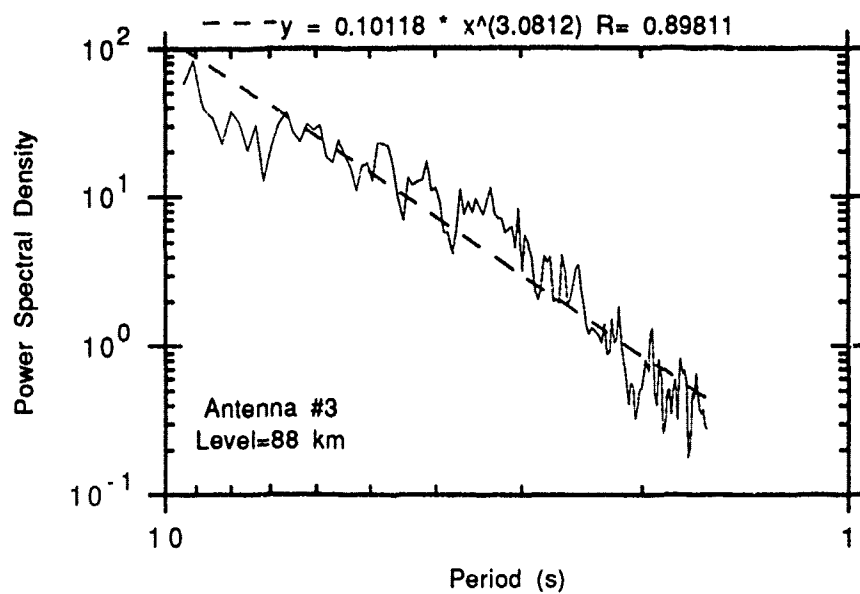


Figure 5.16 (g)

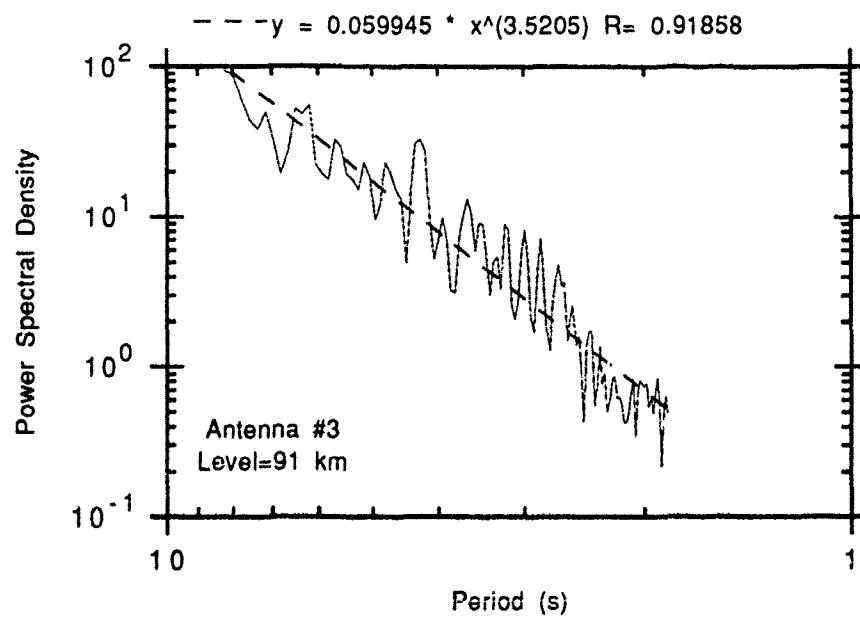


Figure 5.16 (h)

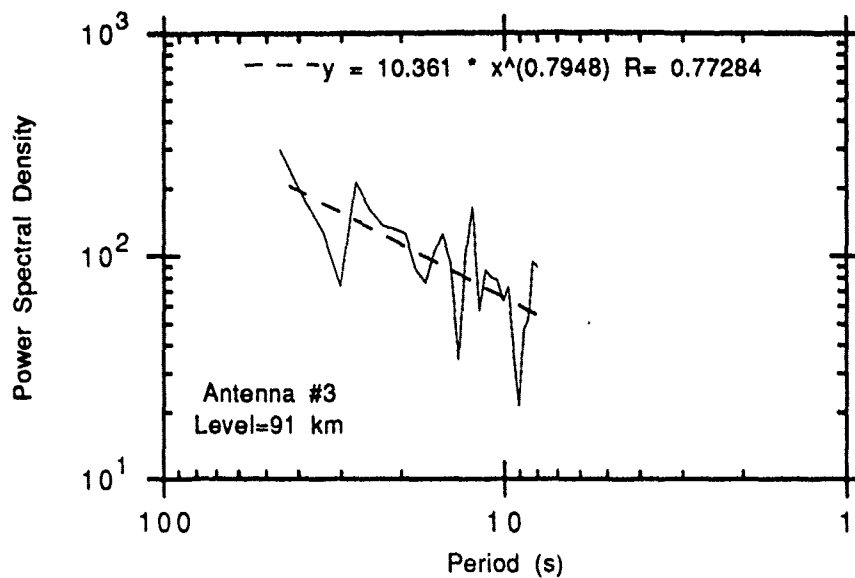


Figure 5.16 (i)

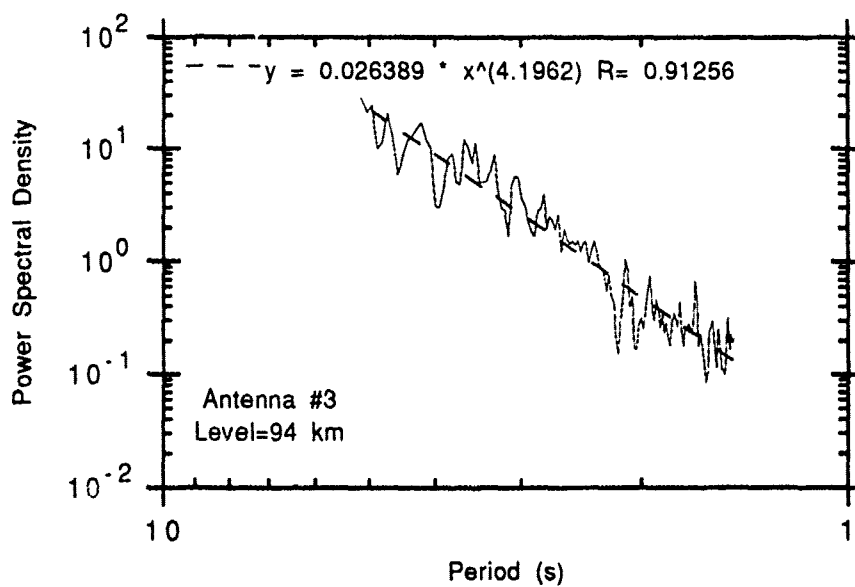


Figure 5.16 (j)

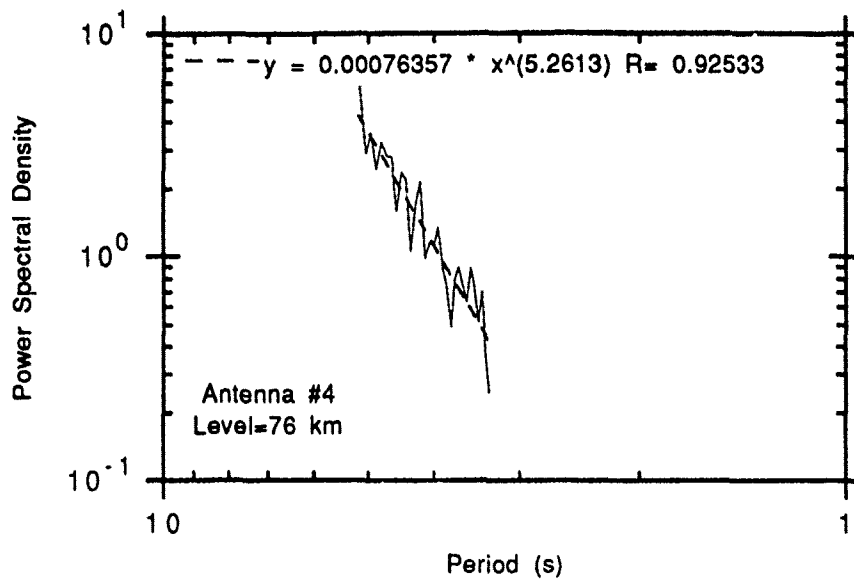


Figure 5.17 (a)

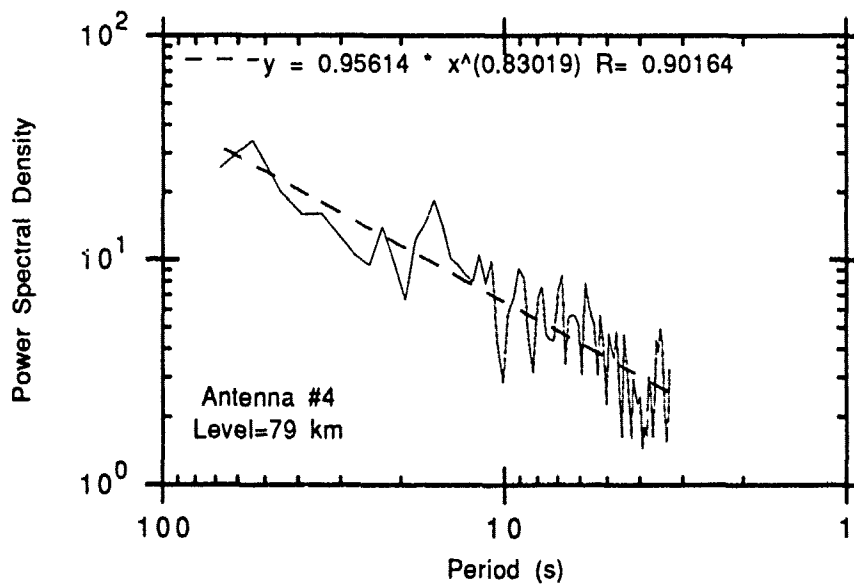


Figure 5.17(b)

Figure 5.17 Power law fits for the power spectra from antenna #4 for (a) 76 km, (b) 79 km, (c) 82 km, (d) 82 km, (e) 85 km, (f) 85 km, (g) 88 km, (h) 88 km, (i) 91 km and (j) 94 km.

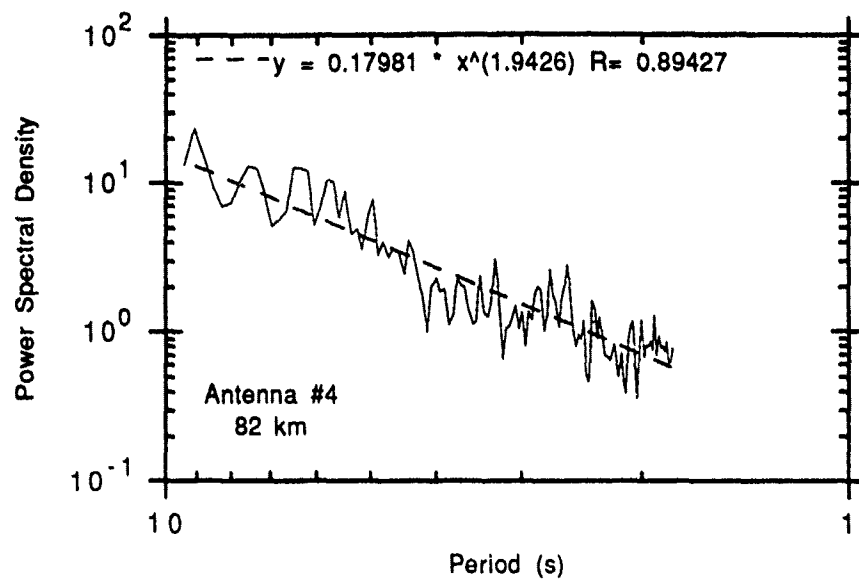


Figure 5.17 (c)

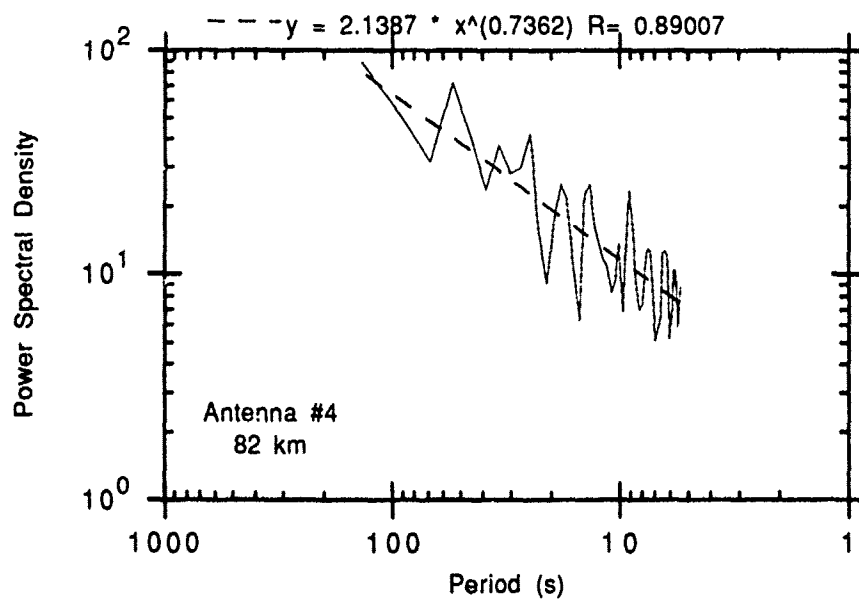


Figure 5.17 (d)

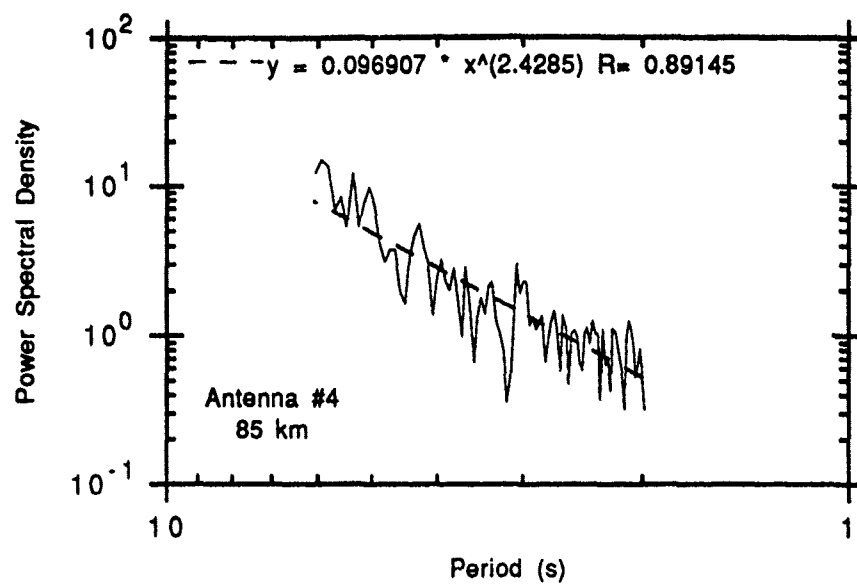


Figure 5.17 (e)

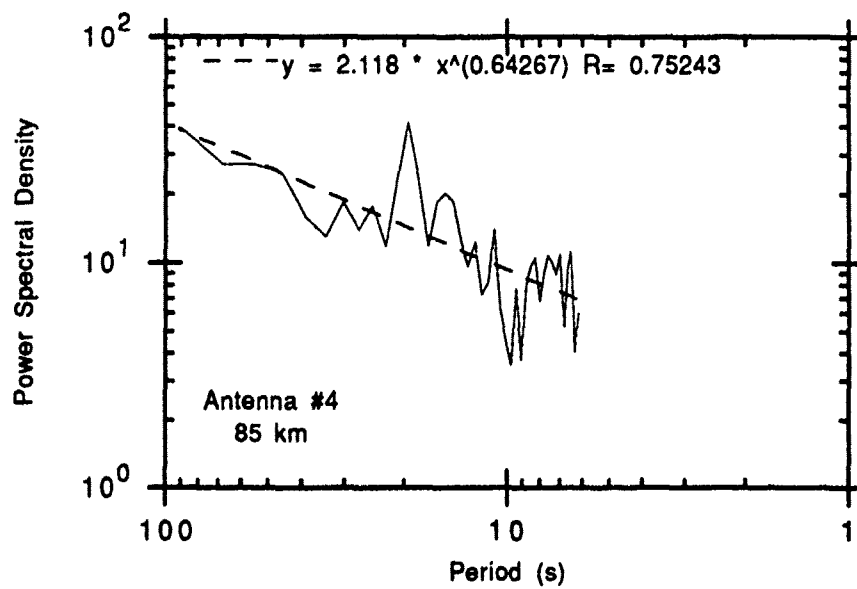


Figure 5.17 (f)

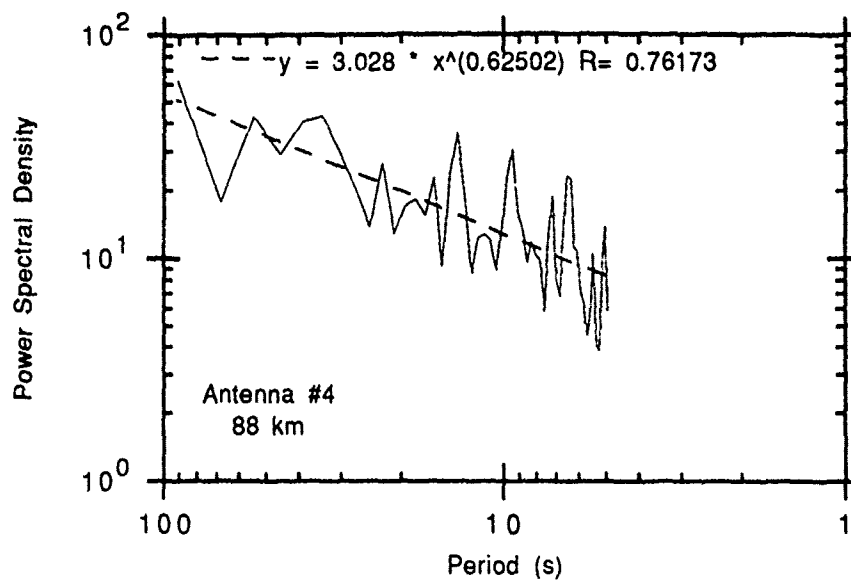


Figure 5.17 (g)

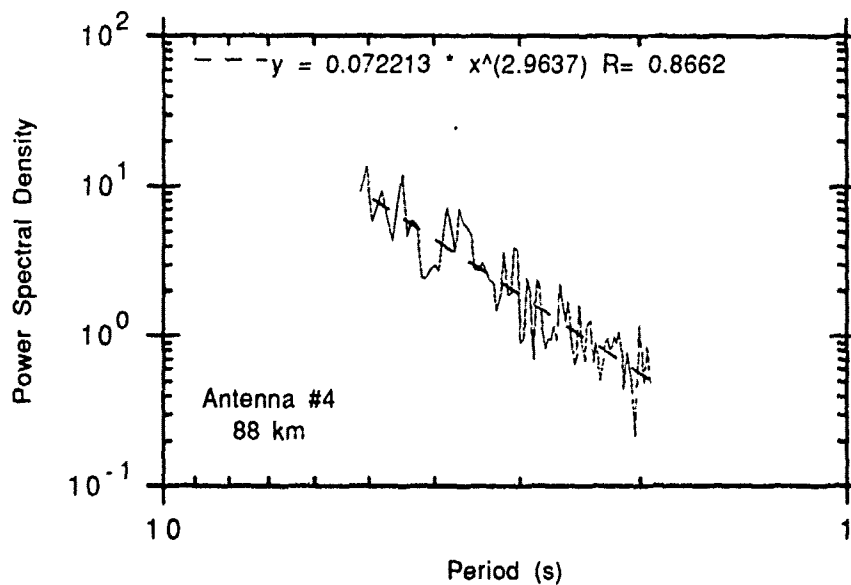


Figure 5.17 (h)

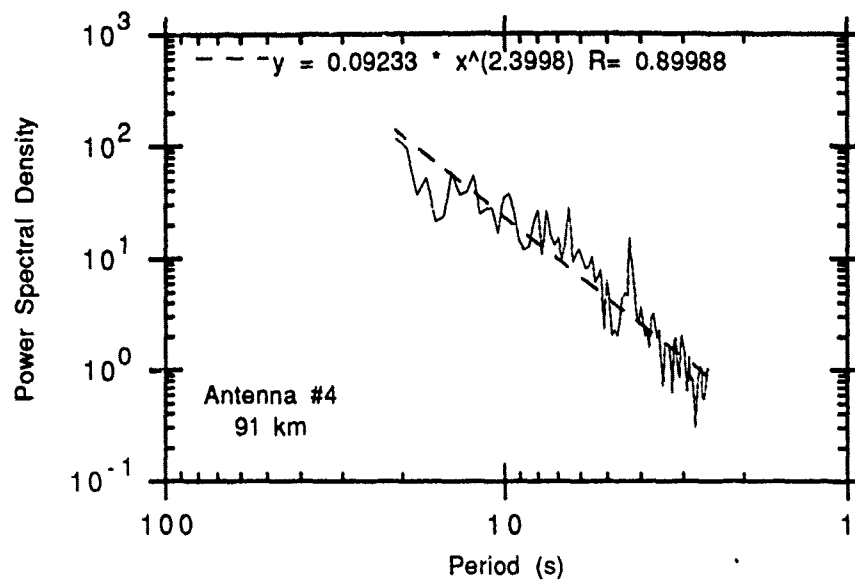


Figure 5.17 (i)

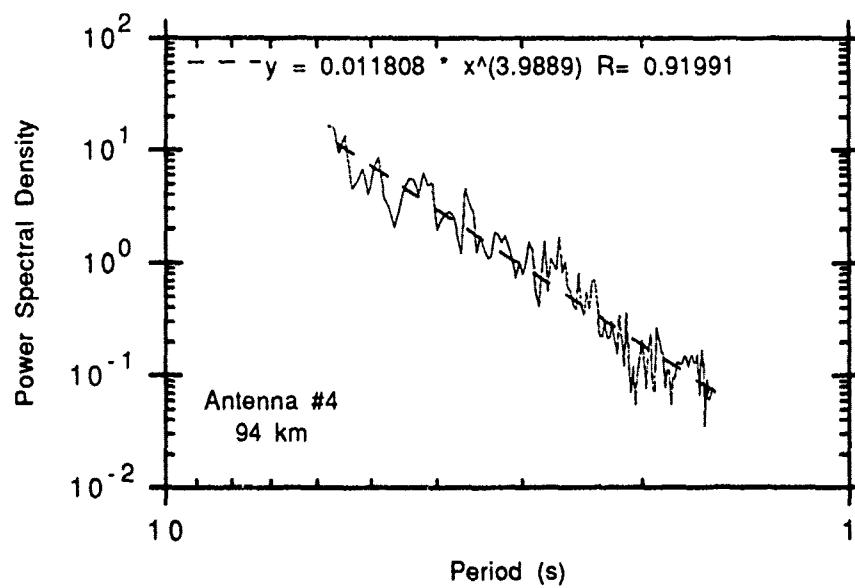


Figure 5.17 (j)

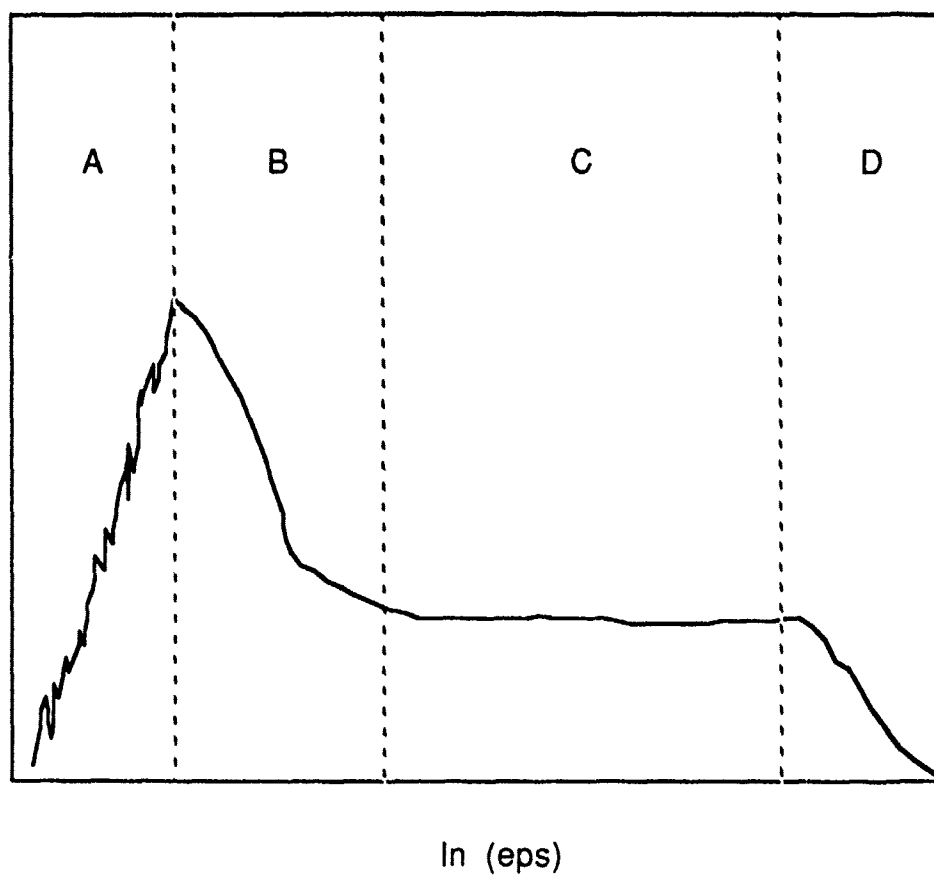


Figure 5.18 Idealized depiction of the slope of the natural logarithm of the correlation integral as a function of ϵ . The figure is divided into four distinct regions as indicated by the dashed lines.

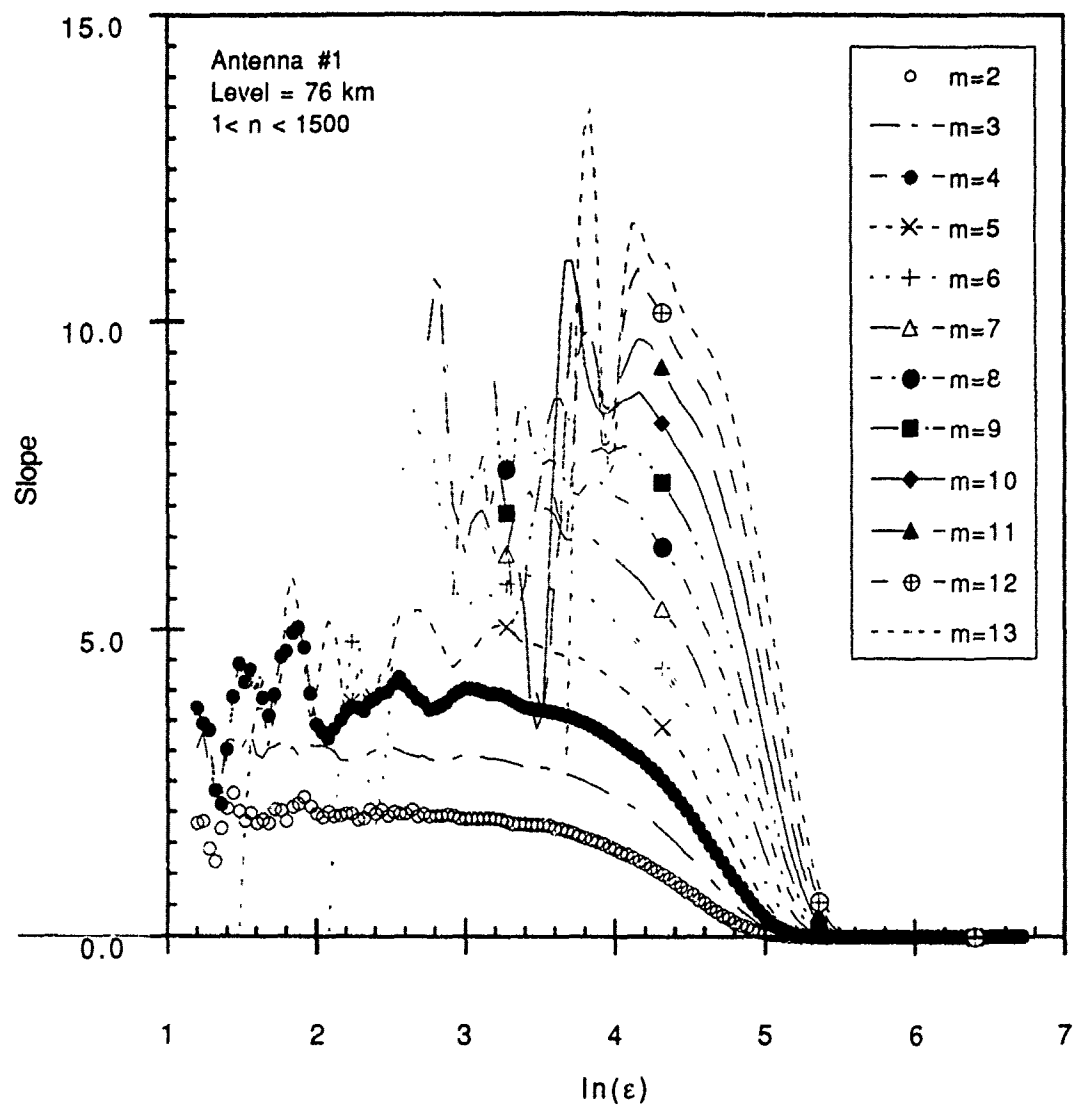


Figure 5.19(a)

Figure 5.19 Slope of the correlation integral plotted as a function of embedding dimension for points 1 through 1500 from antenna 1 for (a) 76 km; (b) 79 km; (c) 82 km; (d) 85 km (e) 88km; (f) 91 km and (g) 94 km.

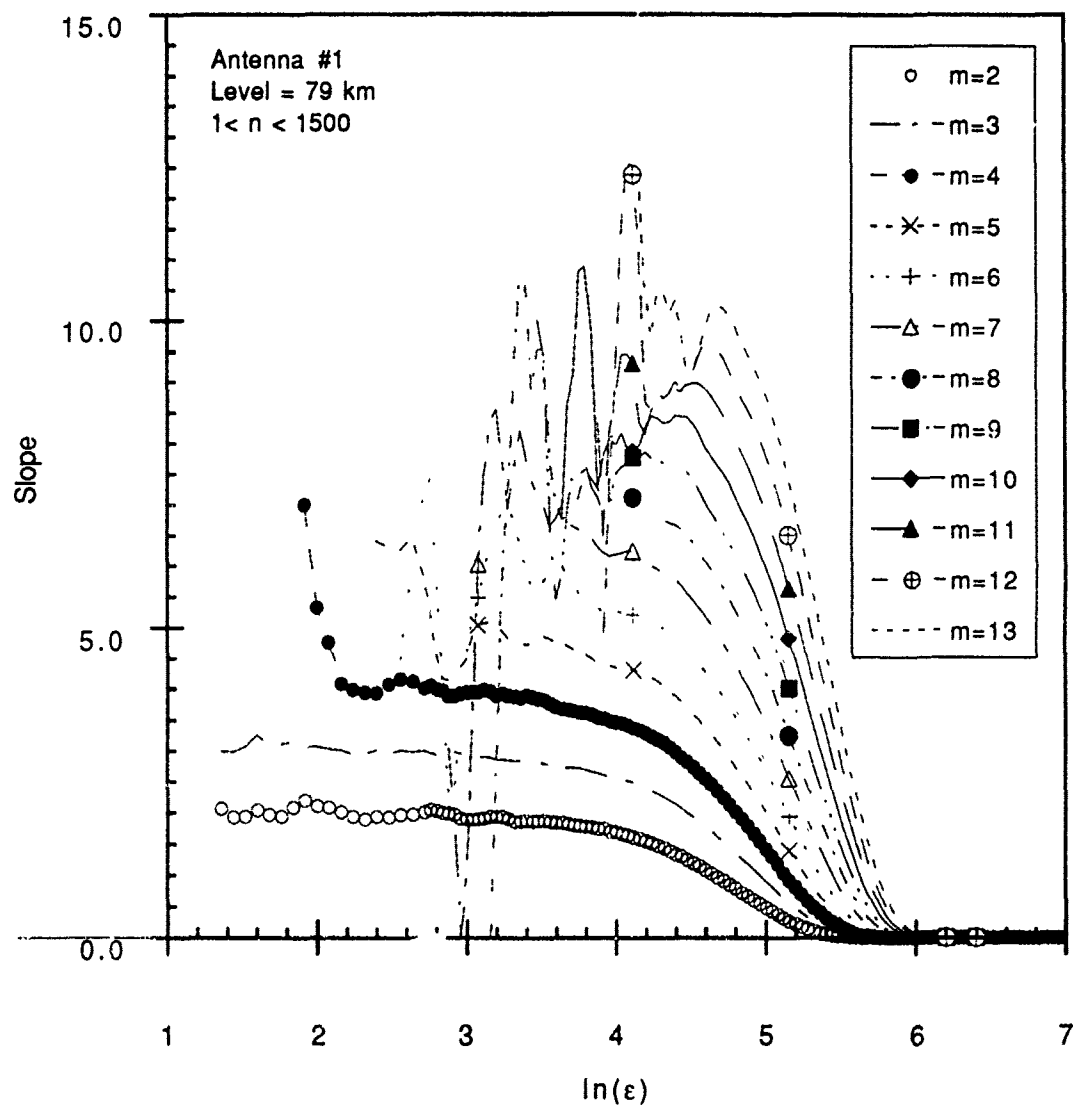


Figure 5.19(b)

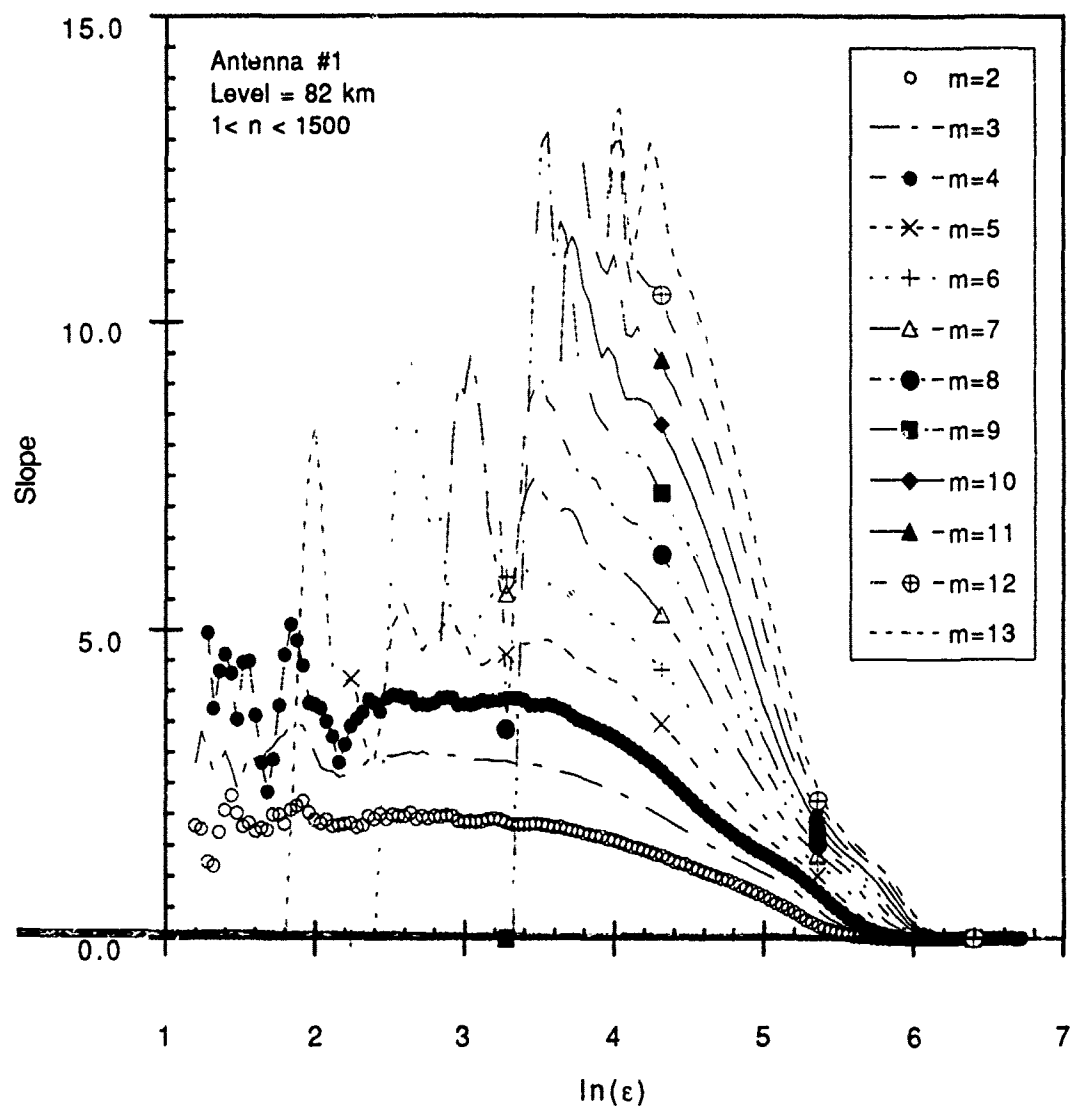


Figure 5.19 (c)

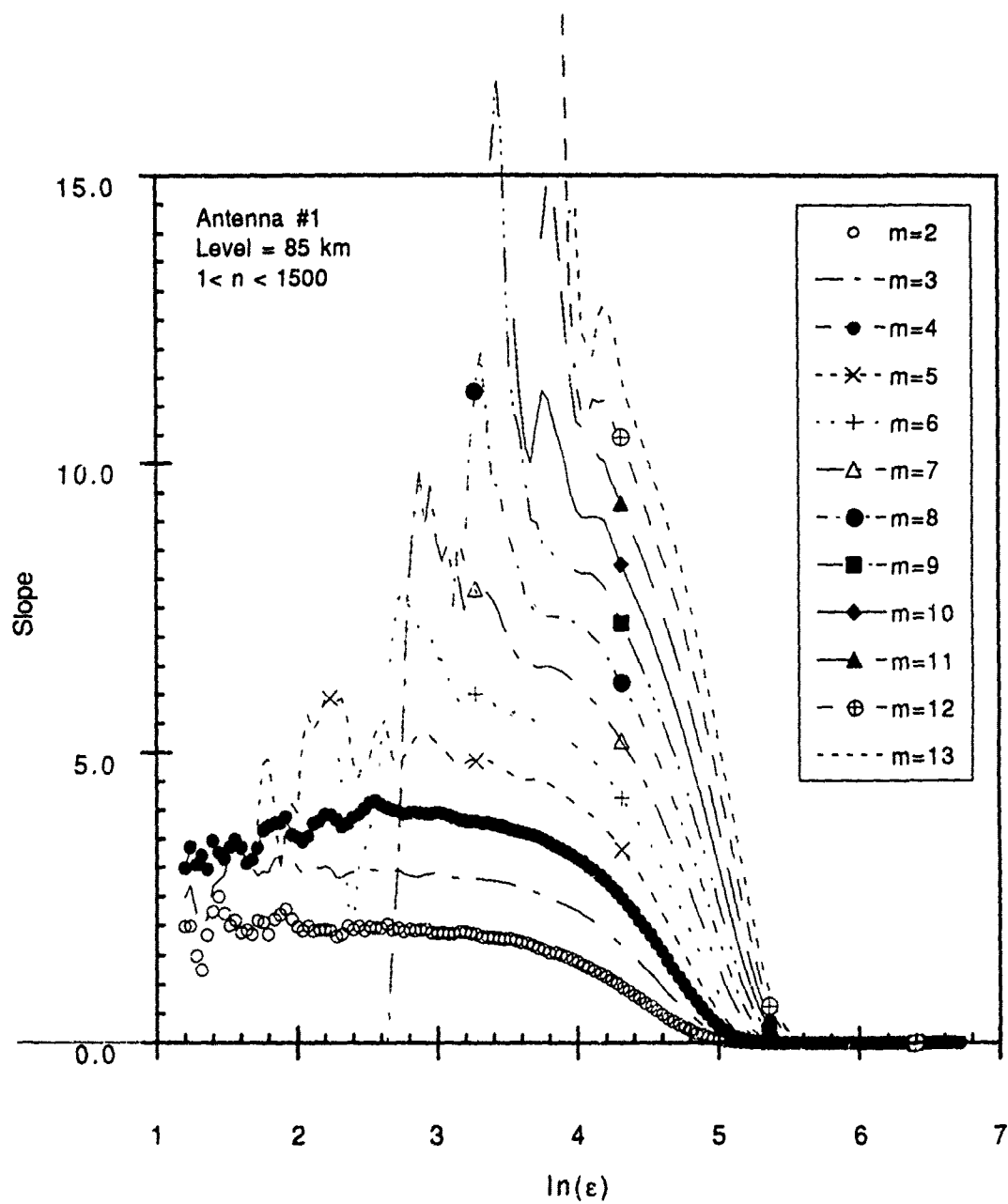


Figure 5.19(d)

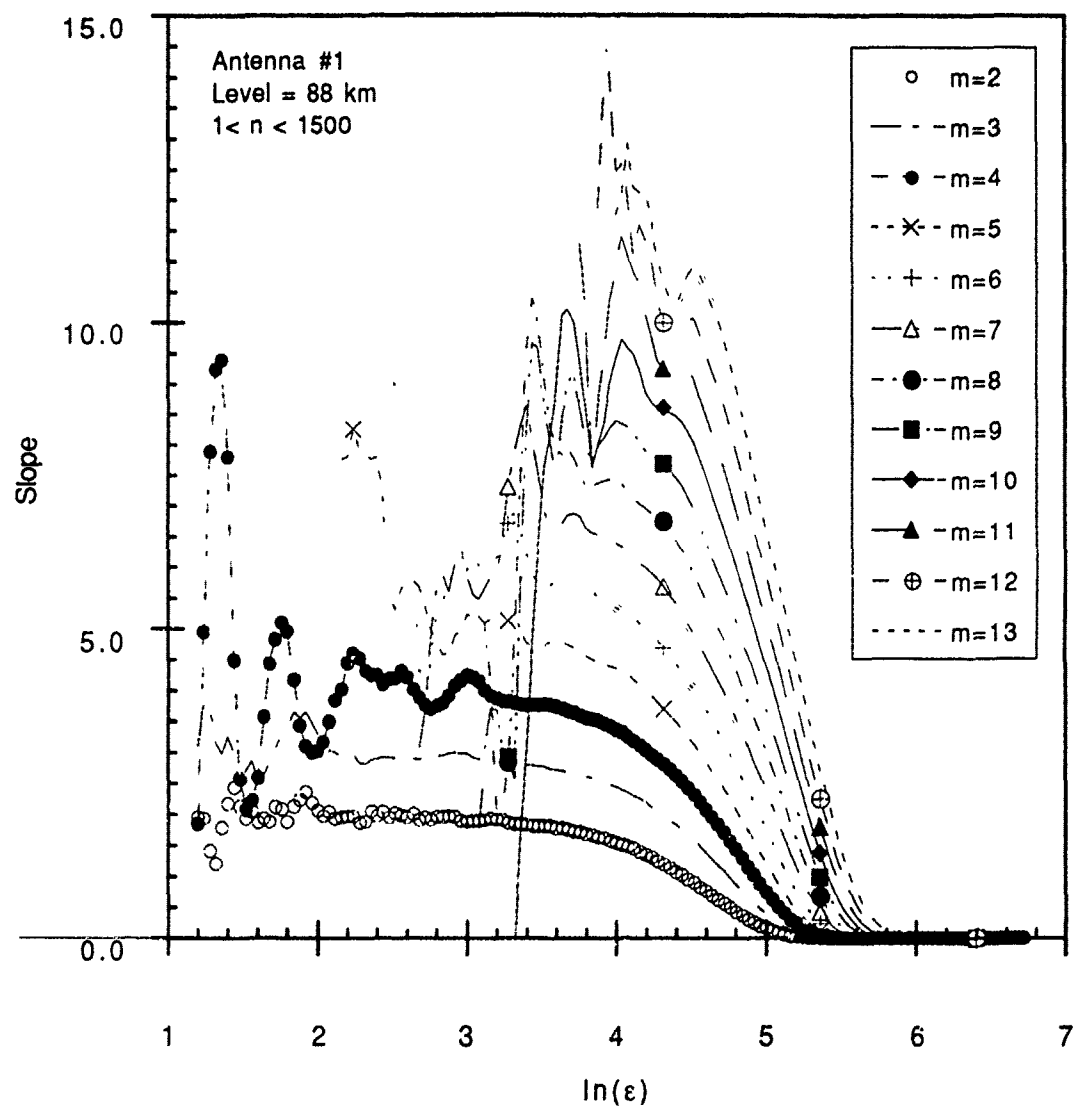


Figure 5.19(e)

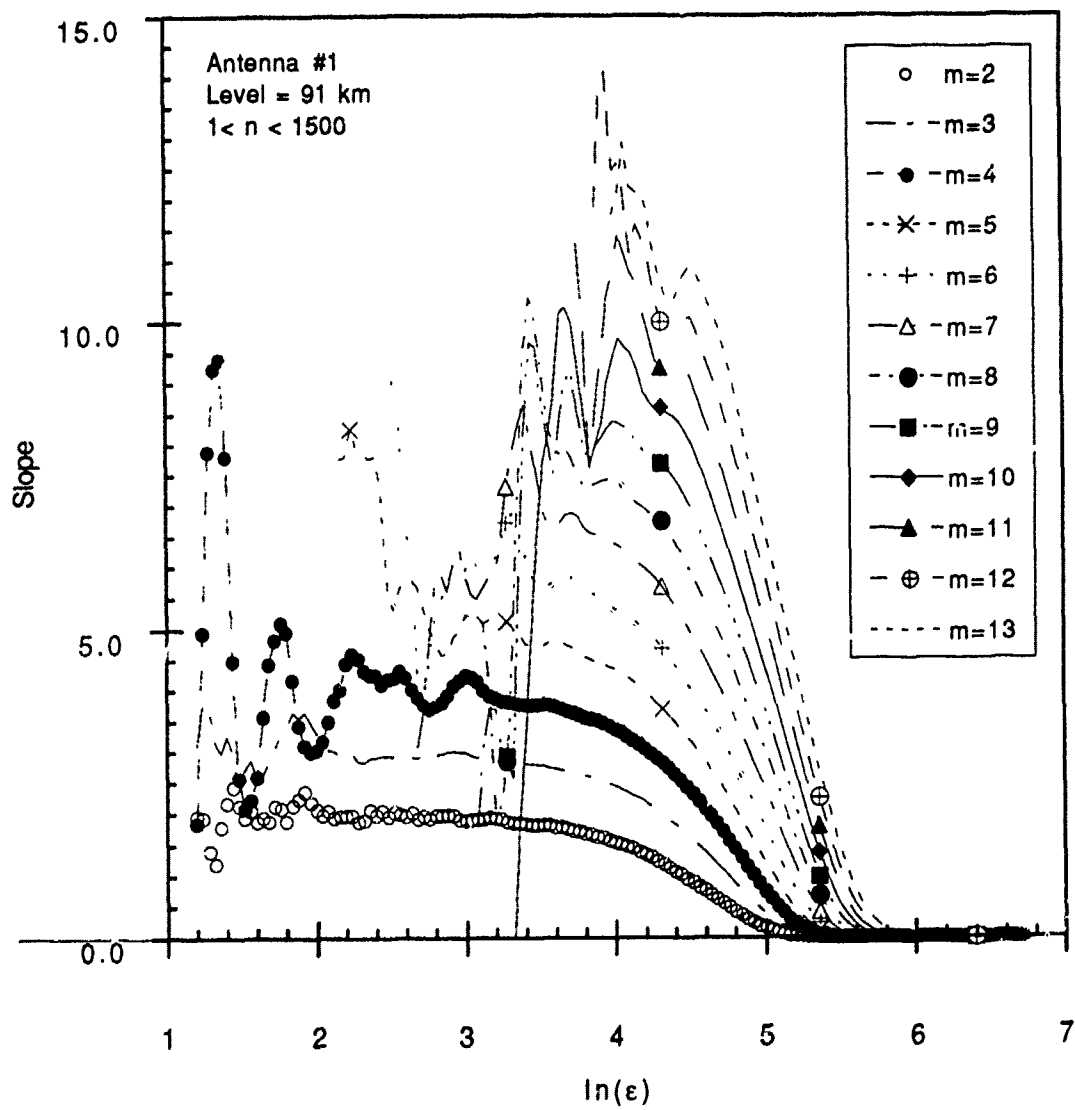


Figure 5.19(f)

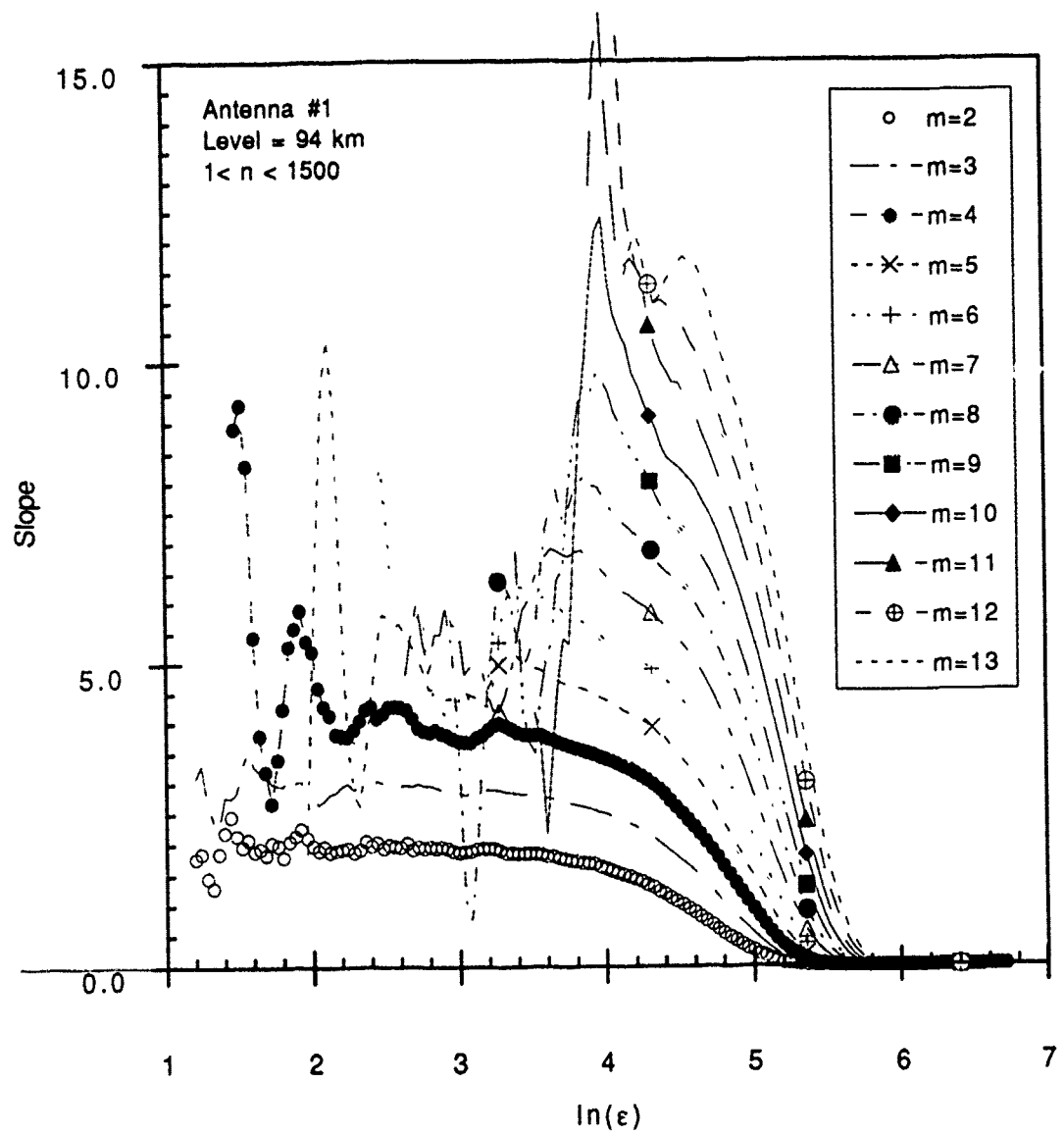


Figure 5.19(g)

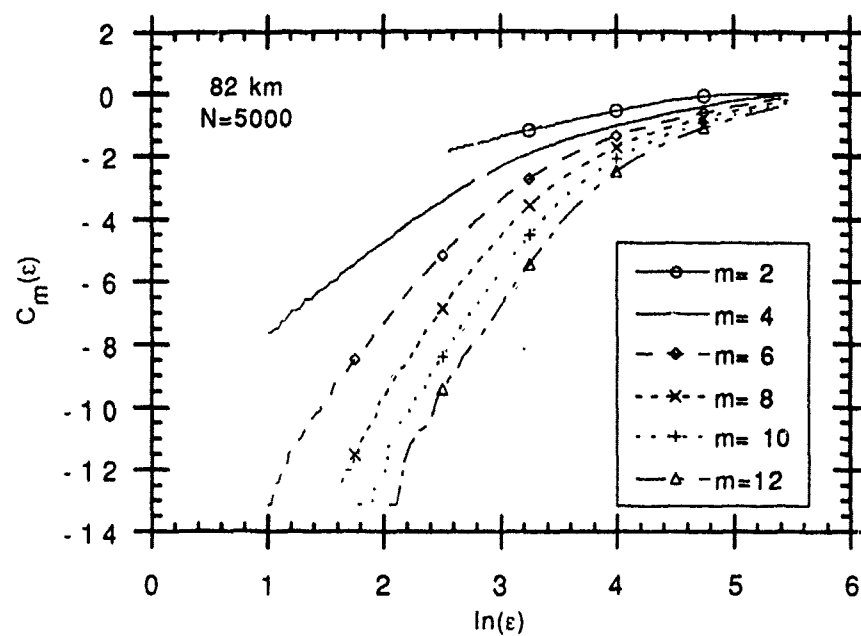


Figure 5.20 (a)

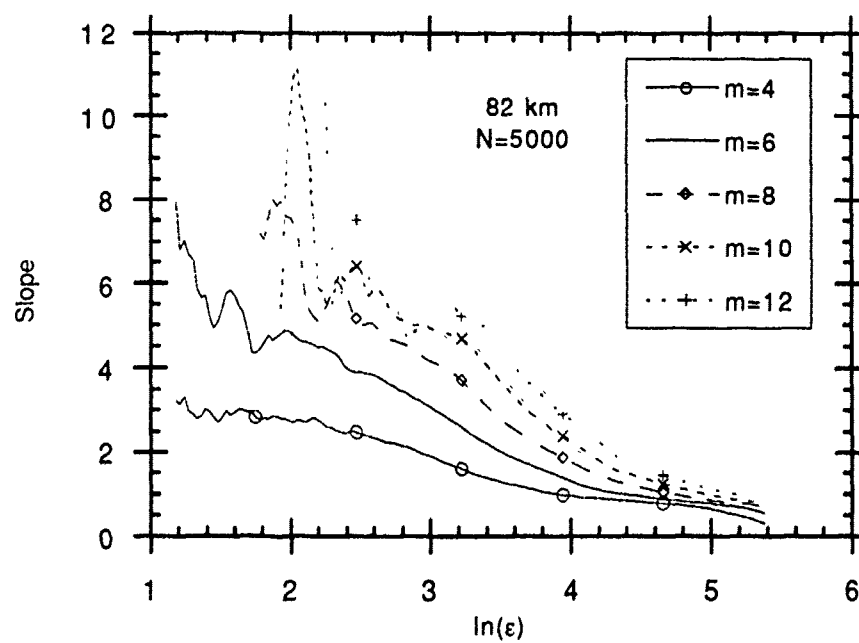


Figure 5.20 (b)

Figure 5.20 Correlation integral (a) and corresponding slope (b) for 82 km for average of all for antennas (N=5000 points).

CHAPTER VI

CONCLUSION AND RECOMMENDATIONS FOR FUTURE WORK

6.1 Conclusions

We did not detect a strange attractor with dimension less than three in the data from the Saskatoon partial reflection radar for the time scales which were studied. While we can not assert that there was only noise in the data set because of the small number of points which were examined, the supporting evidence from the power spectra suggest that we investigated time scales primarily in the viscous and inertial region and that the dimension of this system was greater than 3.

The limited size of the data set was one of the major reasons we can definitively rule out the presence of an attractor of only less than dimension 3. All indications are that the dominant signal was due to noise. We interpret this noise to be isotropic three dimensional turbulence.

The difficulties in detecting a strange attractor in the saturation of middle atmosphere gravity waves have been discussed in Chapter V. It does seem likely that the breaking of a gravity wave (or a spectrum of gravity waves) may be so ephemeral that limitations in the current implementation of the Grassberger-Procaccia algorithm will prevent us from ever detecting it. The decay to turbulence should occur quickly enough, even in the slower slantwise static instability mechanism, that there will not be a statistically significant number of orbits of the attractor to be useful. At least 50 orbits of the attractor are necessary to implement the Grassberger-Procaccia algorithm.

An even bigger consideration remains - if the attractor is so ephemeral is it worth the trouble to study?

A similar question remains as to what a strange attractor might mean physically. In the case of the absorption of gravity waves, it still may provide a clue as to a mechanism by which the wave becomes unstable. As pointed out in previous discussions, the currently accepted conceptual models for gravity wave breaking are most likely wrong if not merely inaccurate. Detecting the presence of a strange attractor and its dimension would provide insight into the route to chaos in this system and perhaps insight into the nature of the mechanism of gravity wave saturation.

If there is an attractor associated with the nonlinear wave-wave interaction, does this reveal anything about the mechanism behind gravity wave saturation or just something about the particular spectrum of waves undergoing saturation in the data set? We must be cautious in generalizing any future results to gravity wave saturation itself.

6.2 Recommendations For Future Work

This study raises many more questions than it has definitively answered. While it seems unlikely that an attractor will be found which describes the transition to chaos over a short time scale in meteorological data, more work is needed before it can be absolutely discounted. The suggestions for further study fall into three areas: work on the technique, extension of this work with better radar data and extension of this work with boundary layer data.

The Grassberger-Procaccia algorithm and its extensions have been used successfully in a number of different theoretical and laboratory studies of chaotic behavior. Its weaknesses have been well studied and documented in the literature, *for the most part*. We are uncertain whether this algorithm

could detect the presence of a strange attractor in the confusing welter of competing signals that make up a typical meteorological data set. The degree of sensitivity of the Grassberger-Procaccia algorithm to a signal that encompasses a wide spectrum of different types of behavior (periodic, noise and chaotic) must be established.

The Grassberger-Procaccia algorithm must be investigated as to its ability to detect a strange attractor amidst noise and a spectrum of periodic signals such as are found in a meteorological data set. This investigation must determine the relative strength of the chaotic signal that is necessary to be detected. It also must determine the number of points needed to make it work.

This study should be extended to other middle atmosphere data sets so that its conclusions may be confirmed. Such data sets must consist of much longer records without the gain changes and contamination of the signal that was found in the data used in this study. It would also be useful to employ this technique on the radar derived winds which are closer to a truer description of gravity waves. The nebulous connection between the signals that are measured by partial reflection radars and the middle atmosphere may obscure the presence of chaotic behavior. Wind measurements deduced from the radar signal do carry a degree of smoothing that could complicate the analysis, but in general they will be more representative of gravity wave behavior.

Other algorithms should be used to supplement the Grassberger-Procaccia algorithm. The improved box counting algorithm (Liebovitch and Toth, 1989) should be examined to determine if it is a useful adjunct to the Grassberger-Procaccia algorithm. The nearest neighbor method of Badii and Politi (1987) should be tried as well as some of the additional extensions of the Grassberger-Procaccia algorithm (Franaszek, 1989; Ellner, 1988). Higuchi (1988) has suggested an algorithm using a fractal length of curve technique which shows promise for low (<2) dimension attractors; this might be tried as well.

The atmospheric boundary layer would be a logical place in which to extend this study. Like the middle atmosphere, it is the home to unstable wave activity that decays to turbulence (e.g., Kelvin-Helmholtz waves). The study of turbulence in the boundary layer is also well advanced. Most importantly, measurements of the boundary layer are of a much higher quality than those of the middle atmosphere. Most boundary layer parameters can be sampled *in situ* rather than deduced by remote sensing techniques as is commonly done in the middle atmosphere. The amount of external noise in boundary layer data is also much less than that for the middle atmosphere. Measurements of several different variables can be made which help provide a better understanding of the dynamics of an attractor if one is found. In addition, measurements of the boundary layer can be made at much higher sampling rates and for longer continuous periods than in the middle atmosphere.

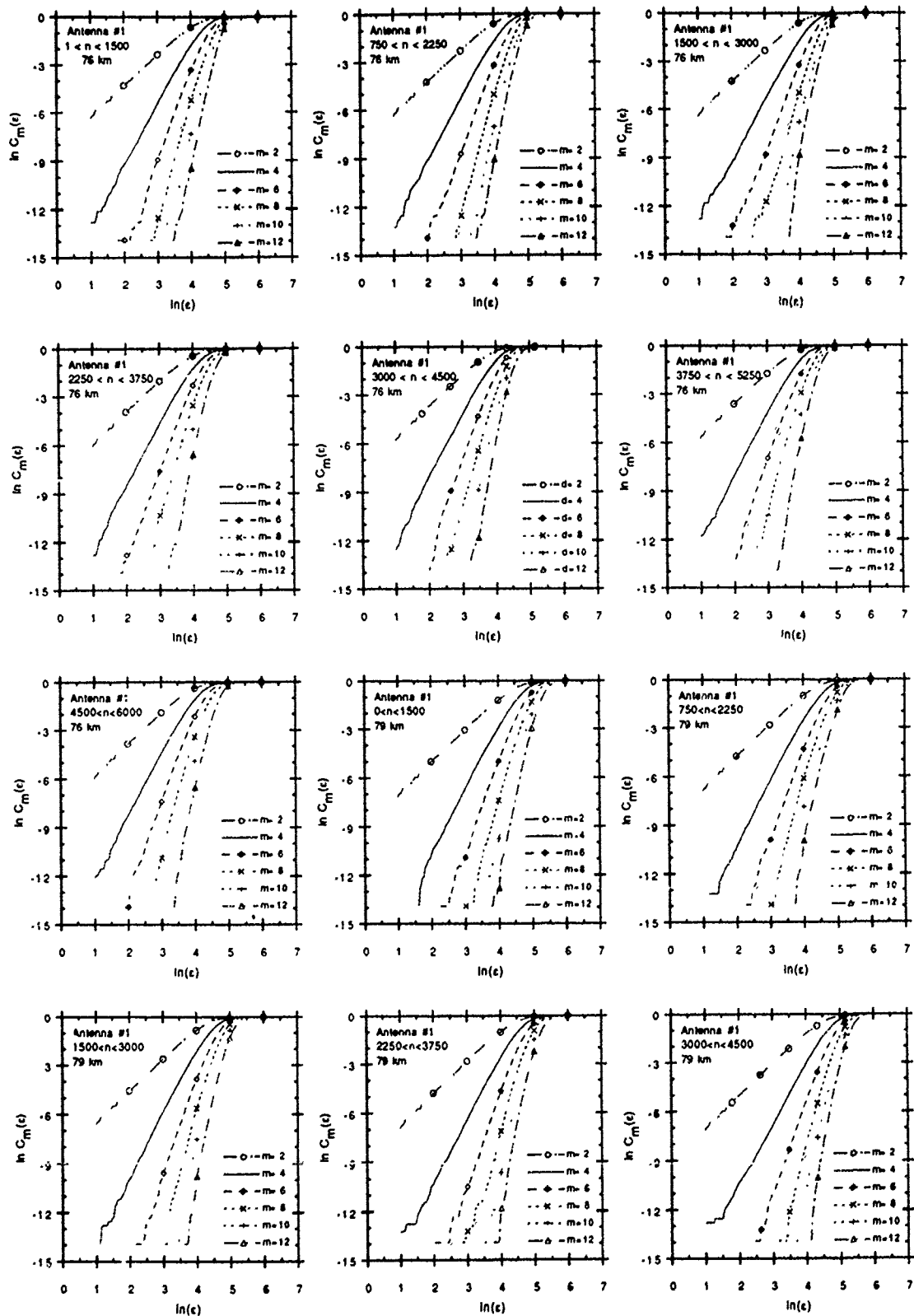
Stationary data sets are perhaps an even greater problem in the boundary layer than in the middle atmosphere. The boundary layer undergoes a tremendous change during the diurnal heating cycle, exhibiting remarkably different types of behavior between daytime and nighttime. The boundary layer study of Tsonis and Elsner (1988) was flawed not only because it did not consider enough points in applying the Grassberger-Procaccia algorithm and the data set was highly non-stationary, but because it offered no reason (i.e., physical insight) as to why there might be a strange attractor in meteorological data over a short time scale.

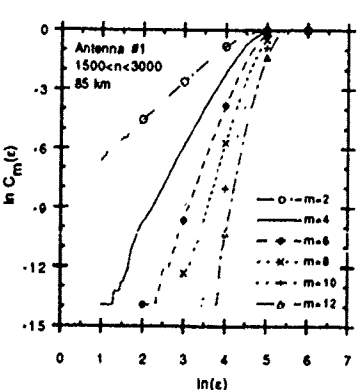
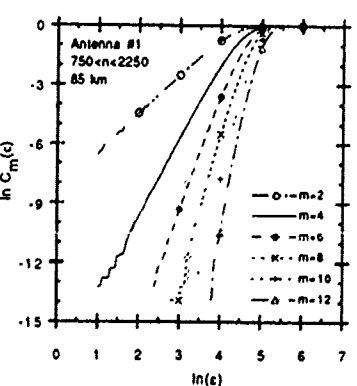
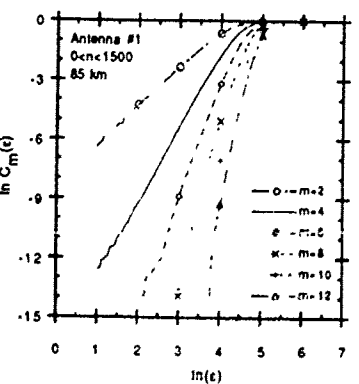
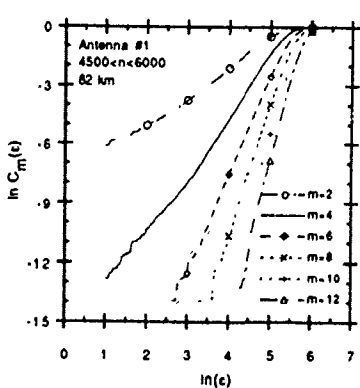
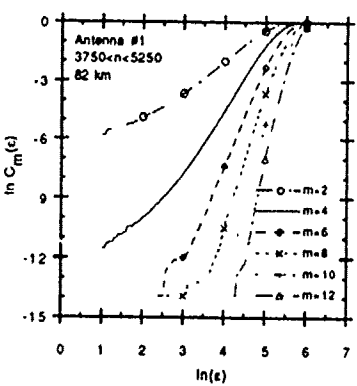
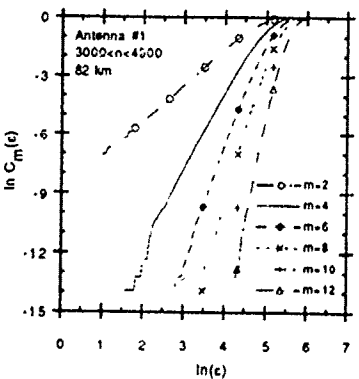
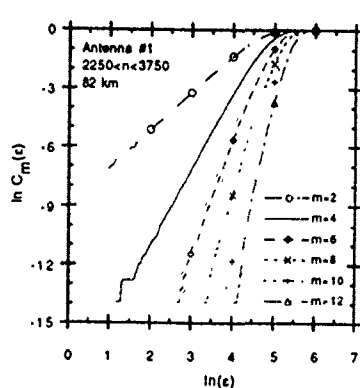
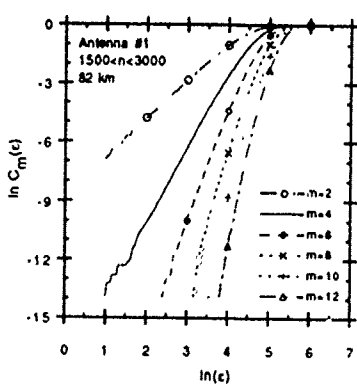
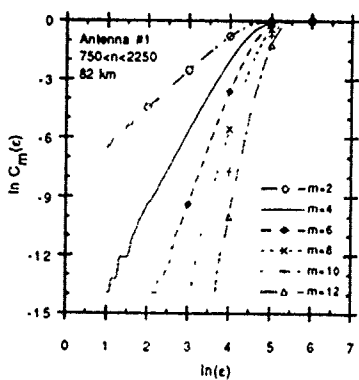
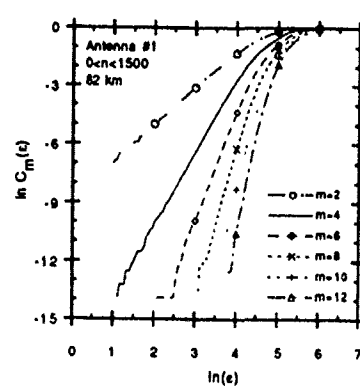
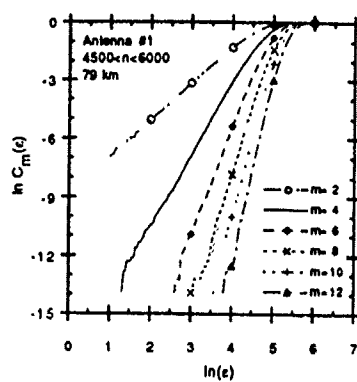
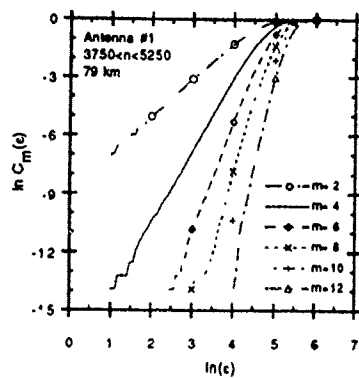
There may a greater chance of finding chaotic behavior in the structure of turbulence rather than the transition from laminar to turbulent flow. Recent work using multi-fractals suggests that the structure of turbulence is fractal in nature (Chhabra et al., 1989; Meneveau and Nelkin, 1989; Smith et al., 1986). There hints of this in the work here for time scales in the viscous region. This is another avenue for research that should be explored.

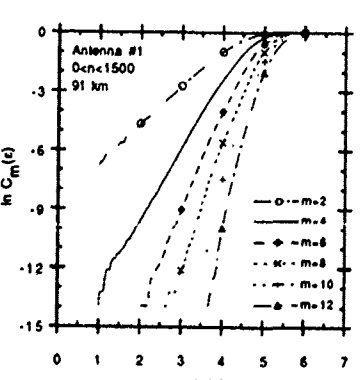
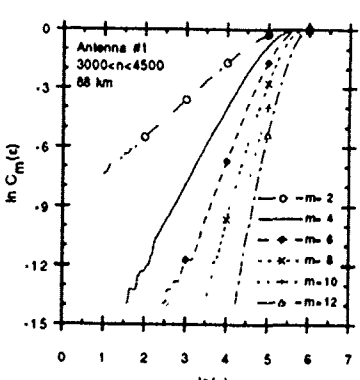
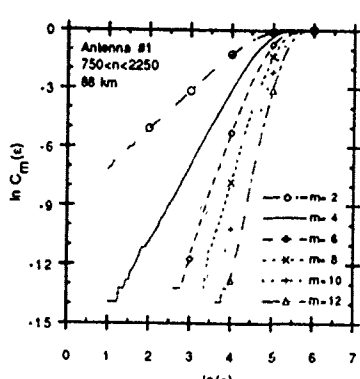
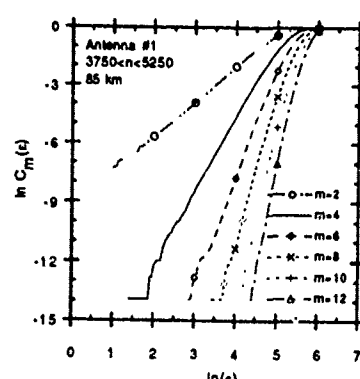
APPENDICES

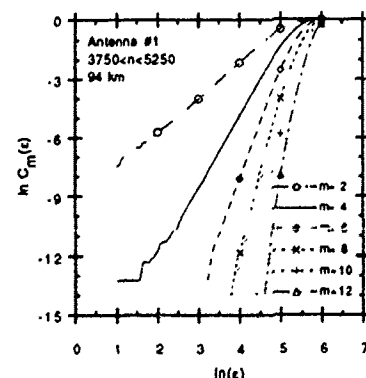
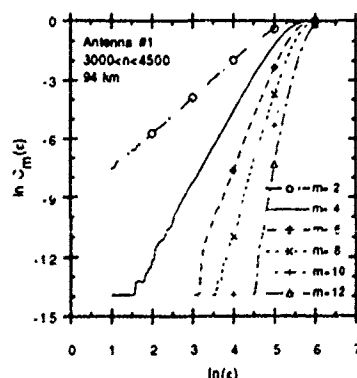
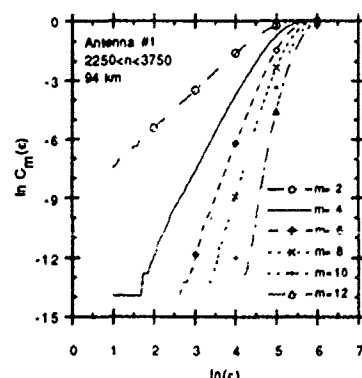
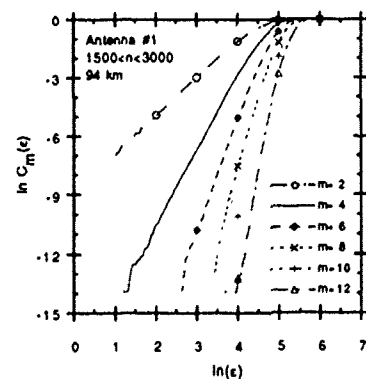
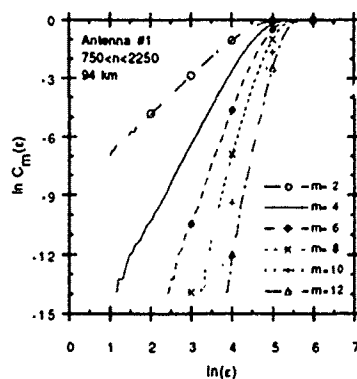
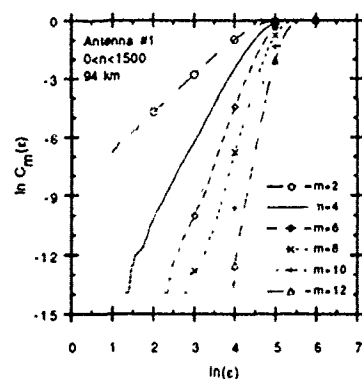
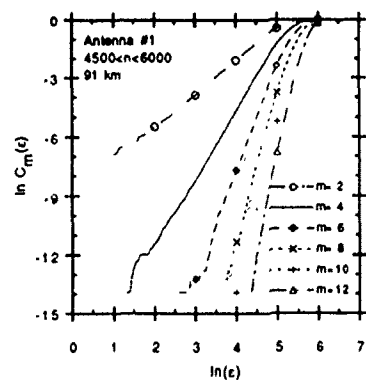
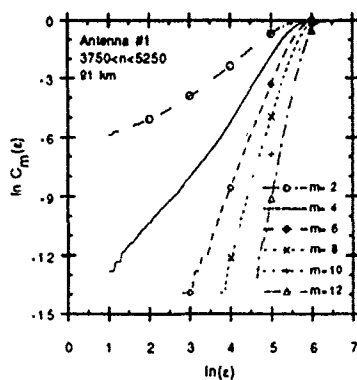
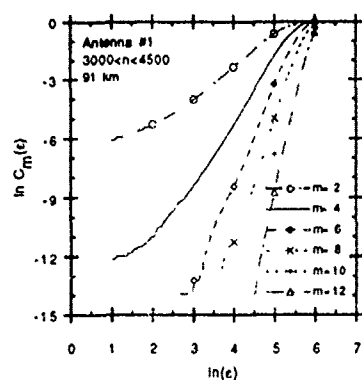
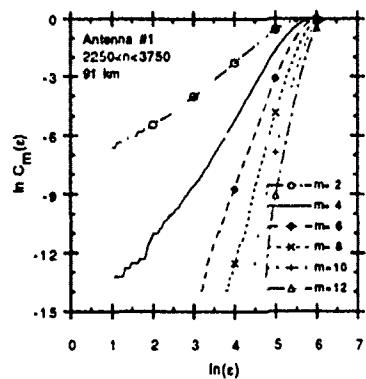
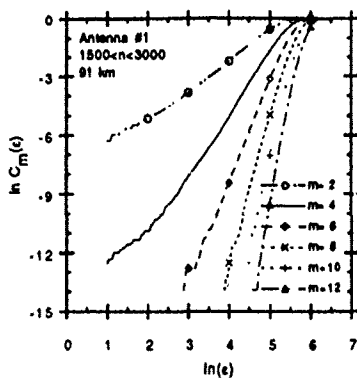
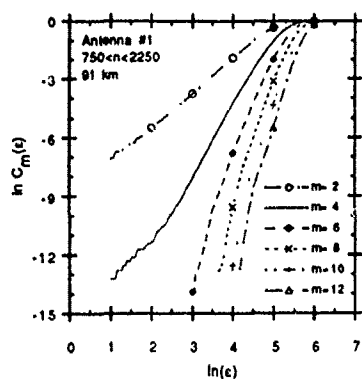
APPENDIX A

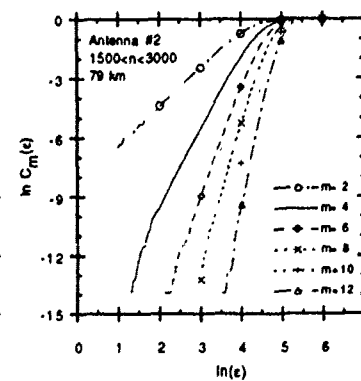
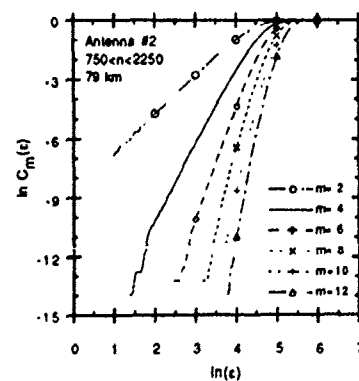
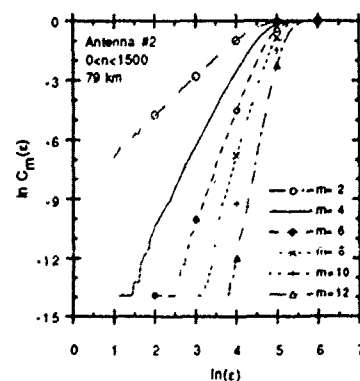
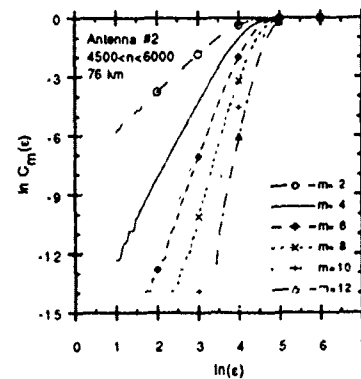
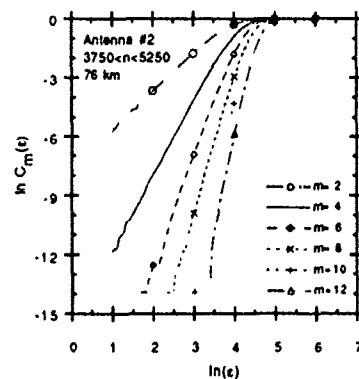
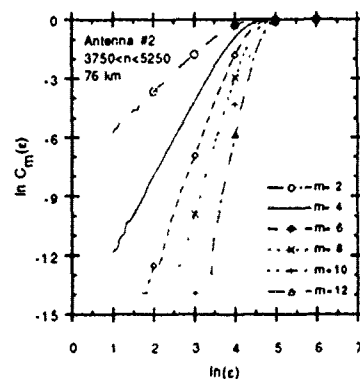
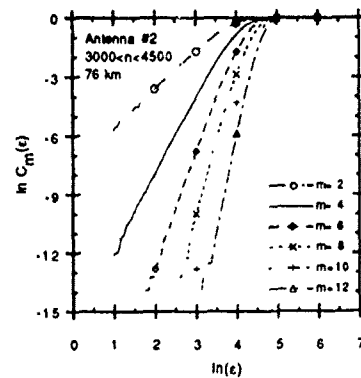
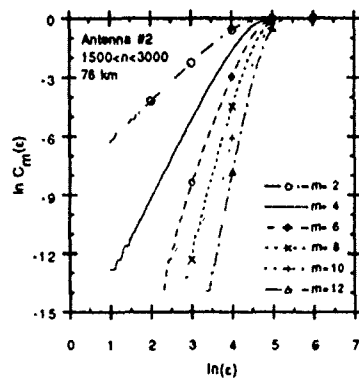
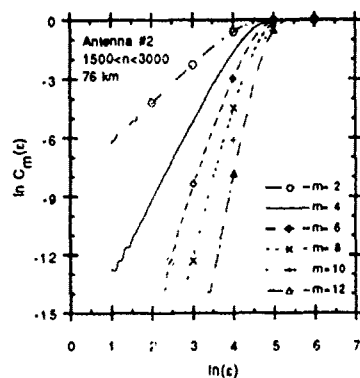
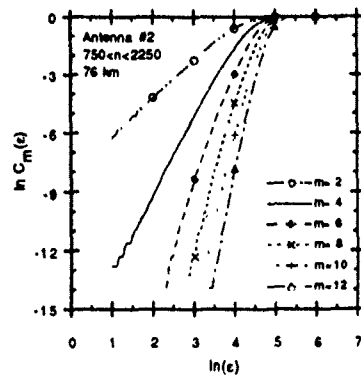
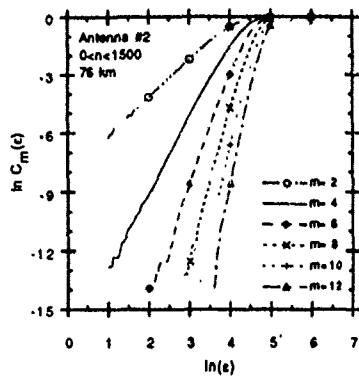
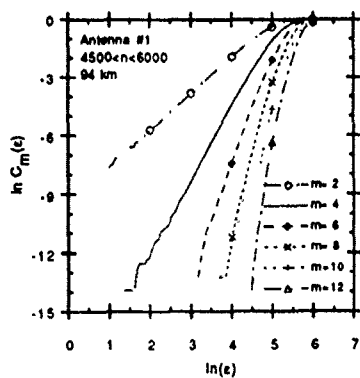
Appendix A contains the figures depicting the results of the correlation integral calculations described in Chapter V for all antennas and levels. Output from only every other embedding dimension are shown in an effort to render the figures more legible.

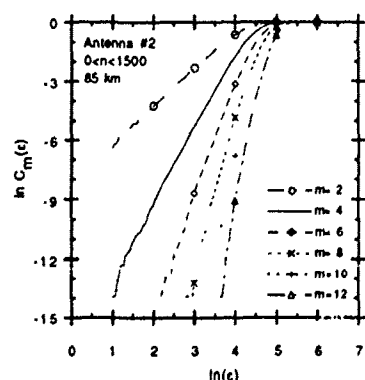
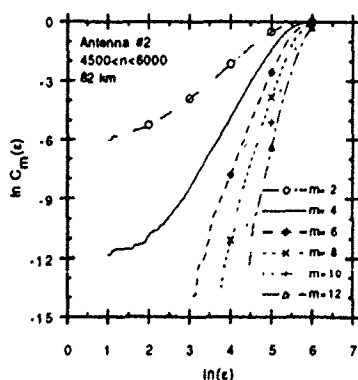
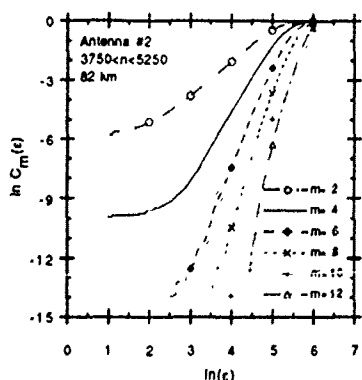
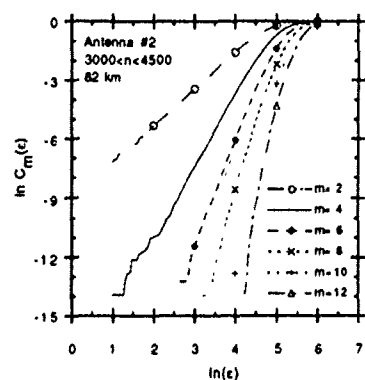
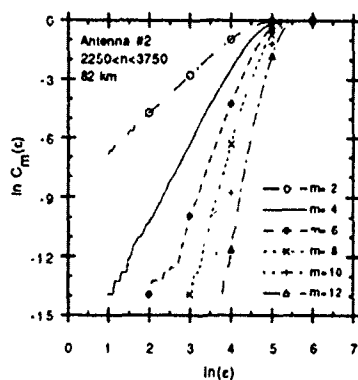
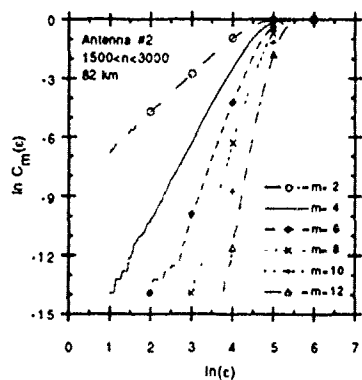
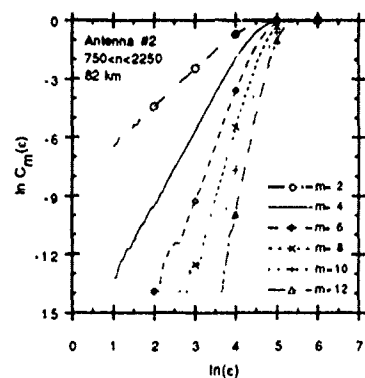
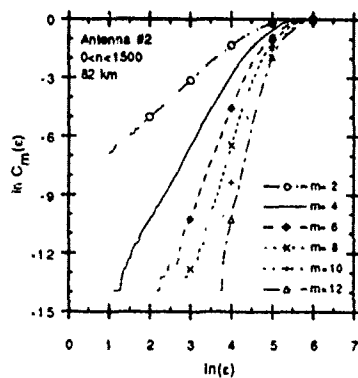
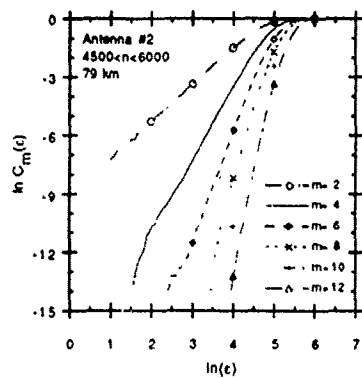
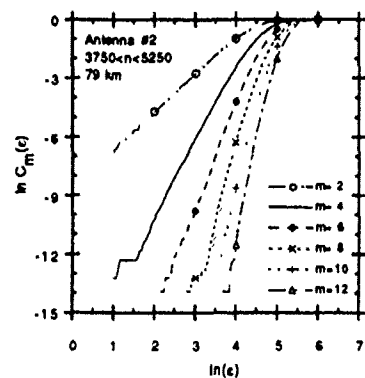
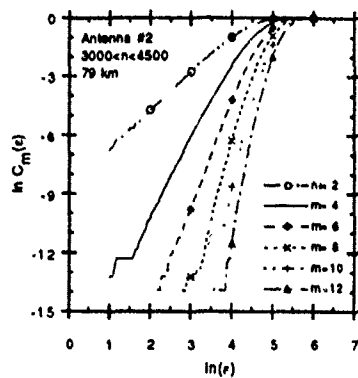
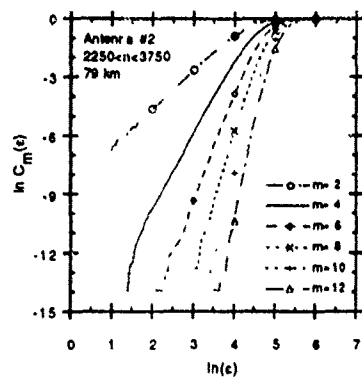


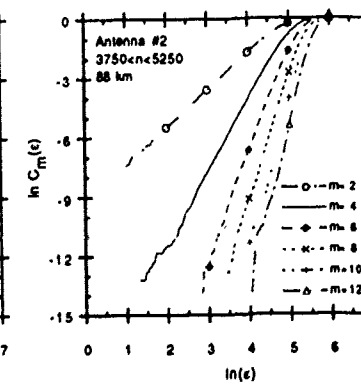
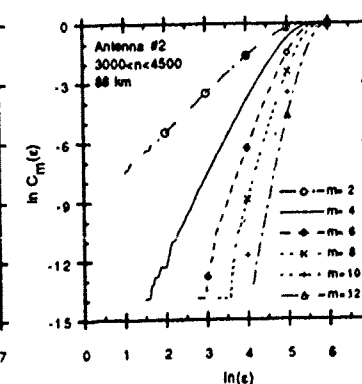
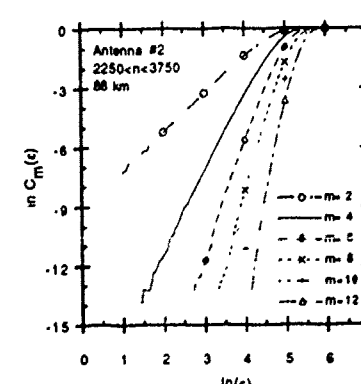
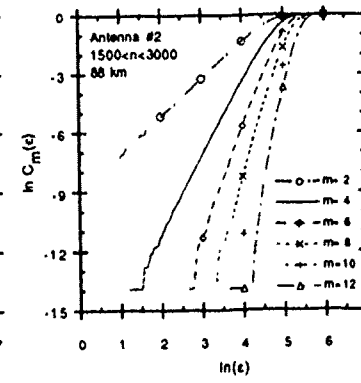
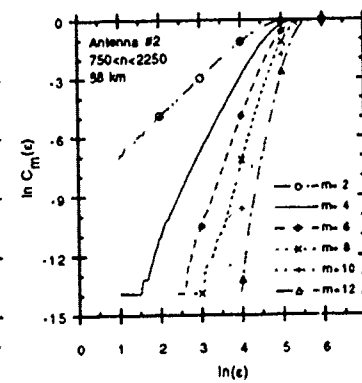
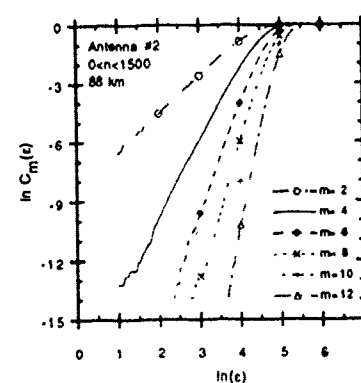
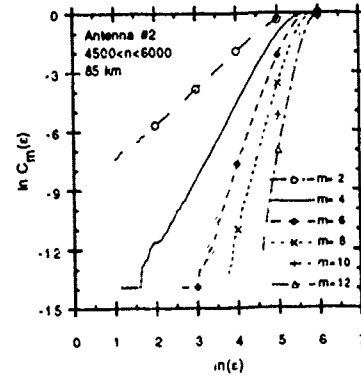
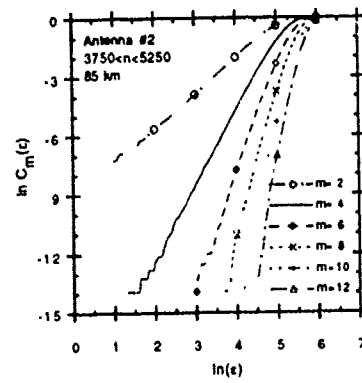
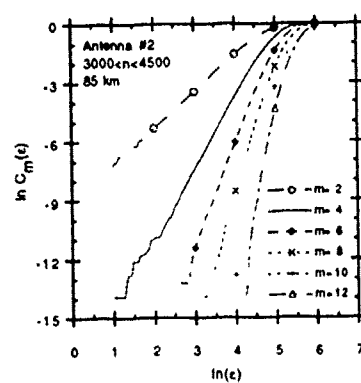
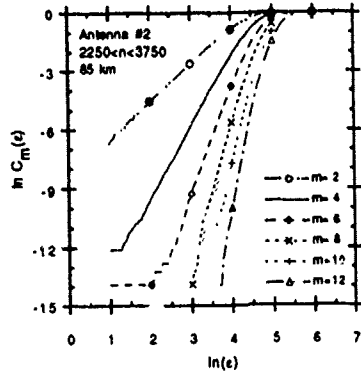
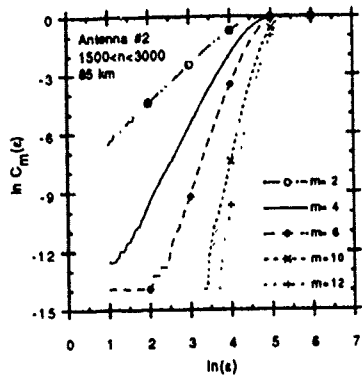
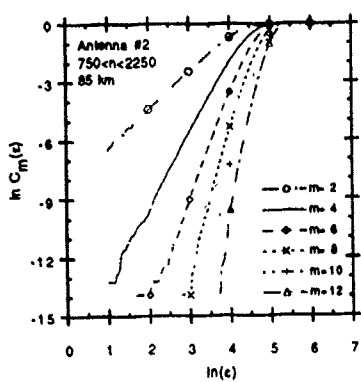


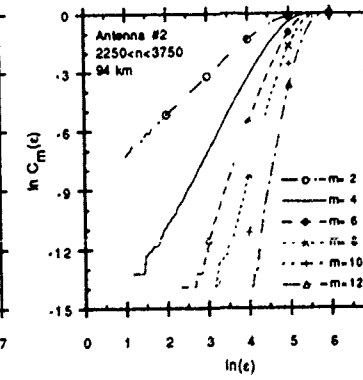
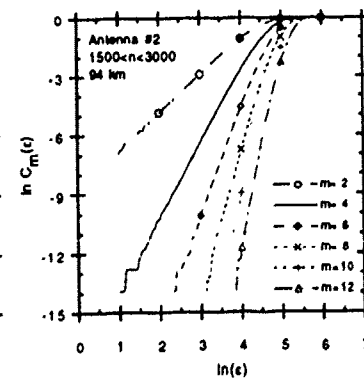
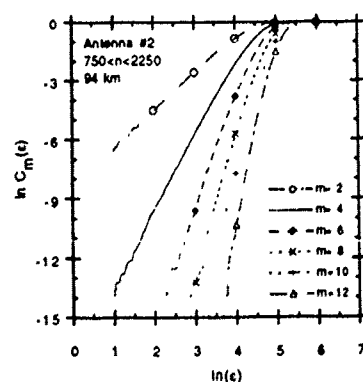
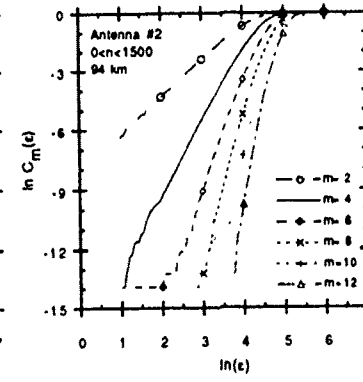
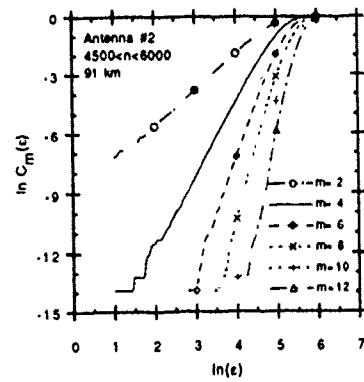
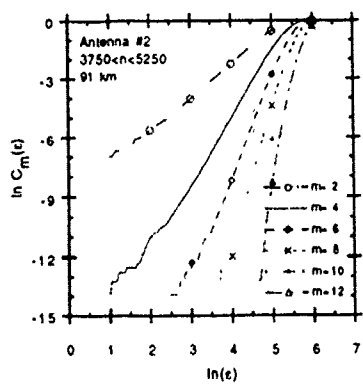
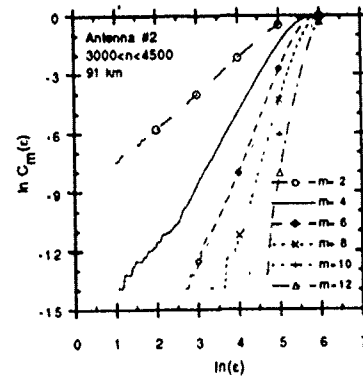
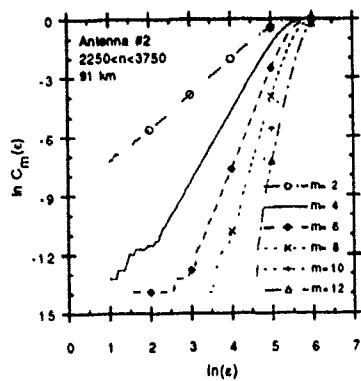
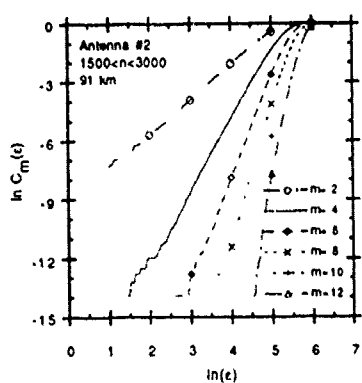
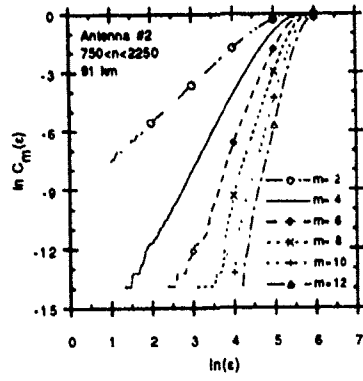
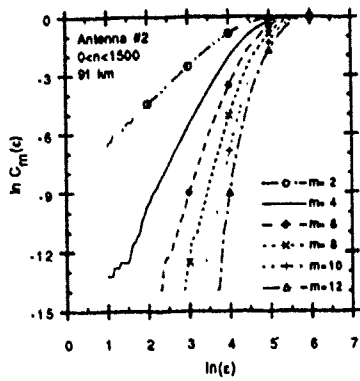
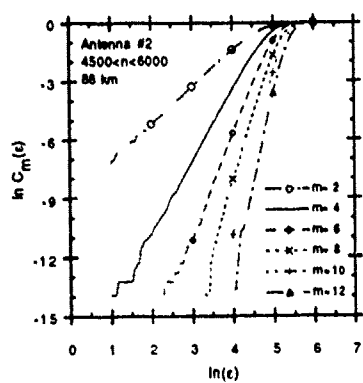


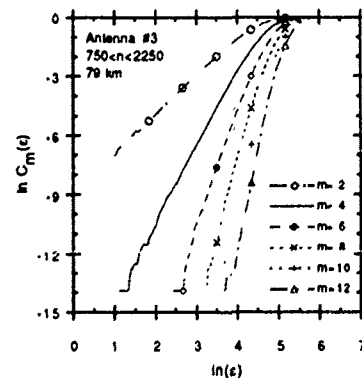
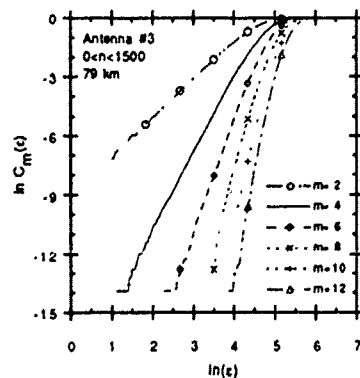
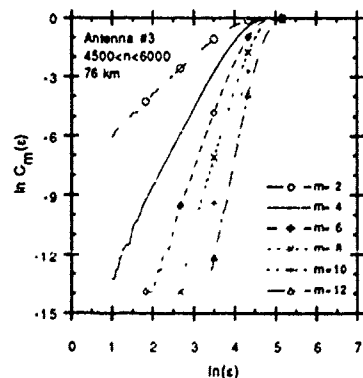
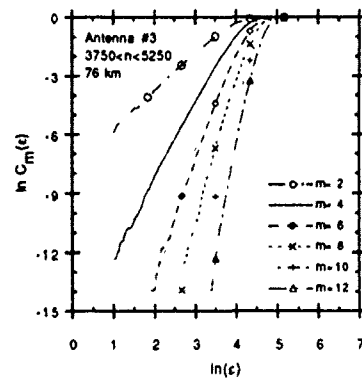
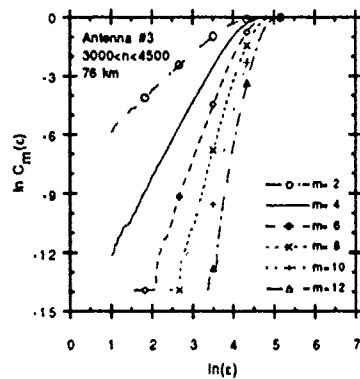
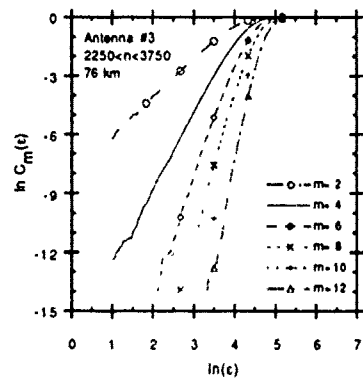
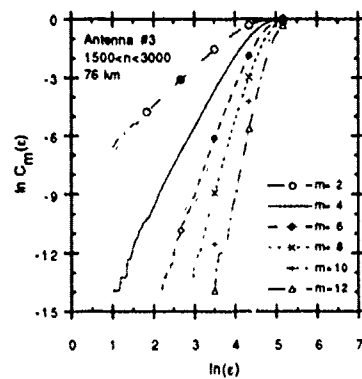
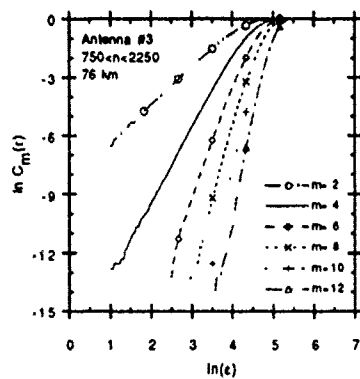
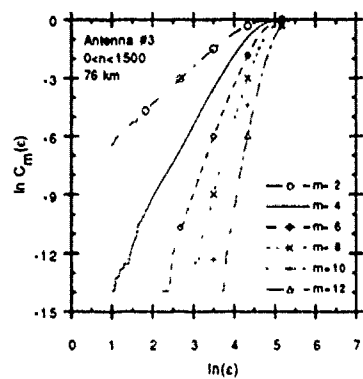
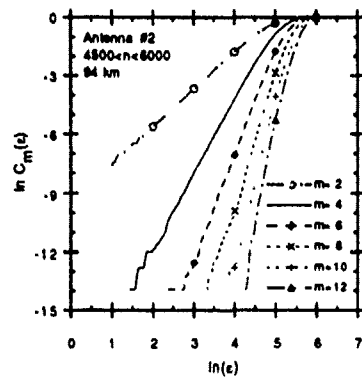
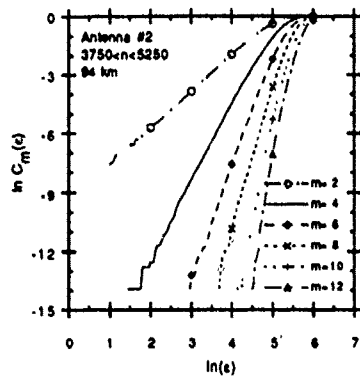
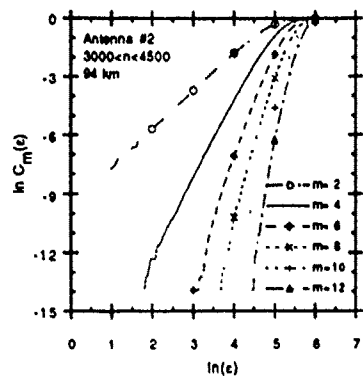


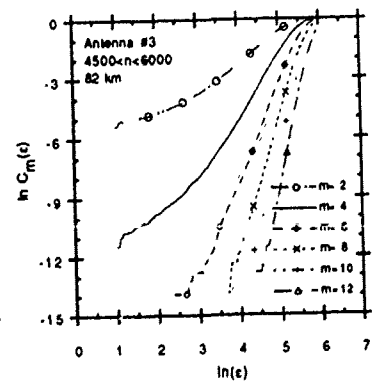
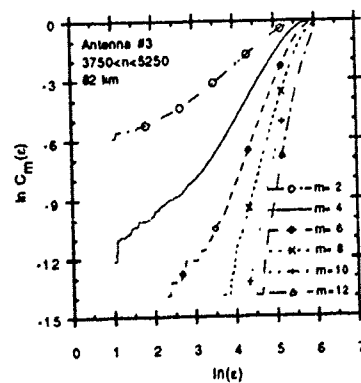
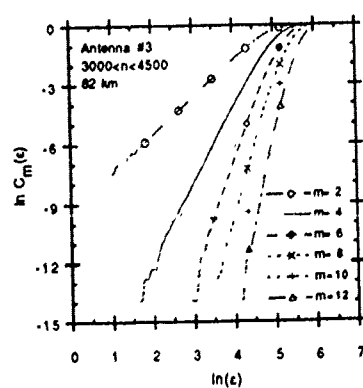
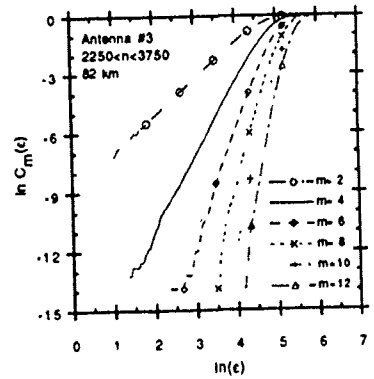
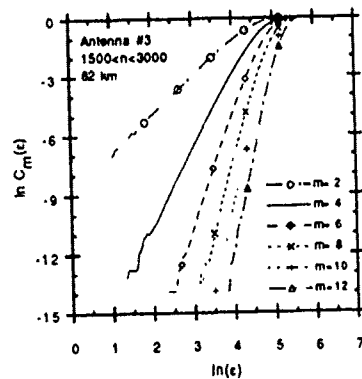
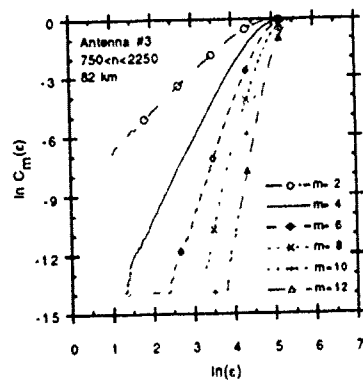
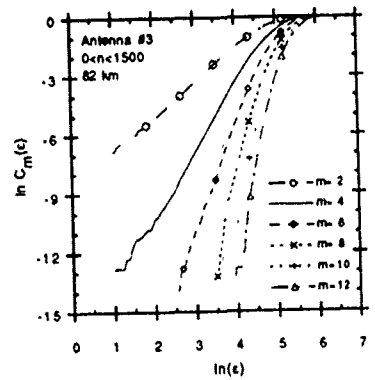
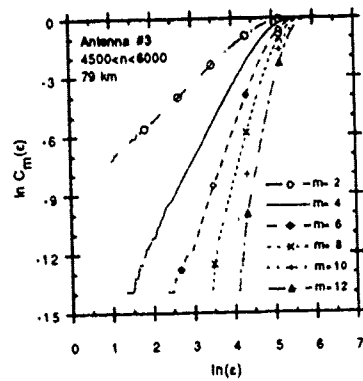
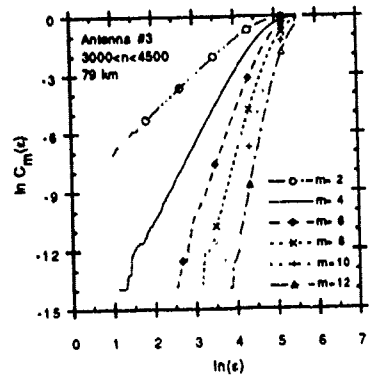


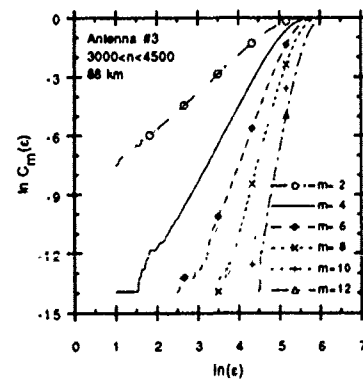
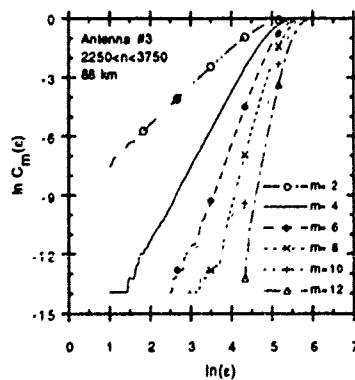
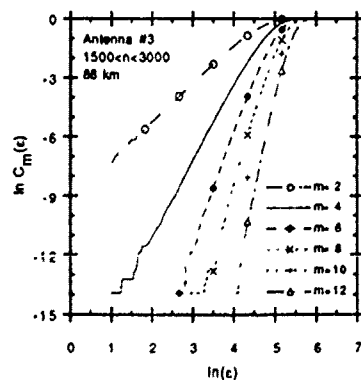
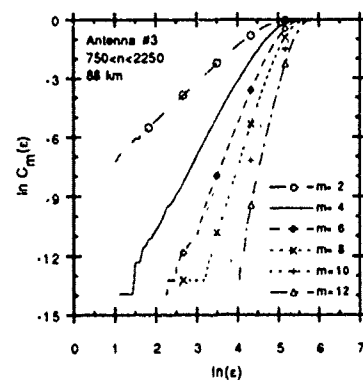
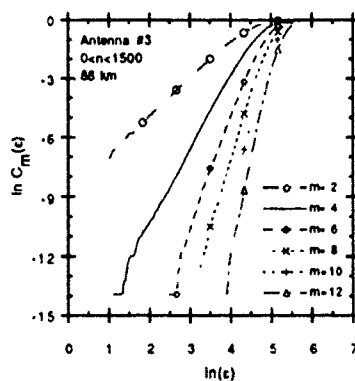
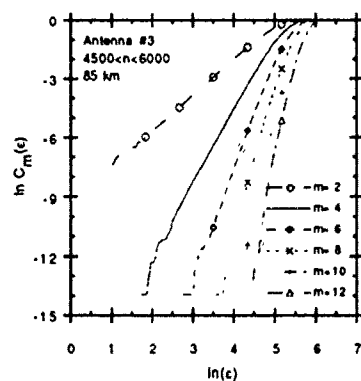
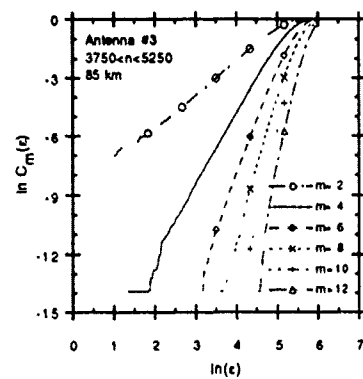
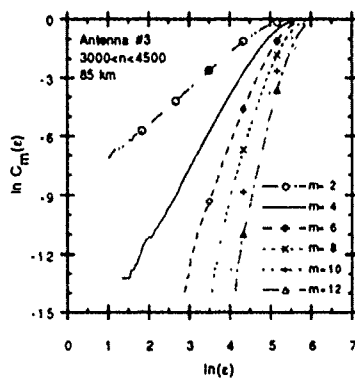
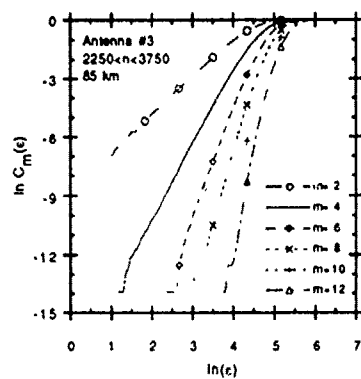
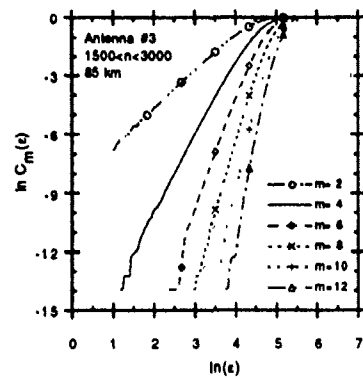
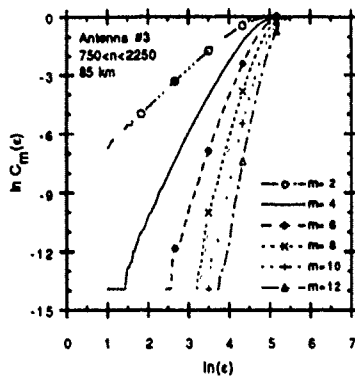
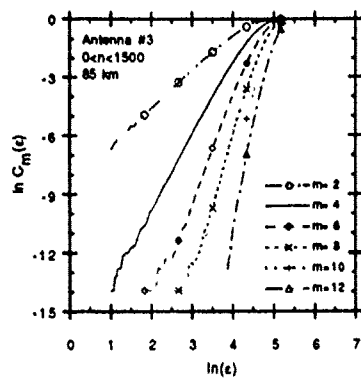


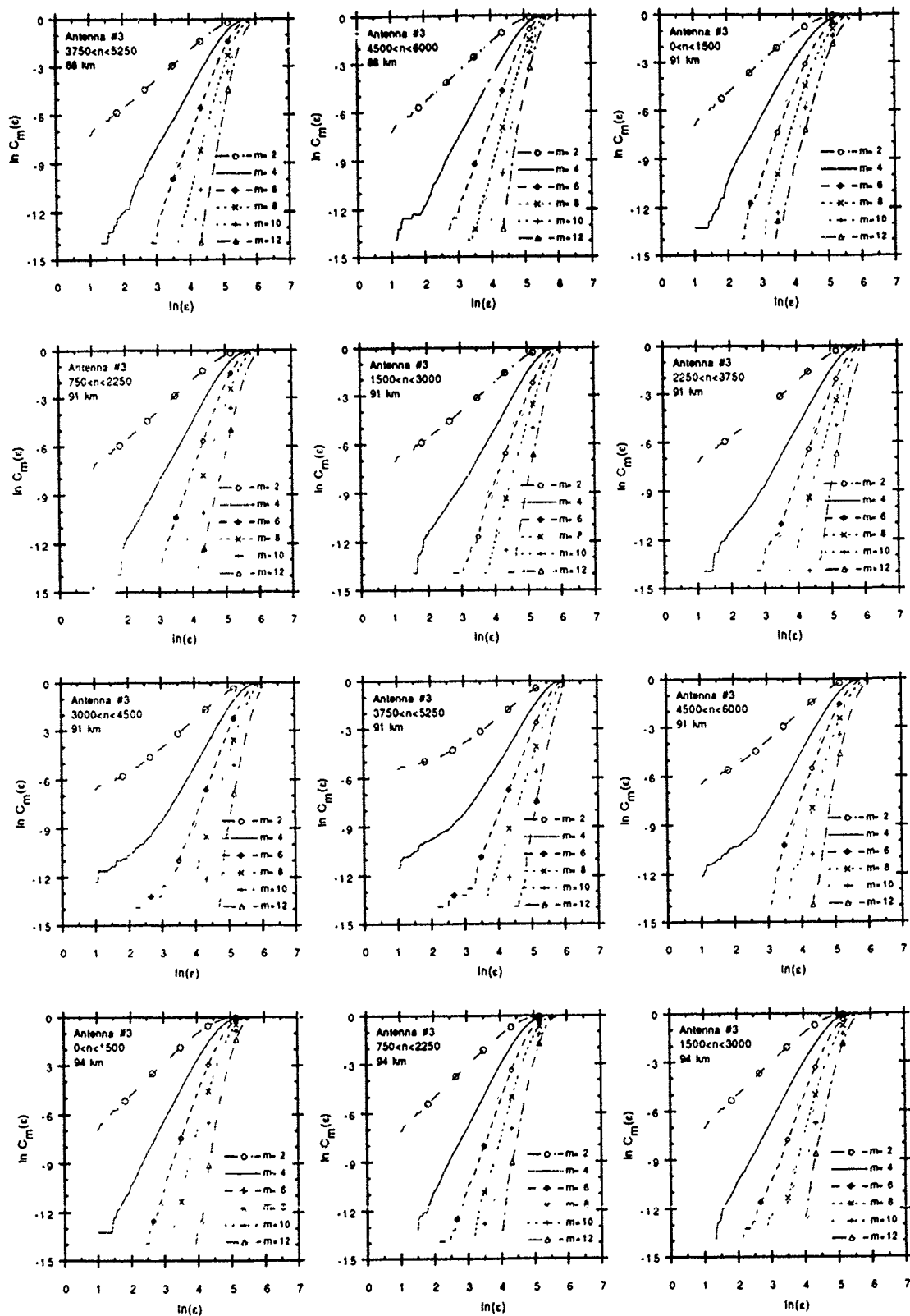


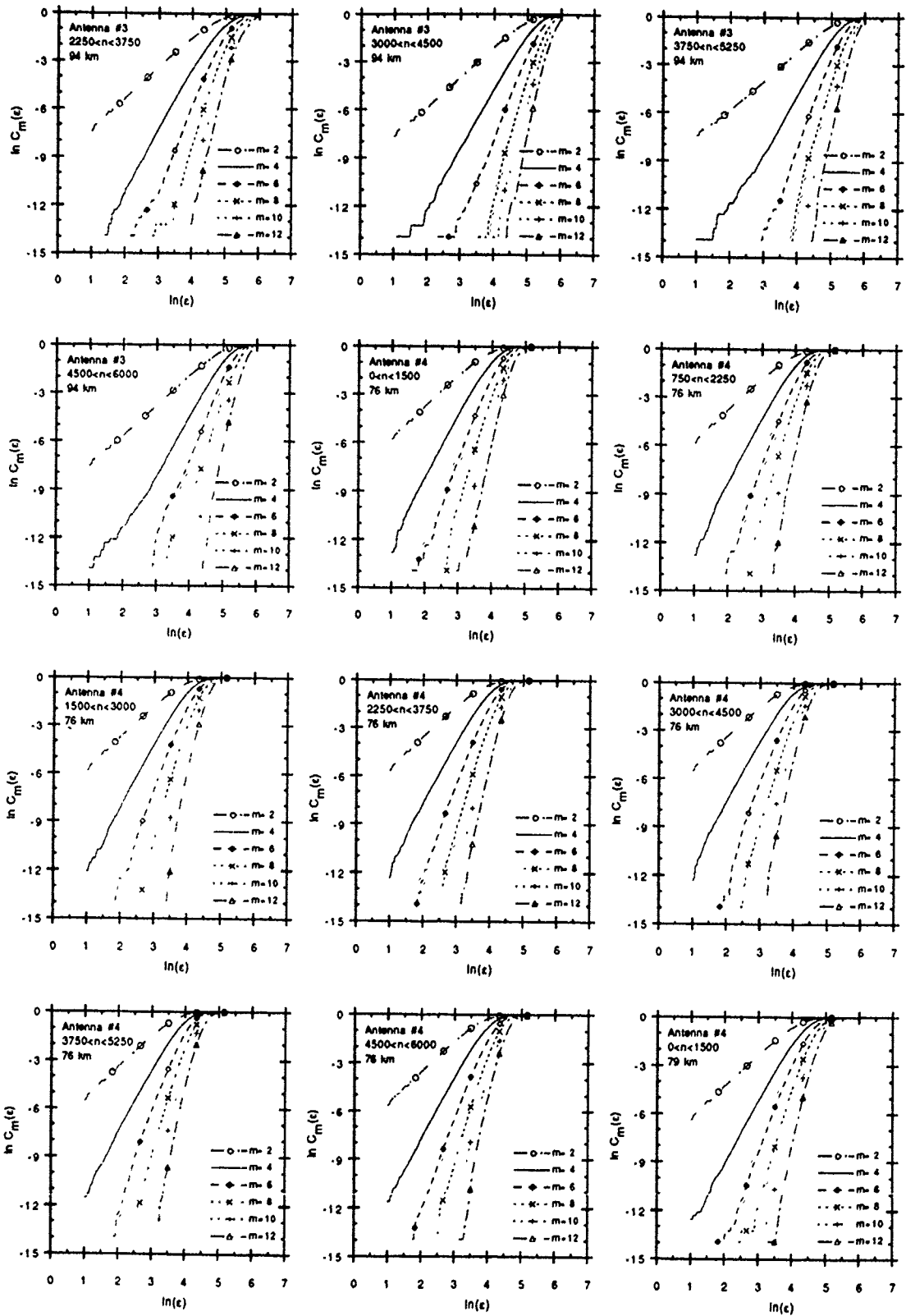


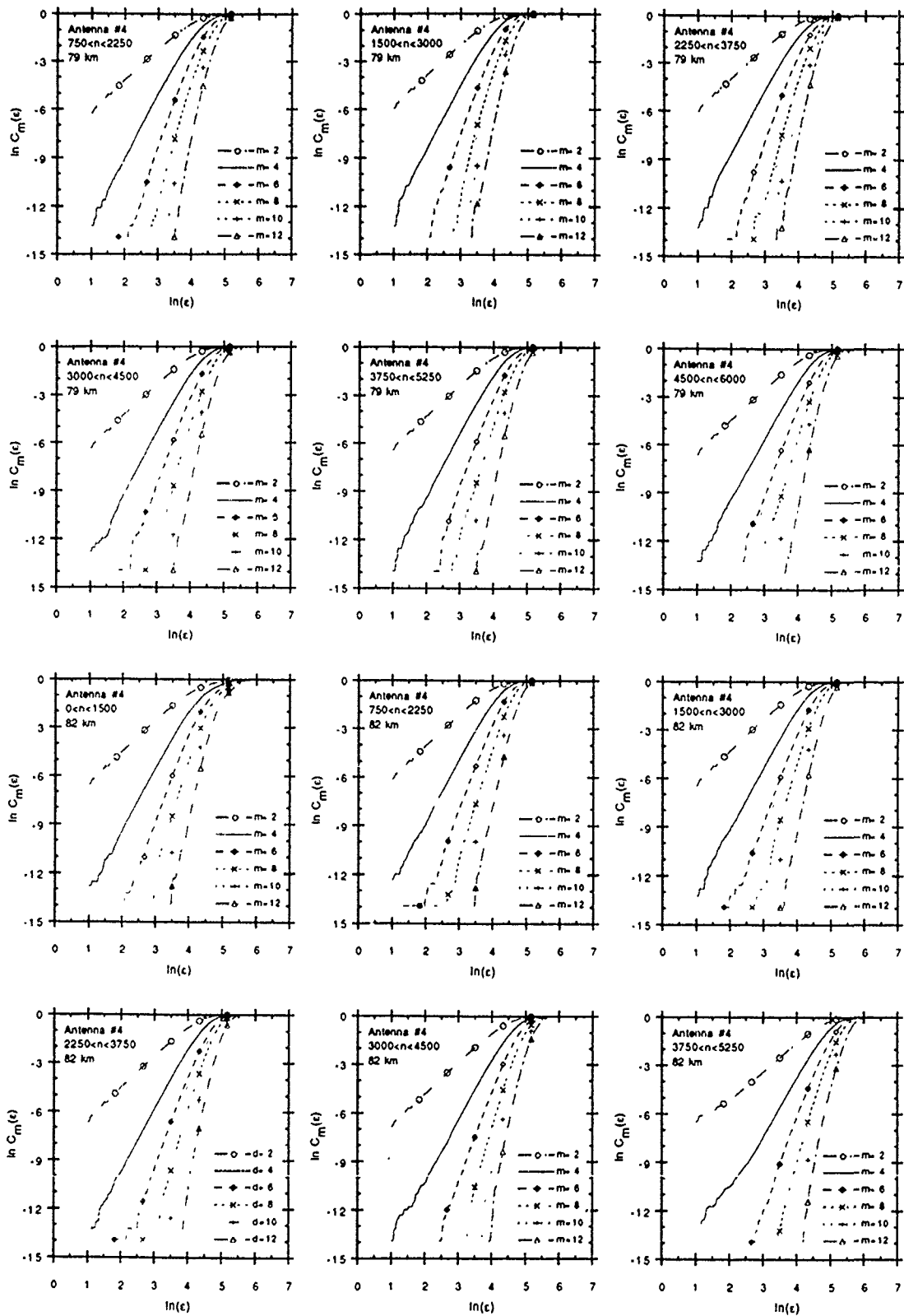


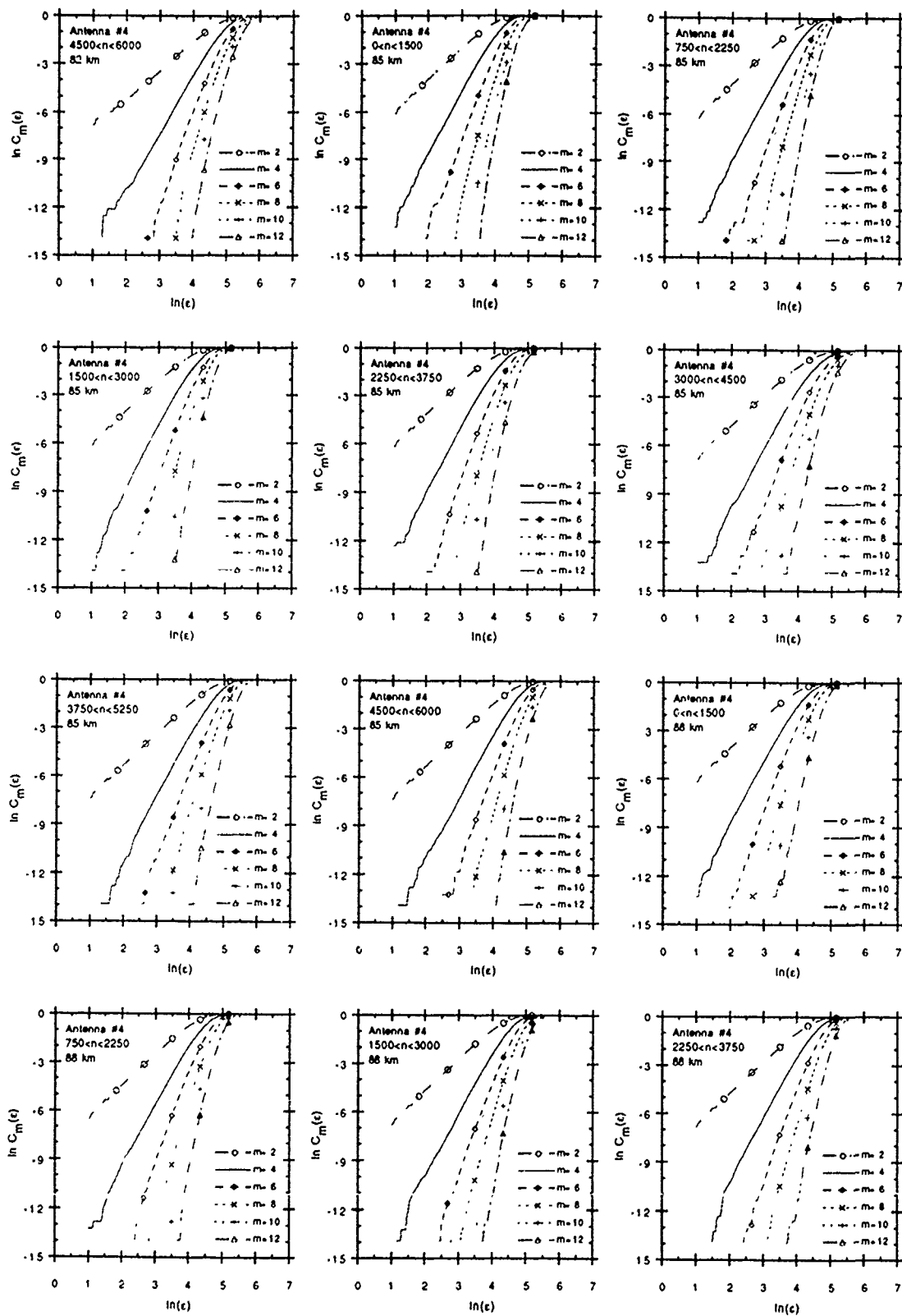


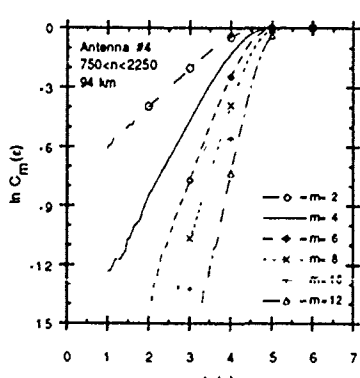
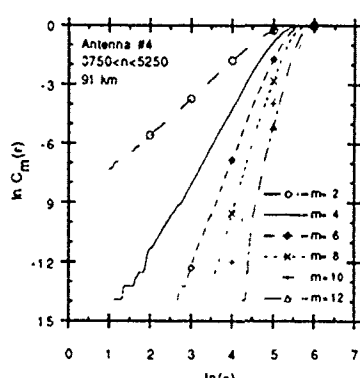
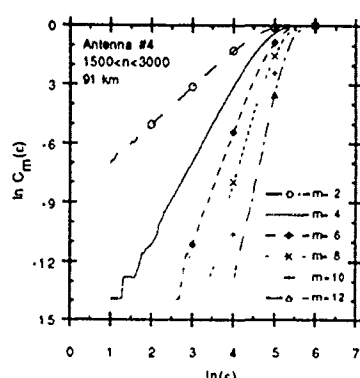
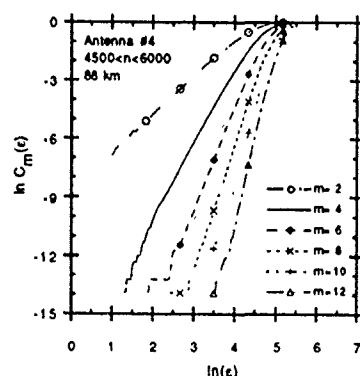


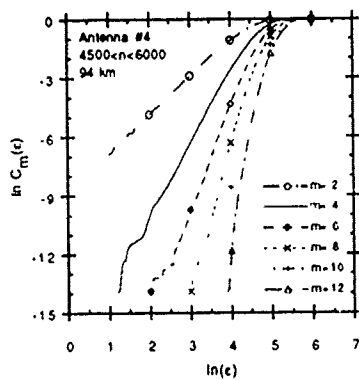
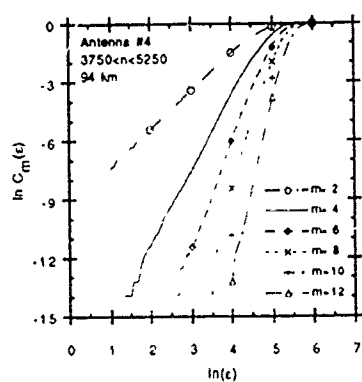
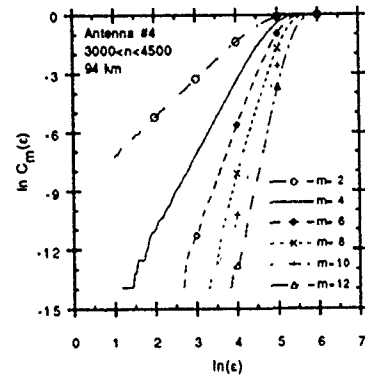
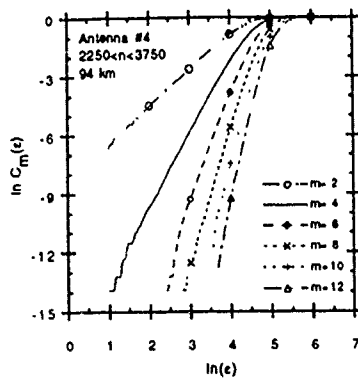
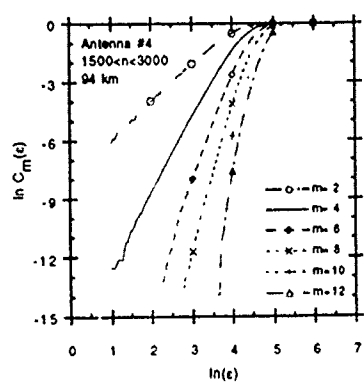






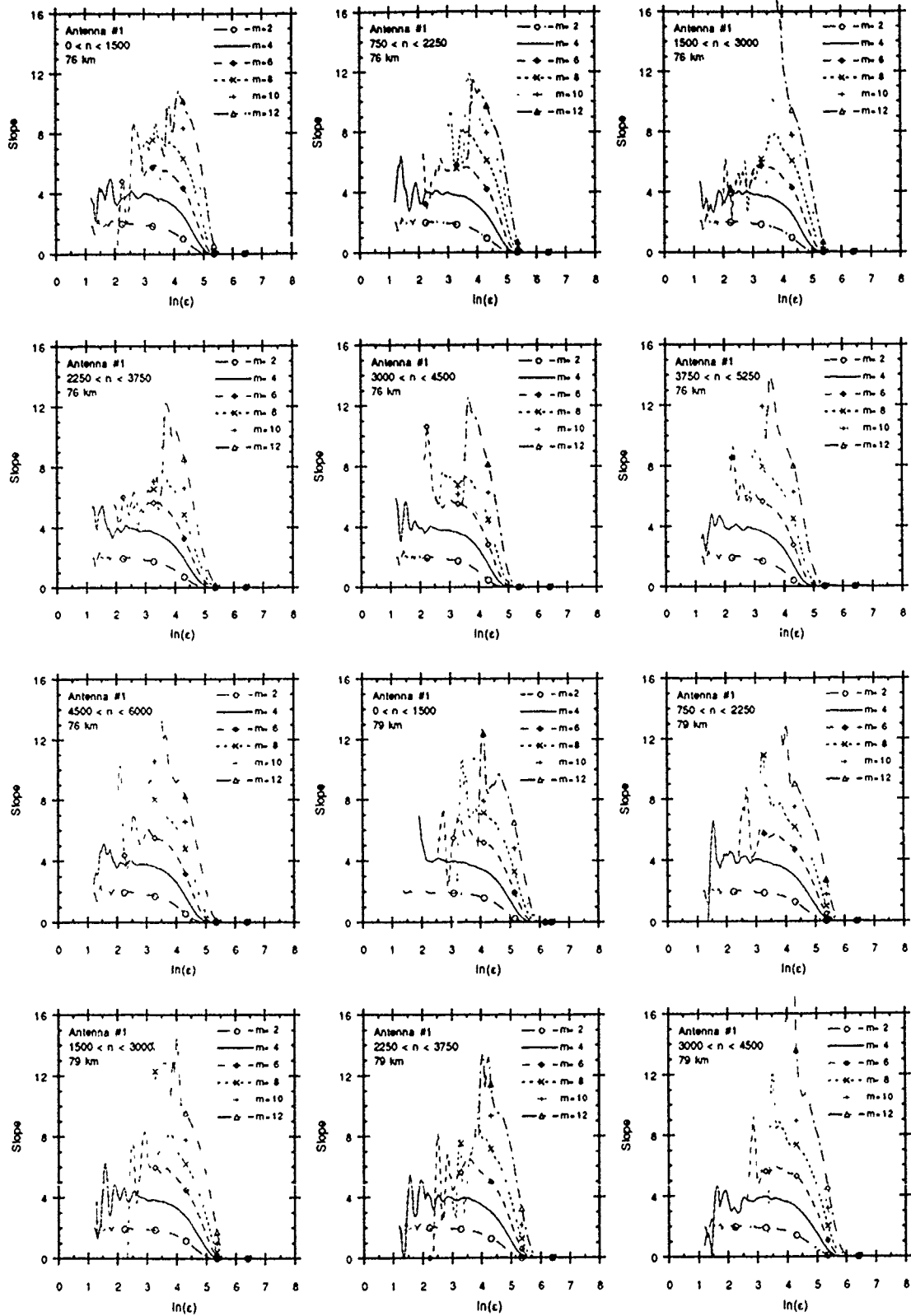


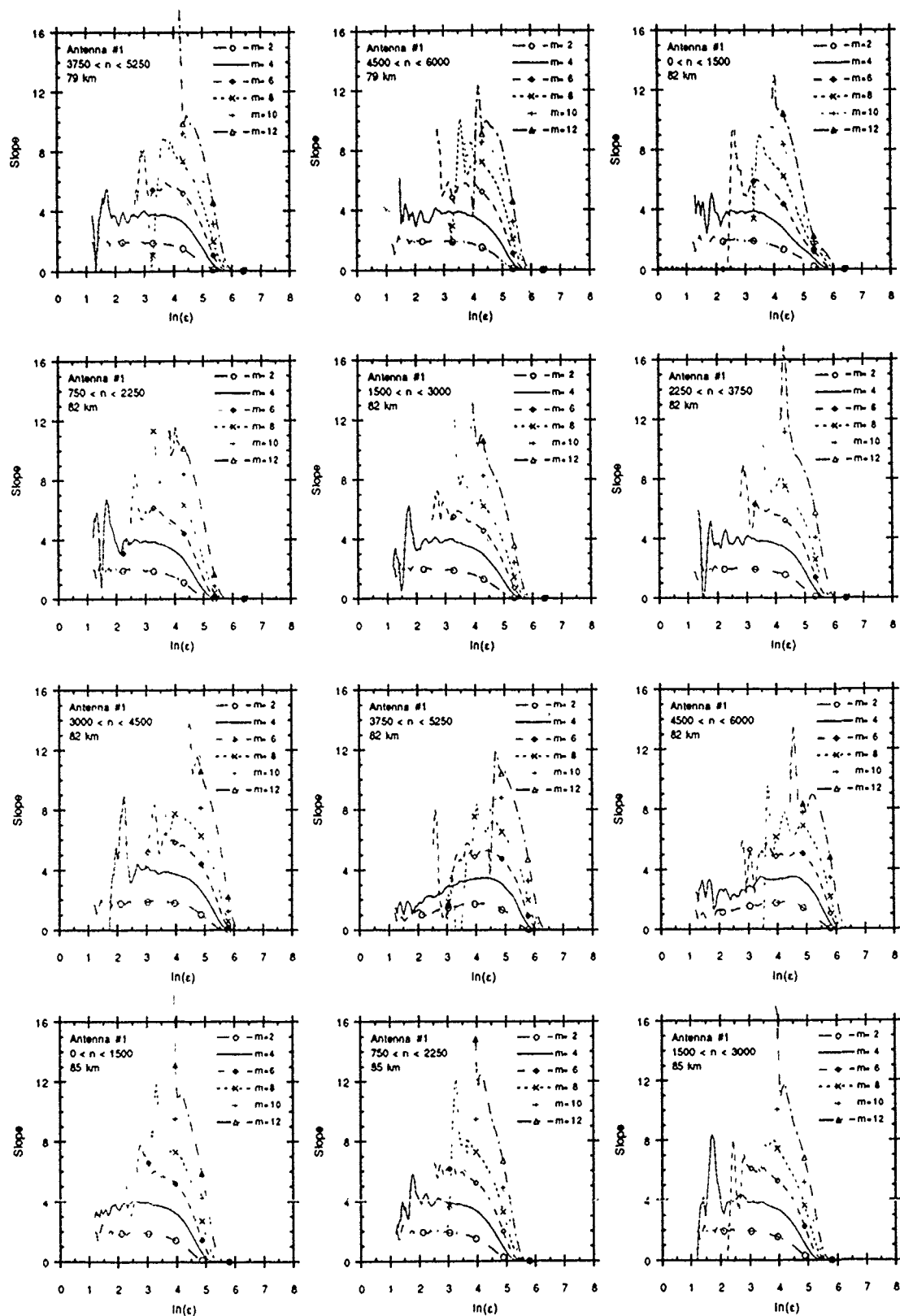


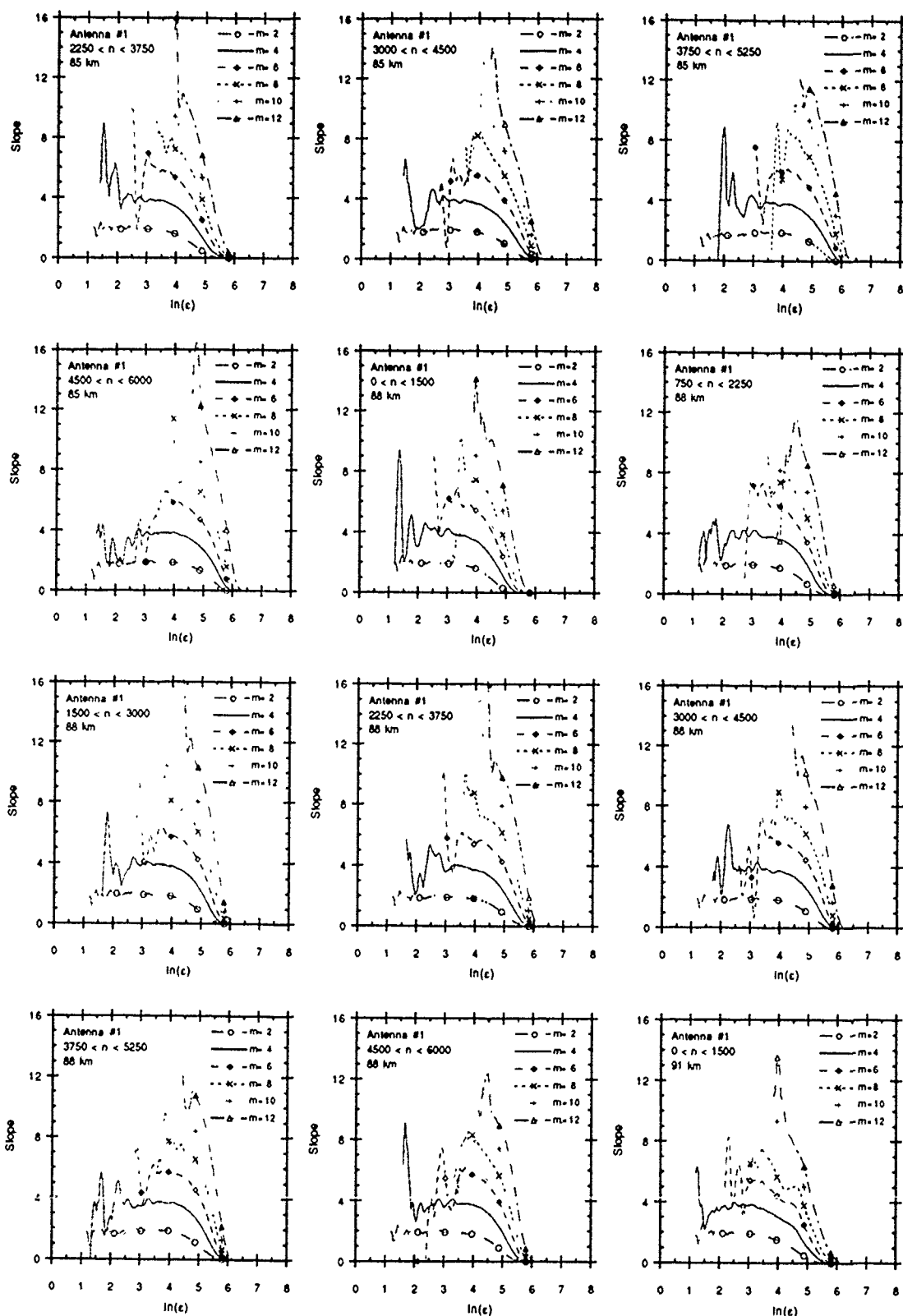


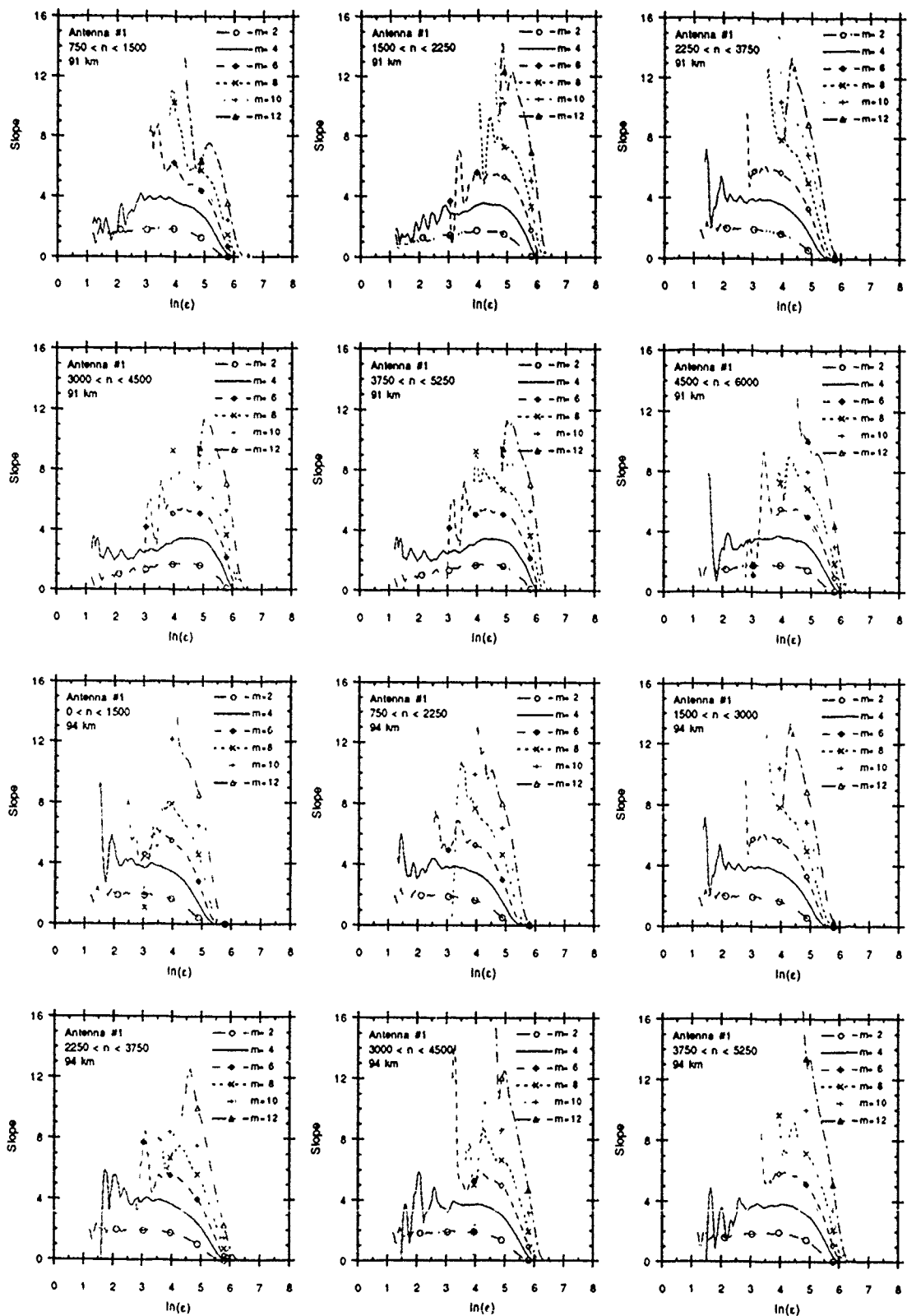
APPENDIX B

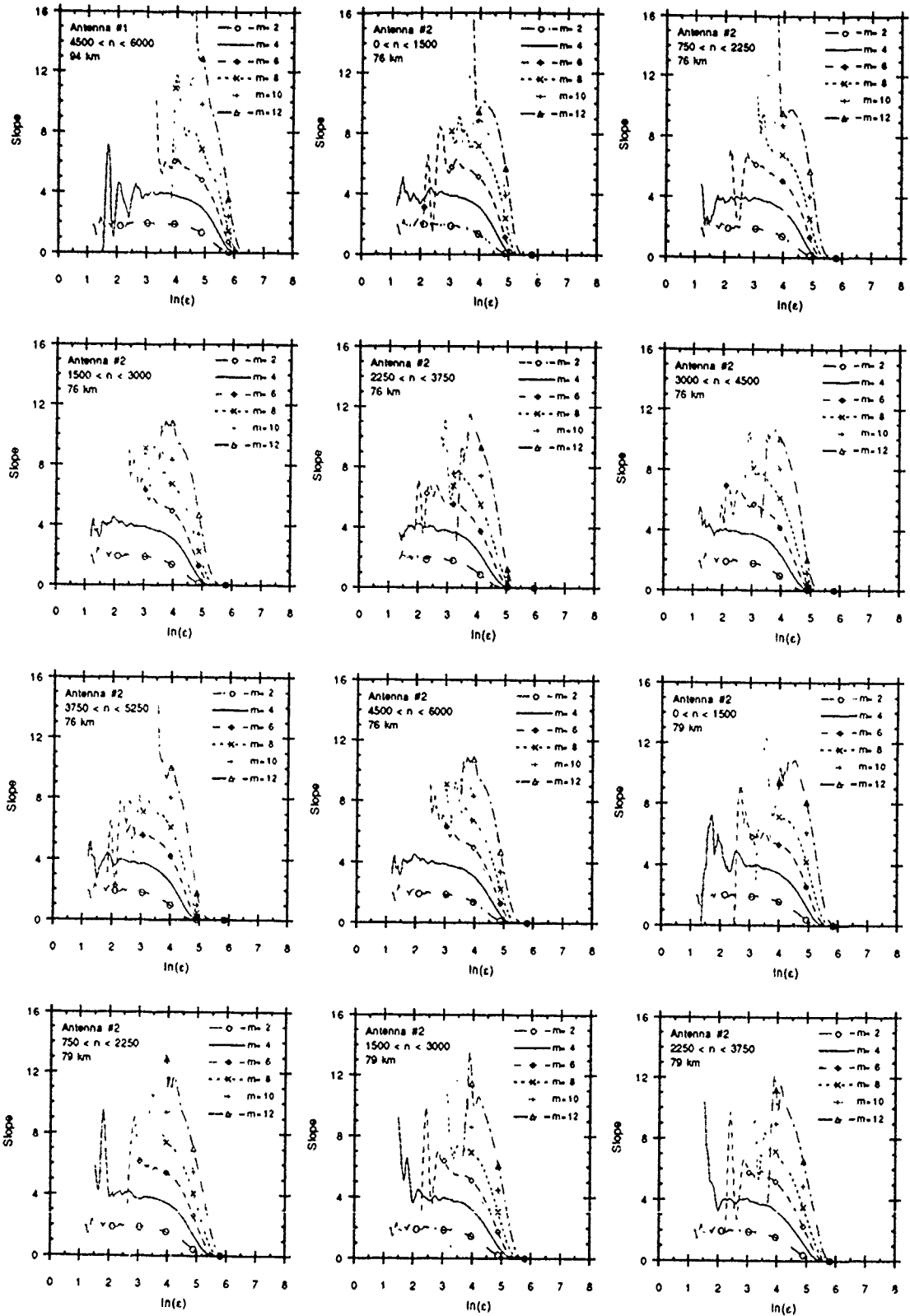
This appendix contains figures depicting the slopes of the correlation integral calculations shown in Appendix A. The slopes were calculated using a seven point fit as described in Chapter V. Output from only every other embedding dimension are shown in an effort to render the figures more legible.

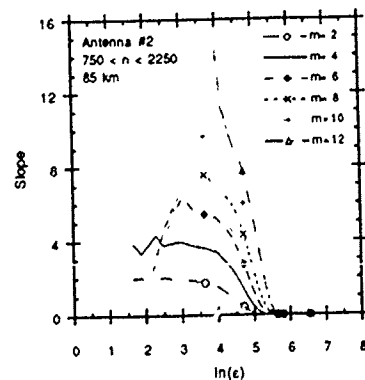
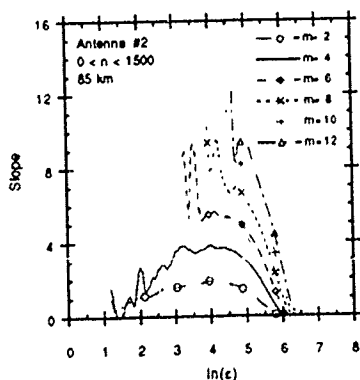
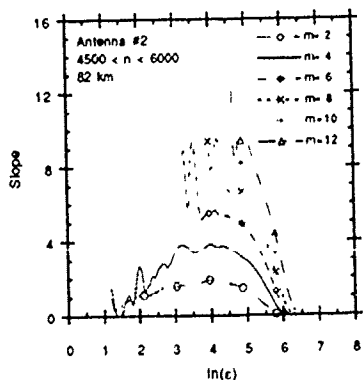
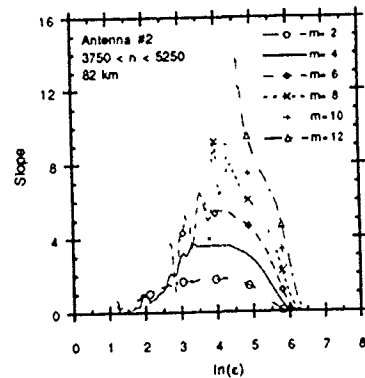
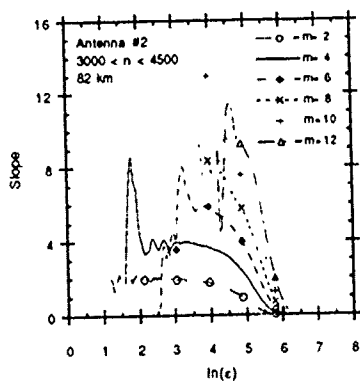
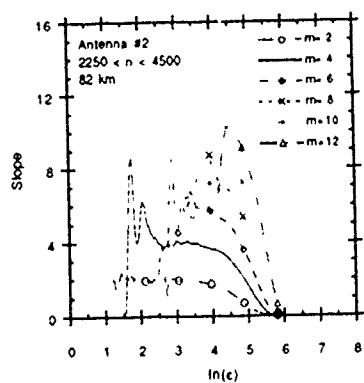
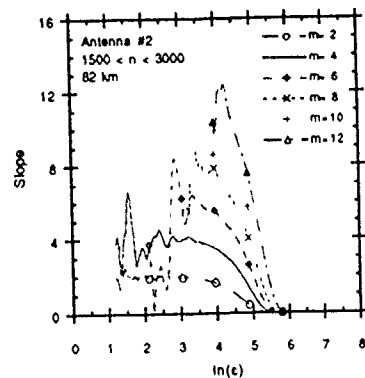
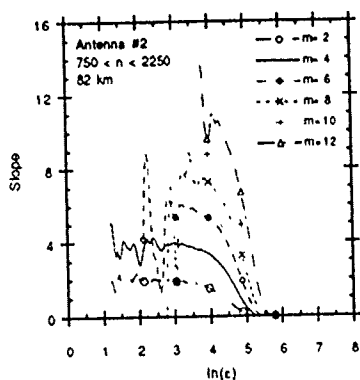
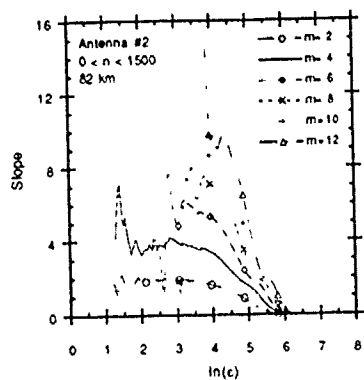
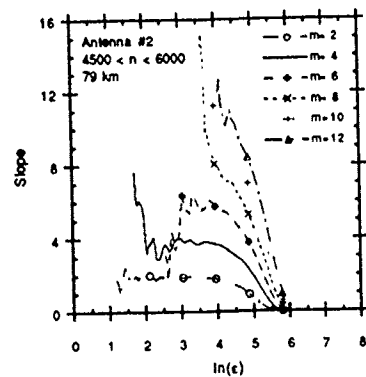
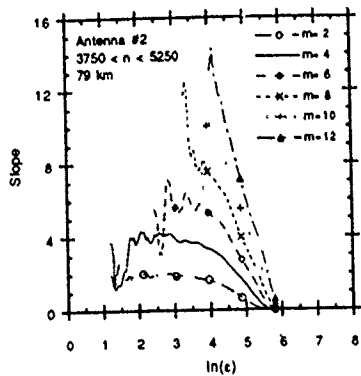
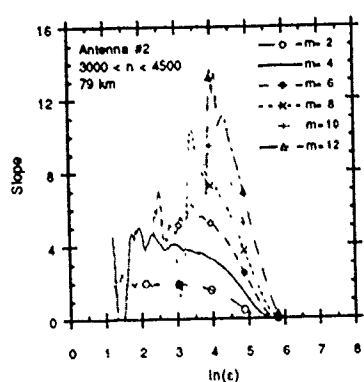


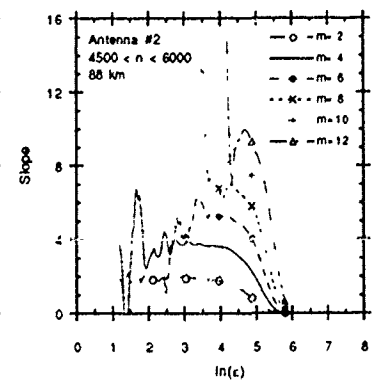
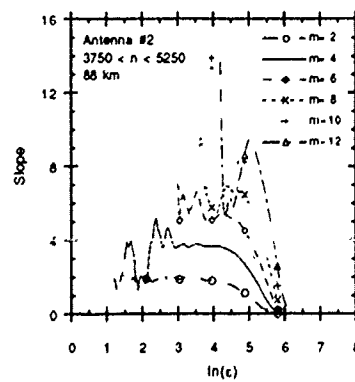
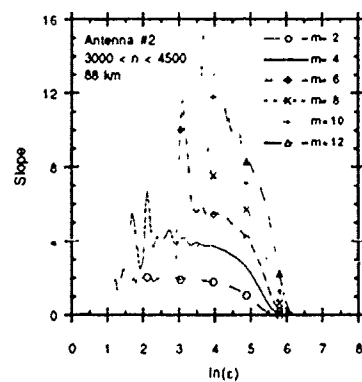
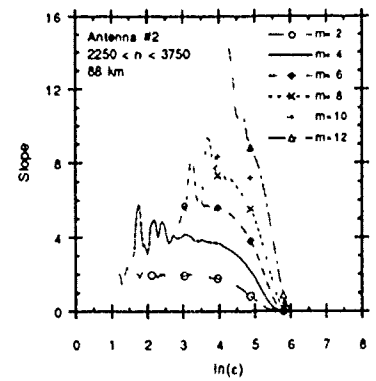
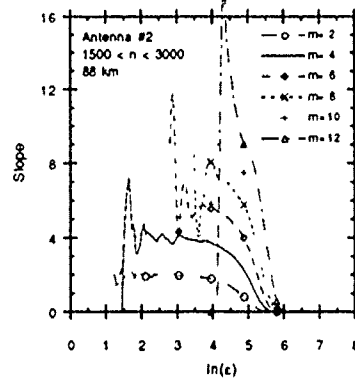
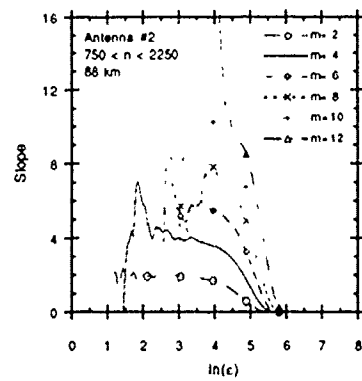
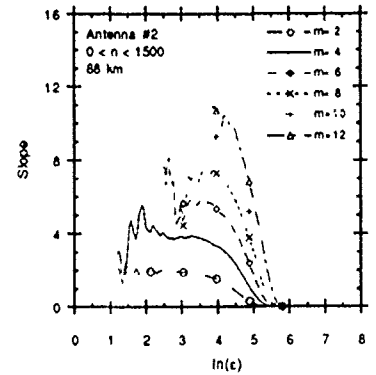
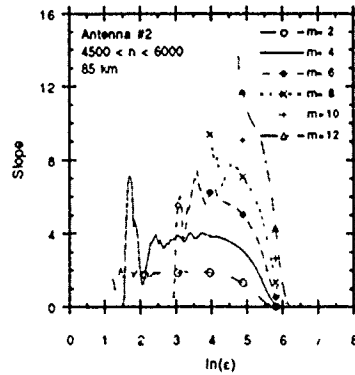
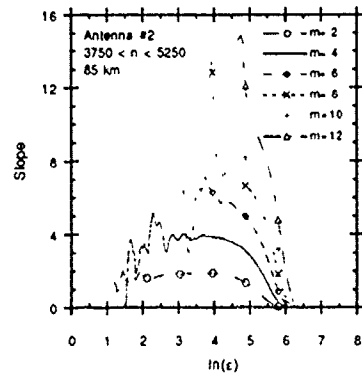
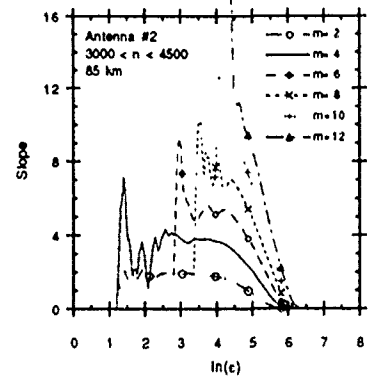
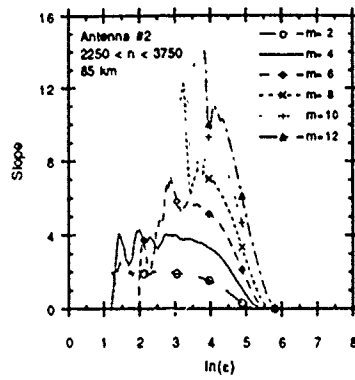
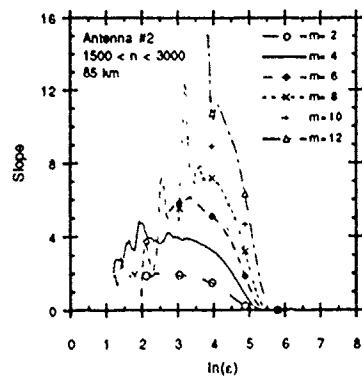


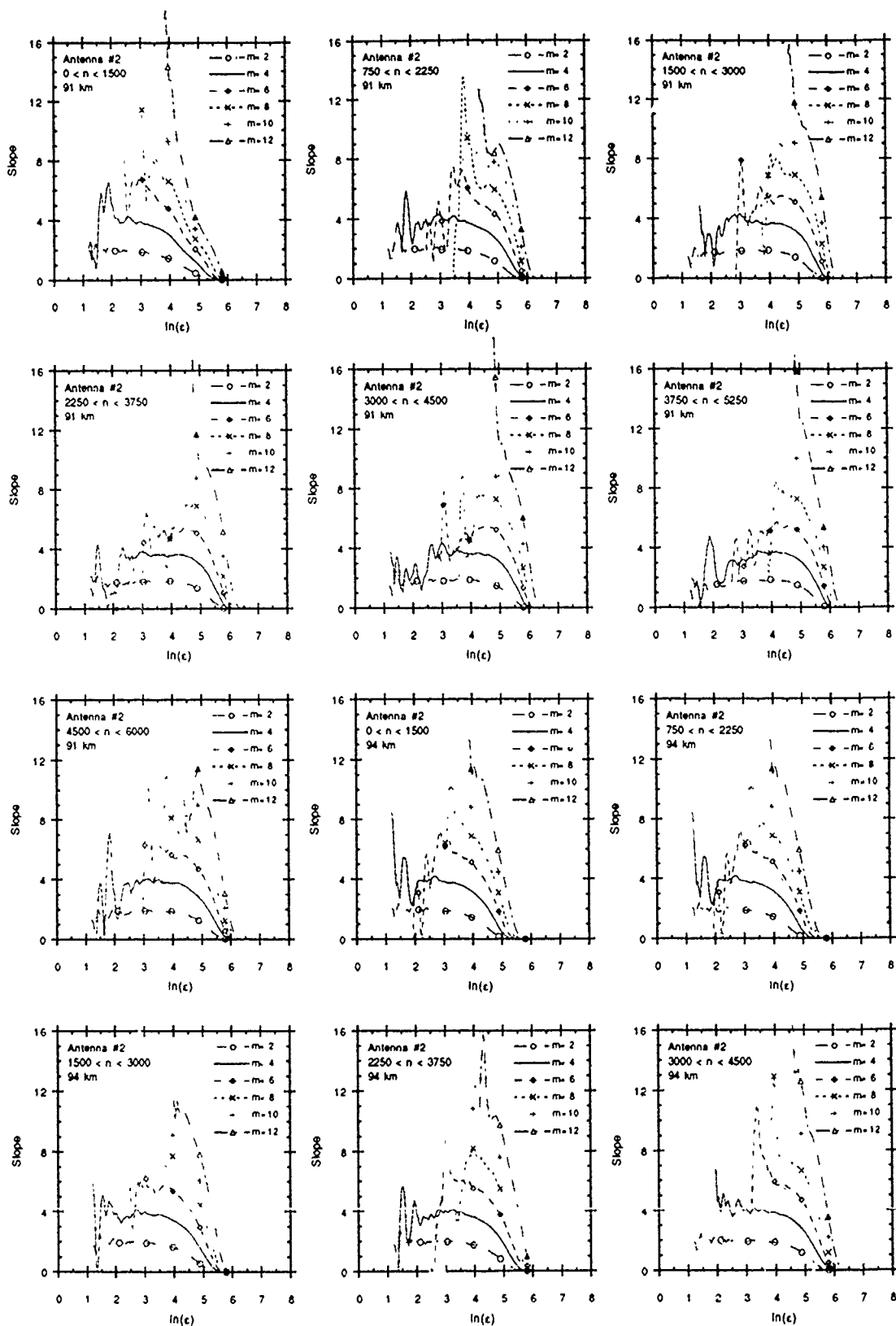


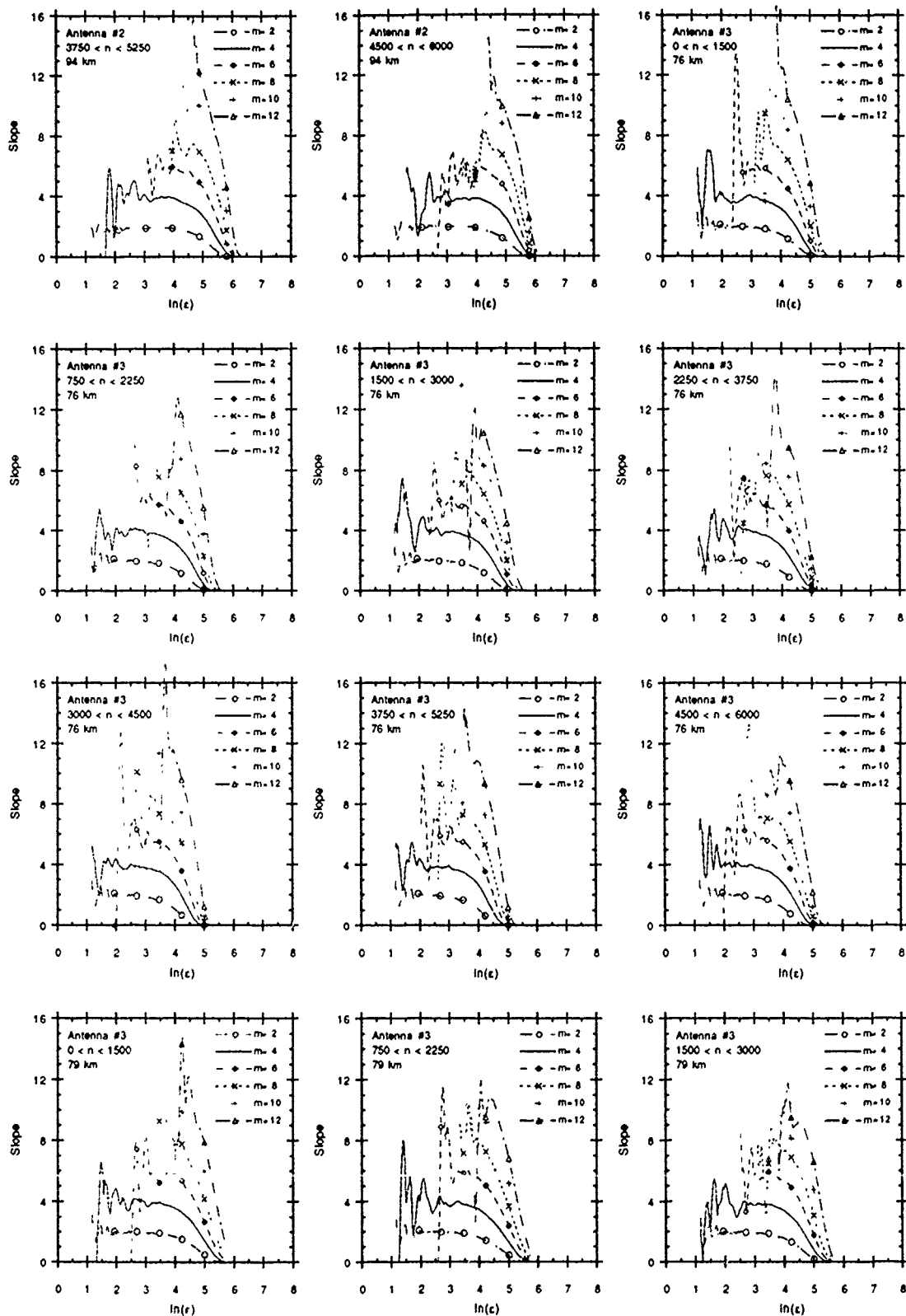


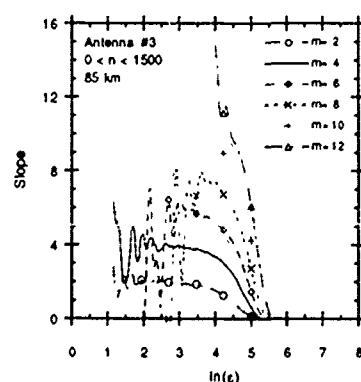
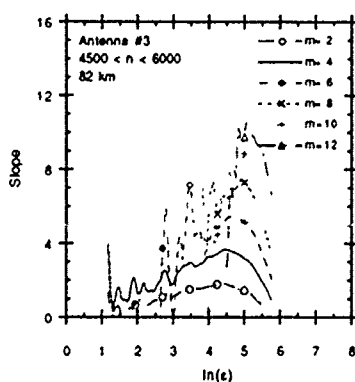
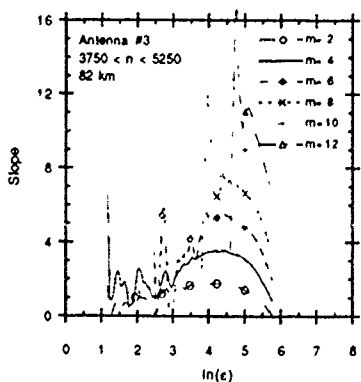
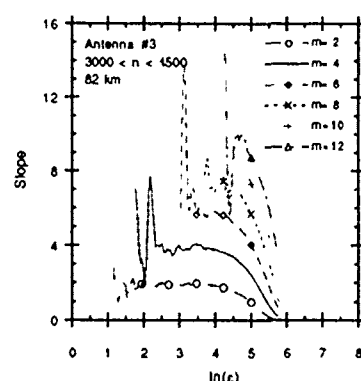
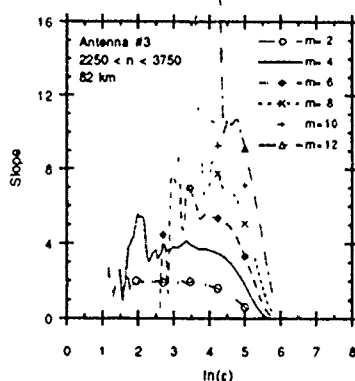
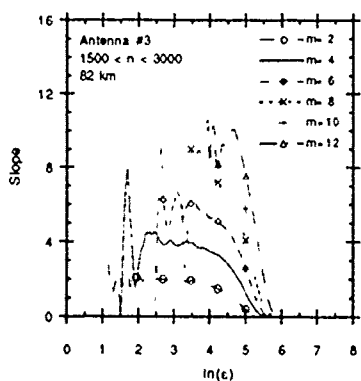
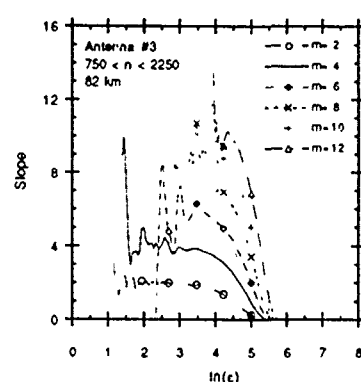
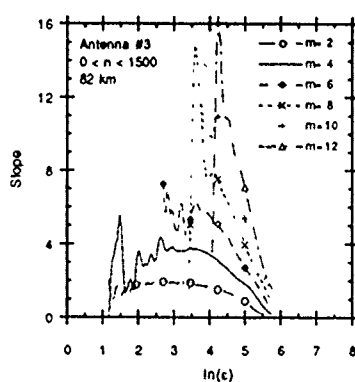
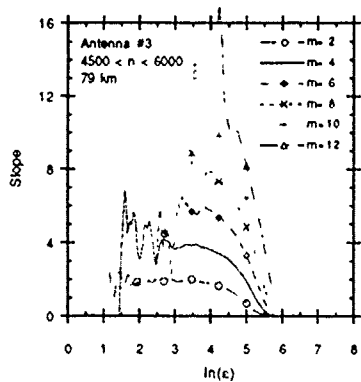
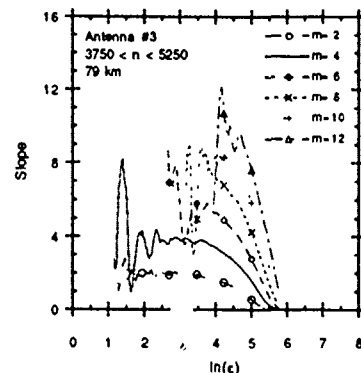
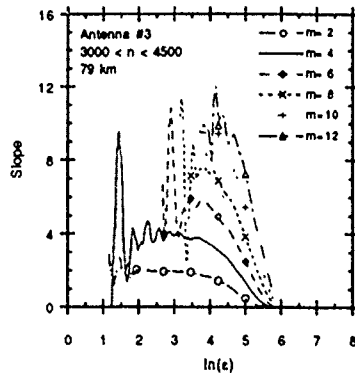
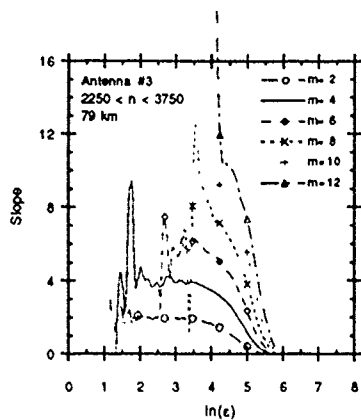


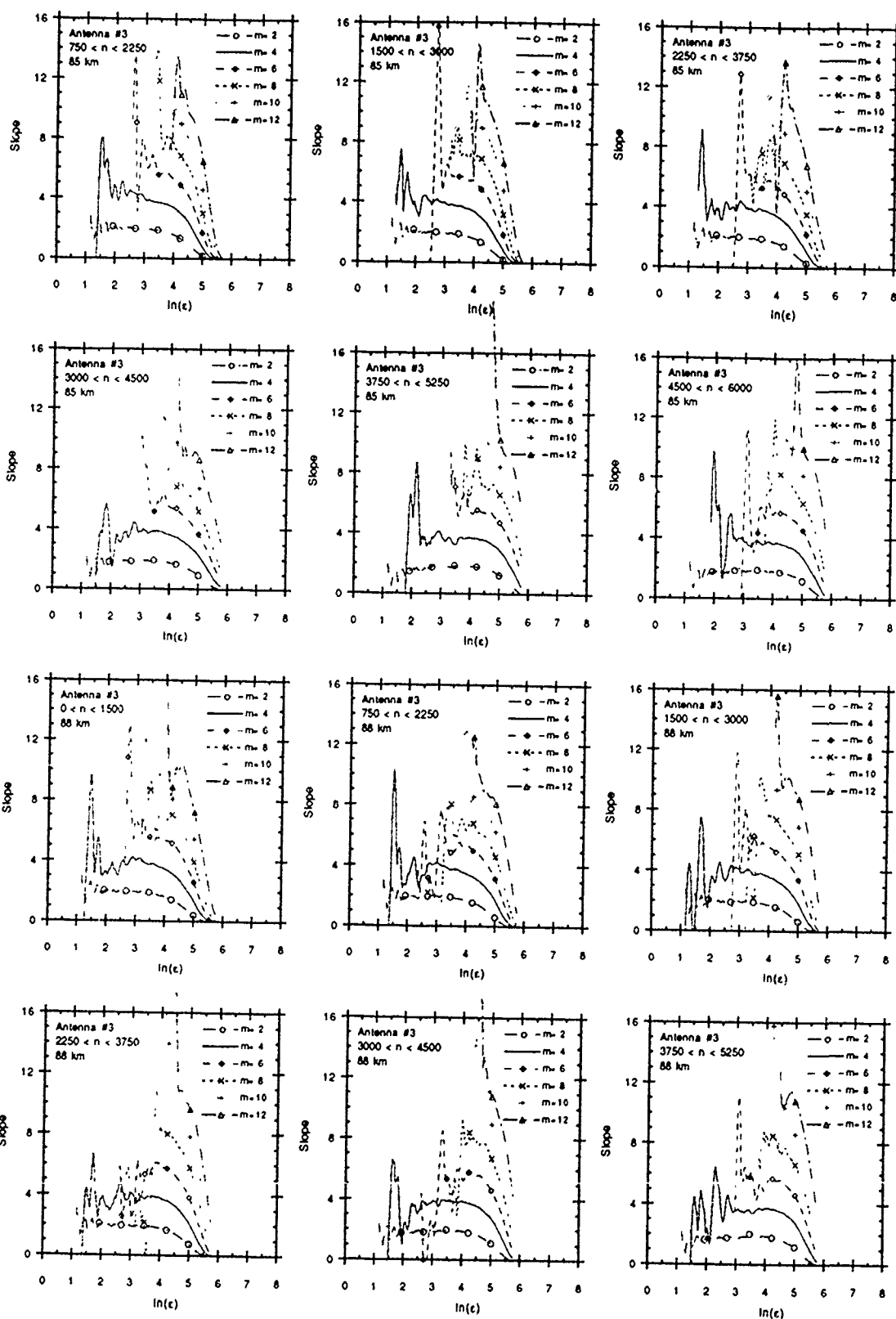


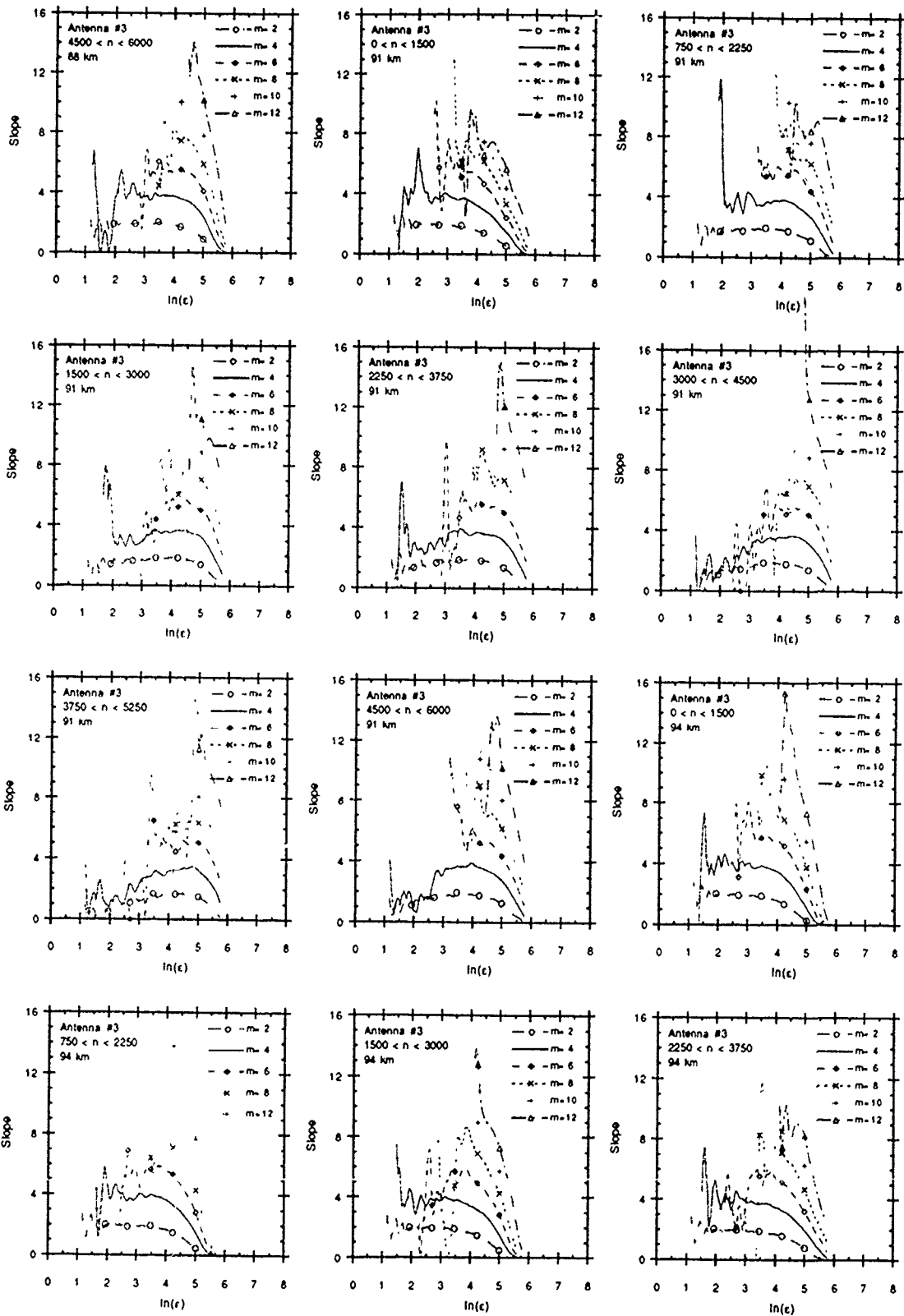


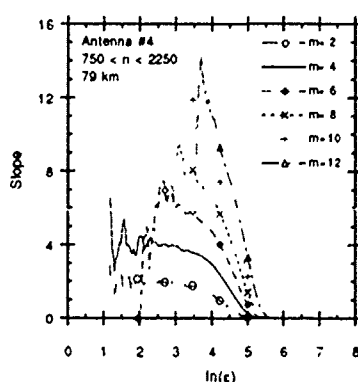
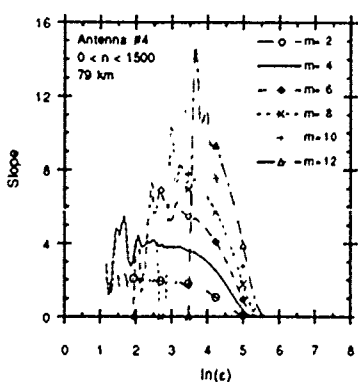
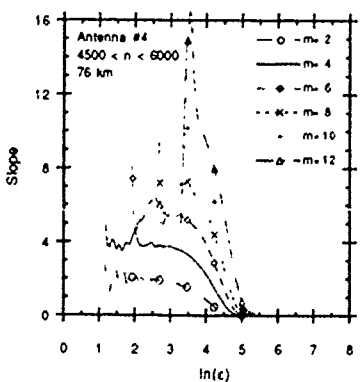
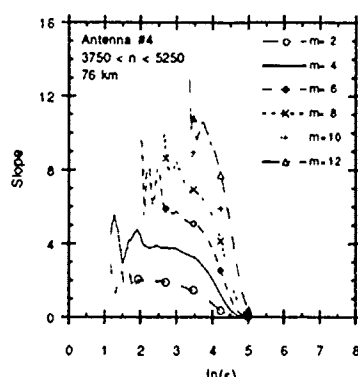
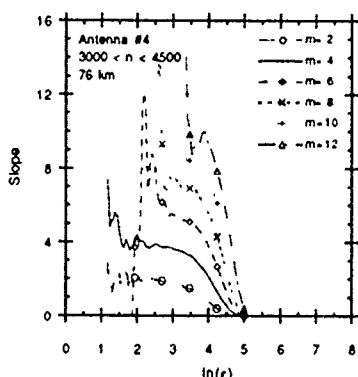
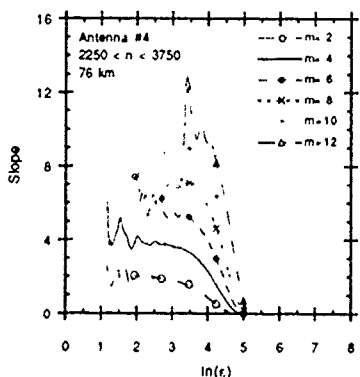
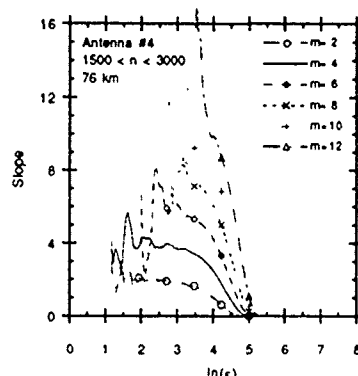
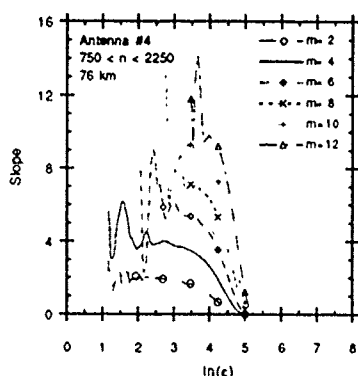
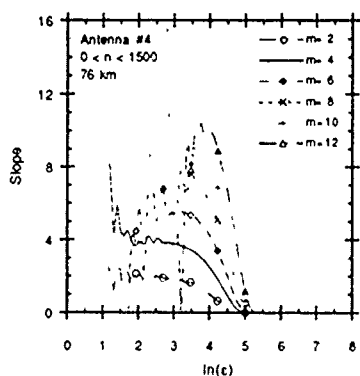
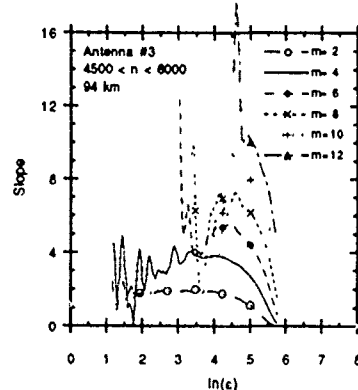
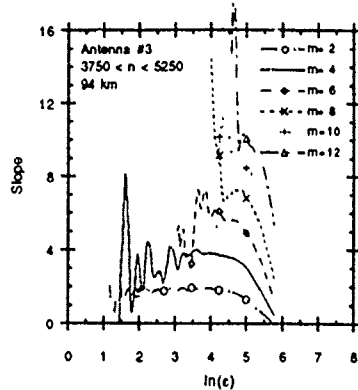
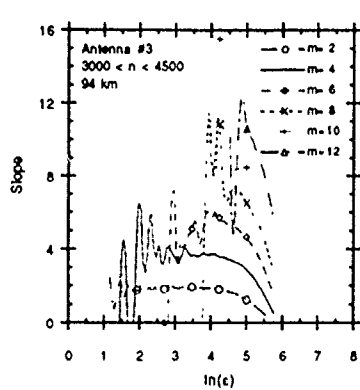


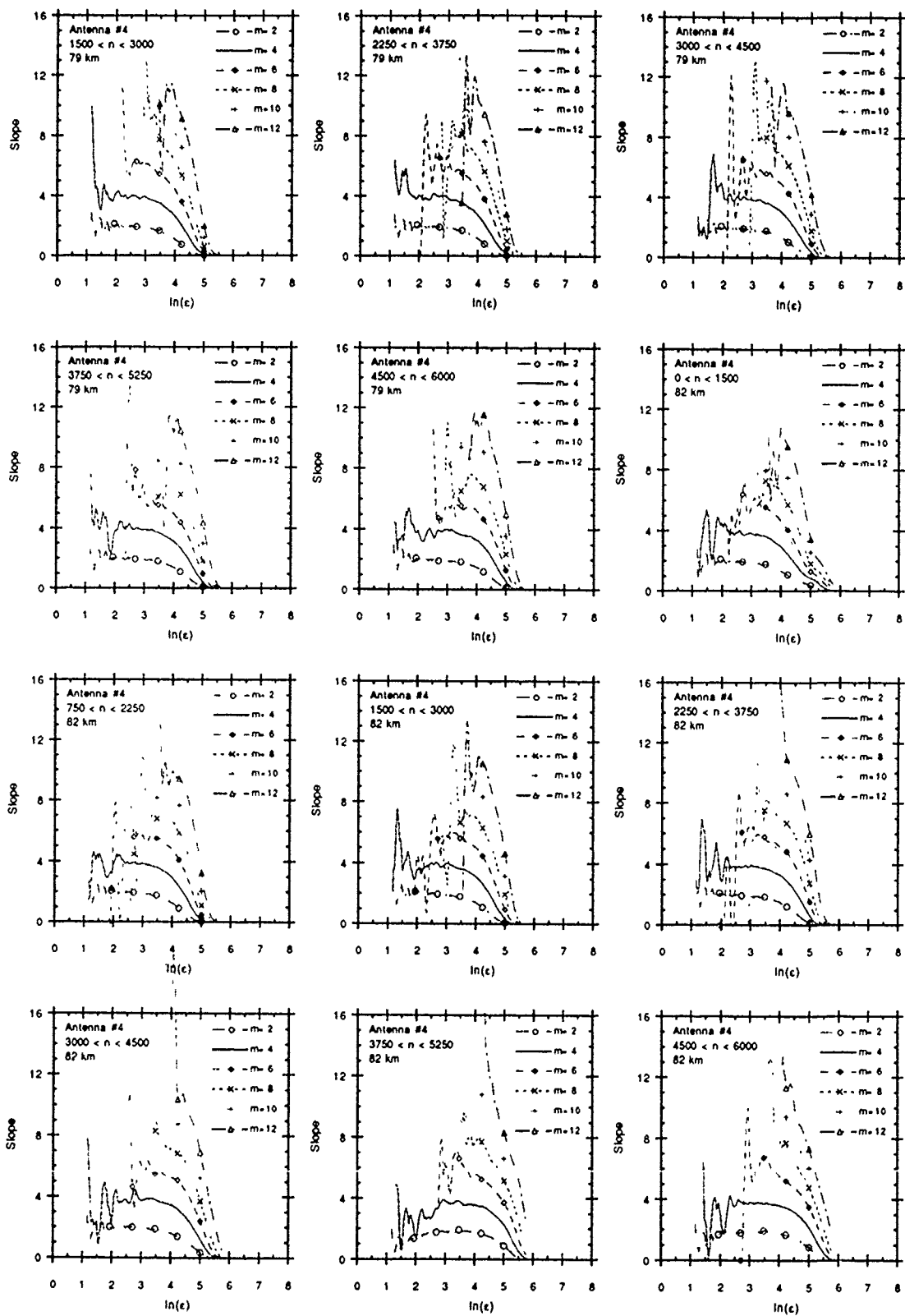


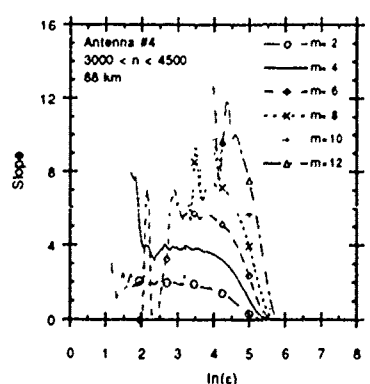
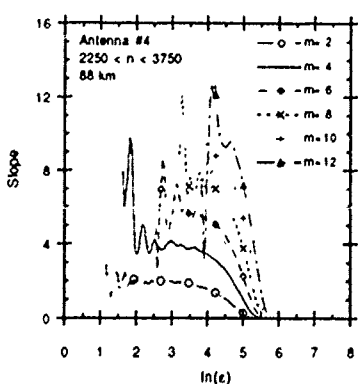
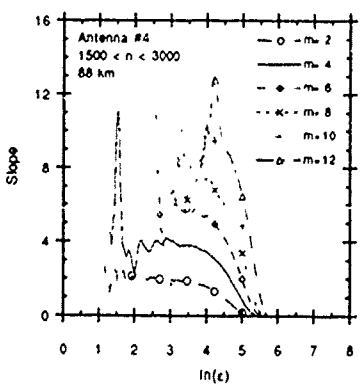
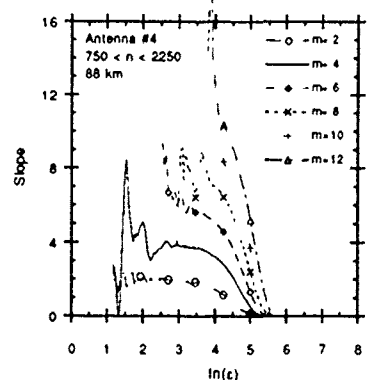
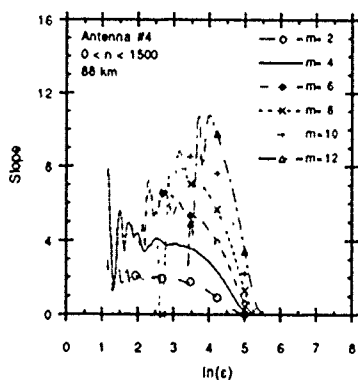
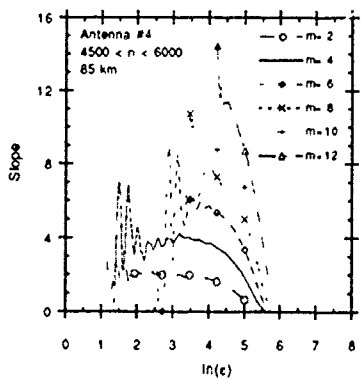
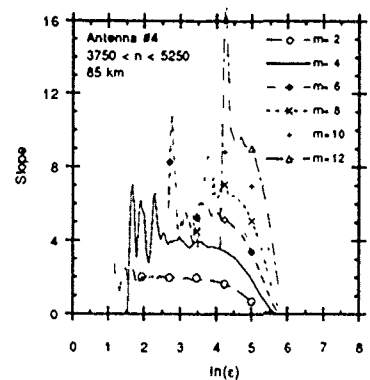
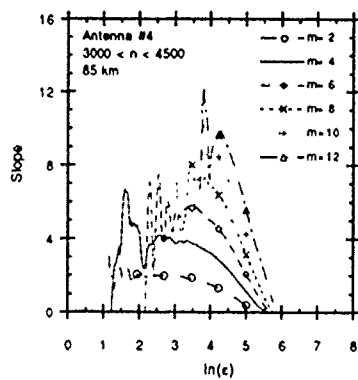
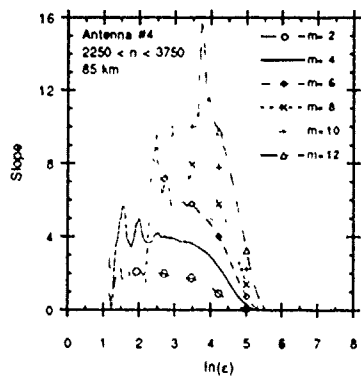
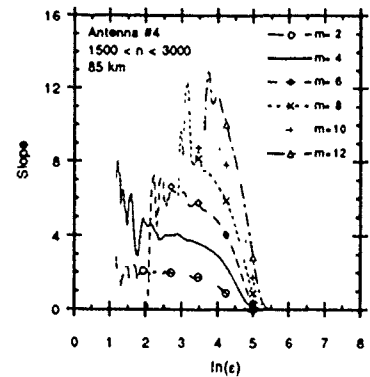
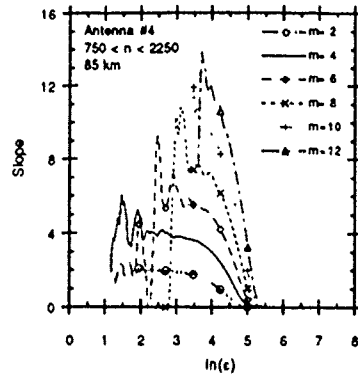
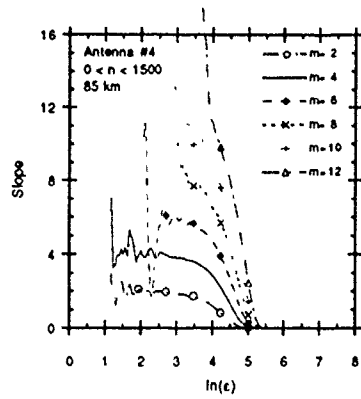


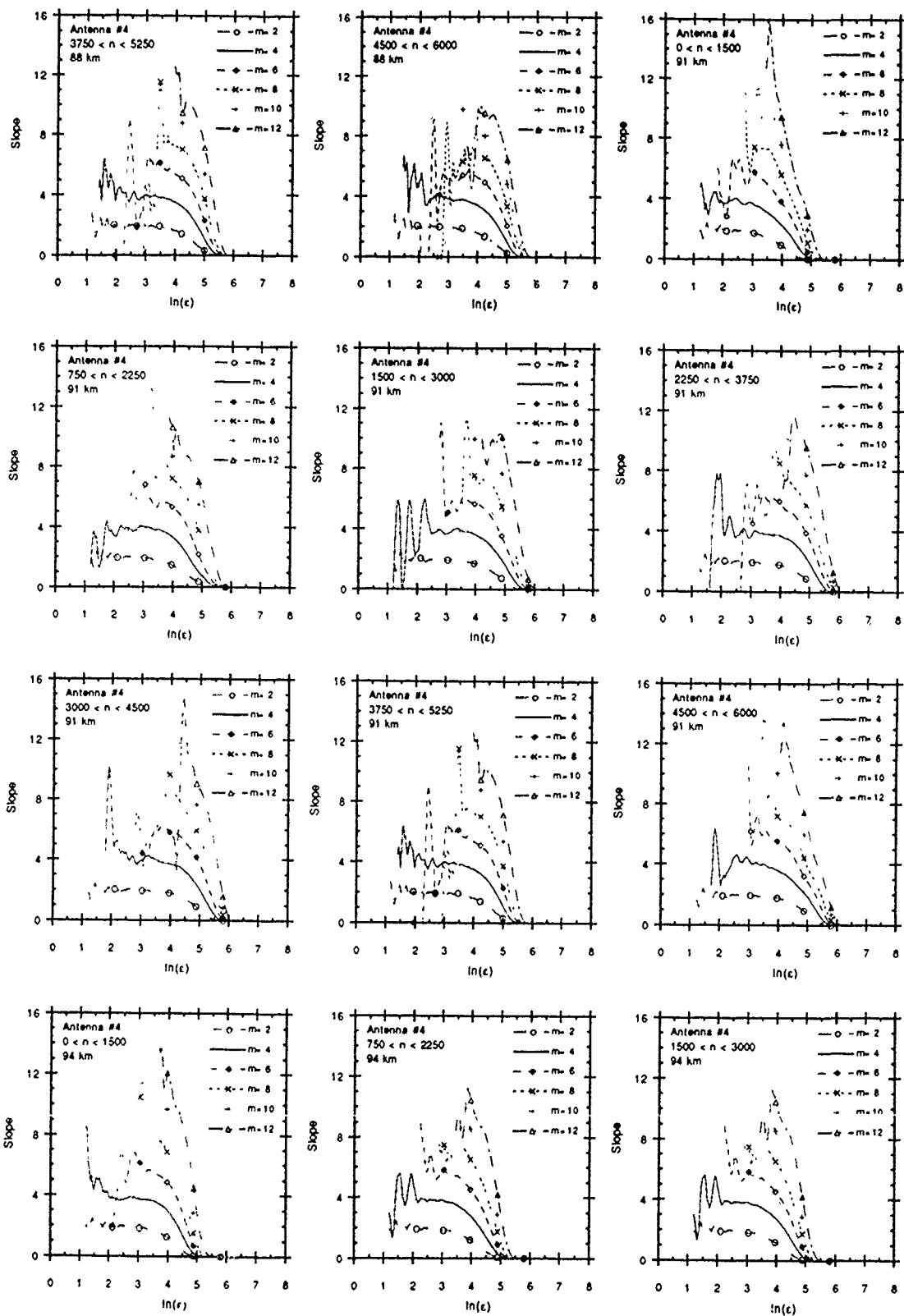


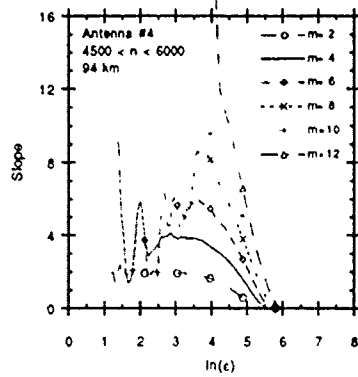
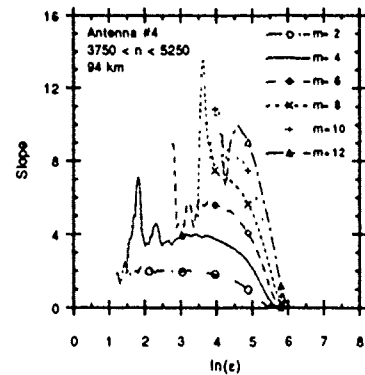
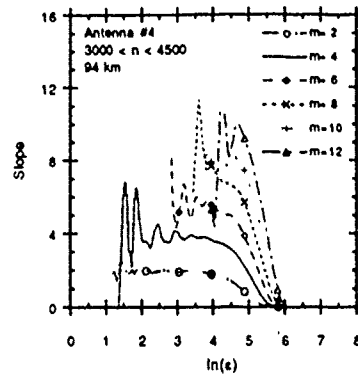
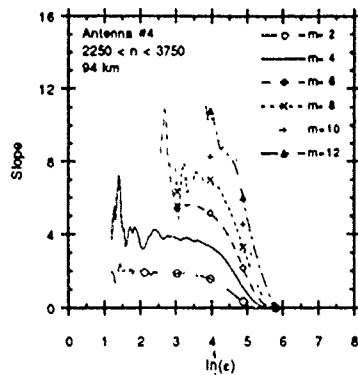












BIBLIOGRAPHY

- Abraham, N. B., A. M. Albano, B. Das, G. De Guzman, S. Yong, R. S. Gioggia, G. P. Puccioni and J. R. Tredicce, 1986: Calculating the dimension of attractors from small data sets. Phys. Lett., 114A, 217-221.
- Albano, A. M., J. Muench, C. Schwartz, A. I. Mees and P. E. Rapp, 1988: Singular-value decomposition and the Grassberger-Procaccia algorithm. Phys. Rev. A, 38, 3017-3026.
- Andrews, D. G., J. R. Holton and C. B. Leovy, 1987: Middle Atmosphere Dynamics. Academic Press, N. Y., 481p.
- Atmanspacher, H., Scheingraber, H. and W. Voges, 1988: Global scaling properties of a chaotic attractor reconstructed from experimental data. Phys. Rev. A, 37A, 1314-1322.
- Badii, R. and A. Politi, 1984: Hausdorff dimension and uniformity factor of strange attractors. Phys. Rev. Lett., 52, 1661-1664.
- Badii, R. and A. Politi, 1987: Renyi dimensions from local expansion rates. Phys. Rev. A, 35, 1288-1293.
- Barnsley, M., 1988: Fractals Everywhere. Academic Press, New York, 394 p.
- Behringer, R. P., 1985: Rayleigh-Bénard convection and turbulence in liquid helium. Rev. Mod. Phys., 57, 657-687.
- Ben-Mizrachi, A. I. Procaccia and P. Grassberger, 1984: Characterization of experimental (noisy) strange attractors. Phys. Rev. A, 29, 975-977.
- Bergé, P., 1989: Chaos and turbulence in Rayleigh-Bénard convection. Physica Scripta, 40, 381-385.

- Bonetti, M. and J-P. Boon, 1989: Chaotic dynamics in open flow: The excited jet. Phys. Rev. A, 40, 3322-3345.
- Brandstätter, A., J. Swift, H. L. Swinney, A. Wolf, J. D. Farmer, E. Jeri and J. P. Crutchfield, 1983: Low dimensional chaos in a hydrodynamic system. Phys. Rev. Lett., 51, 1442-1445.
- Brandstätter, A. and H. L. Swinney, 1987: Strange attractors in weakly turbulent Couette-Taylor flow. Phys. Rev. A, 35A, 2207-2220.
- Broomhead, D. S. and G. P. King, 1986: Extracting qualitative dynamics from experimental data. Physica, 20D, 217-236.
- Chhabra, A., B., C. Meneveau, R. V. Jensen and K. R. Sreenivasan, 1989: Direct determination of the $f(a)$ singularity spectrum and its application to fully developed turbulence. Phys. Rev. A, 40, 5284-5293.
- Delisi, D. P. and G. Corcos, 1973: A study of internal waves in a wind tunnel. Bound. Layer Meteor., 5, 121-137.
- Dewan E. M. and R. E. Good, 1986: Saturation and the "universal" spectrum for vertical profiles of horizontal scalar winds in the atmosphere. J. Geophys. Res., 91, 2742-2748.
- Dunkerton, T. J., 1982: Wave transience in a compressible atmosphere. Part III: The saturation of internal gravity waves in the mesosphere. J. Atmos. Sci., 39, 1042-1051.
- Elgar, S. and G. Mayer-Kress, 1989: Observations of the fractal dimension of deep- and shallow-water ocean surface waves. Physica, 37D, 104-108.
- Ellner, S., 1988: Estimating attractor dimensions from limited data: A new method with error estimates. Phys. Lett. A, 133, 128-133.
- Farmer, J. D., E. Ott and J. A. Yorke, 1983: The dimension of strange attractors. Physica, 7D, 153-180.

- Fraedrich, K., 1986: Estimating the dimensions of weather and climate attractors. J. Atmos. Sci., 43, 419-432.
- Fraedrich, K., 1987: Estimating weather and climate predictability on attractors. J. Atmos. Sci., 44, 722-728.
- Franaszek, M., 1987: Chaotic, nonstrange attractors in the presence of external random noise. Phys. Rev. A, 35, 3162-3165.
- Franaszek, M., 1989: Optimized algorithm for the calculation of correlation integrals. Phys. Rev. A, 39, 5440-5443.
- Fraser, A. M. and H. L. Swinney, 1986: Independent coordinates for strange attractors from mutual information. Phys. Rev. A, 33, 1134-1140.
- Fraser, G. J., 1984: Partial reflection spaced antenna wind measurements. in Middle Atmosphere Program: Handbook for Map Volume 13, Ground based measurements., R. Vincent, ed.
- Fritts, D. C., 1978: The nonlinear gravity wave-critical level interaction. J. Atmos. Sci., 35, 397-413.
- Fritts, D.C., 1984: Gravity wave saturation in the middle atmosphere: A review of theory and observations. Rev. Geophys. Space Phys., 22, 275-308.
- Fritts, D. C., 1985: A numerical study of gravity wave saturation: Nonlinear and multiple wave effects. J. Atmos. Sci., 42, 2043-2058.
- Fritts, D. C. and P. Rastogi, 1985: Convective and dynamic instabilities due to gravity wave motions in the lower and middle atmosphere: Theory and observations. Radio Sci., 20, 1247-1277.
- Froehling, H., J. P. Crutchfield, D. Farmer, N. H. Packard and R. Shaw, 1981: On determining the dimension of chaotic flows. Physica, 3D, 605-617.
- Grassberger, P., 1985: Generalizations of the Hausdorff dimension of fractal measures. Phys. Lett., 107A, 101-105.

Grassberger, P., 1986: Do climatic attractors exist?. Nature, 323, 609-612.

Grassberger, P. and I. Procaccia, 1983: Estimation of the Kolmogorov entropy from a chaotic signal. Phys. Rev. A, 28, 2591-2593.

Grassberger, P. and I. Procaccia, 1984: Dimensions and entropies of strange attractors from a fluctuating dynamics approach. Physica, 13D, 34-54.

Gregory, J. B. and D. G. Stephenson, 1972: High altitude winds from radio reflections. Can. Res. & Dev., 30-34.

Havstad, J. W. and C. L. Ehlers, 1989: Attractor dimension of nonstationary dynamical systems from small data sets. Phys. Rev. A, 39, 845-853.

Henderson, H. W. and R. Wells, 1988: Obtaining attractor dimensions from meteorological time series. Adv. Geophys., 30, 205-237.

Hentschel, H. G. E. and I. Procaccia, 1983: The infinite number of generalized dimensions of fractals and strange attractors. Physica, 8D, 435-444.

Higuchi, T., 1988: Approach to an irregular time series on the basis of fractal theory. Physica, 31D, 277-283.

Hines, C. O., 1960: Internal atmospheric gravity waves at ionospheric heights. Can. J. Phys., 38, 1441-1480.

Hines, C. O., 1988: Generation of turbulence by atmospheric gravity waves. J. Atmos. Sci., 45, 1269-1278.

Hocking, W. K., 1985: Measurement of turbulent energy dissipation rates in the middle atmosphere by radar techniques. Radio Sci., 20, 1403-1422.

Holton, J. R., 1982: The role of gravity wave-induced drag and diffusion in the momentum budget of the mesosphere. J. Atmos. Sci., 39, 791-799.

- Holton, J. R., 1983: The influence of gravity wave breaking on the general circulation of the middle atmosphere. J. Atmos. Sci., 40, 2497-2507.
- Ibrahim, M. M., 1987: Effect of nonlinearity on atmospheric gravity waves. J. Atmos. Sci., 44, 706-720.
- Jackson, E. A., 1989: Perspectives of nonlinear dynamics. Cambridge University Press, New York, 495p.
- Kelley, M. C., 1989: The Earth's Ionosphere: Plasma Physics and Electrodynamics. Academic Press, N. Y., 487p.
- Keppenne, C. L. and C. Nicolis, 1989: Global properties and local structure of the weather attractor over western Europe. J. Atmos. Sci., 46, 2356-2370.
- Kosteilich, E. J. and H. L. Swinney, 1989: Practical considerations in estimating dimension from time series data. Physica Scripta, 40, 436-441.
- Kuo, F., H. Shen, I. Fu, J. Chao, J. Rottger, and C. Liu, 1985: Altitude dependence of vertical velocity spectra observed by VHF radar. Radio Sci., 20, 1349-1354.
- Kurths, J. and H. Herzog, 1987: An attractor in a solar time series. Physica, 25D, 165-172.
- Libchaber, A., S. Fauve and C. Laroche, 1983: Two-parameter study of the routes to chaos. Physica, 7D, 73-84.
- Liebert, W. and H. G. Schuster, 1989: Proper choice of the time delay for the analysis of chaotic time series. Phys. Lett., 142A, 107-111.
- Liebovitch, L. S. and T. Toth, 1989: A fast algorithm to determine fractal dimension by box counting. Phys. Lett., 141A, 386-390.
- Lindzen, R. S., 1981: Turbulence and stress owing to gravity wave and tidal breakdown. J. Geophys. Res., 86, 9707-9714.

- Lindzen, R. S. 1985: Multiple gravity wave breaking levels. J. Atmos. Sci., 42, 301-305.
- Lorenz, E. N., 1963: Deterministic nonperiodic flow. J. Atmos. Sci., 20, 130-141.
- Malraison, B., P. Atten, P. Bergé and M. Dubois, 1983: Dimensions of strange attractors: An experimental determination for the chaotic regime of two convective systems. J. Phys. Lett., 44, 897-902.
- Manson, A. H., J. B. Gregory and D. G. Stephenson, 1974: Winds and wave motions to 110 km at mid-latitudes I. Partial reflection radiowave soundings 1972-1973. J. Atmos. Sci., 31, 2207-2215.
- Manson, A. H. and C. E. Meek, 1987: Small-scale features in the middle atmosphere wind field at Saskatoon, Canada (52° N, 107° W): An analysis of MF radar data with rocket comparisons. J. Atmos. Sci., 44, 3661-3672.
- Mathews, J. and R. L. Walker, 1970: Mathematical Methods of Physics. Benjamin/Cummings Publishing Co., London, 501p.
- Meek, C. E. and A. H. Manson, 1987: Mesospheric motions observed by simultaneous medium-frequency interferometer and spaced antenna experiments. J. Geophys. Res., 92D, 5627-5639.
- Meek, C. E., I. M. Reid and A. H. Manson, 1985: Observations of mesospheric wind velocities. 1. Gravity wave horizontal scales and phase velocities determined from spaced wind observations. Radio Sci., 20, 1363-1382.
- Meek, C. E., I. M. Reid and A. H. Manson, 1985: Observations of mesospheric wind velocities. 2. Cross sections of power spectral density for 48-8 hours, 8-1 hours and 1 hour to 10 minutes over 60-110 km for 1981. Radio Sci., 20, 1383-1402.
- Meneveau, C. and M. Nelkin, 1989: Attractor size in intermittent turbulence. Phys. Rev. A, 39, 3732-3733.
- Möller, M., W. Lange, F. Mitschke, N. B. Abraham and U. Hübner, 1989: Errors from digitizing and noise in estimating attractor dimension. Phys. Lett., 138A, 176-182.

Osborne, A. R., A. D. Kirwan, Jr., A. Provenzale and L. Bergamsco, 1986: A search for chaotic behavior in large and mesoscale motions in the Pacific Ocean. Physica D, 23D, 75-83.

Osborne, A. R. and A. Provenzale, 1989: Finite correlation dimensions for stochastic systems with power law spectra. Physica, 35D, 357-381.

Packard, N. H., J. P. Crutchfield, J. D. Farmer and R. S. Shaw, 1980: Geometry from a time series. Phys. Rev. Lett., 45, 712-716.

Pawelzik, K. and H. G. Schuster, 1987: Generalized dimensions and entropies from a measured time series. Phys. Rev. A, 35, 481-484.

Press, W., H., B. P. Flannery, S. A. Teukolsky and William T. Vetterling, 1986: Numerical Recipes: The Art of Scientific Computing, Cambridge University Press, N.Y.

Ramsey, J. B. and H. J. Yuan, 1989: Bias and error bars in dimension calculations and their evaluation in some simple models. Phys. Lett., 134A, 287-297.

Roux, J. -C., R. H. Simoyi, and H. L. Swinney, 1983: Observation of a strange attractor. Physica, 8D, 257-266.

Sato, T., T. Tsuda, S. Kato, S. Morimoto, S. Fukao and I. Kimera, 1985: High resolution MST observations of turbulence using the MU radar. Radio Sci., 20, 1452-1460.

Schuster, H. G., 1989: Information content of chaotic signals. Physica Scripta, 40, 367-372.

Smith, L. A., J. -D. Fournier and E. A. Spiegel, 1986: Lacunarity and intermittancy in fluid turbulence. Phys. Lett., 114A, 465-468.

Smith, L. A., 1988: Intrinsic limits on dimension calculations. Phys. Lett., 133A, 283-288.

- Swinney, H. L., 1983: Observations of order and chaos in nonlinear systems. Physica, 7D, 3-15.
- Theiler, J., 1986: Spurious dimension from correlation algorithms applied to limited time-series data. Phys. Rev. A, 34, 2427-2432.
- Theiler, J., 1988: Lacunarity in a best estimator of fractal dimension. Phys. Lett., 133A, 195-200.
- Triton, D. J., 1988: Physical Fluid Dynamics. Oxford Science Publications, Clarendon Press, Oxford, 519p.
- Tsonis, A. A. and J. B. Elsner, 1988: The weather attractor over very short time scales. Nature, 333, 545-547.
- Vautard, R. and M. Ghil, 1989: Singular spectrum analysis in nonlinear dynamics, with applications to paleoclimatic time series. Physica, 35D, 395-424.
- Walden, R. W., P. Kolodner, A. Passner and C. M. Surko, 1985: Traveling waves and chaos in convection in binary fluid mixtures. Phys. Rev. Lett., 55, 496-503.
- Walpole, R. E. and R. H. Meyers, 1989: Probability and Statistics for Engineers and Scientists. Macmillan Publishing Co. N. Y., 765p.
- Walterscheid, R. L. and G. Schubert, 1990: Nonlinear evolution of an upward propagating gravity wave: Overturning, convection, transience and turbulence. J. Atmos. Sci., 47, 101-125.
- Weinstock, J., 1984: Gravity wave saturation and diffusion in the middle atmosphere. J. Atmos. Terr. Phys., 46, 1069-1082.
- Weinstock, J., 1985: Theoretical gravity wave spectrum in the atmosphere: Strong and weak wave interactions. Radio Sci., 20, 1295-1300.

Wolf, A., J. B. Swift, H. L. Swinney and J. A. Vastano, 1985: Determining Lyapunov exponents from a time series. Physica, 16D, 285-319.

Yeh, K. C. and C.H. Liu, 1981: The instability of atmospheric gravity waves through wave-wave interaction. J. Geophys. Res., 86, 9722-9728.

Yeh, K. C. and C. H. Liu, 1985: Evolution of atmospheric spectrum by process of wave-wave interaction. Radio Sci., 20, 1295-1300.